Design, Synthesis, and Characterization of Stimuli-Responsive Organic Fluorescent Materials: An Exploration into Functional Molecular Assemblies

by

SUSANNA POULOSE

10CC17A39017

A thesis submitted to the
Academy of Scientific & Innovative Research
for the award of the degree of
DOCTOR OF PHILOSOPHY
in
SCIENCE

Under the supervision of
Dr. Vijayakumar C.

CSIR-National Institute for Interdisciplinary Science and Technology (CSIR-NIIST), Thiruvananthapuram – 695 019

Academy of Scientific and Innovative Research
AcSIR Headquarters, CSIR-HRDC campus
Sector 19, Kamla Nehru Nagar,
Ghaziabad, U. P. – 201 002, India

JULY 2023

Dedicated to,

my Appa & Amma

whose Light shines through these toils...

CSIR-National Institute for Interdisciplinary Science and Technology (NIIST)
Council of Scientific and Industrial Research, Thiruvananthapuram – 695 019, INDIA

Dr. Vijayakumar Chakkooth, PhD

Principal Scientist, Chemical Sciences and Technology Division
Associate Professor, Academy of Scientific and Innovative Research (AcSIR)
Tel: +91-471-2515-484 (O) +91-9447-835-815 (M); E-mail: cvijayakumar@niist.res.in

July 25, 2023

CERTIFICATE

This is to certify that the work incorporated in this Ph.D. thesis entitled, ***"Design, Synthesis, and Characterization of Stimuli-Responsive Organic Fluorescent Materials: An Exploration into Functional Molecular Assemblies"***, submitted by ***Ms. Susanna Poulose*** to the Academy of Scientific and Innovative Research (AcSIR) in fulfillment of the requirements for the award of the Degree of ***Doctor of Philosophy in Science***, embodies original research work carried out by the student. We further certify that this work has not been submitted to any other University or Institution in part or full for the award of any degree or diploma. Research materials obtained from other sources and used in this research work have been duly acknowledged in the thesis. Images, illustrations, figures, tables etc., used in the thesis from other sources, have also been duly cited and acknowledged.

25.07.23

Susanna Poulose

25/07/23

Dr. Vijayakumar C.

(Supervisor)

STATEMENTS OF ACADEMIC INTEGRITY

I Susanna Poulose, a Ph.D. student of the Academy of Scientific and Innovative Research (AcSIR) with Registration No. 10CC17A39017 hereby undertake that, the thesis entitled ***"Design, Synthesis, and Characterization of Stimuli-Responsive Organic Fluorescent Materials: An Exploration into Functional Molecular Assemblies"*** has been prepared by me and that the document reports original work carried out by me and is free of any plagiarism in compliance with the UGC Regulations on *"Promotion of Academic Integrity and Prevention of Plagiarism in Higher Educational Institutions (2018)"* and the CSIR Guidelines for *"Ethics in Research and in Governance (2020)"*.

25.07.23

Susanna Poulose

July 25, 2023
Thiruvananthapuram

It is hereby certified that the work done by the student, under my supervision, is plagiarism-free in accordance with the UGC Regulations on *"Promotion of Academic Integrity and Prevention of Plagiarism in Higher Educational Institutions (2018)"* and the CSIR Guidelines for *"Ethics in Research and in Governance (2020)"*.

25/07/23

Dr. Vijayakumar C.

July 25, 2023
Thiruvananthapuram

DECLARATION

I, Susanna Poulose, AcSIR Registration No. 10CC17A39017 declare that my thesis entitled, ***"Design, Synthesis, and Characterization of Stimuli-Responsive Organic Fluorescent Materials: An Exploration into Functional Molecular Assemblies"*** is plagiarism-free in accordance with the UGC Regulations on *"Promotion of Academic Integrity and Prevention of Plagiarism in Higher Educational Institutions (2018)"* and the CSIR Guidelines for "*Ethics in Research and in Governance (2020)".*

I would be solely held responsible if any plagiarised content in my thesis is detected, which is violative of the UGC regulations 2018.

25.07.23

Susanna Poulose

July 25, 2023

Thiruvananthapuram

ACKNOWLEDGEMENTS

It is with immense pleasure and great respect that I place on record my deep sense of gratitude to Dr. Vijayakumar C., my thesis supervisor, for suggesting the research topic and for his inspiring guidance, immense knowledge, endearing care, constant support, and motivation, leading to the successful completion of this work.

I wish to thank Dr. C. Anandharamakrishnan, Director and Dr. A. Ajayaghosh, former Director of the CSIR-National Institute for Interdisciplinary Science and Technology, for providing me the necessary facilities for carrying out the work.

I sincerely thank Dr. Masayuki Takeuchi and Mr. Akira Nagai for all the help and support during my internship program at NIMS, Japan.

I sincerely acknowledge Dr. R. Luxmi Varma, Dr. C. H. Suresh, and Dr. V. Karunakaran, former and present AcSIR coordinators, CSIR-NIIST for the timely help and advice for the academic procedures of AcSIR.

I am very much thankful to Dr. Biswapriya Deb, Dr. Joshy Joseph, and Dr. B. S. Sasidhar, my Doctoral Advisory Committee members, for their help, support, suggestion and encouragement throughout my PhD period.

I would like to express my gratitude to Dr. K. V. Radhakrishnan, Dr. P. Sujatha Devi, and Dr. R. Luxmi Varma present and former Heads, Chemical Sciences and Technology Division for their endless support.

I like to thank all the AcSIR faculty members of CSIR-NIIST for their help and support during the course work period.

I would like to thank Dr. K. N. Narayanan Unni, Dr. K. R. Gopidas, Dr. V. K. Praveen, Dr. Suraj Soman, Dr. Sreejith Sankar, Dr. Ishita Neogi, Dr. Jubi John, Dr. Adersh Asok, Dr. Sunil Varughese, Dr. K. Yoosaf, Dr. Bijitha Balan, present and former, and all other scientists of the Chemical Sciences and Technology Division, for all the help and support extended to me.

I would like to acknowledge Prof. Akinori Saeki (Osaka University) for the TRMC analysis, Dr. Bhoje Gowd E. (CSIR-NIIST) for the DSC and XRD analysis, Dr. Pongsakorn Kanjanaboos (Mahidol University) for the AFM nanoindentation measurements, Dr. Sudhadevi (IIT Madras) and Ms. Vidhya (M. G. University Kottayam)

for the SCXRD measurements, Dr. Minu Elizabeth (M. G. University Kottayam) for the computational studies.

I would also like to thank Mr. Robert Philip and Mr. Kiran Mohan for the general help and Mrs. Saumini Mathew for NMR analysis, and Mrs. Viji for HRMS data, Mr. Harish Raj for SEM analysis, and Ms. Neethu K. K., Ms. Divya Pillai, Mr. Basavaraja, Ms. Roopasree, Ms. Drishya Elizabeth, Mr. Nayan Dev for helping me with the various experiments.

I am grateful to my present and former labmates Neethi Raveendran, Dr. Dheepika R., Amarjith V. Dev, Avija A. V., Navin Jacob, Riya Martin, Nishana K., Inayathullah, Dr. Naeem K. C., Dr. Tanwistha Ghosh, Dr. Jayanthy S Panicker, Dr. Chinnadurai M., Dr. Suresh Kumar, Dr. John Paul K. P., Christy Prasad, Nayana Krishna, Manesh Mohan, Abhijith S., Neethu M., Devika S for their love, care and support throughout my research period. I also thank M. Sc. project students Ansiya T. S., Sreedevi T. E., Thabsoom T. P., Geethamani K. for all the help and love.

Words are inadequate to express my gratitude to my dear friends at photosciences and photonics section for their care, love, support, and encouragement, which made my life in NIIST memorable. I also thank all the present and former members of the Chemical Sciences and Technology Division and friends at other Divisions of CSIR-NIIST for their help and cooperation.

I am forever grateful to my dear friends Sheba, Shibu, Indu, Vishnu, Nishna, and Vyshnapriya for always being a source of happiness, love and support.

I am deeply indebted to my Appa, Amma, and my sisters Elisba and Sarah, and my cute little nephews Ihan and Jain, brothers Anoop and Sanjay, Mamma, Yayi, Deepu, and other family members for their continued energy, unconditional love, and unerring support in my life. I am deeply grateful to my significant other Ashish for all the patience, understanding, love, and support. I would also like to extend my thanks and appreciation to all my teachers for their help and blessings.

Finally, I sincerely thank the University Grant Commission (UGC) JRF and SRF for financial assistance.

Above all, I thank Almighty for all his blessings.

Susanna Poulose

TABLE OF CONTENTS

LIST OF ABBREVIATIONS

Å	Angstrom
ACN	Acetonitrile
ACQ	Aggregation-caused quenching
AFM	Atomic force microscopy
AIE	Aggregation induced emission
Ar	Argon
A–D–A	Acceptor-donor-acceptor
B3LYP	Becke 3-parameter, Lee-Yang-Parr
BFDH	Bravais-Friedel-Donnay-Harker
calcd.	Calculated
$CDCl_3$	Deuterated chloroform
CH_2Cl_2	Dichloromethane
CH_3CN	Acetonitrile
$CHCl_3$	Chloroform
cm	Centimeter
Conc.	Concentration
CT	Charge transfer
DB	Divinylbenzene-benzoxazole
DCE	Dichloroethane
DCM	Dichloromethane
DFT	Density functional theory
DMF	Dimethylformamide
DMSO	Dimethyl sulfoxide
DNA	Deoxyribonucleic acid
DSC	Differential scanning calorimetry
D–A	Donor-acceptor
D–A–D	Donor-acceptor-donor
EC	Electrochromic
EFC	Electrofluorochromic
equiv.	Equivalent
ESI	Electrospray ionization
et al.	Et alia
EtOAc	Ethyl acetate

EtOH	Ethanol
eV	Electron volt
FT-IR	Fourier transform-infrared
f_w	Water fraction
g	Gram
Gpa	Giga Pascal
h	Hour
HBr	Hydrogen bromide
HCl	Hydrochloric acid
HRMS	High-resolution mass spectrometry
ICT	Intramolecular charge transfer
IR	Infrared
ITO	Indium tin oxide
IVCT	Intervalence charge transfer transitions
J	Coupling constant
K	Kelvin
K_2CO_3	Potassium carbonate
KBr	Potassium bromide
KI	Potassium iodide
KOH	Potassium hydroxide
LE	Locally excited
M	Molar
m.p	Melting point
MCF	Mechanochromic fluorescent
MCL	Mechanochromic luminescence
MeOH	Methanol
MHz	Mega hertz
min	Minute
ML	Mechano luminescence
mL	Millilitre
mM	Millimolar
mol	Mole
MPa	Mega Pascal
MRL	Mechanoresponsive luminescence

Na_2SO_4	Sodium sulphate
$NaHCO_3$	Sodium bicarbonate
NaOH	Sodium hydroxide
NaOH	Sodium hydroxide
NH_3	Ammonia
NIR	Near-infrared
nm	Nanometer
NMR	Nuclear magnetic resonance
ns	Nanosecond
$Pd(PPh_3)_4$	Tetrakis(triphenylphosphine)palladium(0)
PMMA	Polymethyl methacrylate
$POCl_3$	Phosphoryl chloride
ppm	Parts per million
ps	Picosecond
PXRD	Powder X-ray diffraction
s	Seconds
SCXRD	Single crystal X-ray diffraction
SEM	Scanning electron microscopy
t	Time
T	Temperature
TCSPC	Time correlated single photon counting
TEA	Triethylamine
TFA	Trifluoroacetic acid
TGA	Thermogravimetric Analysis
THF	Tetrahydrofuran
TIBO	Thienoindole-benzoxazole
TICT	Twisted intramolecular charge transfer
TiTz	Thienoindole-thiazolothiazole
TMS	Tetramethylsilane
TPE	Tetraphenylethylene
TRMC	Time-resolved microwave conductivity
UV	Ultra Violet
UV-vis	Ultra Violet-visible
XRD	X-ray diffraction

0D	Zero-dimensional
1D	One-dimensional
2D	Two-dimensional
3D	Three-dimensional
$\Delta\lambda$	Change in wavelength
τ_{av}	Average fluorescence lifetime
ϕ	Charge-carrier generation quantum yield
°C	Degree Celsius
τ	Fluorescence lifetime
Φ_F	Fluorescence quantum yield
µL	Microliter
µm	Micrometer
µM	Micromolar
ε	Molar extinction coefficient
%	Percentage
θ	Reflection
$\Sigma\mu$	Sum of charge-carrier mobilities
λ	Wavelength
λ_{abs}	Wavelength of absorption
λ_{em}	Wavelength of emission
λ_{ex}	Wavelength of excitation

PREFACE

"Smart materials", also known as "stimuli-responsive materials", have the unique ability to sense and respond to their surrounding environment in a timely manner. These materials can detect, transmit, or process a stimulus and in response, generate a useful outcome. Such stimuli can range from temperature, pressure, moisture, light, electric or magnetic fields, nuclear radiation, to pH. As a result, these materials exhibit variable physical properties such as color, luminescence, shape, stiffness, viscosity, damping, refractive index, stress or strain distribution, or volume. Importantly, these changes are reversible and can be repeated multiple times. As automation increases, reducing the need for human interaction, the development of smart materials has become increasingly critical, finding applications in sensors, security inks, and actuators. Within this domain, organic materials with reversible solid-state luminescence induced by external stimuli are particularly desirable due to their distinct optical and electronic properties. However, achieving such high-contrast and reproducible switching is a formidable challenge.

One promising strategy is to control the solid-state packing mode of luminescent organic chromophores with an external stimulus. Over the past decade, organic solid-state smart luminescent materials have gained considerable interest due to their exceptional scientific and technological applications. These materials have found wide-ranging uses in various devices, such as organic light-emitting diodes, dye lasers, displays, security printing, data recording and storage, and sensors. This thesis focuses on the design, synthesis, and photophysical properties of various fluorescent organic stimuli-responsive materials. It further highlights how minor molecular structural changes can impact intermolecular interactions, self-assembly, and optical properties, ultimately influencing stimuli-responsive behavior.

The thesis is divided into four chapters. The first chapter provides an overview of fluorescent organic stimuli-responsive materials and the recent advancements in this field. This chapter elaborates on the different non-covalent interactions involved in the molecular self-assembly process. It also discusses various strategies to tune the optical properties of organic fluorophores through structural rearrangement instigated by external stimuli. This chapter delves into specific case studies of molecules that have shown promising results. The study also explores the potential applications of these

organic stimuli-responsive materials, shedding light on their role in real-world scenarios such as optoelectronic devices, security ink, data storage, and more.

In the second chapter, we presented the design and synthesis of three novel acceptor-donor-acceptor type divinylbenzene-benzoxazole-based derivatives with distinct alkyl sidechains. These molecules exhibit thermoresponsive photoluminescence switching in the solid state. The luminescence changes are primarily attributed to heat-induced switching from parallel to orthogonal configurations, toggling charge transfer states 'on' and 'off' within the molecular assemblies formed *via* hydrogen bonding and π–π stacking. Notably, characteristics of the luminescence switching, such as its reversibility, color range, and transition temperature, are found to be dependent on the length of the alkyl chains. This observation underscores the importance of alkyl chain length as a significant parameter in controlling the stimuli-responsive properties of these molecules. Our studies demonstrated that exercising control over the charge-transfer interactions in chromophore assemblies offers a versatile approach for developing functional organic materials characterized by switchable, high-contrast solid-state luminescence.

The third chapter describes the synthesis of a thienoindole-benzoxazole based novel donor-π-acceptor type fluorophore and its light-induced [2+2] cycloaddition reaction and stimuli-responsive properties. This study illustrates the daylight-induced, regioselective and stereospecific, catalyst- and template-free [2+2] cycloaddition of molecule and successfully obtained a photoconductive cyclobutane derivative *via* photodimerization. Donor-acceptor π–π interactions between the monomer units bring the two double bonds closer and arrange them in a specific geometry to yield a single *syn*-HT photodimer during crystallization. X-ray diffraction analysis of the resulting crystals reveals that the cyclobutane derivative forms a one-dimensional assembly through intermolecular hydrogen bonding. This unique molecular arrangement fosters π–π interactions between adjacent 1D assemblies, generating two-dimensional layered structures. Outperforming typical fullerene-based semiconductors in terms of photoconductivity, this material emerges as a potential candidate for use in organic optoelectronic devices.

In the last chapter, we reported the design and synthesis of thienoindole-thiazolothiazole based two novel π-conjugated donor-acceptor-donor type NIR

fluorophores, exhibiting high contrast mechanoresponsive luminescence turn-on in the NIR region with high fluorescence quantum yields (Φ_F > 30%). Our approach relies on the generation of metastable, kinetically trapped states of chromophores that are sensitive to their surrounding environment. When a mechanical stimulus is applied, these metastable states transformed into thermodynamically stable states, unveiling new emission characteristics. A comprehensive understanding of luminescence change has been achieved through precise correlation of optical, morphological, and structural properties. Our results provide an insight into the structure-property relationship of MRL turn-on materials emitting in the NIR region and presents an exciting pathway for the design and synthesis of new organic functional materials intended for high-contrast optical recording, mechanical force sensor, and security application.

Chapter 1

An Overview of Recent Developments in Stimuli-Responsive Organic Fluorescent Materials

1.1. Abstract

Stimuli-responsive or "smart" materials refer to substances that display traceable, measurable, and reversible changes in response to external stimuli such as temperature, light, mechanical force, chemicals, electric fields, or magnetic fields. The ability to control these properties under different stimuli has significantly transformed the realm of supramolecular chemistry. Specifically, the optoelectronic attributes of organic chromophores assembled via various non-covalent interactions can be readily modulated by altering the molecular packing mode and/or supramolecular interactions. Organic materials that exhibit reversible solid-state luminescence under external stimuli are particularly desirable, as they offer broad prospects for advanced applications, including sensors, data storage, and security inks. This chapter highlights the recent advancements in fluorescent organic smart materials, with a special focus on changes induced thermally and mechanically to the molecular packing mode, and photo-induced chemical structural modifications. Finally, the objectives and outline of the thesis are presented.

1.2. Introduction

Luminescent solids based on π-conjugated small organic molecules are currently under intensive study due to their scientific and technological significance in the optoelectronics domain. These materials play crucial roles in creating solid-state lasers, light-emitting diodes, luminescent sensors, optical waveguides, photoswitches, fluorescent markers, and biological probes.[1-7] The prominent benefits of organic materials over their inorganic counterparts include their potential for optoelectronic property modulation through chemical modifications, lower power consumption, and cost-effective fabrication. However, many of these organic materials are prone to aggregation-caused emission quenching (ACQ) due to strong intermolecular π–π interactions in the aggregated state, which impedes the construction of luminescent solid-state emitters.[8] In response to this limitation, Tang and co-workers proposed a novel concept in 2001, termed aggregation-induced emission (AIE), which stands in contrast to the ACQ effect.[9] These AIE materials are highly emissive in their aggregated state, while non-emissive in their diluted state. The development of these AIE characteristics is largely influenced by intermolecular and intramolecular interactions in the aggregated state.[10]

The precise control over the luminescent properties of organic materials has emerged as a central research objective in materials science.[11-13] Pursuit of this goal not only forges the path for the creation of advanced materials with dynamic optical properties, but also contributes to the development of fundamental theories and to the

exploration of luminescent mechanisms.[14-16] Supramolecular strategies simplify the design and production of organic functional materials and bestow dynamic reversibility and stimuli responsiveness upon them through the use of dynamic and reversible noncovalent bonding interactions.[17-19] Among the range of organic luminescent materials, color tunable luminescent materials have particularly drawn attention due to their potential applications in multicolor displays, anti-counterfeiting measures, optical recording, and bioimaging.[20-23]

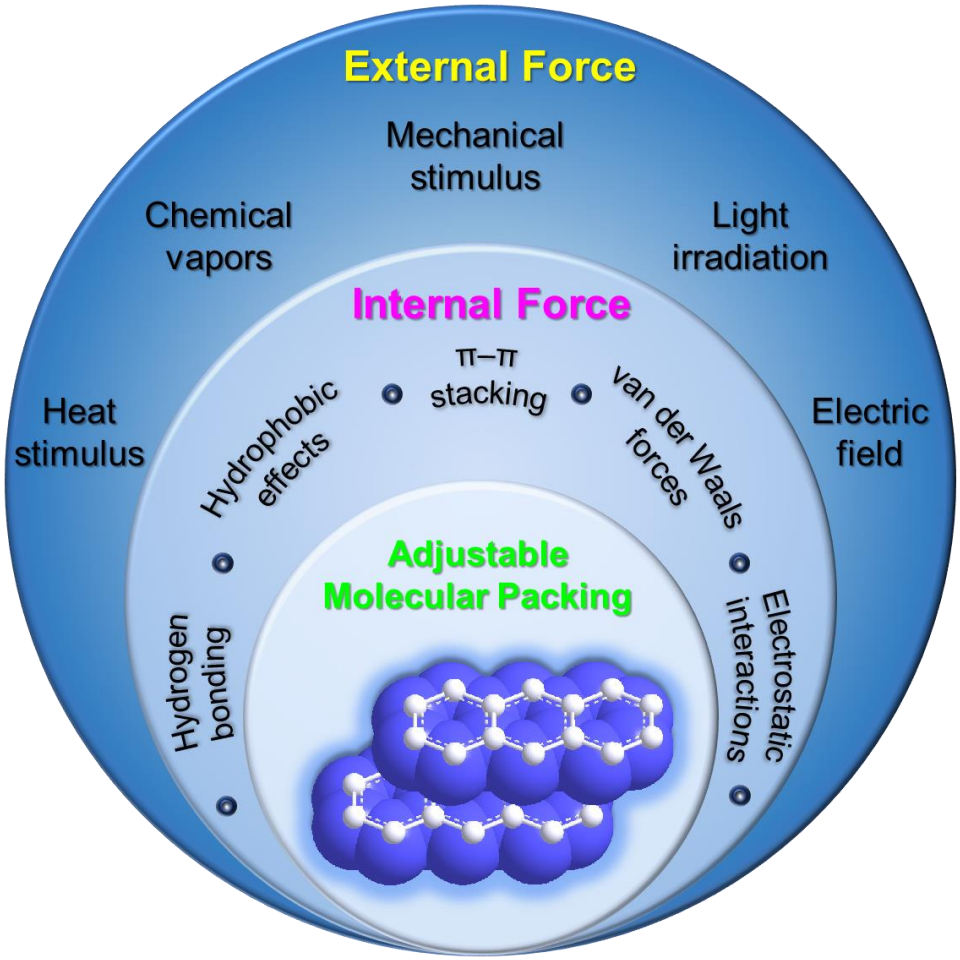

Figure 1.1. Schematic illustration of the factors affecting the molecular packing in organic materials.

Strategies for optimizing the structure-packing-performance relationship of organic materials are depicted in **Figure 1.1**. These include the design of functional molecules, taking into account the steric and electronic effects of the functional group, as well as their self-assembly, which serves as a potent internal force to regulate the interactions among molecules in the assembled state. Subsequently, external stimuli such as heat, light irradiation, mechanical force, and electric fields are applied to investigate the dynamic aggregated assemblies and their functional properties.

1.3. Non-covalent interactions and molecular self-assembly

Molecular self-assembly serves as a powerful tool for constructing unique supramolecular architectures. Typically, molecular self-assembly refers to the spontaneous organization of molecules under thermodynamic equilibrium conditions into stable, structurally well-defined arrangements. This organization occurs through various non-covalent interactions, including electrostatic interactions, hydrogen bonding, π–π stacking, van der Waals forces, and the hydrophobic effect. Within these self-assembled structures, intermolecular forces link the molecular building blocks in a reversible, controllable, and specific manner.[24]

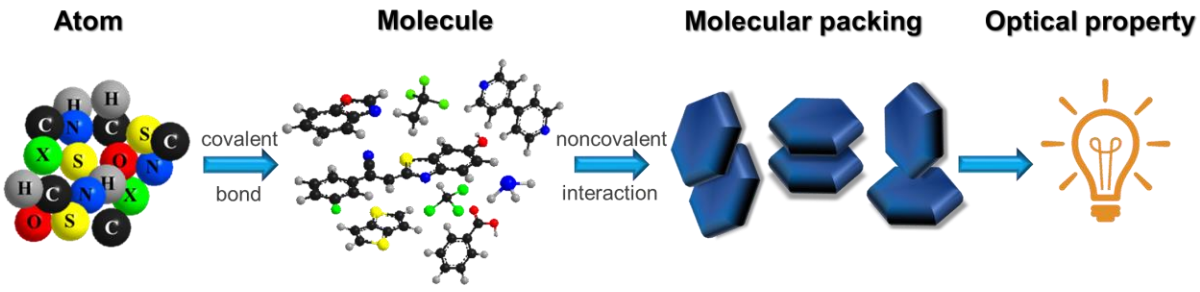

Figure 1.2. Schematic depiction of the construction process of organic functional materials.

Supramolecular chemistry and solid-state chemistry are two intertwined fields that utilize non-covalent interactions as tools to achieve control over solid-state assembly and properties. The supramolecular approach is employed to create dynamic molecular aggregated states in organic materials, with advanced functional properties induced by external forces.[25-26] The following section discusses significant non-covalent interactions used in the construction of supramolecular self-assemblies. **Figure 1.2** provides a schematic overview of the assembly process of these organic functional assemblies.

1.3.1. Electrostatic interaction

Electrostatic interactions play an important role in the stability and functional property of molecular assemblies. The attractive or repulsive interactions occur between charged ions or molecules are electrostatic in nature. Ion-ion, ion-dipole, and dipole-dipole interactions are typical examples of electrostatic interactions, which arise due to the delocalization of charges on organic molecules. These interactions possess a vital role in determining conformation of molecules and thereby the organization of self-assembled structures. Among various electrostatic interactions, attraction between oppositely charged ion-ion interactions are the strongest, which is comparable to the strength of the covalent bond. Ion-dipole interactions, which involve non-covalent bonding between ions and polar molecules, are another type of electrostatic contact. A typical example of this type is the binding of cations (Na^+, K^+, etc.) by crown ethers.[27] Dipole-dipole interactions are formed by the mutual electrostatic attraction between

two adjacent dipoles aligned in an opposite manner.[28] All of these interactions lead to charge-balanced, stable supramolecular arrangements that can self-organize into hierarchical structures.

1.3.2. Hydrogen bonding

A hydrogen bond, X–H···A, is an interaction in which a hydrogen atom is attracted to two atoms, X and A, rather than just one and so acts like a bridge between them.[29] These bonds are specific, short-range, and directional nonbonded interactions and can

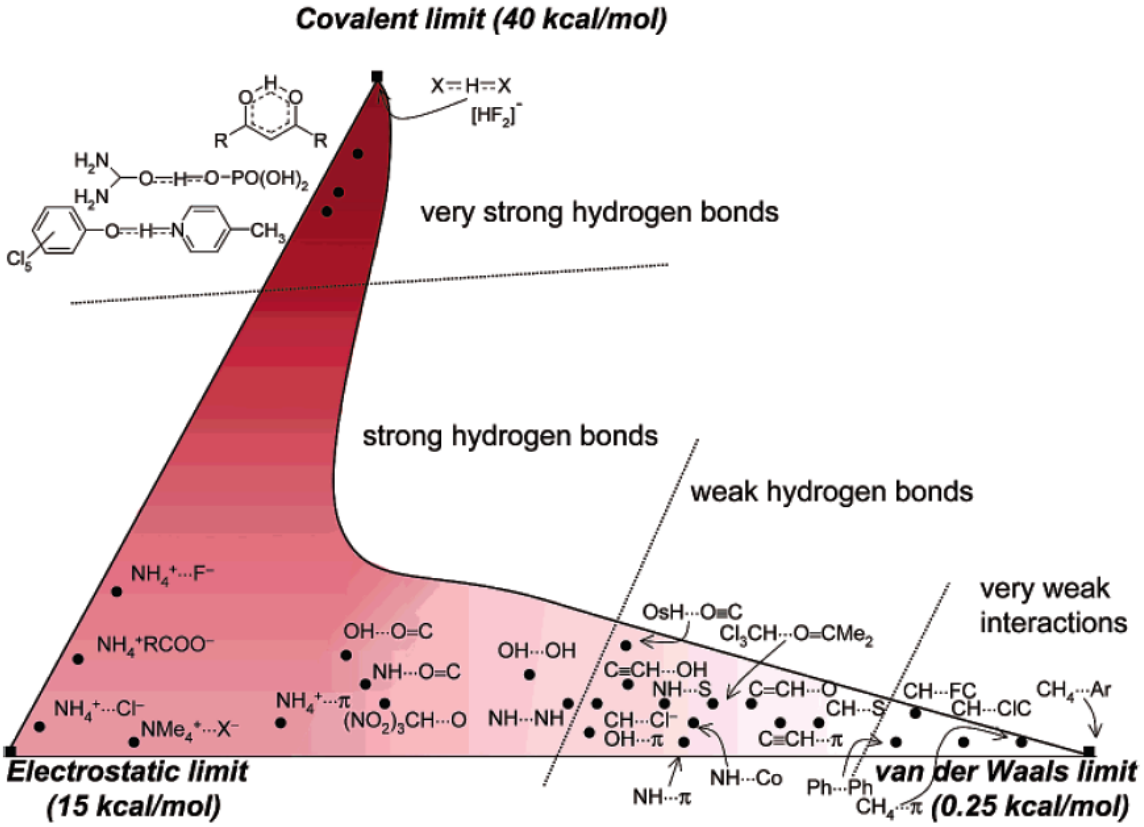

Figure 1.3. The hydrogen bridge. Various types of hydrogen bonds observed in the solid state. (Adapted from reference 29)

tune their strength by structural modifications. As the electronegativity of X and A rises, this attraction always increases, and all hydrogen bonds are considered as a highly electrostatic and sometimes even partly covalent in the classical view. The concept of a hydrogen bond interaction became more relaxed over time. Thus, weaker interactions can be considered as H-bonding if some electrostatic character remains in it. These weak hydrogen bonds have substantial dispersive-repulsive character in the limit and merge into van der Waals interactions.[29] A great variety of hydrogen bonds that observed in the solid state are highlighted in the **Figure 1.3**.

H-bonds are indispensable for the existence of DNA as a double helix and water as a liquid, which makes them crucial for life on Earth. Apart from their fundamental significance, they have the ability to arrange molecules in several ways to create functional supramolecular structures in a variety of shapes with the assistance of other non-covalent interactions. Organic luminescent materials containing hydrogen bonds can form a variety of self-assembled structures, such as nanofibers, molecular sheets, 1D molecular columns and micro-loops.[30-32] Presence of inter- or intramolecular hydrogen bonds in the compounds containing peptide segments or amino acids also afford stable and robust self-assembly.[33-34]

1.3.3. π–π stacking

The π–π interactions are one of the most attractive and significant noncovalent interactions in the molecules having π systems such as unsaturated (poly)cyclic carbonaceous materials. The strong attractive interactions between two or more

neighboring aromatic rings are known as π–π stacking.[35] Additionally, these π–π stacking interactions are particularly interesting in the field of material engineering since they are simple, nondestructive, and reversible.[36] A prominent example of π–π stacking interactions is their role in stabilizing the double helical structure of DNA, alongside hydrogen bonding interactions. π–π stacking plays a very crucial role in the molecular self-assembly process. However, our understanding of how to control π–π interactions remains in its infancy, and extensive research is still required for a more comprehensive understanding.[37-38] π–π stacking often results in excited-state complexes, which promote non-radiative decay and thereby decreases the luminescence intensity. Nevertheless, such effects can be reduced by using rational molecular frameworks.

1.3.4. Van der Waals force

Van der Waals forces consist of attractive and repulsive energies acting on permanent, instantaneous, and induced dipoles between atoms or molecules. These non-directional, weak forces are generated by the polarization of an electron cloud in one atom due to the proximity of an adjacent nucleus in another atom. Depending on the molecules involved in the interaction, van der Waals forces can be classified into three categories: Keesom forces, Debye forces, and London (or dispersion) forces. Keesom forces occur when two polarized molecules interact due to an inherent difference in charge distribution. Debye forces, on the other hand, arise when a molecule with a permanent dipole induces charge redistribution in neighboring molecules without

dipole moments. The third type, London dispersion forces, arise in molecules without permanent dipoles. Among nonpolar molecules lacking permanent dipoles, this London force represents the sole desirable van der Waals contribution.[42] It's important to note, however, that van der Waals forces alone are typically insufficient to bring molecules together to form a supramolecular assembly. In the self-assembled structure, all other potential non-covalent interactions-such as hydrogen bonding, π–π stacking, and the hydrophobic effect-coexist alongside van der Waals forces.

1.3.5. Hydrophobic effect

The hydrophobic effect represents another significant non-covalent interaction observed in molecular assemblies. Essentially, the hydrophobic effect is a combination of the cohesive nature of water and van der Waals interactions between solutes, and it is capable of driving the formation of many supramolecular complexes in nature. Hydrophobic interactions involve the exclusion of non-polar molecules or those that are weakly solvated from water, which is a polar solvent. In other words, hydrophobic effects facilitate the interaction between non-polar molecular surfaces in polar media.[39] This effect can stimulate the mutual attraction between organic moieties in a polar medium, leading to the formation of a stable self-assembly. In this regard, introducing amphiphilic groups or attaching long alkyl chains to organic luminogens represents a straightforward strategy for enhancing their self-assembly potential.[40-41]

1.4. Control methods to tune the optical properties *via* external forces (physical & chemical structural changes)

In the previous section, we discussed various intermolecular interactions employed for the formation of molecular self-assembly or packing. Numerous strategies exist for tuning the optical properties of these functional molecular assemblies through dynamic processes, thanks to the weak and reversible nature of non-covalent interactions that govern molecular packing. The upcoming section will provide details on how external stimuli, such as thermal, mechanical, light, chemical vapors, and electric fields, can efficiently control solid-state optical properties via chemical and physical structural modifications of the molecular stacks.

1.4.1. Thermal stimulus

Thermal stimuli represent a clean source of input energy that typically does not result in covalent structural variations or chemical reactions in the aggregated state. Materials that exhibit changes in their emission color and intensity when heated at specific temperatures are known as thermochromic luminescent materials. The use of heat-induced phase changes is an efficient method for controlling the solid-state luminescence of molecular assembly.[43] In 2010, Yoon *et al.* reported a cyano stilbene based derivative end functionalized with butoxyphenyl group (**1**, **Figure 1.4a**), which uniquely forms luminescent molecular sheets with multi stimuli-responsiveness.[32] The multiple intermolecular C–H···N and C–H···O hydrogen bonds aided in the formation

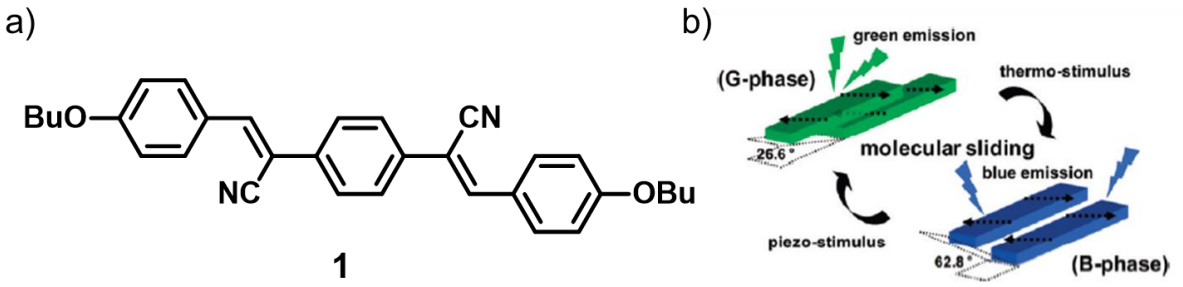

Figure 1.4. a) Chemical structure of **1**. b) Schematic representation of stimuli mediated interconversion between two different modes of slip-stacking in compound **1** molecular sheets. (Adapted from reference 32)

of molecular sheets with stacking and shear-sliding abilities. Compound **1** can exist in two distinct phases: the green-emitting G-phase and the blue-emitting B-phase. Upon heating at 125 °C, G-phase exhibited a smooth slipping of molecular sheets to form B-phase and this switching can be reversed (B-phase to G-phase) by the application of pressure (**Figure 1.4b**). The driving force for this phase transition is triggered by the local dipoles offered by the cyano group. Antiparallel coupling of the local dipoles kinetically stabilizes the metastable G-phase, while thermal induced molecular sliding lead to the formation of B-phase which is having the energetically favored head-to-tail arrangement of the local dipoles.

Zhang and coworkers synthesized a *p*-methoxyphenyl substituted dibenzofulvene derivative (**2**, **Figure 1.5a**), which exhibit AIE behavior.[44] Compound **2** shows polymorphism and can exist in two crystalline forms: **2a** (blue emissive) and **2b** (yellow-green emissive), whereas the amorphous solid shows weak orange emission. Single crystal X-ray analysis confirmed the two distinct molecular conformations in

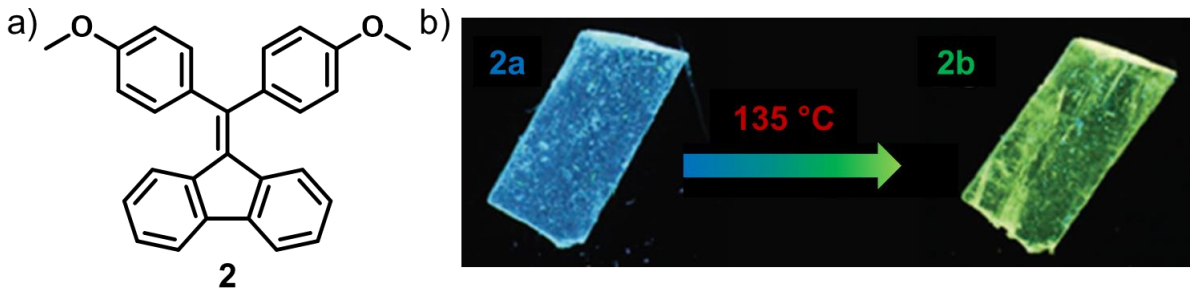

Figure 1.5. a) Chemical structure of **2**. b) Fluorescence microscopic images of the crystal-to-crystal transformation from **2a** to **2b** upon heating at 135 °C. (Adapted from reference 44)

crystalline polymorphs **2a** and **2b**, which is attributed to the different emission colors in these crystalline forms. Upon heating at 135 °C, crystal-to-crystal transformation from **2a** to **2b** was realized (**Figure 1.5b**). The amorphous form can be obtained by heating either of the crystalline forms until they melt, followed by rapid cooling using liquid nitrogen. Additionally, **2a** or **2b** can be partially converted into amorphous form by grinding.

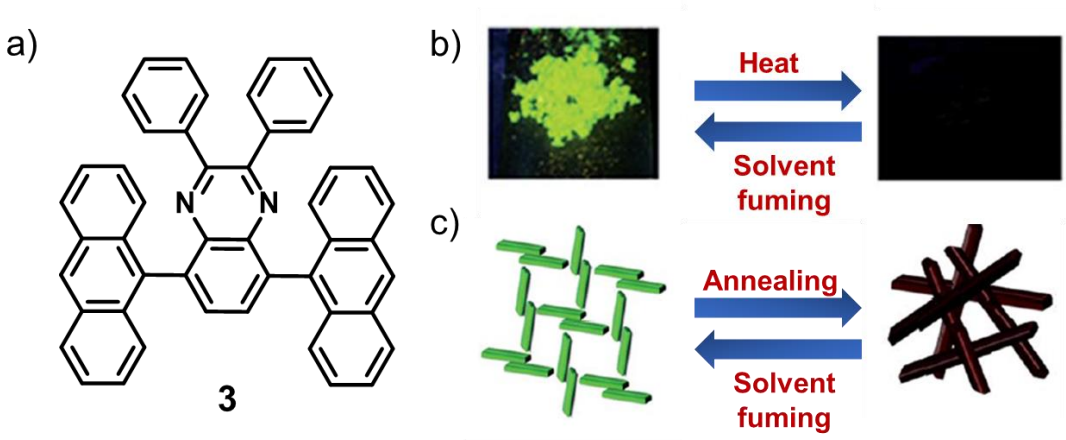

Figure 1.6. a) Chemical structure of **3**. b) Photographic images of heat induced solid-state emission swithching in compound **3** (under 365 nm UV light). c) Schematic representation of the thermochromic response in **3**. (Adapted from reference 45)

A unique luminescence on-off switching induced by thermal stimulus was demonstrated by the Sun's group.[45] They synthesized a D–A–D type molecule using a diphenylquinoxaline core and two anthracene units (**3**, **Figure 1.6a**). Heating the pristine sample of **3** at 170 °C for 5 minutes, the bright green fluorescent pristine form converted into a non-emissive, orange colored solid. This non-emissive state can be reverted back to the original green emissive state by solvent fuming (**Figure 1.6b**). The on-off emission switching observed in **3** is attributed to the transformation from a herringbone arrangement in the pristine state to poorly organized one dimensional *J*-type aggregates. A schematic illustration of the transition from a 2D herringbone structure to 1D *J*-type stack is shown in the **Figure 1.6c**. This study exemplified the thermal induced high contrast reversible on-off luminescence switching as a result of the alterations in the molecular stacking.

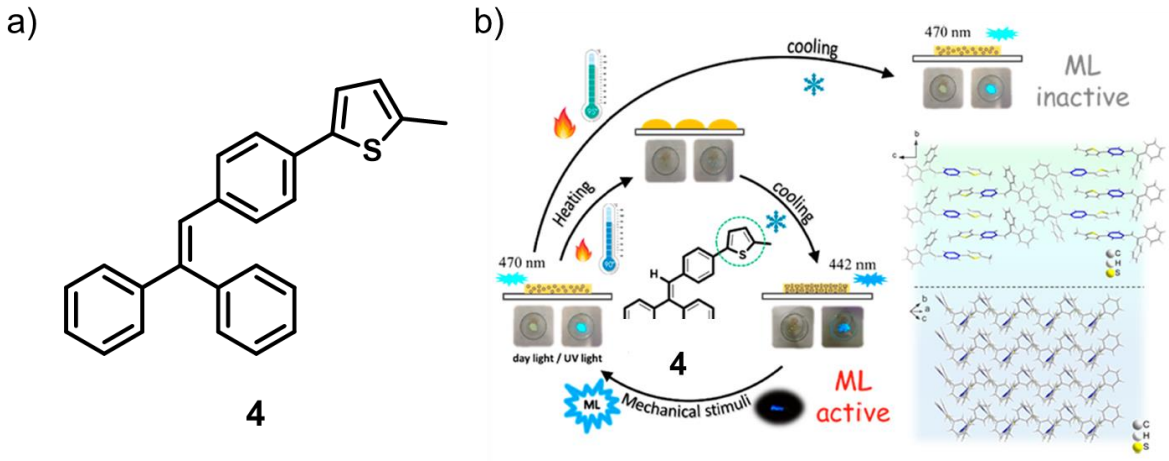

Figure 1.7. a) Chemical structure of **4**. b) Strategy to achieve controllable stimuli-responsivity in **4** through self-assembly. (Adapted from reference 46)

Recently, Wang *et al.* demonstrated an interesting thermal control over the mechanoluminescence (ML) property of an organic molecule consist of an AIEgen and a thiophene unit (**4**, **Figure 1.7a**).[46] Compound **4** shows polymorphic behavior and exists in two different crystalline states having totally different molecular packing and other inter/intramolecular interactions. Switching between these two states can be achieved through mechanical stimuli, precisely controlled by temperature. Pristine powder of **4** has a greenish-blue emission (470 nm), which upon heating at 90 °C (first phase transition) for a few seconds followed by cooling down to room temperature resulted in a blue emissive (442 nm) state. This blue emissive form (crystal P1) was mechanically active and could be reverted back to the amorphous greenish-blue emissive state through mechanical actions. On the other hand, if the pristine sample was heated to 95 °C (the second phase transition), followed by a slow cooling process to encourage recrystallization (into crystal P2), no change in the emission color was observed. Moreover, this state did not exhibit any luminescence change upon grinding. Thus, the two temperature points of 90 °C and 95 °C were found to distinctly differentiate the formation of the two types of crystals. This temperature control made compound **4** exhibit different ML properties because of the effective transformation of molecular packing modes (**Figure 1.7b**).

Recently, Zhang's group introduced a novel ternary solvated cocrystal structure based on a naphthalenediimide (**5**) and coronene (**6**) derivatives with tetrahydofuran (THF) molecules in it (**Figure 1.8a**).[47] This co-assembled system exhibits high contrast

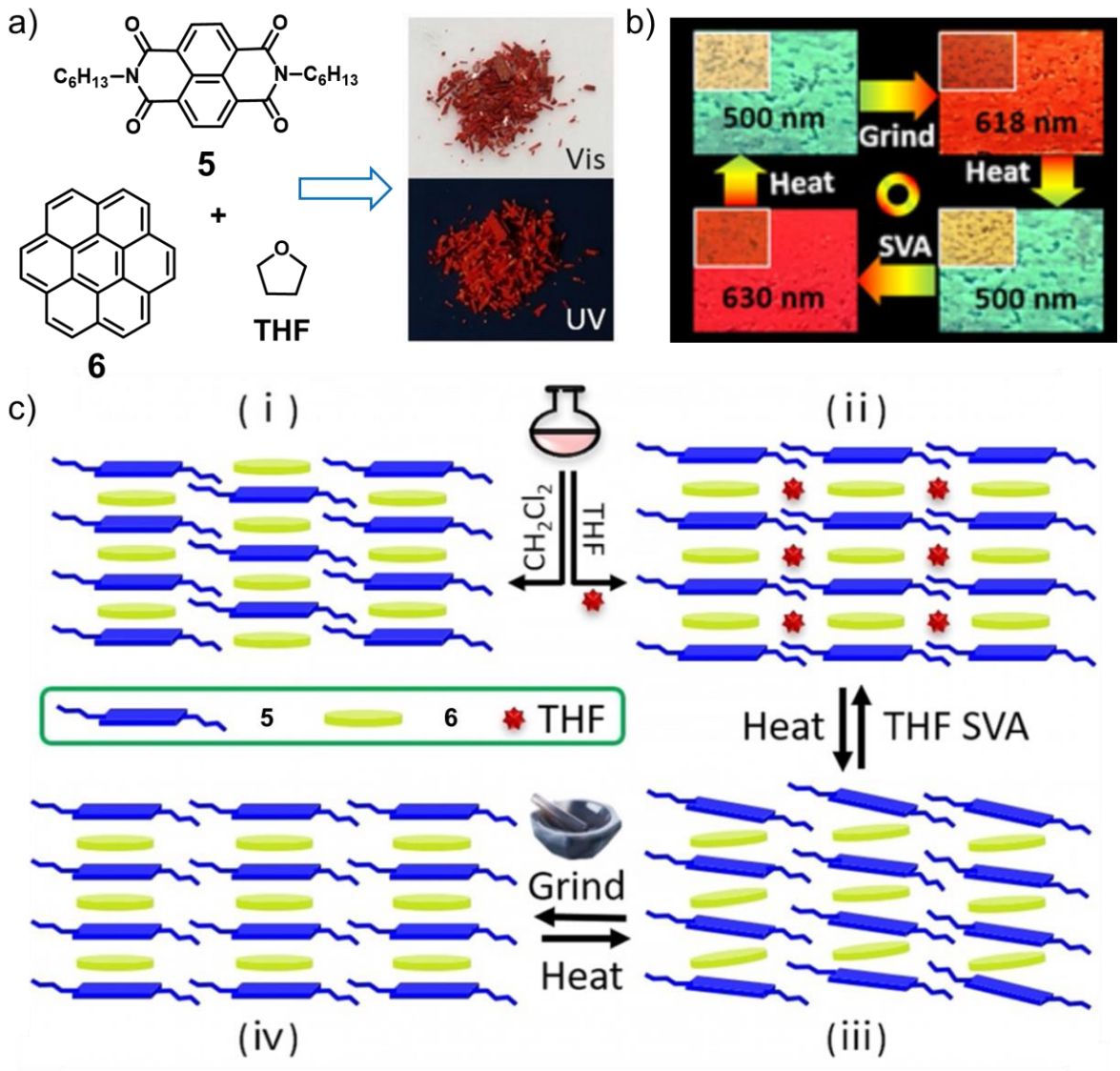

Figure 1.8. a) Chemical structure of **5** (acceptor), **6** (donor) and THF molecules and images of the cocrystal under daylight and 365 nm UV light. b) Images of reversible luminescence switching in response to external stimuli (under 365 nm UV light). c) Schematic illustration of the molecular packing in binary cocrystal (i), ternary cocrystal (ii) and transformations under multi-stimuli. (Adapted from reference 47)

reversible red *versus* green emission color switching in response to external stimuli such as thermal, mechanical, and solvent vapor as shown in **Figure 1.8b**. Inclusion of

THF molecules to the binary system prepared from dichloromethane (DCM, CH_2Cl_2) increases the distance between the donor and acceptor moieties and weakens intermolecular contacts, preparing the system for stimuli-responsive behavior. Under external stimuli a structural rearrangement in the molecular packing occurs, which leads to the alterations in the electrostatic charge transfer (CT) and hydrogen bonding interactions. These variations could be ascribed to the observed changes in the color and emission of the system (**Figure 1.8c**). Development of the organic fluorophores exhibiting thermoluminescence behavior in the solid state are still facing challenges, thus required careful and ingenious molecular design.

1.4.2. Mechanical stimulus

Mechanical forces can indeed modify molecular packing modes and properties, all without breaking covalent bonds. This makes mechanical stimulation a valuable tool for creating dynamic functional materials. Specifically, materials that exhibit fluorescence switching in response to mechanical stimuli are classified as mechanochromic fluorescent (MCF) materials. The dynamic emission switching capabilities of MCF materials have diverse potential applications. They can be used in sensors, memory devices, informational displays, and security features, particularly when working with luminescent materials that are highly sensitive to the molecular packing mode. In such cases, even small changes in molecular packing can lead to significant shifts in luminescence, which can be exploited for various practical purposes.

Several MCF materials have been developed with varying structure-packing-performance relationships. For instance, some MCF materials are designed to shift their luminescence in response to specific mechanical forces, while others may change their

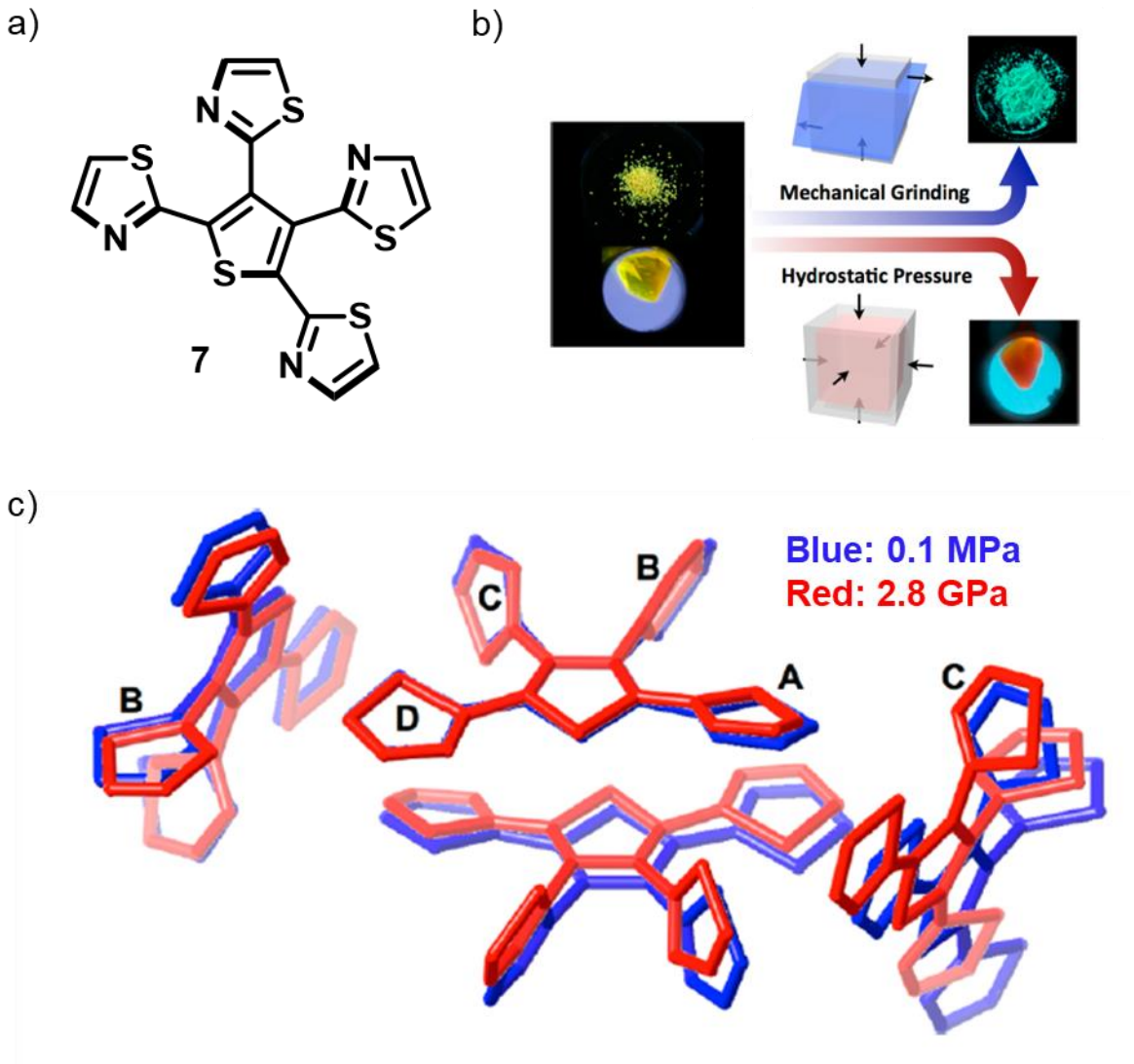

Figure 1.9. a) Chemical structure of **7**. b) Images of **7** under distinct response to mechanical grinding and hydrostatic pressure. c) X-ray crystal packing structures of **7** at ambient pressure (blue) and at 2.8 GPa (red) are shown in superimposed view. (Adapted from reference 48)

luminescence under a broader range of mechanical stimuli. Understanding these relationships can allow researchers to fine-tune the properties of MCF materials, leading to more effective and specialized applications. In the following section, we will delve into the structure-packing-performance relationship of several MCF materials, exploring how their design and assembly processes influence their mechanochromic properties.

The distinct luminescence response to anisotropic pressure by mechanical grinding and isotropic pressure by hydrostatic compression in tetrathiazolylthiophene (**7**, **Figure 1.9a**) molecule was exemplified by Yamaguchi's group.[48] The yellow emissive crystals of **7** displayed a blue shifted emission from yellow (λ_{max} = 556 nm) to green (λ_{max} = 490 nm) upon anisotropic grinding and a red shifted emission to orange (λ_{max} = 609 nm) under isotropic compression (**Figure 1.9b**). As shown in the **Figure 1.9c**, two α-positioned thiazole rings (A and D) and the central thiophene ring adopted a coplanar conformation, forming a π-conjugated backbone. While, the other two rings (B and C) adopted a twisted conformation. The intermolecular C–H···N hydrogen bonding between adjacent molecules facilitated the formation of face-to-face dimeric structure between the π-conjugated skeleton, which lead to the formation of 3D hydrogen-bonded network of **7** in the crystal lattice. Hence, the observed blue shift is ascribed to the suppression of excimer formation due to its transformation from 3D hydrogen-bonded network to a disordered phase (disruption of face-to-face π-stacked structure)

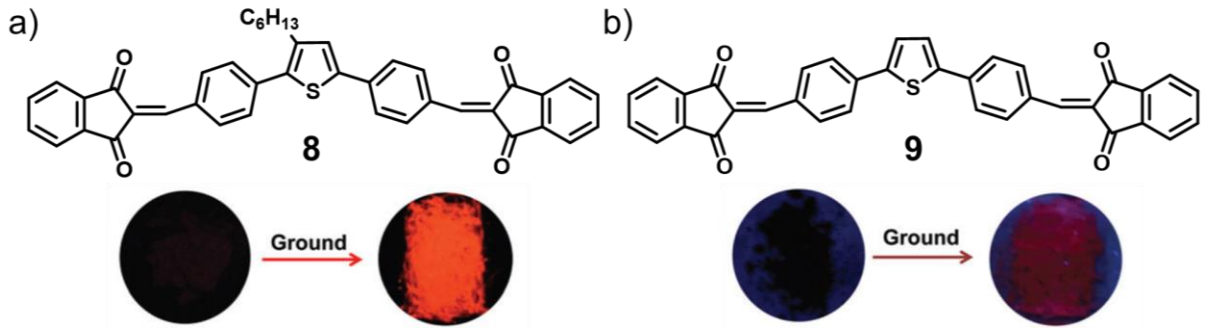

Figure 1.10. a) Chemical structure of **8** and the images of red emission turn-on in their 0D particles under mechanical grinding. b) Chemical structure of **9** and the images of NIR emission turn-on in their 0D particles under mechanical grinding. (Adapted from reference 50)

on grinding. While, the red shift is due to the excimer formation as a consequence of the closer arrangement of face-to-face dimer of **7** under 2.8 GPa pressure than the ambient pressure (0.1 GPa) in 3D hydrogen-bonded network.

Nowadays mechanoresponsive luminescence (MRL) turn-on materials are in high demand compared to those showing mechano responsive luminescence dichromic or quenched features.[49] In 2017, Guo *et al.* achieved a red/NIR MRL turn-on in two slightly twisted A–D–A type NIR fluorophores of diphenylthiophene (donor) and 1,3-indandione (acceptor) units.[50] The quick aggregation (fast evaporation of solvent) of molecules lead to the formation of non-emissive 0D metastable assembly in both the compounds. Because of the random arrangement (disturbed *J* aggregation) of these metastable 0D particles during mechanical grinding, an amorphous solid with a high emission was produced. The hexyl derivative (**8**, **Figure 1.10a**) exhibited remarkable red (λ_{em} = 620 nm) MRL turn-on characteristics with 12% fluorescence quantum yield.

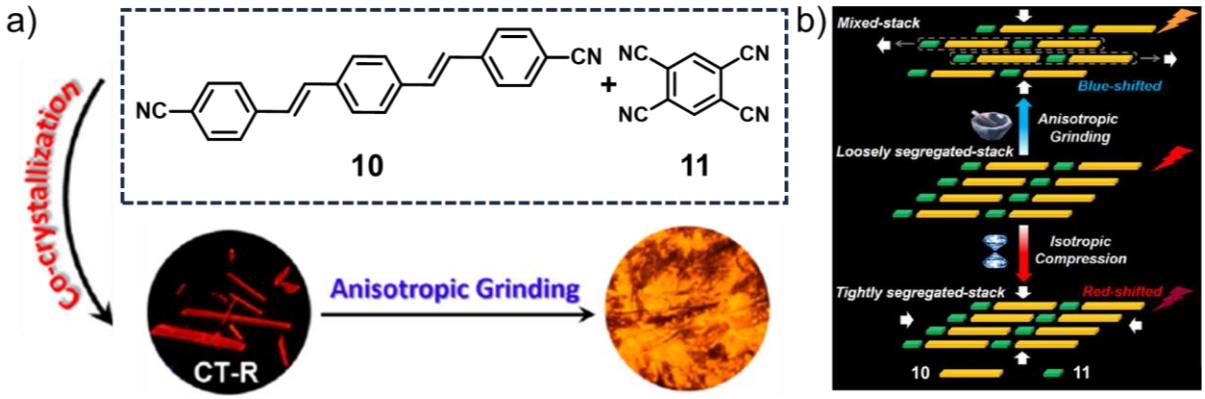

Figure 1.11. a) Chemical structure of **10** and **11** used for the co-crystallization and the fluorescence images of pristine and ground samples of cocrystal CT-R. b) Schematic representation of the molecular packing rearrangement under anisotropic grinding and isotropic compression. (Adapted from reference 51)

While, molecule without hexyl chain (**9**, **Figure 1.10b**) revealed NIR (λ_{em} = 700 nm) MRL turn-on features with 10% quantum yield. The redshifted NIR emission observed in compound **9** was ascribed to the more compact *J* aggregates formed during the fast evaporation process.

The distinct mechanochromic luminescence response to different mechanical forces such as anisotropic grinding and isotropic compression was demonstrated in a donor-acceptor cocrystal system by Tian and coworkers.[51] The red cocrystal was synthesized from cyanostyrylbenzene derivative (**10**, donor) and tetracyanobenzene (**11**, acceptor) unit (**Figure 1.11a**). Under anisotropic mechanical grinding, pristine cocrystal exhibited a 30 nm blueshift from red emissive (λ_{max} = 643 nm) state to a bright orange (λ_{max} = 610 nm) emissive state with enhanced emission. This was attributed to the structural reorganization in molecular stacking mode from a loosely segregated stack

to a mixed stack structure as a result donor-acceptor CT as well as π–π interactions weakened (**Figure 1.11b**). While, under isotropic compression loosely segregated stack rearranged into a tightly segregated stack and exhibited redshifted emission, resulting from the enhanced CT and π–π interactions.

Enomoto's group reported a aminobenzopyranoxanthene based molecule with remarkable reversible luminescence switching in NIR/blue region upon mechanical stimulus.[52] The *cis* and *trans* derivatives of this molecule were synthesized and the chemical structure of *cis* form (**12**) is shown in the **Figure 1.12a**. Only *cis* form exhibits a remarkable NIR fluorescence (λ_{max} = 758 nm), whereas *trans* form emits only in the

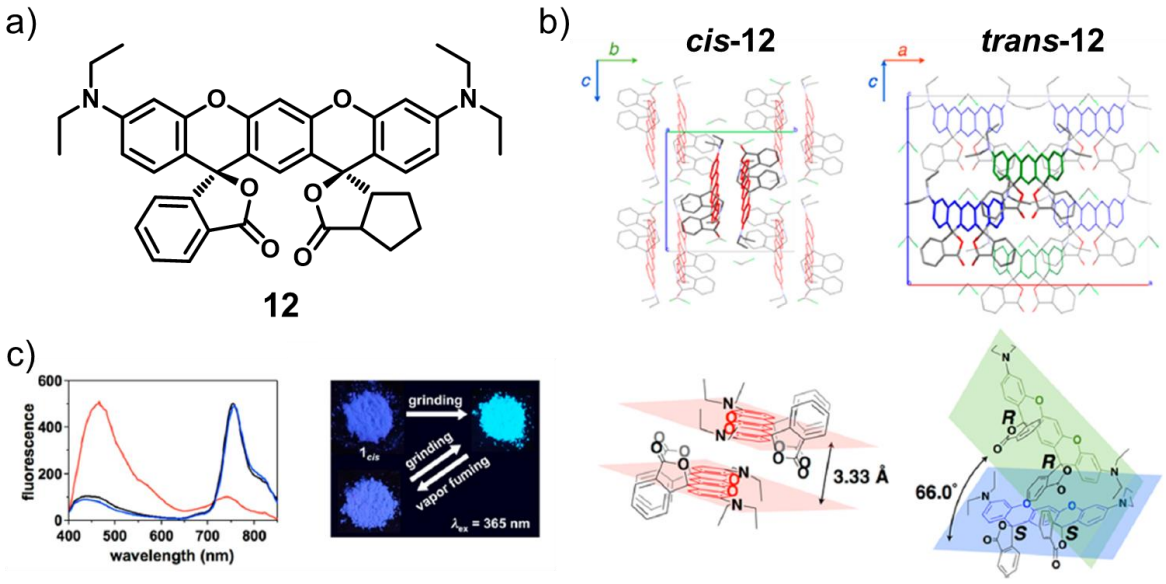

Figure 1.12. a) Chemical structure of **12** *cis* form. b) Molecular packing in *cis* and *trans* forms of **12** in the crystal lattice. c) Solid-state emission spectra of *cis*-**12** under different conditions (black: pristine powder; red: ground powder; blue: ground sample fumed with DCM vapors) and the corresponding images taken under 365 nm UV light. (Adapted from reference 52)

blue region. Thorough single-crystal X-ray investigations revealed that the NIR fluorescence of *cis* form of **12** is due to the fluorescence from slip-stacked dimeric structures of xanthene rings in crystal lattice, while the blue fluorescence is owing to the fluorescence from xanthene ring of *trans* form independently existing as a monomer unit (**Figure 1.12b**). Reversible switching between the two emissive states (NIR to blue) in **12** is achieved by dynamic structural interconversion between the two molecular packing (slipped stack to monomer) arrangements in response to external stimuli such as mechanical grinding and solvent vapor-fuming and the corresponding emission spectrum is also shown in the **Figure 1.12c**.

Liu *et al.* reported a novel concept in the mechanochromic field highlighting the pressure induced blueshifted and enhanced emission.[53] They synthesized a molecule (**13**) consist of anthracene (AN) and tetraphenylethylene (TPE) units and the crystals of

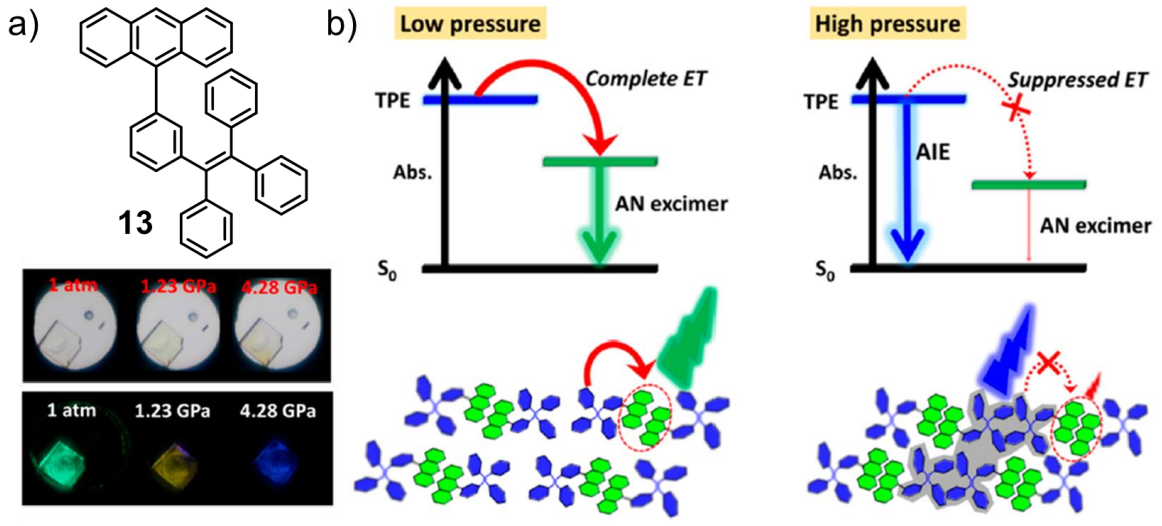

Figure 1.13. a) Chemical structure of **13**. b) Schematic illustartion of the mechanism involved in pressure induced enhancment in the blueshifted emission of **13**. (Adapted from reference 53)

compound **13** exhibited different emission color and the intensity (three step variations) under various pressure (**Figure 1.13a**). The compound **13** crystal displayed a gradual red-shifted emission of the anthracene excimer from green to yellow with decreased emission intensity as the pressure increased from 1 atm to 1.23 GPa. When pressure increased above 1.23 GPa, a new emission band at 438 nm suddenly appeared and then gradually increased with increase in pressure and reached its maximum intensity at 4.28 GPa (blue emission). From 1.23 to 4.28 GPa, the suppressed energy transfer (ET) from TPE to AN dimer caused the appearance of blue-shifted emission features, and the AIE mechanism of TPE units helped to enhance the intensity of the blue emission (**Figure 1.13b**). These two factors worked together to cause pressure-induced emission blueshift and enhancement.

1.4.3. Light irradiation

Light is an ideal external stimuli for regulating molecular conformations, chemical structures, and their associated aggregation states due to its noninvasive nature, allowing for efficient control over molecular systems without causing damage. Its speed and direction can be manipulated with precision, providing temporal and spatial control. In the field of photophysics, photo-induced solid-state reversible luminescence modulation has emerged as a powerful tool. This refers to the change in luminescence behavior, such as color or intensity, of a material induced by light exposure. Such changes can be reversed by either removing the light source or exposing the material to light of a different wavelength. This characteristic has been exploited in the design of

advanced functional materials, including sensors, that react to light in a specific manner by altering their luminescence properties.

Another remarkable effect of light on organic systems is the photosalient effect, where light causes a dramatic physical change in the material, often resulting in an explosive-like response. This effect has been studied extensively in the field of organic crystallography, with crystals undergoing rapid deformation, ejection, or fracture upon light exposure. This fascinating phenomenon holds potential for various applications. For example, it could be used in the creation of actuators, devices that convert energy (in this case light energy) into physical motion. Moreover, the use of light as an external stimulus extends to data storage mediums, where it has revolutionized information technology through the development of optical data storage devices such as CDs and

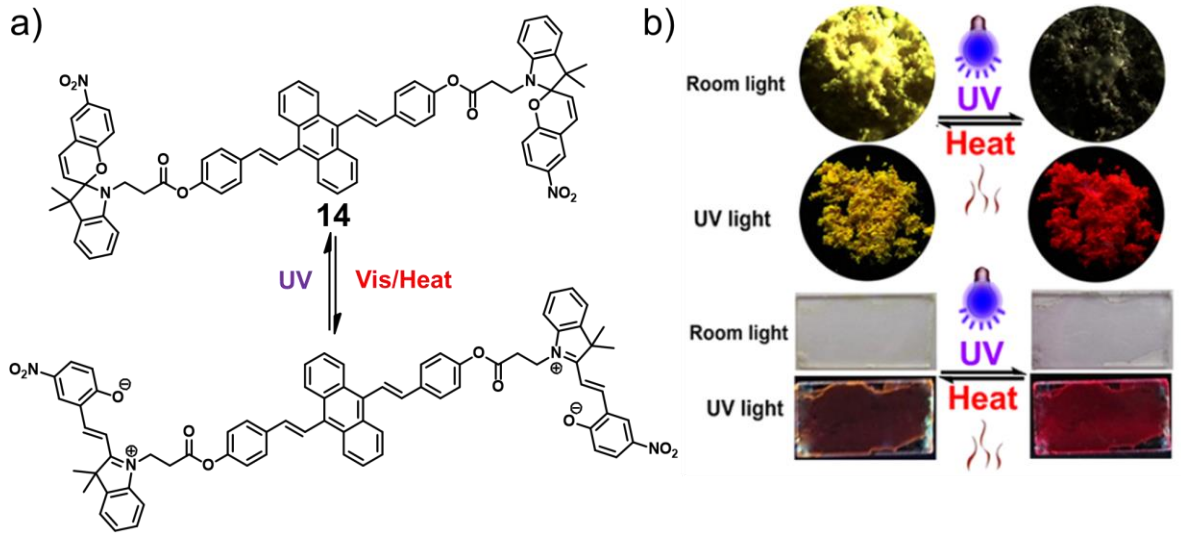

Figure 1.14. a) Chemical structure of **14** and its reversible structural isomerization under various stimuli. b) Images of powders and films of **14** under room light and UV light. (Adapted from reference 54)

DVDs. In the realm of imaging, light-sensitive materials can be used to create high-resolution images, making them invaluable in areas like medical imaging and photography.

In 2017, Qi *et al*. constructed a light induced luminescence switch based on a distyrylanthracene derivative end functionalized with spiropyran units (**14**, **Figure 1.14a**) for anticounterfeiting and super-resolution imaging applications.[54] Reversible

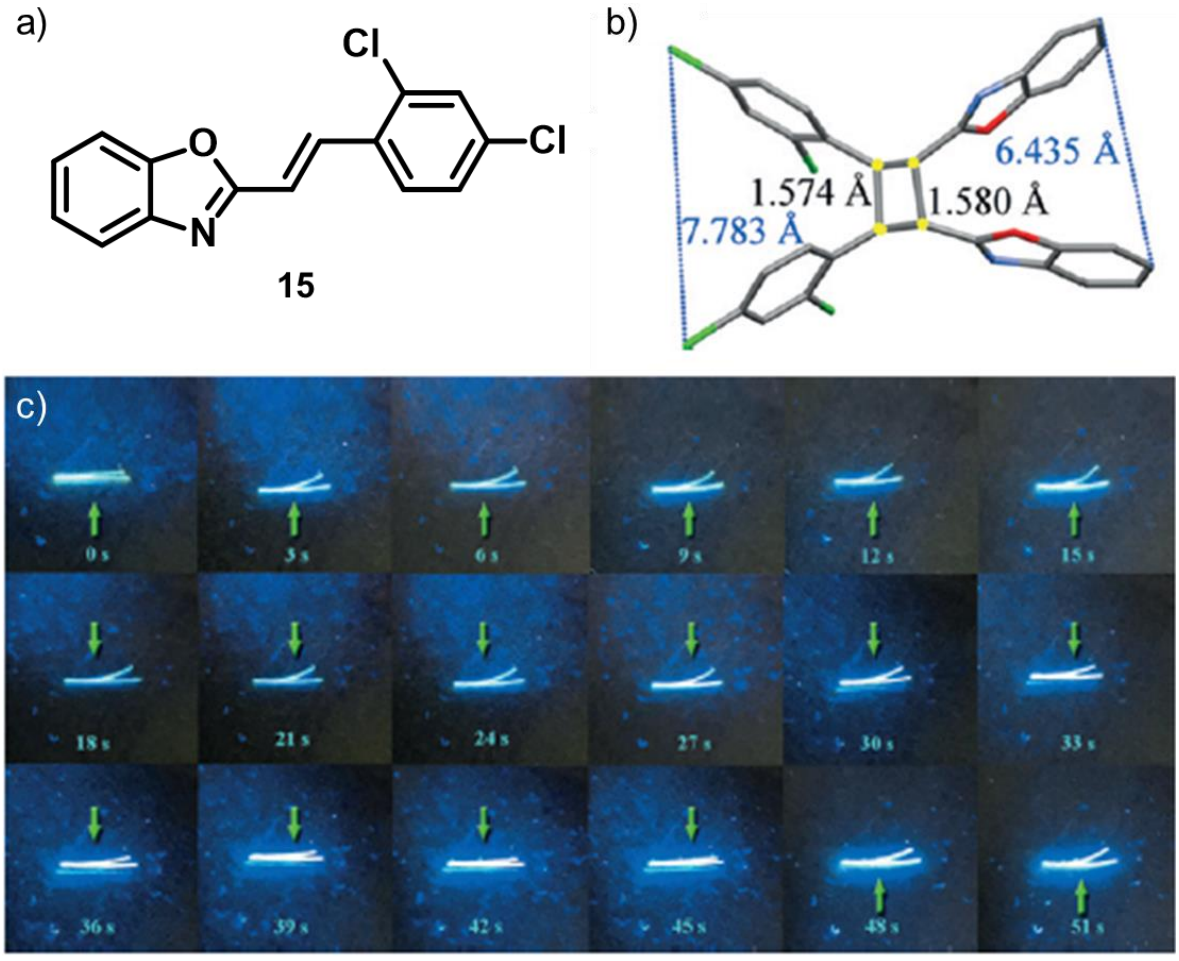

Figure 1.15. a) Chemical structure of **15**. b) Single crystal structure of the cyclobutane molecule formed from the **15**. c) Photographs of the needle-like crystals of **15** before and after irradiating with 365 nm UV light (the arrows indicate the irradiation direction). (Adapted from reference 55)

photo induced switching in both absorption (yellow to dark purple) and emission (yellow to red) was achieved in this system *via* alternating UV and heat treatment (**Figure 1.14b**). Photo induced structural isomerization of **14** from the spiropyran form (unconjugated) to merocyanine (conjugated) form was facilitated by the large free volumes induced by bulky nonplanar structure of styryl moieties, as well as the intramolecular hydrogen bonding between the styryl and merocyanine moieties.

An interesting photomechanical properties such as bending, rolling, curling, and salient behavior of styrylbenzoxazole based crystal (**15**, **Figure 1.15a**) was reported from the Lu's group.[55] Driving force for the photosalient behavior observed for **15** is ascribed to the photo induced [2+2] cycloaddition reaction between the C=C double bond. When the geometric requirements for [2+2] cycloaddition are met by the packing mode of conjugated olefin molecules in the crystallized state through π–π interactions, the topophotochemical reaction can occur, which lead to the photomechanical motion. The single crystal structure of the formed cyclobutane ring upon photo irradiation of **15** is shown in **Figure 1.15b** and the images of needle-like crystals of **15** before and after irradiation with 365 nm UV light with different irradiation directions are shown in **Figure 1.15c**. The bending direction of the crystal is altered by changing the irradiation direction and this type materials are significant in the generation of controllable photomechanical devices.

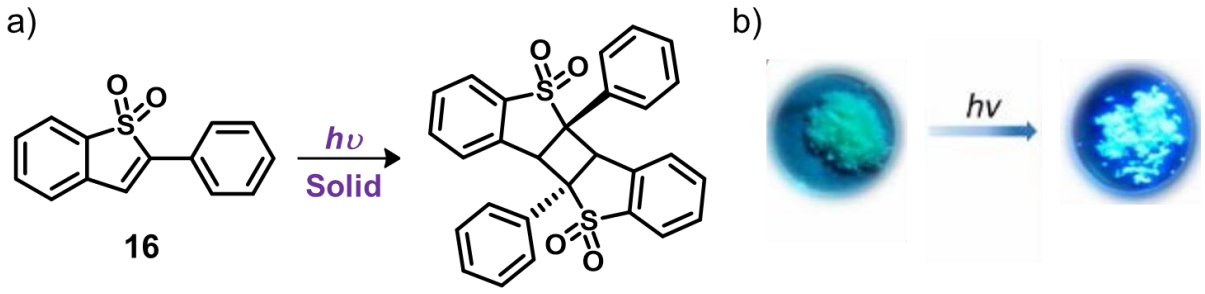

Figure 1.16. a) Chemical structure of **16** and the synthetic method to obtain corresponding photodimer. b) Images of the powders of **16** before and after UV irradiation (emission turn-on). (Adapted from reference 56)

Recently, Guo *et al*. reported a phenyl substituted benzothiophene derivative (**16**, **Figure 1.16a**) and demonstrated its fascinating photomechanicacl properties like splitting, hopping, bending and photoinduced fluorescence turn-on features.[56] These properties of the **16** is owing to the formation of photodimer under UV light irradiation.

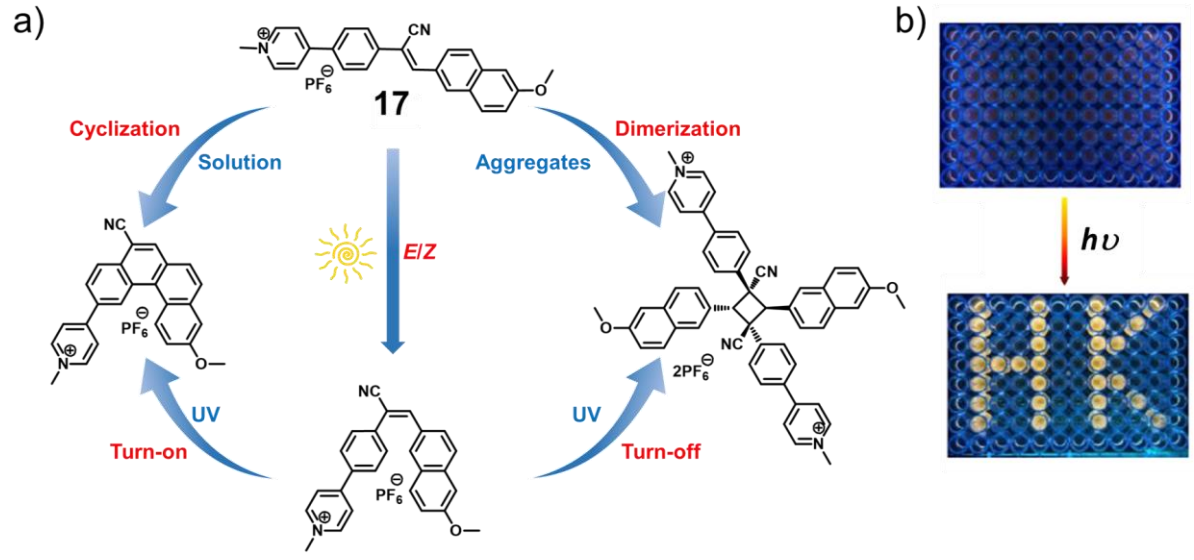

Figure 1.17. a) Chemical structure of **17** and its multiple photoreactions under various conditions. b) Images of photopatterns generated in CH_3CN/H_2O mixtures of **17** (f_w = 0% for letters H and K; f_w = 99% for other parts in the 96 well plate, conc. = 1 x 10^{-5} M) after irradiating with 365 nm UV light. (Adapted from reference 57)

The cyclobutane derivative was poorly conjugated, yet the photodimer exhibited remarkable AIE behavior with an intense blue fluorescence (λ_{em} = 415 nm, Φ_F = 96.2%) in the solid powder (**Figure 1.16b**), due to its excellent intramolecular through-space conjugation and restriction of intramolecular vibration.

A single AIEgen system consisting of α-cyanostilbene-based zwitter ionic molecule (**17**, **Figure 1.17a**) showing various but controllable photoreactions was developed by Tang and his coworkers.[57] The compound **17** exhibited *Z*/*E* isomerization in organic solvent under thermal stimulus and room light, and it underwent photocyclization under UV light and observed a significant enhancement in emission intensity. Molecules of **17** photodimerized in aggregated states (aqueous mixture) with microcrystal formation and exhibited a huge decrease in emission intensity. This emission turn-on and turn-off behavior of **17** under various conditions employed for the fabrication of photopatterns as shown in Figure **1.17b**.

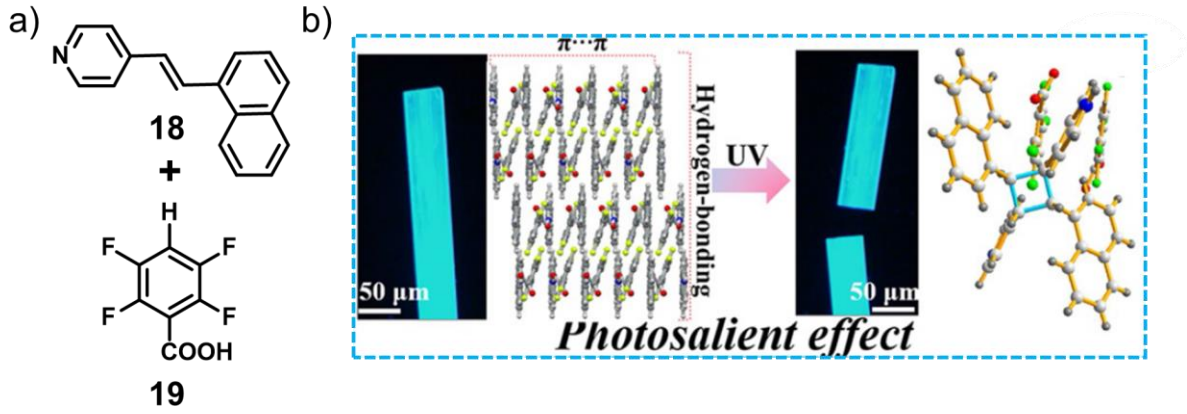

Figure 1.18. a) Chemical structures of **18** and **19** forming cocrystal system. b) Photosalient behavior of cocrystal and the photoinduced structural change. (Adapted from reference 58)

Li *et al.* constructed a hydrogen bonded cocrystal from naphthylvinylpyridine (**18**) with coformer tetrafluorobenzoicacid (**19**),[58] shown in **Figure 1.18a**. This cocrystal displayed dynamic photomechanical properties like mechanical popping, splitting, and macro movements upon UV light irradiation owing to the photo induced solid-state [2+2] cycloaddition (**Figure 1.18b**). Conversion of light energy into mechanical energy is due to the strain formed and released during the photodimerization reaction. These results thus provided a deep understanding about the mechanism behind hydrogen-bonded self-assembly and the dynamic light-driven mechanical performances in molecular crystalline materials. Utilizing the methods covered in this section would pave the way for the development of novel actuators and photonic materials for more efficient energy conversion.

1.4.4. Chemical vapors

Building "smart materials" for a variety of uses, including artificial molecular switches, can be achieved through chemically activated unique colour and fluorescence switching in solid-state. This approach employs a process known as configurational transition, which essentially refers to a structural change or rearrangement in a molecule's geometry that results from exposure to a certain chemical stimulus.[59] This can be effectively harnessed in creating molecular switches that are exceptionally sensitive to their environment. For instance, a molecule may exist in two configurations: an off-state that is colorless and an on-state that exhibits bright fluorescence. Exposure to a specific chemical can induce the transition from the off-

state to the on-state, and this change in fluorescence can be easily detected, thereby signalling the presence of the chemical in question.

Such chemically activated switches have wide-ranging potential applications. In biosensing, they could be used to detect specific biological markers for diseases, effectively acting as early warning systems for various health conditions. In data storage, these switches can represent binary data (with the off and on states representing the binary digits 0 and 1), enabling the creation of high-density memory devices. The development of these unique 'smart materials' enables the creation of highly sensitive and selective detection systems and lays the groundwork for the next generation of molecular electronic devices. The concept of chemically activated molecular switches is a testament to the potential of materials science and chemistry to revolutionize our everyday technology and improve our understanding of the world on a molecular level.

Su *et al.* reported a novel TPE-spiropyran based fluorescent molecular switch (**20**, **Figure 1.19a**), which exhibited a high contrast fluorescence switching between three

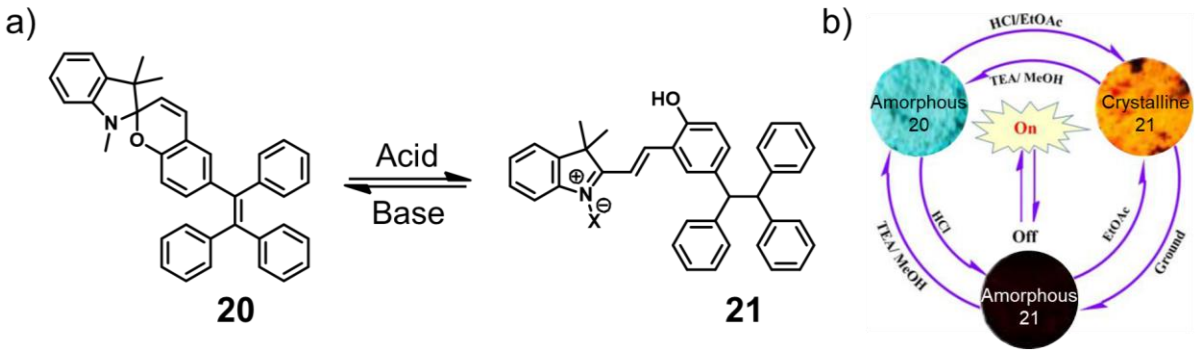

Figure 1.19. a) Chemical structures of **20** (ring closed form) and **21** (ring open form). b) Fluorescence switching between three different states under various stimuli. (Adapted from reference 60)

different emissive states under acid/base, organic solvent vapors, and mechanical stimuli as shown in the **Figure 1.19b**.[60] The compound **20** displayed stable cyan emission in its amorphous solid state and showed a fast response towards acid fumes, which induced a structural change from **20** (ring closed spiropyran form) to **21** (ring open protonated merocyanine form) accompanied with emission turn-off. When the acid and a solvent were introduced together, compound **20** transformed into a orange emissive crystalline state. The cyan emission of **20** is coming from the localized excited state, whereas intramolecular charge transfer is responsible for the orange emission in **21** due to the planar molecular conformation and high dipole moment compared to its ring closed form. Acid/base fumes or mechanical force/solvent vapor interaction was used to achieve the reversible control over any two of the three distinct emissive states.

Ramström's group developed multiple stimuli-responsive molecular switches based on enaminitrile derivatives.[61] Molecular configurational transformation associated with

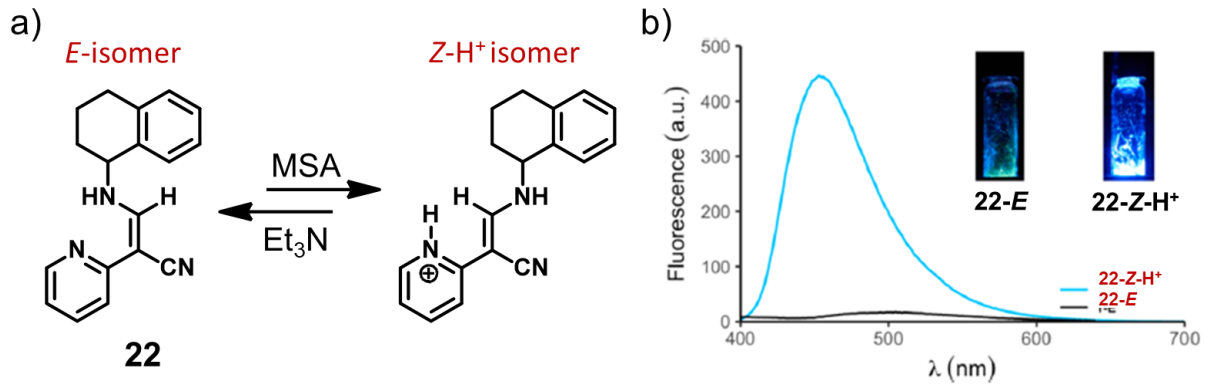

Figure 1.20. a) Chemical structure of **22** and acid/base induced switching between *E*-form and *Z*-H⁺ form. b) Emission profiles of **22-*E*** and **22-*Z*-H⁺** films; inset: corresponding images of **22** taken under 365 nm UV light. (Adapted from reference 61)

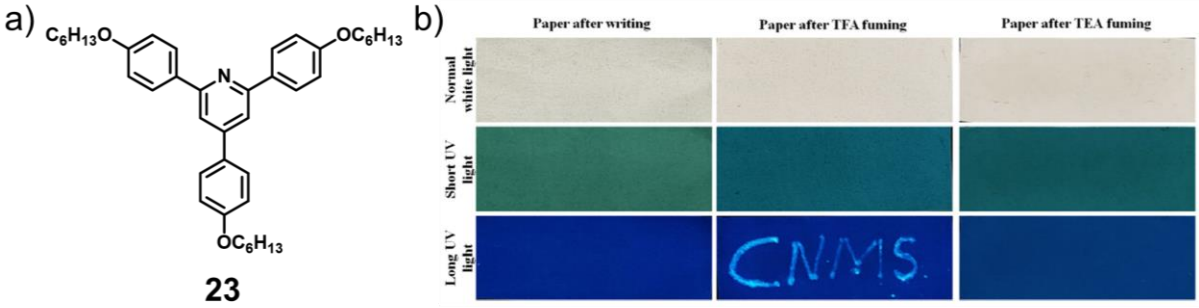

Figure 1.21. a) Chemical structure of **23**. b) Demonstration of anti-counterfeiting features of **23** based on the acid–base vapor sensing. (Adapted from reference 62)

enaminitrile derivative (**22**) under acid/base activated condition is shown in the **Figure 1.20a**. The compound **22** existed in *E*-configuration under neutral/basic conditions, while it underwent structural reconfiguration to *Z*-H^+ form under acidic condition. Protonation induced AIE behavior was observed for **22-Z-H^+** showing blue fluorescence with 40% quantum yield in the solid state. Film state photoluminescence spectra of **22** in both the configurations were shown in **Figure 1.20b** and the corresponding images are shown inside the graph.

A novel triphenylpyridine based AIE molecule was reported by Ahipa and coworkers (**23**, **Figure 1.21a**),[62] which is employed as an anti-counterfeiting agent. This molecule exhibit significant changes in the fluorescence upon treatment with acid/base vapors. Data encryption and decryption was demonstrated using **23** (**Figure 1.21b**), eventhough it exhibit AIE characteristics, owing to its low emission in the aggregated state. Ethanol solution of **23** was used as the security ink for this purpose and wrote the word “CNMS” on a filter paper, which was invisible under normal light and UV light.

The encrypted data was decrypted by treating the paper with trifluoroacetic (TFA) acid vapors, then the word was only visible under 365 nm UV light and showed an intense cyan emission. Subsequently, the cyan emission of the word "CNMS'' turned-off by treating it with triethylamine (TEA) vapors. This coding and decoding of word "CNMS" could be done several times with good reversibility. These type of fascinating fluorescence on-off effects that were generated by acid/base and solvent vapors in the solid state could be utilized for developing optical data storage devices, sensors, security ink, molecular switches etc.

1.4.5. Electric field

Electric fields represent an intriguing source of external stimulus that can significantly modify the optical properties of certain materials, such as their absorbance, transmittance, reflectance, or emission. This typically occurs via an electrochemical redox process where the application of an electric field induces an oxidation or reduction reaction within the material, which in turn leads to a change in its optical characteristics. The materials that undergo such transformations fall into a category of 'smart materials' known as electrochromic (EC) or electrofluorochromic (EFC) materials.[63-64] Electrochromic materials are able to change their color when an electric field is applied, whereas electrofluorochromic materials have the unique ability to alter their fluorescence intensity and/or color under the influence of an electric field. Electrochromic and electrofluorochromic materials have garnered considerable attention due to their potential in a wide array of practical applications. For instance, in

the realm of visual display technology, these materials can be leveraged to create multicolor displays, or E-papers, where the color and intensity of individual pixels can be precisely controlled using electric fields.

Similarly, in the realm of architectural design and energy efficiency, these materials find application in 'smart windows'. In this context, windows made of electrochromic materials can be electrically controlled to modulate the amount of light and heat they transmit or reflect, enabling regulation of indoor temperatures and light levels, and hence reducing energy consumption for heating, cooling, and lighting buildings. The adaptability of these materials also opens the door to their use in other unique applications like camouflage materials, where the color or pattern of a surface can be rapidly changed to blend into its surroundings, sunglasses that can adjust their tint level

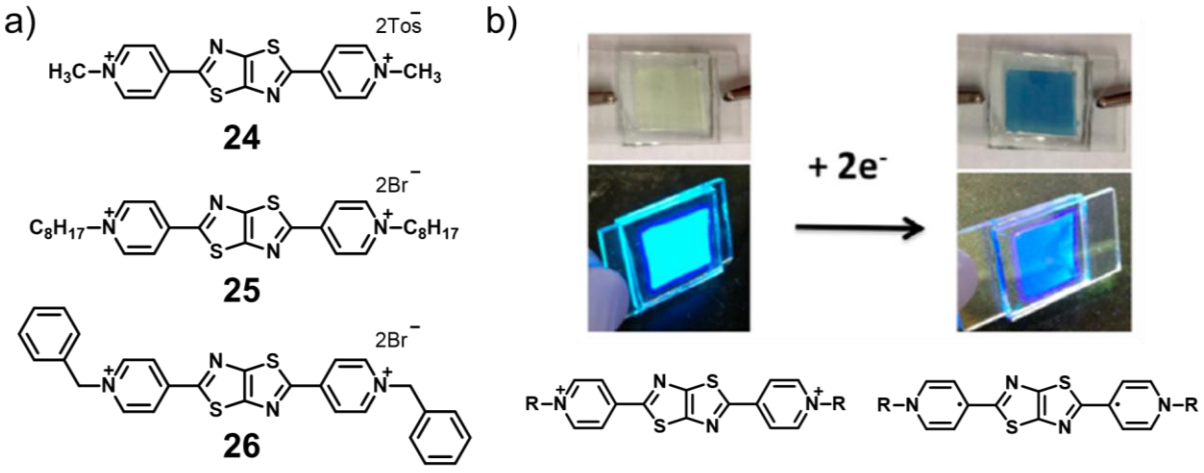

Figure 1.22. a) Chemical structures of thiazolothiazole viologen derivatives **24**, **25**, and **26**. b) Photographs of the electrochromic device of **25** in neutral and reduced states under normal light and UV light; proposed reduced state structure of these derivatives is shown below the photographs. (Adapted from reference 65)

in response to changing light conditions, and switchable rear-view mirrors that can modify their reflectance to avoid dazzling the driver in low-light conditions.

Woodward *et al.* reported three thiazolothiazole based dipyridinium derivative with varying substitution at pyridyl nitrogen such as methyl (**24**), octyl (**25**), and benzyl (**26**) groups as depicted in the **Figure 1.22a**.[65] These viologen derivatives exhibited strong blue fluorescence and reversible electrochromic features in solution associated with the distinct color switching from yellow to dark blue at low reduction potentials. In addition to this, the strong blue emission was suppressed upon two electron reduction process (**Figure 1.22b**).

A high contrast electrochromic switching from colorless to all black covering entire NIR region was demonstrated in dibenzofulvene based derivatives by Corrente *et al.*[66] They synthesized a series of mixed valence molecules by functionalizing the exocyclic bond of fulvene with different groups. Among them only compound **27** (**Figure 1.23a**) having alkyl chain substitution at exocyclic bond afforded colorless neutral state. Thus,

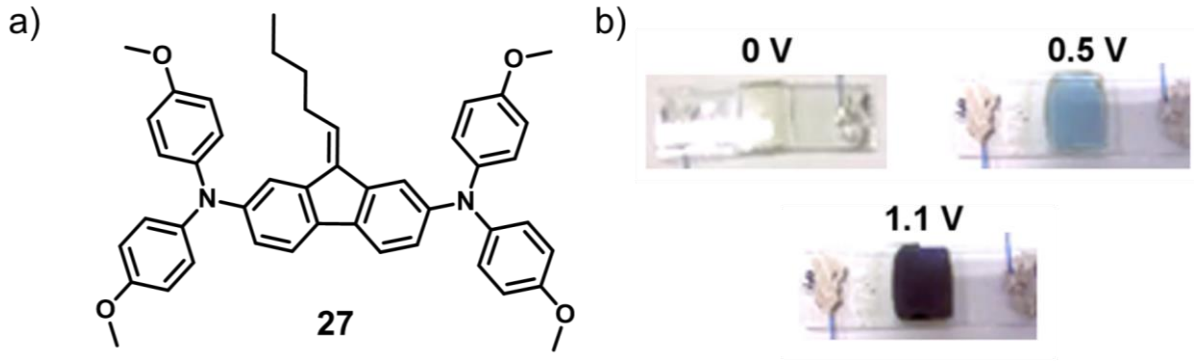

Figure 1.23. a) Chemical structure of **27**. b) Photographs of the electrochromic device of **27** at different voltages. (Adapted from reference 66)

this type of system found application in the field of smart windows and e-papers. Optically induced intervalence charge transfer transitions (IVCT) are the source of observed NIR electrochromism in the system. An electrochromic device of **27** was fabricated and the images of device at different voltages (colorless to black) are shown in the **Figure 1.23b**. The device exhibited high optical contrast, fast response time, and high cyclic stability over 10000 cycles.

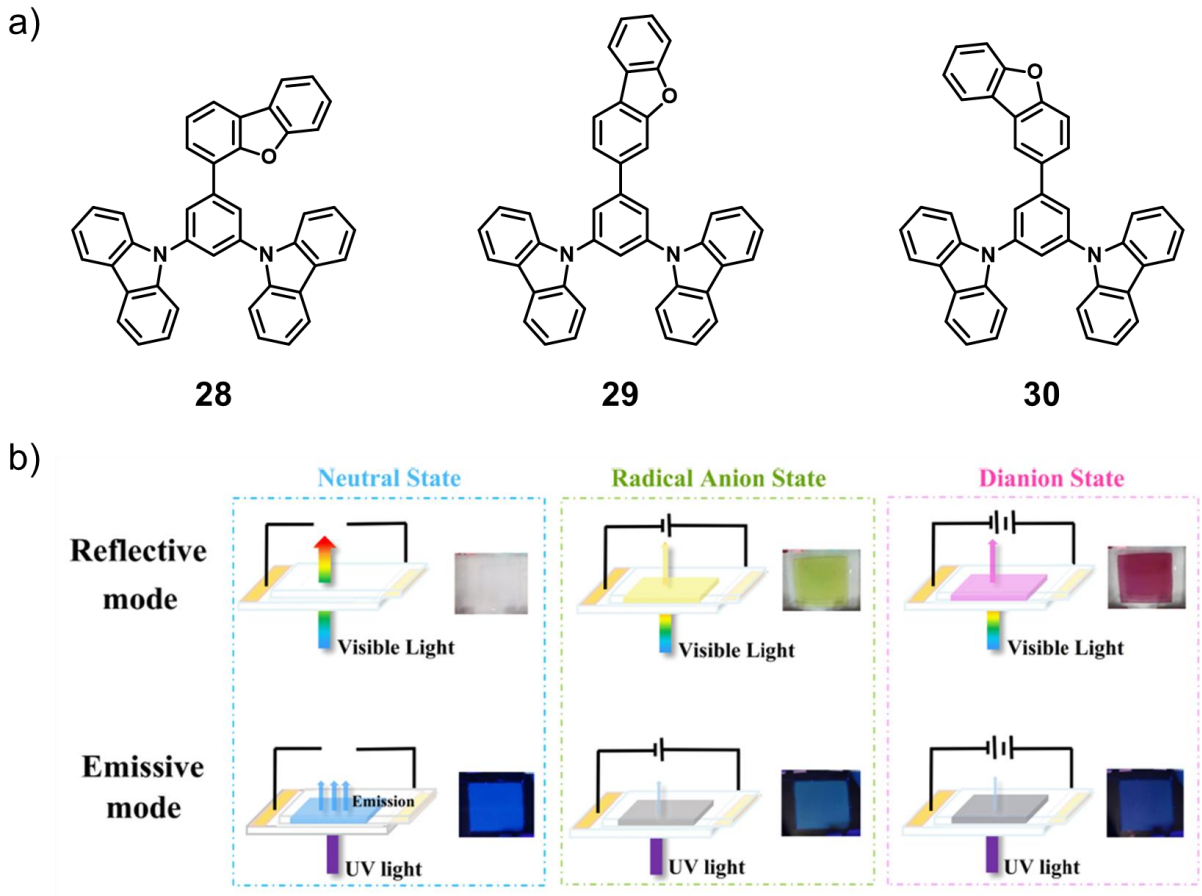

Figure 1.24. a) Chemical structure of the regioisomers **28**, **29**, **30**. b) Photographs of the electrochromic and electrofluorochromic devices of **29**. (Adapted from reference 67)

Meng and coworkers developed a series of carbazole-dibenzofuran based regioisomeric small molecules (**Figure 1.24a**) that showed cathodically coloring electrochromic features.[67] Neutral state of all the derivatives was highly transparent, while color of the reduced states was tuned across the entire visible region. Modulation of fluorescence between on and off states was also observed for **28** (*ortho* isomer), **29** (*meta* isomer), and **30** (*para* isomer). Compound **28** changed its color from transparent (neutral state) to light green (radical anion state) and then to red color (dianion state), whereas **29** exhibited a color change from neutral transparent state to yellow and then magenta, and compound **30** displayed a color variation from neutral state to light blue and then blue in their corresponding radical anion and dianion states. Schematic illustration of the working principle of electrochromic and electrofluorochromic devices used for smart displays are shown in the **Figure 1.24b**.

1.5. Applications of stimuli-responsive materials

The development of luminescent organic materials with stimuli-responsive features have attracted much attention in recent years due to their wide applications as sensors, thermal indicators, memory storage devices, security inks, luminescent molecular switches, bioimaging, functional coatings, smart windows and displays. A significant number of smart organic materials with color-tunable luminescence have been designed and synthesized as a result of the swift development in the area of supramolecular chemistry. The established link between structure-property relationship in functional

molecular assemblies encourage the development of more effective stimuli-responsive systems from fundamental research to real-world applications.

1.5.1. Optical sensors

Solid-state luminescent materials are becoming increasingly significant in the field of optical sensing due to their ability to interact and respond to a variety of environmental stimuli such as temperature, pressure, and chemical vapors. These unique properties have led to their exploration and application in several innovative ways. In the context of temperature sensing, these materials can serve as optical thermometers, changing their luminescent properties with variations in temperature. This functionality is particularly valuable in environments where traditional thermometers may not be suitable, such as in extreme conditions or hard-to-reach areas. For example, they can be used to monitor temperature changes in industrial processes, or even for tracking temperature variations in biological systems, contributing to fields like medical diagnostics and thermal therapy.

Regarding pressure sensing, solid-state luminescent materials can alter their luminescent properties under different mechanical stresses or pressures, which makes them perfect candidates for developing pressure-sensitive devices. These could be used in a variety of applications, from monitoring structural integrity in engineering or construction to assessing the pressure exerted in touch-sensitive devices. In terms of chemical sensing, these materials can be tailored to respond to specific chemical vapors by changing their luminescence. This offers a visually detectable and potentially highly

sensitive method for identifying the presence and possibly even the concentration of specific chemical substances. This is especially beneficial in fields like environmental monitoring, where these sensors can detect harmful pollutants, or in industries where it's crucial to monitor specific chemicals for safety and quality control.

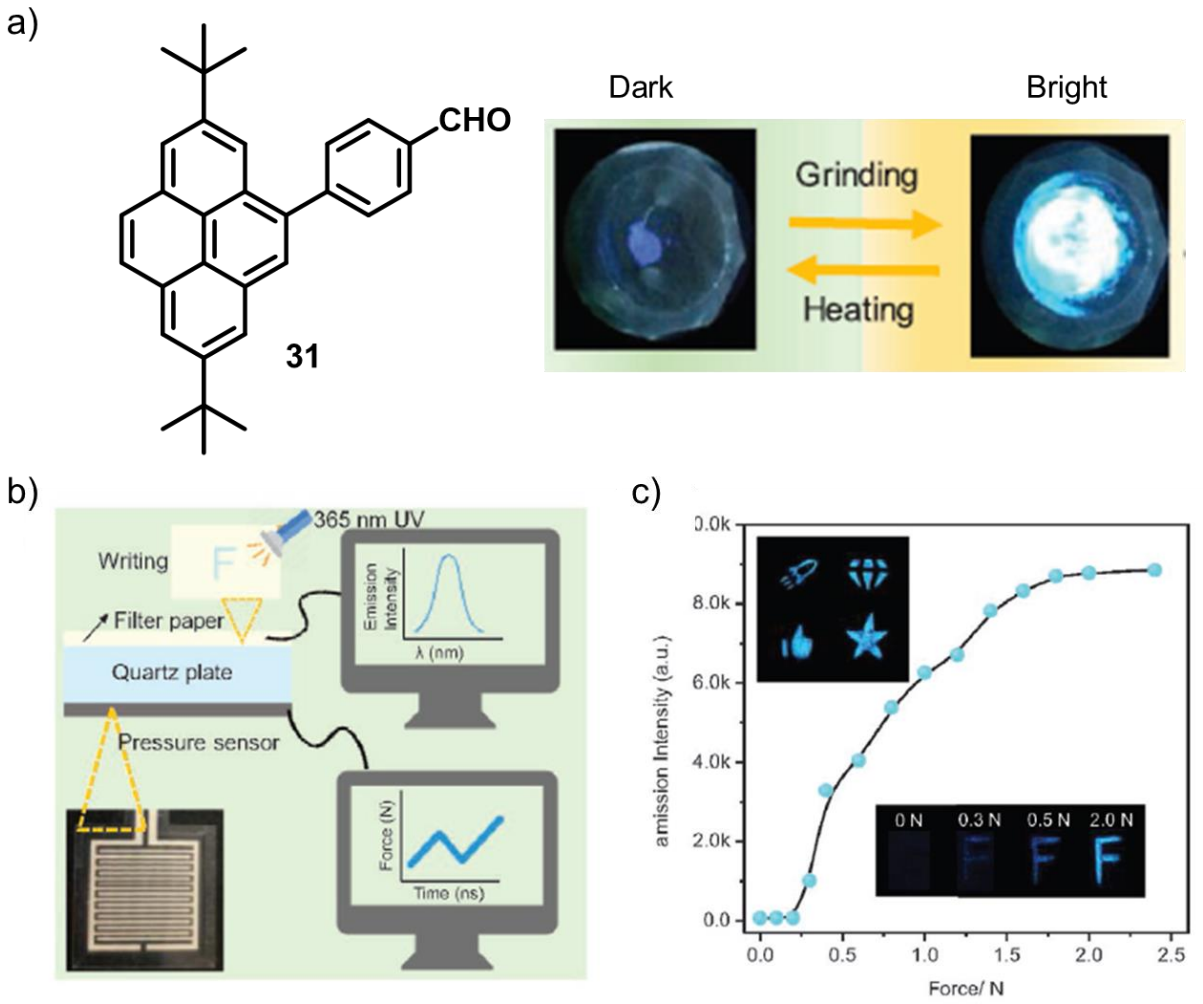

Figure 1.25. a) Chemical structure of **31** and its on-off luminescence switching under mechanical grinding and heating. b) Schematic illustration of the experimental setup for monitoring the pressure force and emission intensity. c) Plot of force *vs*. emission intensity; inset: fluorescent images of different patterns drawn using pristine powders of **31** (top), emission image of letter "F" written by **31** under different force. (Adapted from reference 68)

Recently, Li's group demonstrated a pressure sensor based on a pyrene derivative (**31**) owing to its off-on mechanochromic luminescence behavior (**Figure 1.25a**).[68] In pristine form, compound **31** was in emission quenched state with 0.05% quantum yield, upon grinding the sample bright cyan emission (λ_{em} = 461 nm, Φ_F = 20%) was turned on with very high contrast. To show the practical relevance, the quantitative link between pressure force and emission intensity was further examined for this molecule. As shown in **Figure 1.25b**, pristine powder of **31** was evenly placed on the filter paper, which was kept on top of a quartz plate attached to the pressure sensor. The letter "F" was wrote by grinding the powder of **31** with varying pressure and the corresponding force measured using pressure sensor and the emission intensity monitored by fluorescence spectrophotometer. When the applied force was at 2N, it exhibited 137-fold intense emission and reached the maximum (**Figure 1.25c**). It proved that **31** may be used successfully for pressure sensing applications.

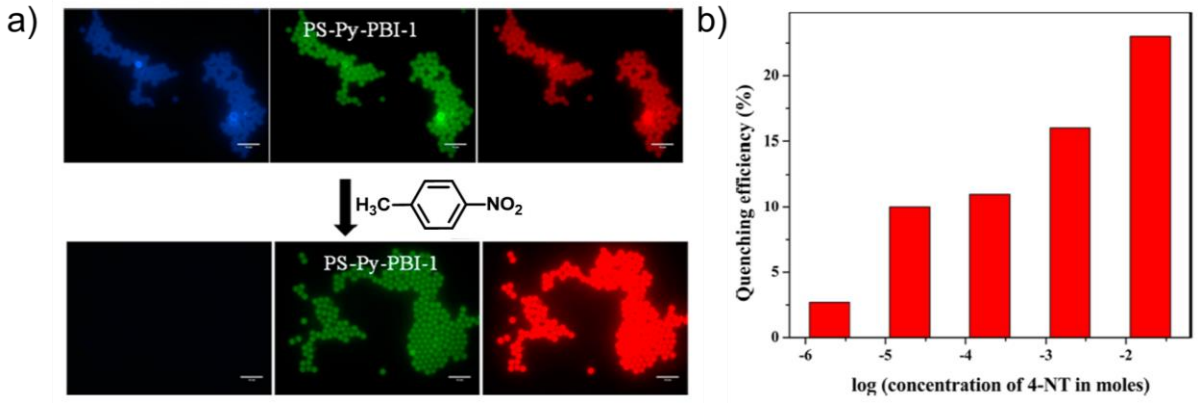

Figure 1.26. a) Fluorescence microscopic images of polystyrene bead before and after being exposed to vapors of 4-nitrotoluene. b) Plot of quenching efficiency as a function of log of concentration of 4-nitrotoluene vapors. (Adapted from reference 69)

An efficient optical sensor for 4-nitrotoluene (4-NT) vapors was developed by Asha's group.[69] They fabricated polystyrene beads by incorporating blue emissive pyrene acrylate and orange-green emitting perylenebisimide unit as cross-linker into a polymer backbone. Monomeric emission from pyrene fluorophore (340-500 nm) was sensitive to the vapors of 4-NT, whereas emission from perylenebisimide beyond 500 nm was unaffected (**Figure 1.26a**). The limit of detection for 4-NT vapors was calculated as 2.7 ppm (**Figure 1.26b**). This selectivity towards nitro aromatics is owing to the pyrene's electron-rich character, which makes it sensitive to electron-deficient materials.

1.5.2. Optical recording

Stimuli-responsive organic molecules have vast potential in the field of optical recording, a technology that records, stores, and retrieves data using light. These materials can undergo changes in their properties, such as their luminescent behavior, in response to external stimuli like light, heat, pressure, and chemical interactions. In the context of optical recording, these molecules can act as "data storage units" because they can exhibit different luminescent states in response to certain stimuli. For example, molecules could switch between an on-state (luminescent) and an off-state (non-luminescent), which could represent the binary 1s and 0s in digital data storage. Moreover, molecules that can exhibit multiple luminescent states could allow for multi-level data storage, significantly increasing data storage density.

These molecules can also be utilized for rewriting and erasing data. The reversibility of stimuli-responsive behaviors means that the luminescent state of these molecules can be switched multiple times without degradation, which could enable the erasure and rewriting of data. One exciting possibility for these materials is in the development of high-density, light-based memory storage systems, such as optical discs and holographic storage. These systems could potentially offer much higher storage capacities compared to conventional magnetic or solid-state storage devices. Furthermore, these systems could potentially offer higher speeds for data transfer, as light can carry much more information per unit time than electrical signals.

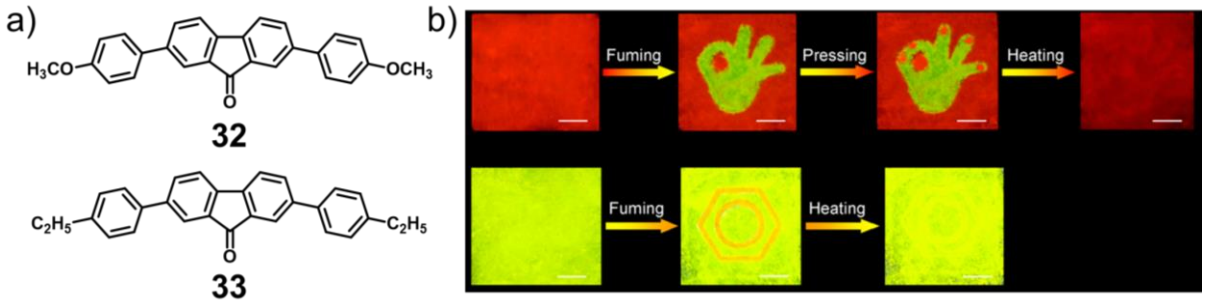

Figure 1.27. a) Chemical structures of **32** and **33**. b) Images of stimuli-responsive writing and erasing for **32** (top) and **33** (bottom). (Adapted from reference 70)

Yuan *et al.* synthesized diphenylfluorenone derivatives (**32** and **33**, **Figure 1.27a**), which exhibited high solid-state luminescence as well as reversible stimuli-responsive two color luminescence switching.[70] They demonstrated its potential application as optical recording by stimuli-responsive writing and erasing under solvent vapors and heat. As shown in the **Figure 1.27b**, red film of **32** turned to yellow at the solvent vapor

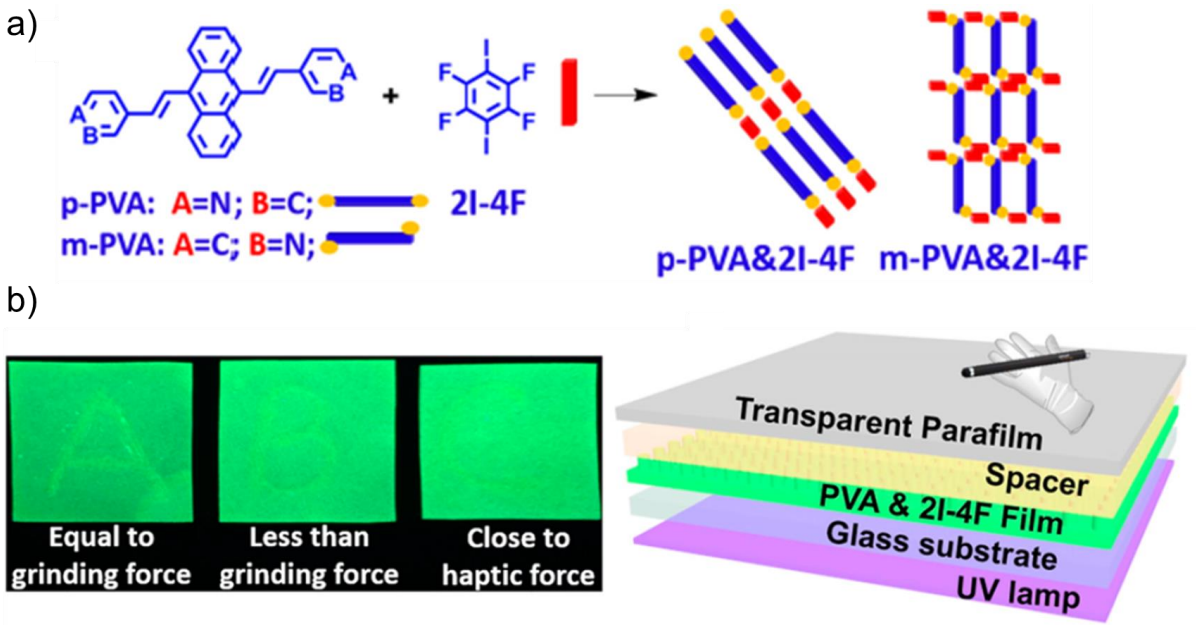

Figure 1.28. a) Chemical structures of p-PVA, m-PVA, 2I-4F and their corresponding selfassembled states. b) Fluorescence images of haptic device after touch writing with different strength and the schematic illustration of the haptic memory device architecture. (Adapted from reference 71)

fumed region ("OK" sign), so the red "paper" was stamped with an yellow "OK" sign. Subsequently, the red "nails" of the "OK" symbol were obtained by pressing at the exact positions as shown in the figure. Further, yellow "OK" symbol was easily erased by heating the entire "paper" at 120 °C for 1 minute. In similar manner, compound **33** displayed write and erase of an orange "benzene ring" from yellow "paper". These results imply that these materials could be used as optical recording materials.

Zhao and coworkers developed two piezochromic halogen bond assisted supramolecular assemblies formed between vinylpyridine substituted anthracene derivatives (p-PVA and m-PVA) with tetrafluorodiiodobenzene (2I-4F) as depicted in the **Figure 1.28a**. Further, a haptic memory device was constructed using this material

as shown in **Figure 1.28b**. The contacted area immediately changed its emission color upon simple pressing with a metal spatula or glass rod.[71]

1.5.3. Anti-counterfeiting

Stimuli-responsive smart luminescent materials have increasingly drawn attention due to their potential applications in the field of anti-counterfeiting.[72] Based on their unique abilities to form dynamic molecular assemblies and modulate their fluorescence in response to external stimuli, these materials can be employed to design advanced security systems. Such materials can exhibit a variety of luminescent states that can be reversibly toggled by different forms of external stimuli, such as light, heat, pressure, and chemical interactions. This could allow for the creation of complex security markings or codes that can only be revealed or decoded using specific stimuli. For instance, a label could be designed to show one message under normal conditions, and a different message when heated or exposed to a certain type of light.

Additionally, the ability of these materials to form dynamic molecular assemblies could allow for the creation of multi-component security systems. Different components could react to different stimuli, adding further layers of complexity to the anti-counterfeiting system. For example, one component could respond to heat, while another could respond to light, each revealing different parts of a security code. These smart luminescent materials could also be incorporated into various substrates, such as paper, plastic, or metal, allowing them to be used in a wide range of applications, from banknotes and passports to luxury goods and pharmaceuticals. The advanced security

features offered by these stimuli-responsive smart luminescent materials could make counterfeiting extremely difficult, thereby enhancing the security of a wide range of items. This could be particularly valuable in sectors such as finance and pharmaceuticals, where counterfeiting can have serious consequences.

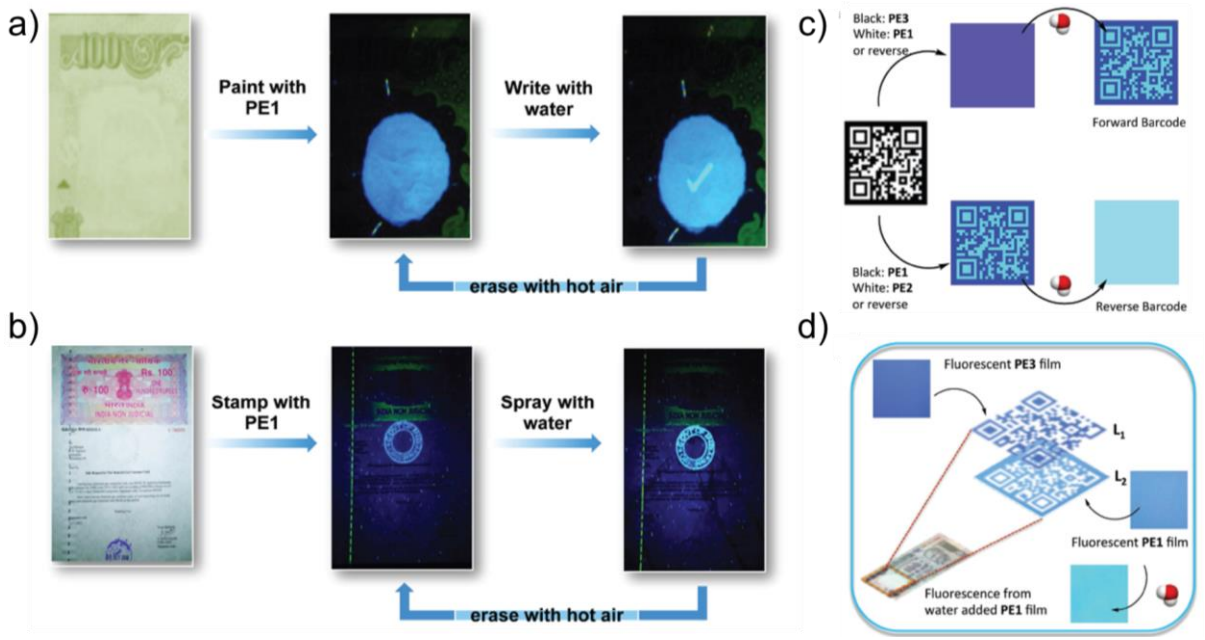

Figure 1.29. Images of water as a security marker demonstrated on PE1 coated a) currency and b) document under normal light and under 365 nm UV light. c) Design strategies employed for the barcode generation with PE derivatives. d) Demonstration of an ideal two-layer design of hidden barcode over a currency note. (Adapted from reference 73)

Ajayaghosh's group developed a series of phenyleneethynylene based derivatives named as PE1 (blue emission), PE2 (cyan emission), and PE3 (blue emission), among them only PE1 exhibited self reversible water induced luminescence change from blue to intense cyan.[73] The mechanism behind this reversible luminescence switching is associated with the controlled molecular slipping with an external stimulus. The water

responsive fluorescent molecular assembly of PE1 was used as a security label for verifying the authenticity of currency note and documents (**Figure 1.29a** and **29b**). A cyan emissive "tick mark" on currency coated with PE1 was obtained using water, and the fluorescence of stamp on document changed when water sprayed on it. Further, they developed a water responsive hidden two layer barcode using PE3 (layer 1) and PE1 (layer 2) as a super security feature. Design strategies to create forward (PE1 and PE3) and reverse barcode (PE1 and PE2) is shown in the **Figure 1.29c** and they demonstrated a two layer hidden barcode with PE1 and PE3 over a currency note (**Figure 1.29d**).

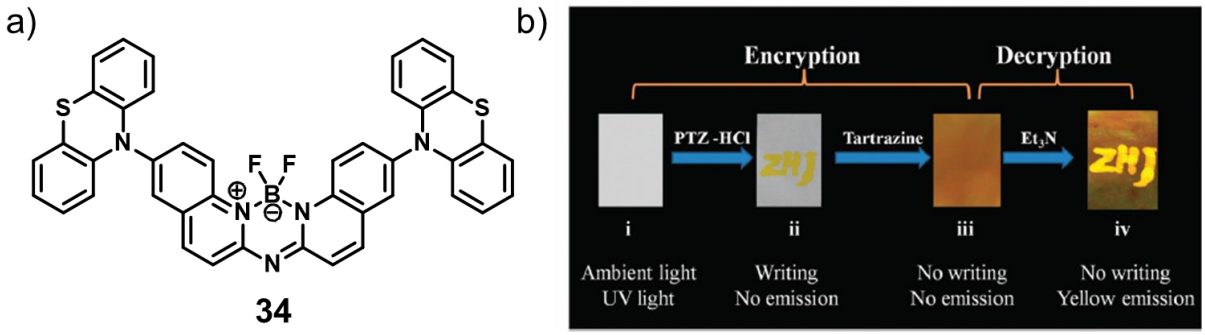

Figure 1.30. a) Chemical structure of **34**. b) Images of the data encryption and decryption demonstrated on a filter paper. (Adapted from reference 74)

An AIE active phenothiazine based borondifluoride system (**34**, **Figure 1.30a**) was developed by Zhu *et al.* and it exhibited color and luminescence switching under various stimuli such as mechanical grinding, organic solvent vapors and acid/base fumes.[74] They also demonstrated the protonation and deprotonation effect in data protection as shown in the **Figure 1.30b**. For this purpose **34-HCl** (no emission) was used as the cryptographic ink and tartrazine dye was employed for making security

paper, which hid the encrypted data under ambient light and under UV light. Data decryption was achieved through exposing this paper to triethylamine vapors, then the data was only visible under 365 nm UV light with yellow emission. These results suggests the applicability of this type of stimuli-responsive fluorescent materials as anti-counterfeiting agents.

1.5.4. Smart windows/displays

Functional electrochromic materials represent a rapidly evolving field of research, with promising applications particularly in multicolor displays and smart windows. These materials have the unique ability to change their optical properties, such as color, reflectance, and transmittance, in response to electric fields. By manipulating these properties, we can control and adjust the way these materials interact with light, which has led to their widespread use in numerous industries. In the realm of multicolor displays, electrochromic materials can provide a wide range of colors with high contrast ratios and brightness, which is advantageous for devices such as televisions, smartphones, tablets, and computer monitors. These materials can also be engineered to have low power consumption and fast response times, improving the efficiency and performance of these devices. In particular, organic electrochromic materials have become increasingly popular due to their flexible and lightweight nature, allowing for the creation of bendable or foldable displays.

Smart windows represent another key application area for functional electrochromic materials. These are windows whose light transmission properties can be altered in

response to voltage, allowing the windows to automatically adjust their tint in response to changes in the external environment. This can help regulate the temperature inside a building, reducing the need for air conditioning or heating, and leading to significant energy savings. Smart windows can also improve comfort by reducing glare and ultraviolet radiation, making them popular in both residential and commercial settings. Electrochromic materials in smart windows can range from inorganic materials, like tungsten oxide, to organic compounds, and even to nanomaterials. The choice of material depends on a variety of factors, including the desired color range, switching speed, durability, and cost. Few examples of smart windows and displays based on organic materials are shown below.

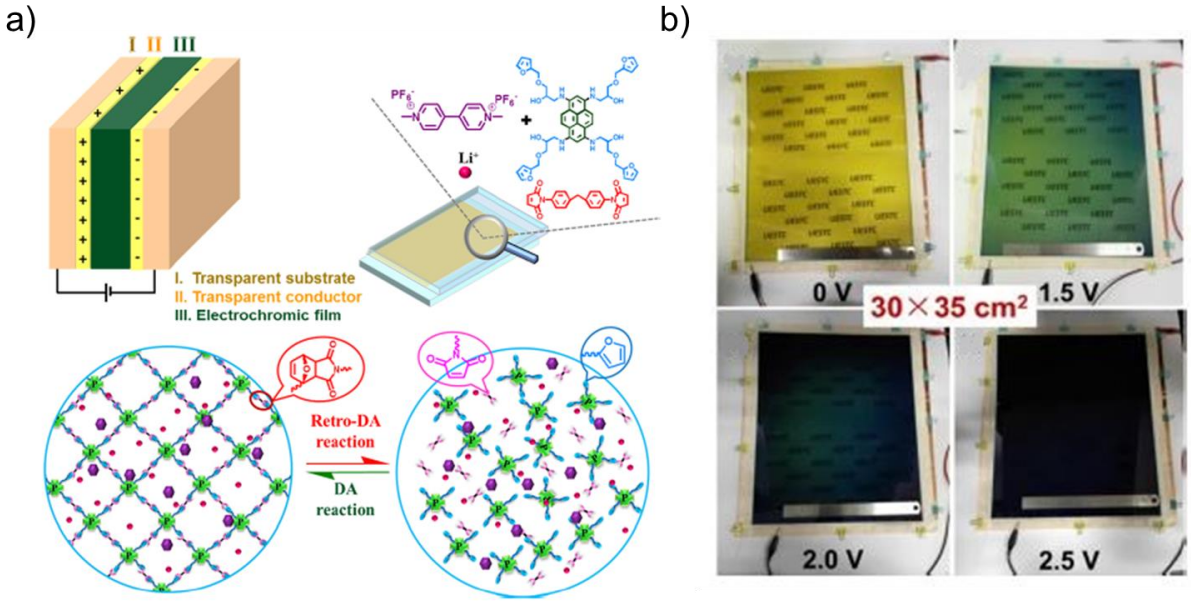

Figure 1.31. a) Schematic illustration of the all-in-one electrochromic device and its self-healing property, and chemical structure of components used in it. b) Photographs of the large area (30 x 35 cm^2) electrochromic smart window at different potentials. (Adapted from reference 23)

Zheng *et al.* developed a large area, easily-assembled smart window using an all-in-one self-healing electrochromic material based on pyrene (**Figure 1.31a**).[23] The all-in-one electrochromic material performed exceptionally well with high ion diffusivity (1.13 x 10^{-5} cm^2 s^{-1}), quick color switching (3.9/3.7 s), good coloration efficiency (413 cm^2 C^{-1}), and great stability (sustain 88.7% after 1000 cycles). In addition, they fabricated a large area smart window of 30 x 35 cm^2 using all-in-one electrochromic material and exhibited excellent electrochromic performance (**Figure 1.31b**). Smart window displayed a faint yellow color initially, this changed to greenish-yellow (1.5 V), then to deep green (2.0 V) and finally dark green (2.5 V). This all-in-one device architecture decreased the high making cost and manufacturing difficulty. All-in-one self-healing material is a novel technique that can be used in high-performance and stable smart windows for green buildings and aircraft in the near future.

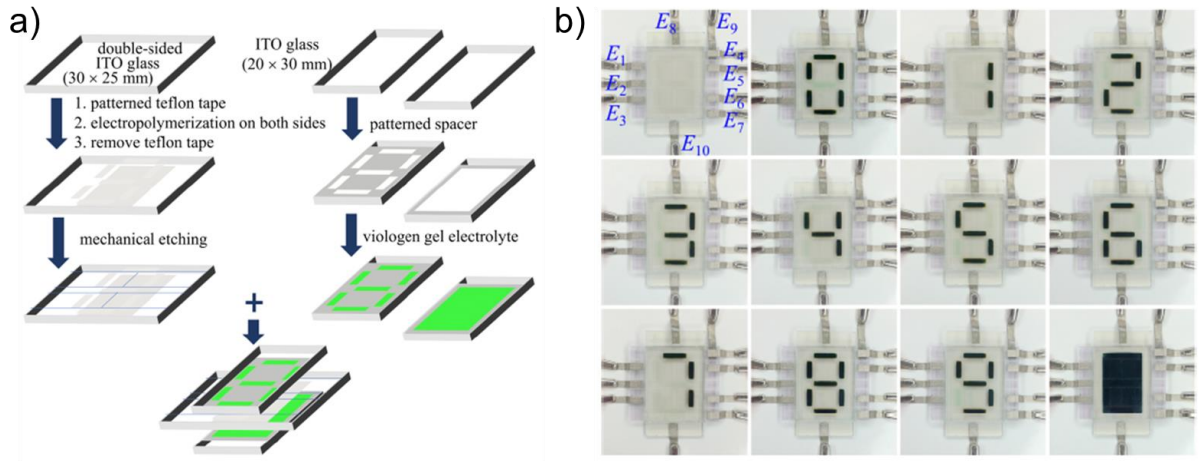

Figure 1.32. a) Pictorial representation of the construction diagram of multifunctional display. b) Photographs of the smart window and bifunctional autodigital display after applying potentials to various electrodes controlled by ten switches. (Adapted from reference 75)

Zhou's group developed an electrochromic polymer PTPA-HDI, consisting of a non-conjugated core of cyclohexane-1,2,4,5-tetracarboxylic diimide connected to two triphenylamine group.[75] They achieved colorless to black electrochromism from binary electrochromes, PTPA-HDI and viologen derivative. Using the binary electrochromes, a bifunctional electrochromic device with an autodigital display and smart window features was designed and demonstrated (**Figure 1.32**). In this bifunctional device polymer was deposited on both sides of the double sided ITO glass. On one side, pattern "8" was deposited and divided it into seven segments as shown in the figure and controlled by E1-E7 electrodes and on the other side polymer was deposited in rectangular shape. The electrolyte gel containing viologen derivative was deposited on another patterned ITO, which act as E8. While, other side of the double sided ITO glass was constructed as smart window controlled by E9 and E10 electrodes.

1.6. Objective of the present investigation

The principal aim of this investigation is to develop organic molecules capable of exhibiting dynamic, high-contrast, and reproducible luminescence switching in solid-state, a critical challenge with vast implications for various optoelectronic applications. To create these superior stimuli-responsive materials, we must first gain a comprehensive understanding of the relationships between molecular structure, packing, and performance. Moreover, strategic molecular design is essential, incorporating different substituents as functional units to modify various intermolecular interactions. Supramolecular self-assembly has been identified as an efficient approach

for arranging functional molecules into nano- or microscopic structures, achieved through various non-covalent interactions. This method enables the manipulation of the optoelectronic properties of the assembled organic chromophores, primarily by altering the molecular packing mode or modulating the supramolecular interactions. This study focuses on using external stimuli to effectively control the solid-state molecular stacking mode of functional chromophores.

In light of recent advancements in stimuli-responsive fluorescent materials, our investigation has three primary objectives. Firstly, we aim to investigate heat-induced variations in molecular assembly, specifically focusing on how these affect intermolecular charge-transfer interactions within divinylbenzene-based chromophore assemblies. To facilitate this, we have designed and synthesized three acceptor-donor-acceptor type divinylbenzene-benzoxazole derivatives with varying alkyl chains. Secondly, we aim to discern the correlation between molecular structure, self-assembly, and photodimerization in systems based on organic chromophores. To accomplish this, we have designed and synthesized a donor-π-acceptor type fluorophore, comprising N-hexylthienoindole as the donor and benzoxazole as the acceptor units, connected through a C=C double bond. We have studied the stimulus-responsive features associated with it, specifically light, and observed the formation of a photoconductive 2D network of the corresponding photodimer. In addition, we have also explored the luminescence changes in response to mechanical and acid/base stimuli. Lastly, we aim to showcase the creation of metastable, kinetically trapped states of chromophores that

respond to their environment. We aim to establish a link between optical, morphological, and structural properties connected with solid-state luminescence switching. For this purpose, we have studied the near-infrared (NIR) mechanoresponsive luminescence turn-on in two linear π-conjugated donor-acceptor-donor type NIR fluorophores, utilizing thienoindole as the donor and thiazolothiazole as the acceptor components. We conducted an in-depth investigation of the photophysical properties and crystal structure analysis to gain a comprehensive understanding at the molecular and supramolecular level, elucidating the factors driving luminescence switching in the solid state.

1.7. References

1. J. Gierschner, S. Varghese, S. Y. Park, *Adv. Opt. Mater.* **2016**, *4*, 348.
2. T. Higuchi, H. Nakanotani, C. Adachi, *Adv. Mater.* **2015**, *27*, 2019.
3. T. L. Mako, J. M. Racicot, M. Levine, *Chem. Rev.* **2019**, *119*, 322.
4. S. Li, B. Lu, X. Fang, D. Yan, *Angew. Chem. Int. Ed.* **2020**, *59*, 22623.
5. W. A. Velema, W. Szymanski, B. L. Feringa, *J. Am. Chem. Soc*. **2014**, *136*, 2178.
6. J. Qi, C. Sun, A. Zebibula, H. Zhang, R. T. K. Kwok, X. Zhao, W. Xi, J. W. Y. Lam, J. Qian, B. Z. Tang, *Adv. Mater.* **2018**, *30*, 1706856.
7. A. Reisch, A. S. Klymchenko, *Small* **2016**, *12*, 1968.
8. K. Zhang, J. Liu, Y. Zhang, J. Fan, C.-K. Wang, L. Lin, *J. Phys. Chem. C* **2019**, *123*, 2470.
9. J. Luo, Z. Xie, J. W. Y. Lam, L. Cheng, H. Chen, C. Qiu, H. S. Kwok, X. Zhan, Y. Liu, D. Zhu, B. Z. Tang, *Chem. Commun.* **2001**, *18*, 1740.
10. J. Mei, N. L. C. Leung, R. T. K. Kwok, J. W. Y. Lam, B. Z. Tang, *Chem. Rev.* **2015**, *115*, 11718.

11. A. Lavrenova, D. W. R. Balkenende, Y. Sagara, S. Schrettl, Y. C. Simon, C. Weder, *J. Am. Chem. Soc.* **2017**, *139*, 4302.
12. T. Yuan, M. Vazquez, A. N. Goldner, Y. Xu, R. Contrucci, M. A. Firestone, M. A. Olson, L. Fang, *Adv. Funct. Mater.* **2016**, *26*, 8604.
13. S. K. Park, I. Cho, J. Gierschner, J. H. Kim, J. H. Kim, J. E. Kwon, O. K. Kwon, D. R. Whang, J. H. Park, B. K. An, S. Y. Park, *Angew. Chem. Int. Ed.* **2016**, *55*, 203.
14. Z. Chi, X. Zhang, B. Xu, X. Zhou, C. Ma, Y. Zhang, S. Liu, J. Xu, *Chem. Soc. Rev.* **2012**, *41*, 3878.
15. S. Yagai, S. Okamura, Y. Nakano, M. Yamauchi, K. Kishikawa, T. Karatsu, A. Kitamura, A. Ueno, D. Kuzuhara, H. Yamada, T. Seki, H. Ito, *Nat. Commun.* **2014**, *5*, 4013.
16. S. Yoshimitsu, T. Hanna, L. Jie, O. Yuji, S. Stephen, T. Nobuyuki, W. Christoph, *J. Am. Chem. Soc.* **2021**, *143*, 5519.
17. Y. Tianyu, V. Mariela, N. G. Amanda, X. Yan, C. Rafael, A. F. Millicent, A. O. Mark, F. Lei, *Adv. Funct. Mater.* **2016**, *26*, 8604.
18. J. Li, J. X. Wang, H. X. Li, N. Song, D. Wang, B. Z. Tang, *Chem. Soc. Rev.* **2020**, *49*, 1144.
19. C.-Y. Shi, Q. Zhang, H. Tian, D.-H. Qu, *SmartMat.* **2020**, e1012.
20. Y.-N. Jing, S.-S. Li, M. Su, H. Bao, W.-M. Wan, *J. Am. Chem. Soc.* **2019**, *141*, 16839.
21. L. Gu, H. Wu, H. Ma, W. Ye, W. Jia, H. Wang, H. Chen, N. Zhang, D. Wang, C. Qian, Z. An, W. Huang, Y. Zhao, *Nat. Commun.* **2020**, *11*, 944.
22. J. Song, H. Lee, E. G. Jeong, K. C. Choi, S. Yoo, *Adv. Mater.* **2020**, *32*, 1907539.
23. R. Zheng, Y. Wang, J. Pan, H. A. Malik, H. Zhang, C. Jia, X. Weng, J. Xie, L. Deng, *ACS Appl. Mater. Interfaces* **2020**, *12*, 27526.
24. P. Anees, V. K. Praveen, K. K. Kartha, A. Ajayaghosh, in *Comprehensive Supramolecular Chemistry II*, ed. J. L. Atwood, Elsevier, **2017**, pp. 297-320.

25. Q. Li, Z. Li, *Acc. Chem. Res.* **2020**, *53*, 962.
26. L. R. MacGillivray, in *Comprehensive Supramolecular Chemistry II*, ed. J. L. Atwood, Elsevier, **2017**, pp. 1.
27. G. Sun, J. Pan, Y. Wu, Y. Liu, W. Chen, Z. Zhang, J. Su, *ACS Appl. Mater. Interfaces* **2020**, *12*, 10875.
28. J. Li, J. Xie, R. Zhang, S. Guo, F. Zhang, K. Guo, S. Dong, *Chem. Commun.* **2018**, *54*, 11455.
29. G. R. Desiraju, *Acc. Chem. Res.* **2002**, *35*, 565.
30. Y. Sagara, S. Yamane, M. Mitani, C. Weder, T. Kato, *Adv. Mater.* **2016**, *28*, 1073.
31. Z. Xie, B. Yang, F. Li, G. Cheng, L. Liu, G. Yang, H. Xu, L. Ye, M. Hanif, S. Liu, D. Ma, Y. Ma, *J. Am. Chem. Soc.* **2005**, *127*, 14152.
32. S.-J. Yoon, J. W. Chung, J. Gierschner, K. S. Kim, M.-G. Choi, D. Kim, S. Y. Park, *J. Am. Chem. Soc.* **2010**, *132*, 13675.
33. A. Rananaware, R. S. Bhosale, K. Ohkubo, H. Patil, L. A. Jones, S. L. Jackson, S. Fukuzumi, S. V. Bhosale, S. V. Bhosale, *J. Org. Chem.* **2015**, *80*, 3832.
34. H. Li, J. Cheng, H. Deng, E. Zhao, B. Shen, J. W. Y. Lam, K. S. Wong, H. Wu, B. S. Li, B. Z. Tang, *J. Mater. Chem. C* **2015**, *3*, 2399.
35. C. Chipot, R. Jaffe, B. Maigret, D. A. Pearlman, P. A. Kollman, *J. Am. Chem. Soc.* **1996**, *118*, 11217.
36. M. Cao, A. Fu, Z. Wang, J. Liu, N. Kong, X. Zong, H. Liu, J. J. Gooding, *J. Phys. Chem. C* **2014**, *118*, 2650.
37. M. Lübtow, I. Helmers, V. Stepanenko, R. Q. Albuquerque, T. B. Marder, G. Fernandez, *Chem. Eur. J.* **2017**, *23*, 6198.
38. T. Chen, M. Li, J. Liu, *Cryst. Growth Des.* **2018**, *18*, 2765.
39. A. J. de Jesus, H. Yin, in *Comprehensive Supramolecular Chemistry II*, ed. J. L. Atwood, Elsevier, **2017**, pp. 311-328.
40. N. Li, Y. Y. Liu, Y. Li, J. B. Zhuang, R. R. Cui, Q. Gong, N. Zhao, B. Z. Tang, *ACS Appl. Mater. Interfaces* **2018**, *10*, 24249.

41. M. Zhang, X. Yin, T. Tian, Y. Liang, W. Li, Y. Lan, J. Li, M. Zhou, Y. Ju, G. Li, *Chem. Commun.* **2015**, *51*, 10210.
42. J. H. Adair, E. Suvaci, J. Sindel, in *Encyclopedia of Materials: Science and Technology*, ed. K. H. J. Buschow, R. W. Cahn, M. C. Flemings, B. Ilschner, E. J. Kramer, S. Mahajan and P. Veyssière, Elsevier, **2001**, pp. 1-10.
43. K. C. Naeem, V. C. Nair, *Mol. Syst. Des. Eng.* **2018**, *3*, 142.
44. X. Gu, J. Yao, G. Zhang, Y. Yan, C. Zhang, Q. Peng, Q. Liao, Y. Wu, Z. Xu, Y. Zhao, H. Fu, D. Zhang, *Adv. Funct. Mater.* **2012**, *22*, 4862.
45. R. Rao M, C.-W. Liao, W.-L. Su, S.-S. Sun, *J. Mater. Chem. C* **2013**, *1*, 5491.
46. C. Wang, Y. Yu, Z. Chai, F. He, C. Wu, Y. Gong, M. Han, Q. Li, Z. Li, *Mater. Chem. Front.* **2019**, *3*, 32.
47. Z. Wang, F. Yu, W. Chen, J. Wang, J. Liu, C. Yao, J. Zhao, H. Dong, W. Hu, Q. Zhang, *Angew. Chem. Int. Ed.* **2020**, *59*, 17580.
48. K. Nagura, S. Saito, H. Yusa, H. Yamawaki, H. Fujihisa, H. Sato, Y. Shimoikeda, S. Yamaguchi, *J. Am. Chem. Soc.* **2013**, *135*, 10322.
49. F. Khan, A. Ekbote, G. Singh, R. Misra, *J. Mater. Chem. C* **2022**, *10*, 5024.
50. K. Guo, F. Zhang, S. Guo, K. Li, X. Lu, J. Li, H. Wang, J. Cheng, Q. Zhao, *Chem. Commun.* **2017**, *53*, 1309.
51. Y. Liu, Q. Zeng, B. Zou, Y. Liu, B. Xu, W. Tian, *Angew. Chem. Int. Ed.* **2018**, *57*, 15670.
52. M. Tanioka, S. Kamino, A. Muranaka, Y. Ooyama, H. Ota, Y. Shirasaki, J. Horigome, M. Ueda, M. Uchiyama, D. Sawada, S. Enomoto, *J. Am. Chem. Soc.* **2015**, *137*, 6436.
53. H. Liu, Y. Gu, Y. Dai, K. Wang, S. Zhang, G. Chen, B. Zou, B. Yang, *J. Am. Chem. Soc.* **2020**, *142*, 1153.
54. Q. Qi, C. Li, X. Liu, S. Jiang, Z. Xu, R. Lee, M. Zhu, B. Xu, W. Tian, *J. Am. Chem. Soc.* **2017**, *139*, 16036.

55. H. Wang, P. Chen, Z. Wu, J. Zhao, J. Sun, R. Lu, *Angew. Chem. Int. Ed.* **2017**, *56*, 9463.
56. J. Guo, J. Fan, X. Liu, Z. Zhao, B. Z. Tang, *Angew. Chem. Int. Ed.* **2020**, *59*, 8828.
57. P. Wei, J.-X. Zhang, Z. Zhao, Y. Chen, X. He, M. Chen, J. Gong, H. H.-Y. Sung, I. D. Williams, J. W. Y. Lam, B. Z. Tang, *J. Am. Chem. Soc.* **2018**, *140*, 1966.
58. S. Li, B. Lu, X. Fang, D. Yan, *Angew. Chem. Int. Ed.* **2020**, *59*, 22623.
59. I. Aprahamian, *Chem. Commun.* **2017**, *53*, 6674.
60. X. Su, Y. Wang, X. Fang, Y.-M. Zhang, T. Zhang, M. Li, Y. Liu, T. Lin, S. X.-A. Zhang, *Chem. Asian J.* **2016**, *11*, 3205.
61. Y. Ren, S. Xie, E. S. Grape, A. K. Inge, O. Ramström, *J. Am. Chem. Soc.* **2018**, *140*, 13640.
62. D. Devadiga, T. N. Ahipa, *Soft Matter* **2022**, *18*, 8008.
63. M. Wałęsa-Chorab, W. G. Skene, *ACS Appl. Mater. Interfaces* **2017**, *9*, 21524.
64. G. A. Corrente, D. A. González, E. Aktas, A. L. Capodilupo, G. Mazzone, F. Ruighi, G. Accorsi, D. Imbardelli, C. Rodriguez-Seco, E. Martinez-Ferrero, E. Palomares, A. Beneduci, *Adv. Optical Mater.* **2023**, *11*, 2201506.
65. A. N. Woodward, J. M. Kolesar, S. R. Hall, N.-A. Saleh, D. S. Jones, M. G. Walter, *J. Am. Chem. Soc.* **2017**, *139*, 8467.
66. G. A. Corrente, E. Fabiano, F. Manni, G. Chidichimo, G. Gigli, A. Beneduci, A.-L. Capodilupo, *Chem. Mater.* **2018**, *30*, 5610.
67. Y. Sun, M. Shi, Y. Zhu, I. F. Perepichka, X. Xing, Y. Liu, C. Yan, H. Meng, *ACS Appl. Mater. Interfaces* **2020**, *12*, 24156.
68. Y. Gong, S. He, Y. Li, Z. Li, Q. Liao, Y. Gu, J. Wang, B. Zou, Q. Li, Z. Li, *Adv. Optical Mater.* **2020**, *8*, 1902036.
69. S. L. Sonawane, S. K. Asha, *ACS Appl. Mater. Interfaces* **2016**, *8*, 10590.
70. M.-S. Yuan, D.-E Wang, P. Xue, W. Wang, J.-C. Wang, Q. Tu, Z. Liu, Y. Liu, Y. Zhang, J. Wang, *Chem. Mater.* **2014**, *26*, 2467.

71. L. Bai, P. Bose, Q. Gao, Y. Li, R. Ganguly, Y. Zhao, *J. Am. Chem. Soc.* **2017**, *139*, 436.
72. B. Yoon, J. Lee, I. S. Park, S. Jeon, J. Lee, J.-M. Kim, *J. Mater. Chem. C* **2013**, *1*, 2388.
73. R. Thirumalai, R. D. Mukhopadhyay, V. K. Praveen, A. Ajayaghosh, *Sci. Rep.* **2015**, *5*, 9842.
74. X. Zhu, R. Liu, Y. Li, H. Huang, Q. Wang, D. Wang, X. Zhu, S. Liu, H. Zhu, *Chem. Commun.* **2014**, *50*, 12951.
75. X. Yu, M. Chang, W. Chen, D. Liang, X. Lu, G. Zhou, *ACS Appl. Mater. Interfaces* **2020**, *12*, 39505.

Chapter 2

Heat-Induced 'Parallel' to 'Orthogonal' Switching in Divinylbenzene-Benzoxazole-based Fluorophores and Reversible Luminescence Changes

2.1. Abstract

Organic crystals that exhibit reversible solid-state luminescence triggered by heat stimulus have garnered great research interest in recent years. In this work, we demonstrate thermoresponsive, reversible color and photoluminescence switching in divinylbenzene-benzoxazole derivatives. The fluorescence switching is caused by differential chromophore packing and the resulting charge transfer On/Off states induced by heat. It is noteworthy that the reversibility, range of colors, and transition temperature associated with the luminescence switching are dependent on the length of the alkyl chains. Our results suggest that controlling charge-transfer interactions in chromophore assemblies may offer a versatile approach for creating functional organic materials with switchable, high-contrast solid-state luminescence. These findings have implications for the development of sensors, data storage devices, dynamic optical materials, and security inks.

2.2. Introduction

Organic luminescent crystals have a wide range of applications, including lasers, light-emitting diodes, data storage devices, and solar concentrators.[1-14] In recent years, many solid-state photoluminescent materials that respond to temperature, light, pressure, mechanical force, chemical, and electrical stimuli have been reported.[15-24] These smart materials undergo reversible changes to their superstructures or crystalline phases in response to external stimuli, resulting in different emission colors. Among organic smart materials, those that exhibit thermoresponsive luminescence, or reversible emission color induced by heat, have gained particular attention due to their potential for use in next-generation thermal sensors, information storage devices, dynamic optical materials, and anti-counterfeiting paintings.[25-33] As a result, research groups have focused on developing advanced luminescent organic materials with improved temperature sensing performance. In this context, controlling molecular packing modes to fine-tune emission characteristics of luminescent crystals has become increasingly crucial, paving the way for innovations in the field.[34-43]

Araki *et al.* were among the first to report on the efficient on-off switching of solid-state luminescence through heat-induced conversion in a terpyridine derivative (**1**, **Figure 2.1**).[44] This molecule yields two types of crystals: non-luminescent needle-like formations and luminescent plate-like structures, which emit strong blue luminescence. The phenomenon of heat-induced luminescence on-off switching was linked to alterations in the molecular packing within the crystal lattice. Specifically,

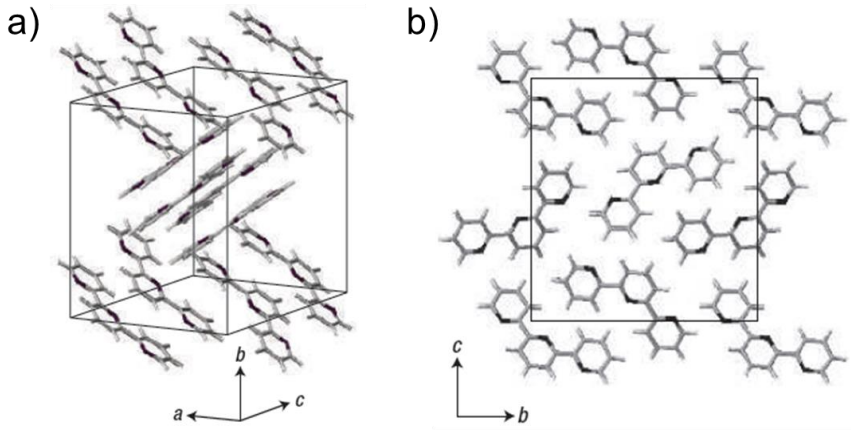

Figure 2.1. X-ray crystallographic pictures of terpyridine (**1**) crystals. The a) plate crystal and b) needle crystal along the *a*-axis. The black parts in each molecule indicate nitrogen atoms. (Adapted from reference 44)

needle crystals comprise columnar stacks of molecules, a characteristic absent in plate crystals of the terpyridine derivative. Consequently, this divergence results in the observed conformational changes within the crystals. The mode of molecular assembly can be effectively altered by controlling the heating and cooling of the solid sample. This manipulation leads to the switching between luminescent and non-luminescent states.

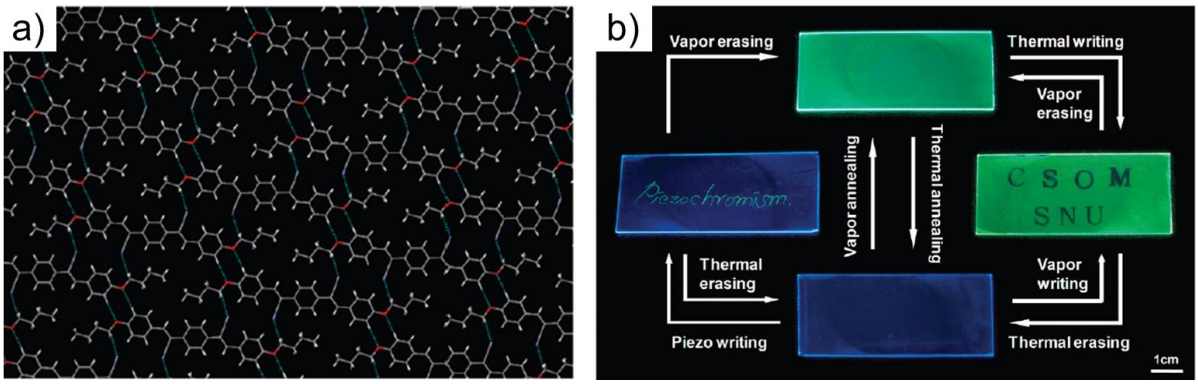

Figure 2.2. a) Top view of hydrogen-bonded molecular sheet in the G-phase of DBDCS (**2**) molecules in the crystal lattice. b) Images of the luminescence writing/erasing cycle in DBDCS/PMMA film under various stimuli. (Adapted from reference 40)

Park *et al.* developed a cyanostilbene-based material (**2**, DBDCS) that showcased a change in luminescence due to the two-dimensional sliding capability of the molecular layers. This was achieved through intermolecular hydrogen bonds formed by C–H···N and C–H···O, which were triggered by external stimuli.[40] This molecule exists in two emissive state, which are green emitting G-phase and blue emitting B-phase. The transition from G-phase to B-phase was achieved through heating the sample at 125 °C for an hour and the reversible transition was achieved through solvent vapor annealing or mechanical stimulus. In G-phase, antiparallel coupling of the local dipoles resulted in a weak excitonic coupling but efficient excimer formation, whereas in B-phase, a head-to-tail arrangement of the local dipoles resulted in diminished excimer formation and substantially increased excitonic interaction. The origin of this luminescence switching is the two-dimensional sliding capability of molecular sheets formed through intermolecular hydrogen bonds (**Figure 2.2a**). Further, they demonstrated a multi-stimuli-responsive rewritable fluorescent optical recording media using DBDCS/PMMA film as shown in the **Figure 2.2b**.

Rao *et al.* reported on quinoxaline-anthracene based molecule exhibiting thermoresponsive on-off emission.[45] This behavior was due to the transformation from a two-dimensional herringbone structure to one-dimensional *J*-type stacks. In the herringbone structure, the minimal electronic couplings between the molecules result in a strong emission. Conversely, the *J*-type stacks lead to increased electronic

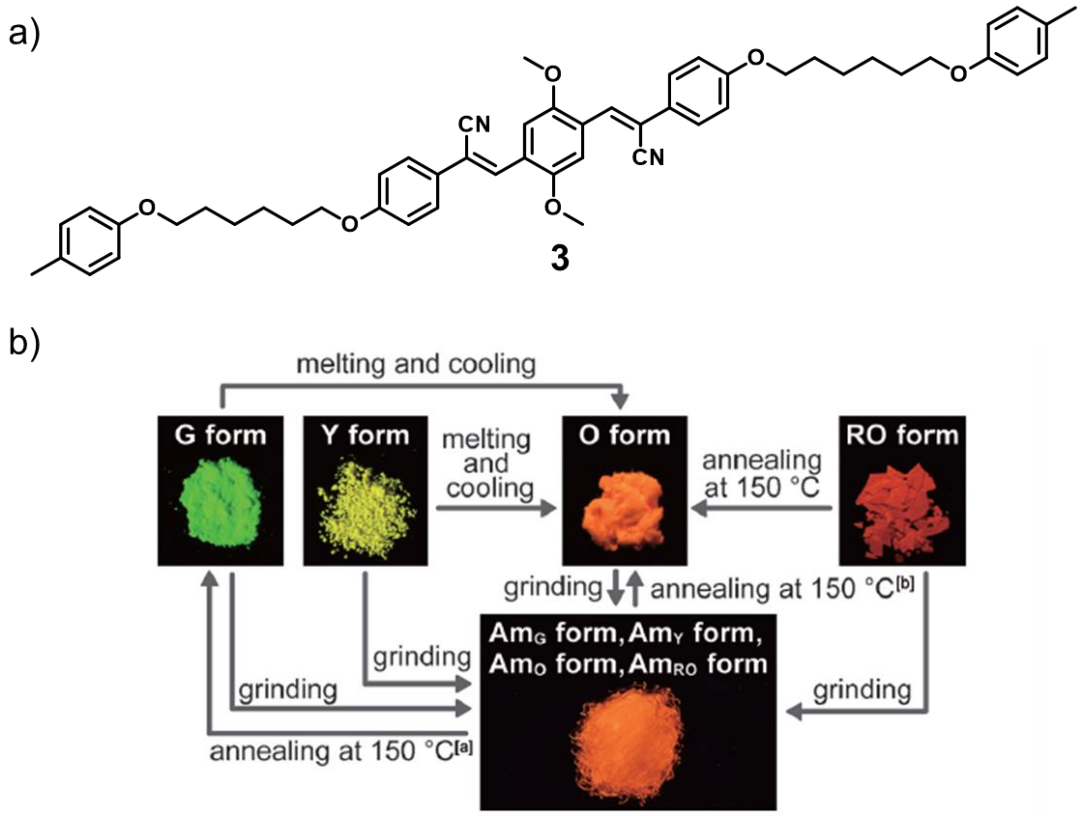

Figure 2.3. a) Chemical structure of **3**. b) Photographs of the five different emissive forms of **3** under 365 nm UV light at room temperature. (Adapted from reference 46)

couplings between donor and acceptor moieties of adjacent molecules, which in turn causes an emission-quenched state.

Weder and co-workers synthesized a derivative of cyanostilbene capable of forming five distinct solid-state molecular assemblies, exhibiting changes in luminescence in response to thermal and mechanical stimuli, as depicted in **Figure 2.3**.[46] Compound **3** forms four polymorphic states: G form, Y form, O form, and RO form. These states were obtained by either precipitation or crystallization from solution, displaying green, yellow, orange, and red-orange emissions, respectively.

Under mechanical stimulus, the crystalline polymorphs transitioned to amorphous states, which emit an orange light. Upon annealing the amorphous state at 150 °C, recrystallization occurred. The G form could be regenerated by annealing the AmG form, while the O form was restored from the AmO or AmRO form. However, annealing the AmY form resulted in a yellow-green emission due to the coexistence of two polymorphs. Single-crystal X-ray analysis suggested that the peripheral tolyloxyalkoxy group, appended at the end of the chromophore backbone, plays a pivotal role in the solid-state arrangements and the diversity of emissive forms.

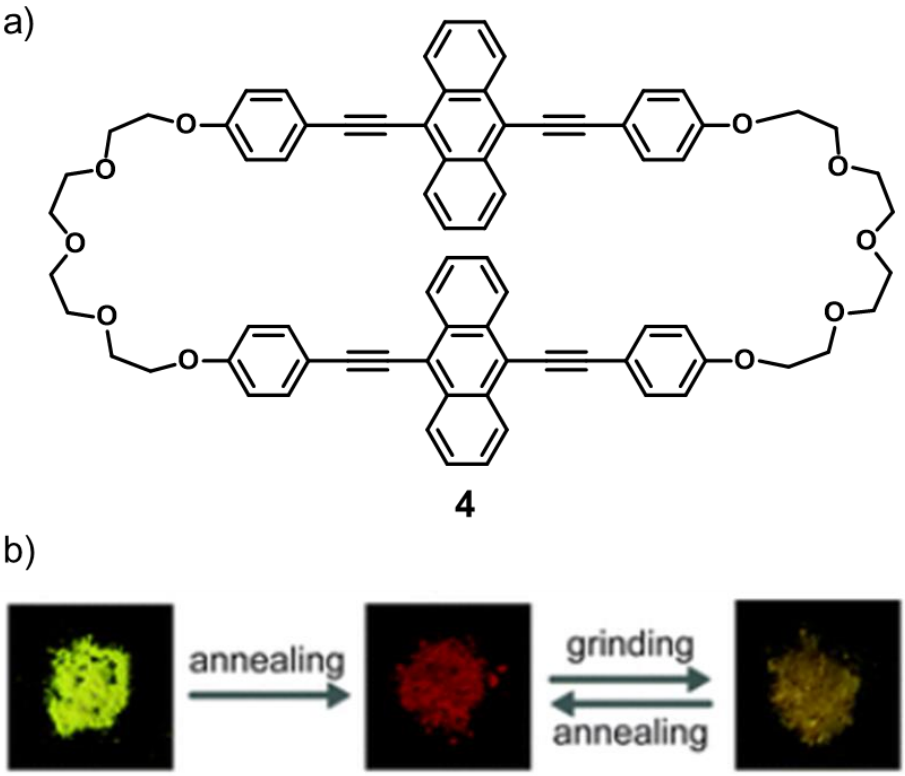

Figure 2.4. a) Chemical structure of **4**. b) Photographs of thermal and mechanical stimuli responsive luminescence switching in **4**. (Adapted from reference 23)

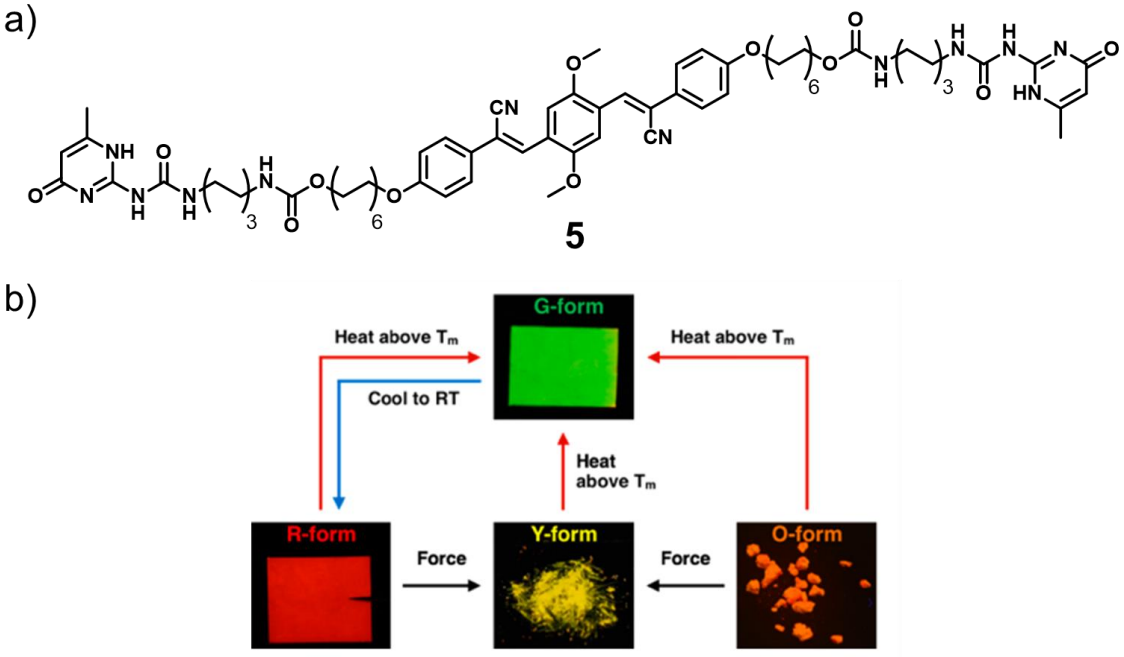

Figure 2.5. a) Chemical structure of **5**. b) Photographs of **5** in different forms under 365 nm UV light. (Adapted from reference 47)

The same group also developed a derivative of cyclophane that displays changes in solid-state fluorescence in response to mechanical and thermal stimuli, a process facilitated by alterations in molecular assembly, as illustrated in **Figure 2.4a**.[23] The thermal and mechanical stimuli responsive luminescent behavior of **4** is summarized in **Figure 2.4b**. Recently, this group developed a supramolecular polymer that exhibits a thermoresponsive luminescence.[47] A variety of self-supporting shapes were derived from the supramolecular polymer, that results from the self-assembly of compound **5**. These samples displayed four distinct emission colors, orange (O-form), red (R-form), yellow (Y-form), and green (G-form), depending on the thermomechanical stimuli and the environmental conditions (**Figure 2.5**). The orange

and red-emissive forms are due to the formation of ground-state chromophore aggregates and excimers, respectively. Heating the compound above its melting temperature triggered green emission from the monomer state. Meanwhile, yellow light emission, achieved through scratching, correlated to the formation of excimers. However, the emissive species of the Y-form differed from those in the orange and red emissive states. Collectively, these findings suggest that adjusting molecular stacking modes serves as an effective strategy for refining the optical and electronic properties of π-conjugated organic materials.

Recent advancements in the field of thermoresponsive luminescent materials, as documented in numerous scientific studies, are noteworthy. These materials are increasingly critical in fields such as sensing technologies and optoelectronics. Yet, a clear understanding gap persists concerning how to accurately modulate the charge transfer interactions within molecular assemblies to enable high-contrast luminescence switching. Charge transfer interactions, the exchange of electrons between donor and acceptor units, are paramount in determining the luminescence properties of a material. However, managing these interactions is complex due to the nuanced nature of the molecular structures involved. Key factors such as the balance between donor and acceptor units, their relative positioning, proximity, and the overarching assembly dynamics significantly influence the efficiency of charge transfer, hence affecting the luminescent characteristics. This chapter aims to fill this understanding gap by providing a detailed analysis of how to manipulate acceptor-

donor-acceptor (A-D-A) type molecules for optimal performance in thermoresponsive applications. The A-D-A configuration is of particular interest, where the donor unit is sandwiched by two acceptor units. This specific design promotes a higher potential for electron movement, which could lead to an improved luminescent response.

2.3. Results and discussion

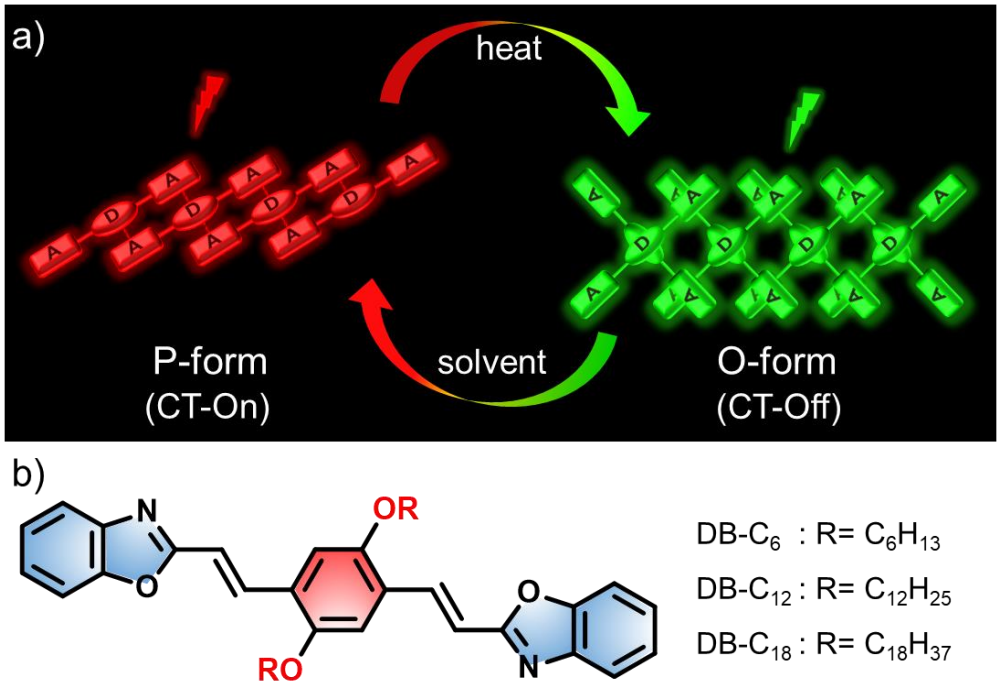

Figure 2.6. a) Schematic illustration of the heat-induced switching of molecular packing in divinylbenzene-benzoxazole derivatives, leading to the charge transfer On/Off (CT-On/Off) states and corresponding luminescence color changes. b) Chemical structures of the divinylbenzene-benzoxazole derivatives under study.

In this chapter, we demonstrate reversible On/Off control of charge transfer interaction between A-D-A type molecules through a 'crystal' to 'crystal' transition, which involves a change in fluorophore stacking mode from "parallel" (P-form) to "orthogonal" (O-form), resulting in efficient switching of solid-state luminescence

with high contrast (**Figure 2.6a**). To achieve this, we designed and synthesized three derivatives of divinylbenzene-benzoxazole-based molecules containing different lengths of alkyl sidechains: hexyl (**DB-C_6),** dodecyl (**DB-C_{12}**), and octadecyl (**DB-C_{18}),** as shown in **Figure 2.6b**. Our findings reveal that the reversibility, transition temperatures, and range of wavelengths associated with luminescence switching can be controlled by varying the alkyl chain length.

2.3.1. Synthetic strategy

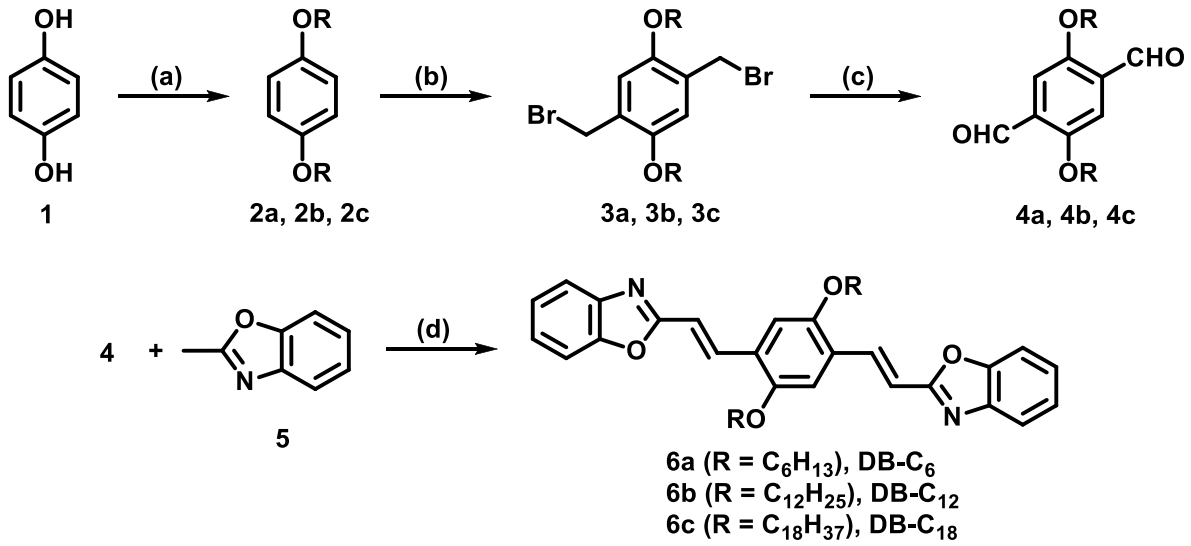

Scheme 2.1. Synthesis of **DB-C_n**; *Reagents and conditions:* (a) alkyl bromide, NaOH, DMF, 100 °C, 24 h. (b) paraformaldehyde, 33% HBr in acetic acid, 70 °C, acetic acid, 2-8 h. (c) $NaHCO_3$, DMSO, 115 °C, 0.5 h.[48] (d) KOH, DMF, rt or 55 °C, 3 h.[49]

The molecules under study were synthesized *via* Knoevenagel condensation reaction between alkoxy-substituted terephthalaldehyde and 2-methylbenzoxazole. Details of the reagents and reaction conditions are shown in **Scheme 2.1**. All

compounds were obtained in good yield and characterized by various analytical techniques such as ^{1}H NMR, ^{13}C NMR, and high-resolution mass spectrometry. They were soluble in common organic solvents like hexane, toluene, tetrahydrofuran (THF), *N*,*N*-dimethylformamide (DMF) etc.

2.3.2. Thermal characterization

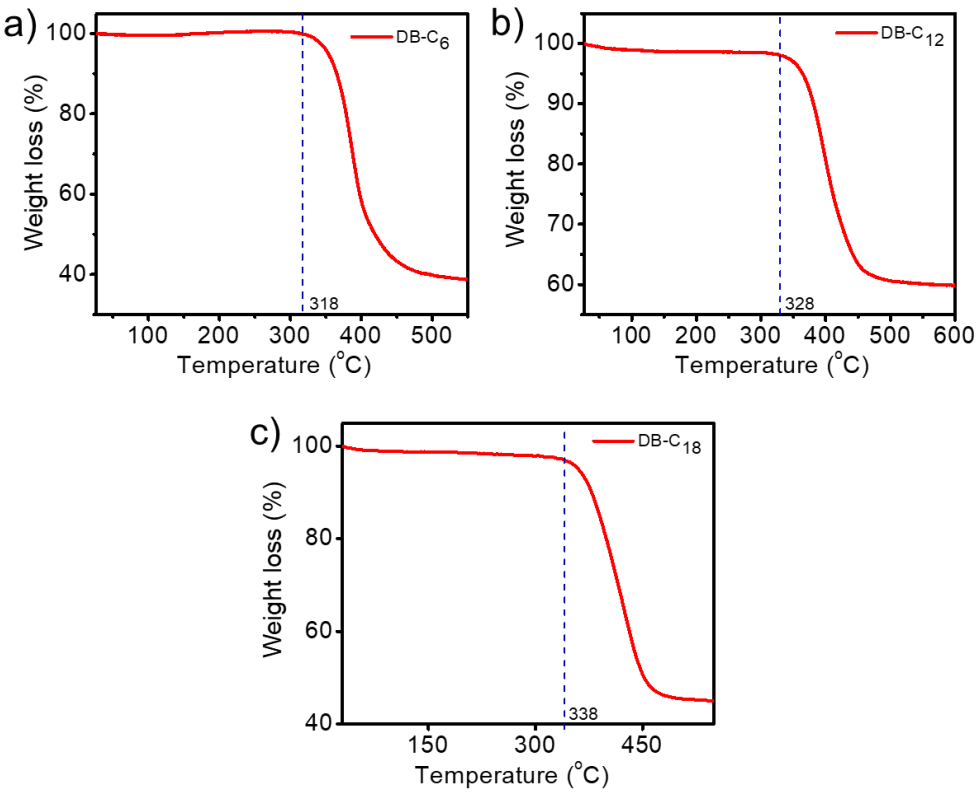

Figure 2.7. Thermogravimetric analyses of a) **DB-C$_6$**, b) **DB-C$_{12}$**, and c) **DB-C$_{18}$**.

Thermal gravimetric analysis (TGA) was carried out to characterize the thermal properties of the material in the bulk state. The thermal stability of **DB-C$_6$**, **DB-C$_{12}$**, and **DB-C$_{18}$** in the solid-state were obtained from TGA profile. All three derivatives displayed good thermal stability up to 300 °C (**Figure 2.7**). The T_5 value, which

corresponds to the temperature at which the material loses 5% of its initial weight, is a quantitative measure of thermal stability. The T_5 values of **DB-C$_6$**, **DB-C$_{12}$**, and **DB-C$_{18}$** were found to be at 318, 328, and 338 °C respectively. Thermal stability increased with increase in alkyl chain length indicating that the stronger intermolecular interactions in **DB-C$_{18}$** at the molecular level provide better thermal stability to the bulk material.

2.3.3. Photophysical properties in the solution state

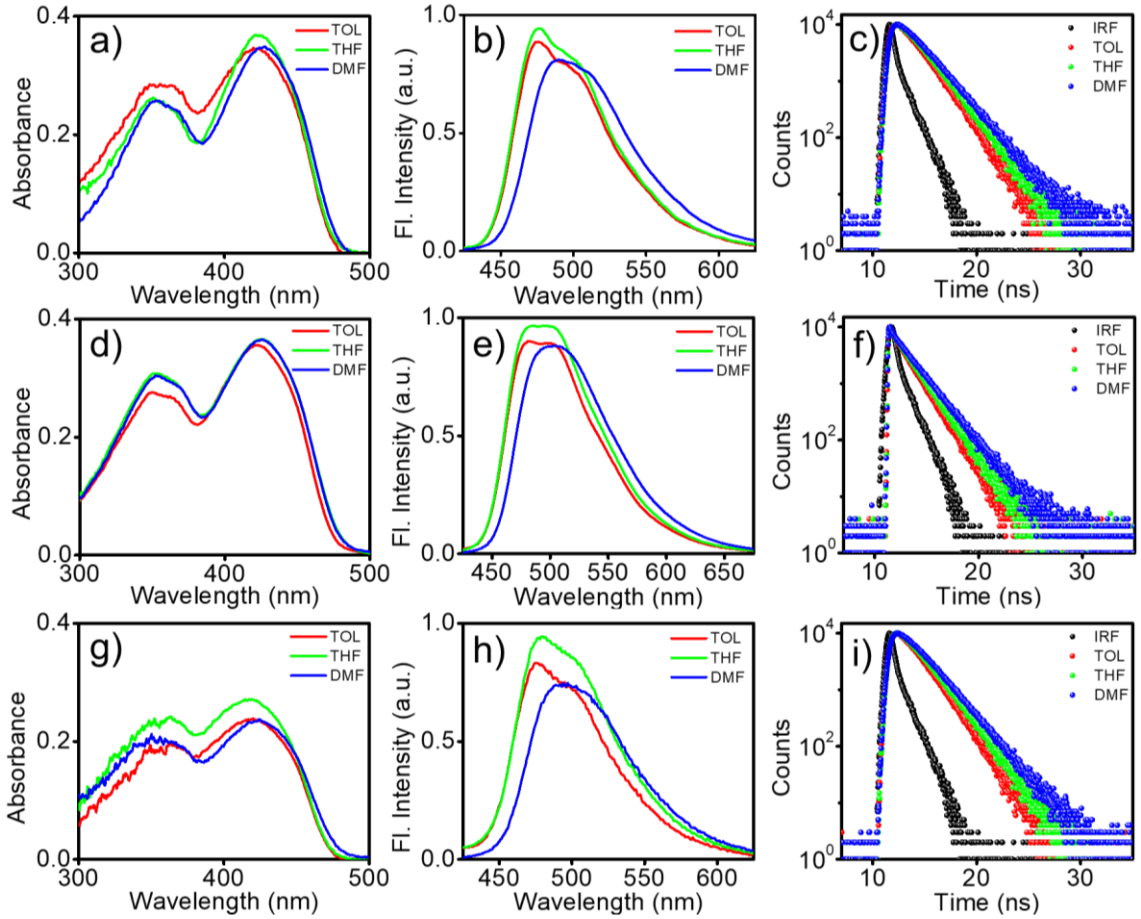

Figure 2.8. a, d, g) Absorption spectra; b, e, h) emission spectra; and c, f, i) time-resolved fluorescence decay profile recorded in different solvents (conc. = 10^{-5} M; pathlength, l = 1 cm) for **DB-C$_6$**, **DB-C$_{12}$**, and **DB-C$_{18}$** respectively.

The UV-vis absorption and fluorescence properties of the molecules were recorded in different solvents with increasing polarity (toluene, THF, and DMF; concentration = 10^{-5} M) as shown in **Figure 2.8**. The observed photophysical parameters are summarized in **Table 2.1**. The absorption spectra were relatively unchanged by variations in solvent polarity (λ_{abs} = 355 ± 1 nm and 422 ± 4 nm). The absorption band around 355 nm originates from the aromatic π–π* transitions and the major absorption band in the visible region (400-500 nm) is ascribed to the intramolecular charge transfer (ICT). But the emission spectra exhibited a notable shift towards red (~ 475-490 nm) as the solvent polarity increased. Excited-state lifetime displayed a slight increase with increase in solvent polarity and was obtained from time-correlated single-photon counting analysis using 410 nm laser light as the excitation source.

These findings imply that the dipole moments of the excited states are slightly greater than those of the ground states. Localization of the π-electrons towards acceptors in more polar solvents is because of the linking of donor and acceptor moieties to form a conjugated backbone resulted in an ICT state. The vibrational levels of the molecules are disturbed by solvent relaxation processes in more polar solvents, which results in a broadening of the emission spectra. In other words, the direct excitation of these molecules leads to a locally excited (LE) state with approximately the same dipole moment as the ground state, which then transforms into a more polar emissive state *via* an ICT process. Fluorescence quantum yields of

these derivatives showed negligible changes with an increase in the solvent polarity (**Table 2.1**). The variation in alkyl chain length did not have any significant impact on the photophysical properties of the molecules in solution.

Table 2.1. Absorption maximum, extinction coefficient (ε), emission maximum, fluorescence quantum yield (Φ_f), and average fluorescence lifetime (τ_f) of **DB-C$_6$**, **DB-C$_{12}$**, and **DB-C$_{18}$** in various solvents.

Solvent	Compound	λ_{abs} (nm)	ε x 10^5 (M^{-1} cm^{-1})	λ_{em} (nm)	Φ_f	τ_f (ns)
Toluene	DB-C_6	354, 422	0.28, 0.34	475, 500	0.69	1.55
	DB-C_{12}	355, 422	0.27, 0.36	477, 500	0.78	1.55
	DB-C_{18}	356, 422	0.19, 0.24	475, 500	0.64	1.55
THF	DB-C_6	355, 424	0.26, 0.37	478, 502	0.66	1.76
	DB-C_{12}	355, 424	0.30, 0.37	479, 500	0.82	1.73
	DB-C_{18}	356, 420	0.31, 0.43	478, 503	0.61	1.87
DMF	DB-C_6	355, 426	0.26, 0.35	489	0.66	1.95
	DB-C_{12}	355, 424	0.30, 0.37	492	0.79	2.00
	DB-C_{18}	355, 424	0.21, 0.24	491	0.60	1.97

2.3.4. Heat-induced solid-state luminescence switching

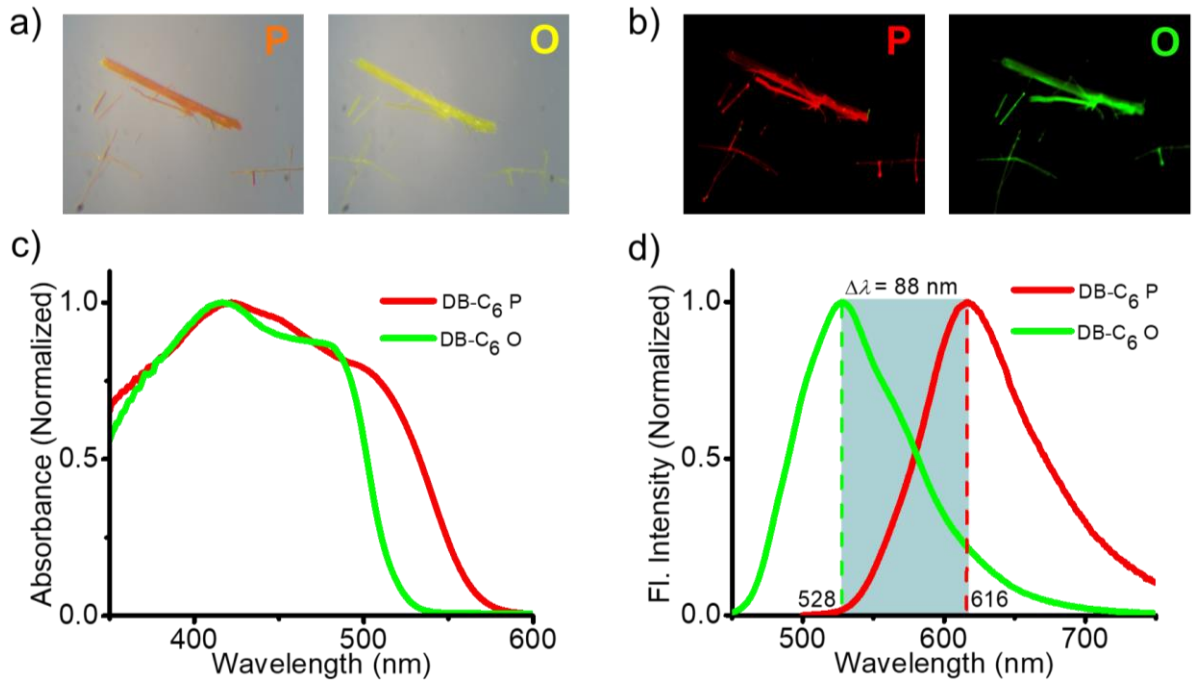

Figure 2.9. Photographs of **DB-C$_6$** crystals in the parallel (P-form) and orthogonal (O-form) states under a) room light and b) 365 nm UV light at room temperature. The corresponding normalized c) absorption and d) photoluminescence spectra of the crystals.

High quality single crystals of **DB-C$_6$** were synthesized through the slow evaporation of its saturated solution in a 1:1 volume ratio of CH_2Cl_2/CH_3OH. Upon heating, the orange color of the crystals changed to yellow and the emission switched from red to green. **Figure 2.9a** and **2.9b** show photographs of the parallel (P-form) and orthogonal (O-form) crystals under room light and 365 nm UV light, respectively. The P-form displayed broad absorption in the visible region with an onset at 565 nm and an absorption maximum at 420 nm (**Figure 2.9c**). Upon heating at 65 °C (O-form), the absorption onset was significantly blue-shifted to 520 nm with a slight

blue-shift of 5 nm to the absorption maximum. **DB-C$_6$** exhibited two emissive states corresponding to the P- and O-forms. The P-form had an emission maximum at 616 nm with red luminescence. Upon heating, the emission maximum shifted to 528 nm with a green luminescence (**Figure 2.9d**). The absolute quantum yield of the P- and O-forms were 37% and 54%, respectively. The O-form was stable at ambient temperature, maintaining the same emission maximum and intensity. The P-form was recovered by dissolving the O-form in a suitable solvent (such as chloroform, dichloromethane, or tetrahydrofuran) and then precipitating it by adding cold hexane.

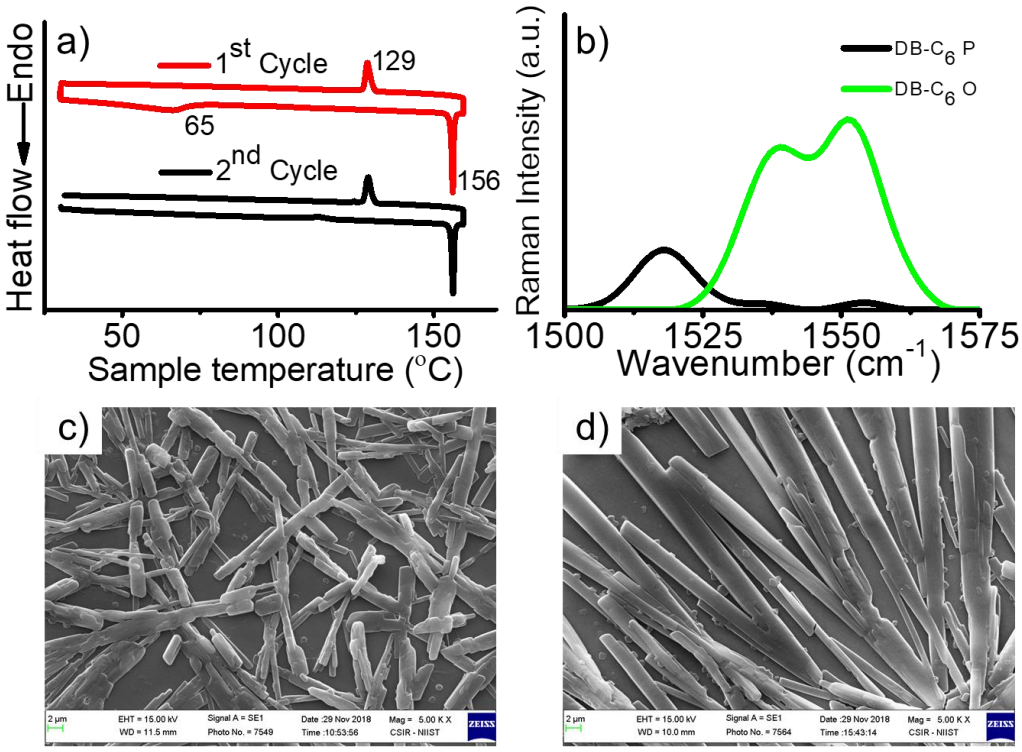

Figure 2.10. a) DSC thermogram and b) Raman spectra of **DB-C$_6$** at different conditions; P (parallel) is the pristine sample and O (orthogonal) is the sample heated at transition temperature (65 °C) followed by air cooling to room temperature. Morphology of **DB-C$_6$** in c) P- and d) O-form imaged using FE-SEM (scale bar represents 2 μm).

The phase transition related to the change in luminescence was studied using differential scanning calorimetry (DSC; as shown in **Figure 2.10a**). A wide endothermic peak was observed at 65 °C during the initial heating cycle, corresponding to the transformation of P-form to the O-form. However, this peak was not observed during the second heating cycle, indicating that the change from O- to P-form is irreversible upon cooling. A sharp endothermic transition was also seen at 156 °C, which is the melting point of the sample, and the exothermic change at 129 °C is believed to be the result of the regeneration of O-form.

Raman spectroscopy was used to analyze the molecules, as it would provides precise structural information such as the degree of π-electron delocalization, molecular order, and supramolecular arrangement.[50-52] The Raman spectra of the P- and O-forms were recorded using a laser excitation source of 785 nm (**Figure 2.10b**). The most intense Raman bands in the 1200-1700 cm^{-1} region are associated with the skeletal C=C/C–C stretching vibrations of the conjugated backbone. Notably, a vibrational band at 1520 cm^{-1} in the P-form showed a significant upward frequency shift to 1545 cm^{-1} ($\Delta\nu$ = 25 cm^{-1}) in the O-form. This frequency shift indicates changes in the structural π-conjugation between the benzoxazole unit and the central phenyl group due to changes in the torsional dihedral angle. The associated changes in intensity patterns suggest differences in the intermolecular interactions operating in both the P- and O-forms. Milani *et al*. demonstrated that higher intermolecular interactions due to efficient molecular packing can induce "pinning effects," resulting

in reduced Raman intensity.[50] Therefore, it can be concluded that the P-form has more effective packing compared to the O-form. The morphologies of the P-form and O-form were studied using scanning electron microscopy (SEM), which showed that the transformation from P-form to O-form was accompanied not only with fluorescence switching, but also with changes in the supramolecular morphology (**Figure 2.10c** and **2.10d**).

To understand the heat-induced switching of color and luminescence of **DB-C$_6$**, we conducted single-crystal X-ray diffraction (SCXRD) analysis on both P- and O-form crystals. Both have a triclinic crystal system with a space group of *P*-1 (**Table 2.2 and 2.3**). The P-form crystals form planar molecular sheets through the combination of four intermolecular C–H···N (2.69 Å) and two intramolecular C–H···O (2.22 Å) hydrogen bonds, as well as π-π stacking between donor-acceptor moieties and van der Waals interactions between alkyl chains (**Figure 2.11a**). As the central phenyl ring with two alkoxy-substituents is electron-rich (electron donor, D) while the outer benzoxazole moieties are electron-poor (electron acceptors, A), **DB-C$_6$** belongs to the class of A-D-A-type molecules, which have two local dipoles that add up to a net zero dipole moment. Upon self-assembly, antiparallel dipole coupling places the central 'D' ring of the upper sheet just above the 'A' ring of the lower sheet (**Figure 2.11b**), resulting in parallel arrangement of molecules. The distance between

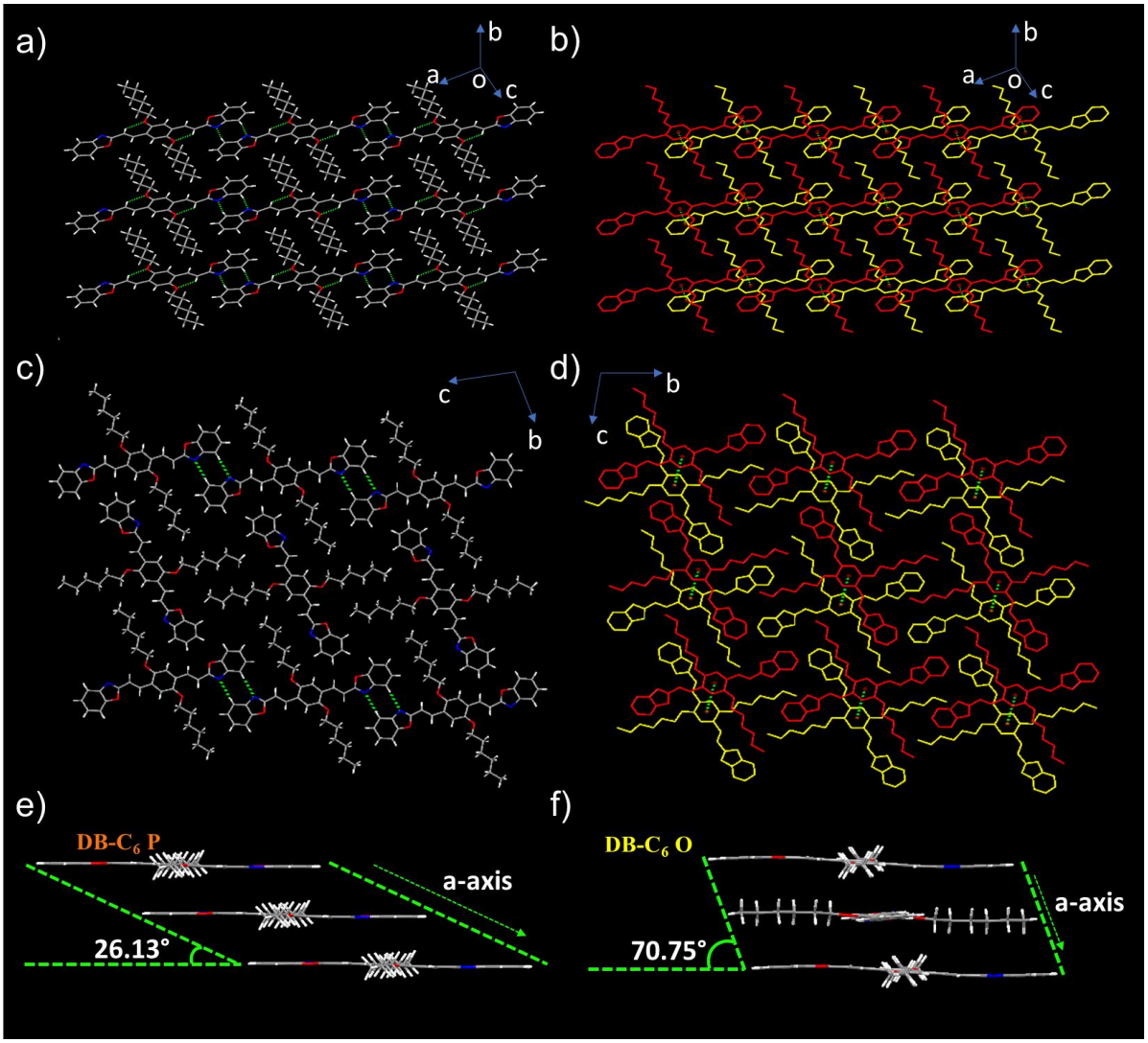

Figure 2.11. Molecular packing of **DB-C$_6$** in P- and O-forms; a) Molecular sheets in P-form with a 'parallel' arrangement of chromophores; green lines indicate the intermolecular C-H···N hydrogen-bonding (distance of 2.69 Å) and intramolecular C-H···O hydrogen-bonding (distance of 2.22 Å) b) Stacking of donor - acceptor units in two adjacent molecular sheets in P-form; green lines indicate the π-stacking (distance of 3.68 Å) c) Molecular sheets in O-form with a 'orthogonal' arrangement of chromophores; green lines indicate the intermolecular C-H···N hydrogen-bonding (distance of 2.65 Å) and intramolecular C-H···O (distance of 2.24 Å) d) Stacking of donor - donor units in two adjacent molecular sheets in O-form; green lines indicate the π-stacking (distance of 4.15 Å). Side view and illustration of slip angle of **DB-C$_6$** molecules in e) P-form and f) O-form.

Table 2.2. Crystallographic data of **DB-C_6** (P-form).

Sample	**DB-C_6 P**	
Empirical formula	C36H40N2O4	
Formula weight	564.70	
Temperature	297(2) K	
Wavelength	0.71073 Å	
Crystal system	Triclinic	
Space group	*P*-1	
Unit cell dimensions	a = 8.3639(7) Å	α = 85.133(4)°
	b = 8.9367(9) Å	β = 69.361(3)°
	c = 11.3538(11) Å	γ = 87.336(3)°
Volume	791.19(13) $Å^3$	
Z	1	
Density (calculated)	1.185 Mg/m^3	
Absorption coefficient	0.077 mm^{-1}	
F(000)	302	
Crystal size	0.200 x 0.150 x 0.150 mm^3	
Theta range for data collection	3.369 to 26.998°	
Index ranges	-10<=h<=10, -11<=k<=11, -14<=l<=14	
Reflections collected	30554	
Independent reflections	3441 [R(int) = 0.0627]	
Completeness to theta = 25.242°	99.5 %	
Absorption correction	Semi-empirical from equivalents	
Max. and min. transmission	0.7467 and 0.6347	
Refinement method	Full-matrix least-squares on F^2	
Data / restraints / parameters	3441 / 1 / 191	
Goodness-of-fit on F^2	1.032	
Final R indices [I>2sigma(I)]	R1 = 0.0471, wR2 = 0.1075	
R indices (all data)	R1 = 0.0875, wR2 = 0.1296	
Largest diff. peak and hole	0.138 and -0.133 $eÅ^{-3}$	

Table 2.3. Crystallographic data of **DB-C$_6$** (O-form).

Sample	**DB-C$_6$ O**	
Empirical formula	C36H40N2O4	
Formula weight	564.70	
Temperature	297(2) K	
Wavelength	1.54178 Å	
Crystal system	Triclinic	
Space group	*P*-1	
Unit cell dimensions	a = 8.3068(3) Å	α = 103.9740(10)°
	b = 12.5635(4)	β = 100.101(2)°
	c = 16.5540(5)	γ = 101.288(2)°
Volume	1598.42(9) Å^3	
Z	2	
Density (calculated)	1.173 Mg/m^3	
Absorption coefficient	0.604 mm^{-1}	
F(000)	604	
Crystal size	0.550 x 0.059 x 0.045 mm^3	
Theta range for data collection	3.997 to 65.497°	
Index ranges	-9<=h<=9, -14<=k<=14, -19<=l<=19	
Reflections collected	47551	
Independent reflections	5398 [R(int) = 0.0774]	
Completeness to theta = 65.497°	98.0 %	
Absorption correction	Semi-empirical from equivalents	
Max. and min. transmission	0.7531 and 0.4589	
Refinement method	Full-matrix least-squares on F^2	
Data / restraints / parameters	5398 / 3 / 382	
Goodness-of-fit on F^2	1.043	
Final R indices [I>2sigma(I)]	R1 = 0.0944, wR2 = 0.2563	
R indices (all data)	R1 = 0.1139, wR2 = 0.2967	
Largest diff. peak and hole	0.795 and -0.308 eÅ^{-3}	

adjacent molecular sheets is 3.7 Å, consistent with the typical π-π stacking distance. O-form crystals also form molecular sheets through multiple intermolecular C–H···N (2.65 Å) and intramolecular C–H···O (2.24 Å) hydrogen bonds (**Figure 2.11c**).

However, unlike P-form, π-π stacking is observed between the donor moieties of neighboring molecules in O-form, with a relatively larger interlayer distance of 4.15 Å (**Figure 2.11d**). Additionally, the molecular arrangement in O-form is different, with two neighboring molecules from adjacent layers stacked in an orthogonal manner. Only alternate molecules within the layer have four intermolecular and two intramolecular hydrogen bonds due to the 74° turning of alternate molecules in the same layer along the *b*-axis. The molecular sheets in the P-form crystal are arranged in slip stacks along the *a*-axis with a slipping angle of 26° (**Figure 2.11e**), while the O-form consists of cross-stacked layers along the *a*-axis with a larger slipping angle of 71° (**Figure 2.11f)**.

The alteration in angle demonstrates a smooth sliding of molecules in adjacent layers accompanied along with the transition from a parallel to an orthogonal arrangement. The heat-induced transformation from a slipped "parallel" stacking of molecules in the P-form to "orthogonal" cofacial arrangement in the O-form is unprecedented. The dihedral angle between the central benzene ring and the terminal benzoxazole rings is 3.08° in the P-form, while it is 8.27° in the O-form (**Figure 2.12**). The P-form consists of one molecule per unit cell, while the O-form has two molecules per unit cell. Additionally, volume of the O-form unit cell is 102 % larger

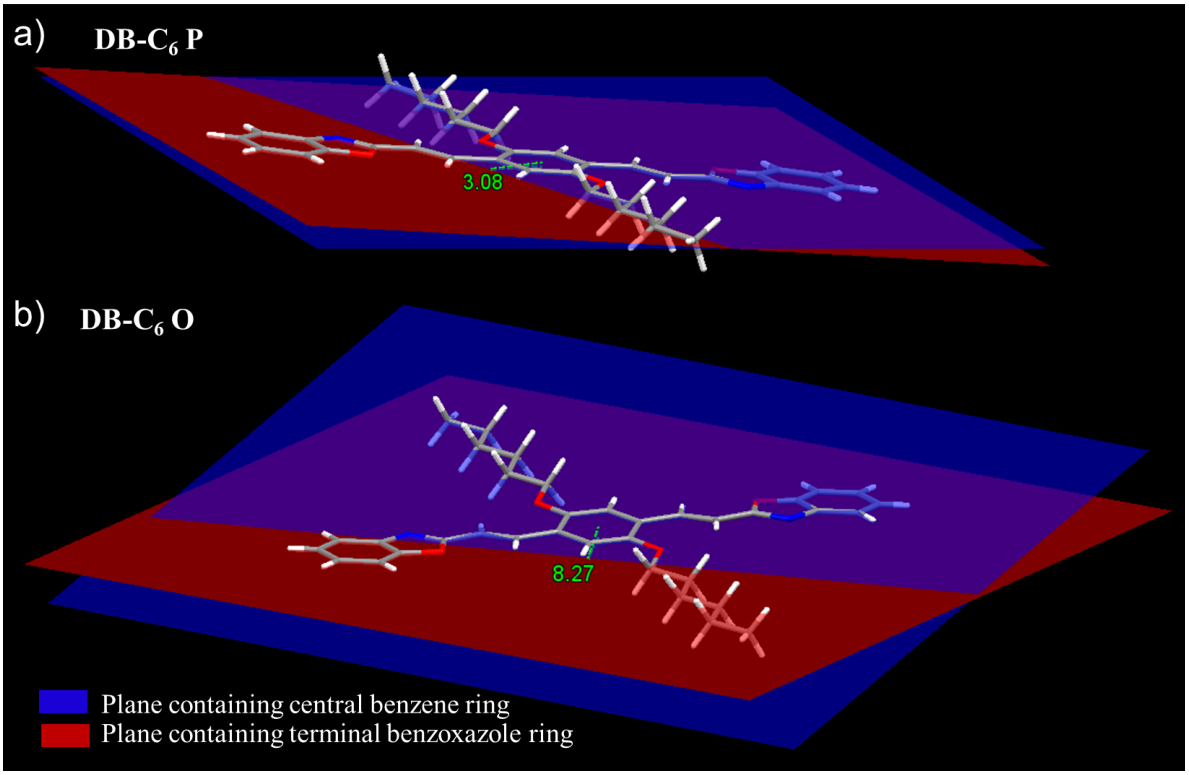

Figure 2.12. Dihedral angle between the planes containing central benzene ring and terminal benzoxazole ring in a) **DB-C$_6$** P-form and b) **DB-C$_6$** O-form.

(1598.42 Å^3) than the P-form unit cell (791.19 Å^3). These observations are in accordance with the Raman analysis. The driving force behind the P- to O-form transition could be the entropy gain that occurs during heating, which promotes loose packing in the latter and reduces H-bonding interactions and overlap of π-systems. In contrast, the driving force for the O- to P-form transition might be the enthalpy gain through compact packing in the P-form, aided by H-bonding, charge transfer, π-π, and van der Waals interactions.

The observed switching in color and luminescence can be explained by analyzing the molecular packing in the P- and O-form crystals. The donor-acceptor interaction

between two neighboring molecular sheets in the P-form facilitates intermolecular charge transfer interaction (CT-On state), leading to red-shifted absorption and emission characteristics. Since the supramolecular binding interactions are weak, heating results in molecular rearrangements (O-form), turning off the charge transfer wavelengths. The increase in absolute quantum yield from the P-form (37%) to the O-form (54%) can be attributed to changes in chromophore packing. In the P-form, parallel arrangement of molecules promotes strong donor-acceptor interactions between adjacent molecules, increasing non-radiative pathways resulting in lower fluorescence quantum efficiency. In contrast, the O-form's orthogonal cross-stacking configuration weakens hydrogen bonding, π-π, and donor-acceptor interactions, reducing non-radiative pathways yielding improved quantum efficiency.

Two additional derivatives of the chromophore consisting of dodecyl (**DB-C_{12}**) and octadecyl (**DB-C_{18}**) chains were synthesized to investigate the influence of the alkyl chain on thermochromic properties. An attempt was made to prepare single crystals of these molecules using the method employed for **DB-C_6**, but it was unsuccessful due to the presence of longer alkyl chains, which give the molecules an amorphous nature. However, both derivatives showed a similar trend in heat-induced luminescence switching as that of **DB-C_6** (**Figure 2.13a** and **2.13b**). The P-form of **DB-C_{12}** has an emission maximum at 636 nm, which was blue-shifted about 95 nm with an emission maximum centered at 541 nm upon heating at 80 °C, and subsequently cooling to room temperature (O-form). As a result, the emission color

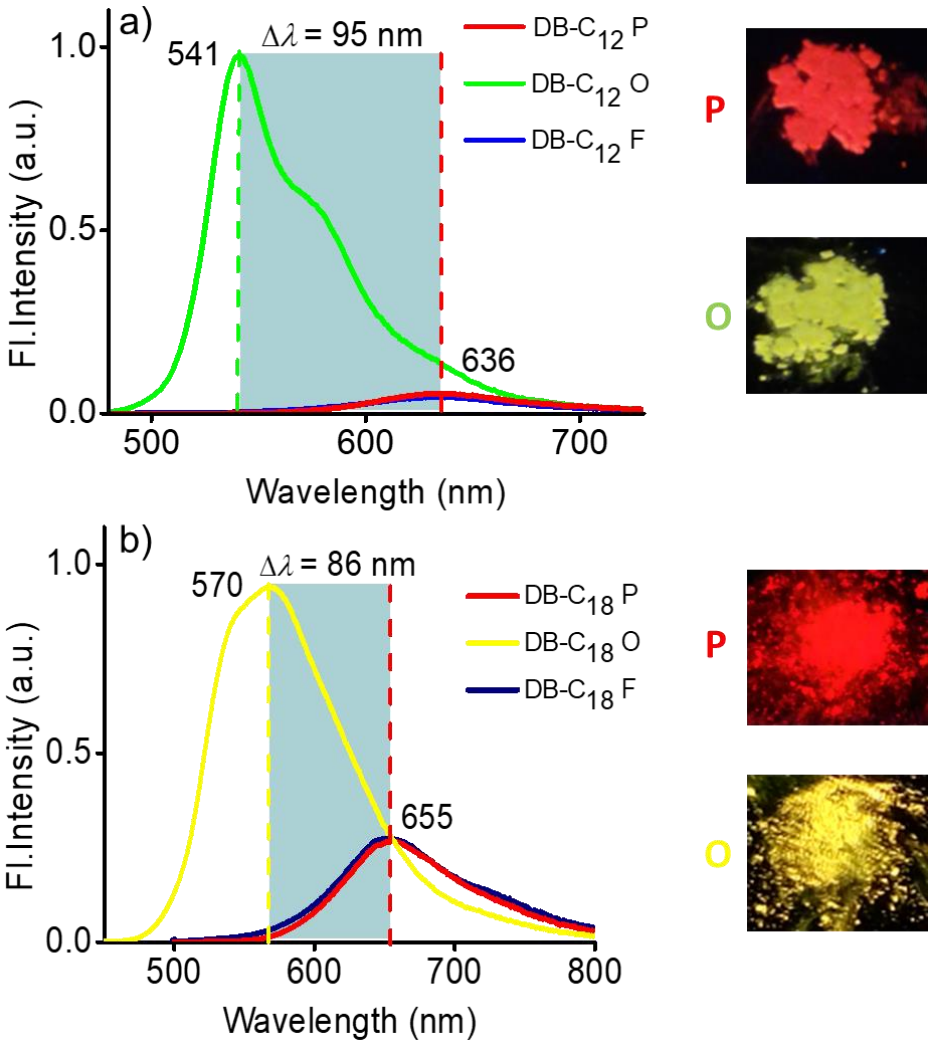

Figure 2.13. Photoluminescence spectra of a) **DB-C$_{12}$** and b) **DB-C$_{18}$** in pristine powder form (P), heated at transition temperature and cooled to room temperature (O), and after solvent fuming (see supporting information) of the O-form (F). Photographs of the P- and O-forms under UV light (365 nm) are shown on the right side of the corresponding graphs.

changed from red to greenish-yellow. The P-form has an absolute quantum yield of 45%, while the O-form has a quantum yield of 56%. For **DB-C$_{18}$**, the P-form has an emission maximum at 655 nm with red emission, which upon heating at approximately 95 °C, followed by cooling to room temperature, exhibited about 85

nm blue-shifted emission with a maximum centered at 570 nm and bright yellow emission (O-form). The P-form has an absolute quantum yield of 39%, while the O-form has a higher quantum yield of 59%.

The lower energy shoulder observed at ~580 nm for **DB-C$_{12}$** suggests the presence of distinct vibrational levels in the excited state of the molecule. Emission spectra are associated with radiative transitions between electronic energy levels, typically from an excited state to a lower energy state, such as the ground state. Vibrational features in the emission spectrum arise from transitions between vibrational energy levels associated with the molecular structure of the material. As molecules absorb or emit energy, they can undergo vibrational transitions in addition to electronic transitions, which can result in peaks or bands in the emission spectrum that correspond to the energy difference between different vibrational levels. In fact, the O-forms of all three derivative exhibit the lower energy shoulders in their emission spectra, with the slight

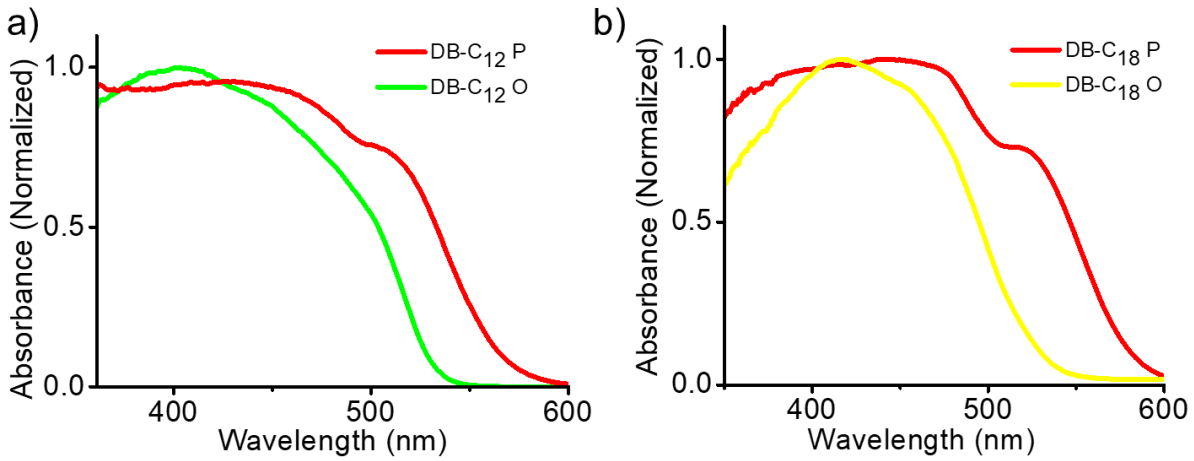

Figure 2.14. Solid-state absorption spectra of a) **DB-C$_{12}$** and b) **DB-C$_{18}$**.

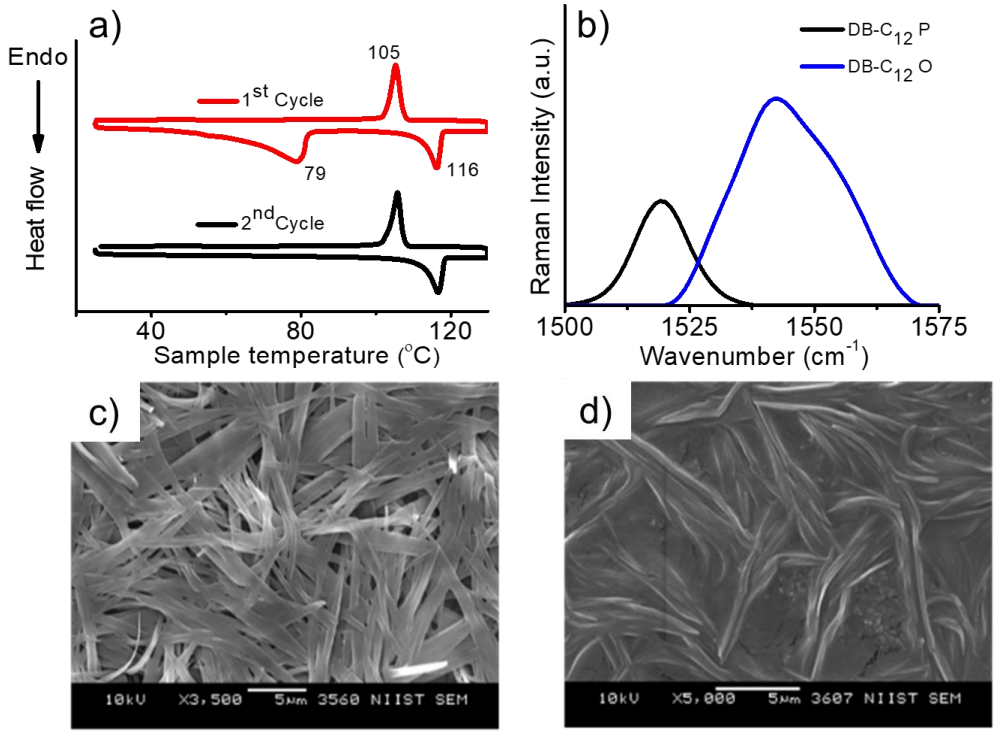

Figure 2.15. a) DSC thermogram and b) Raman spectra of **DB-C$_{12}$** at different conditions; P (parallel) is the pristine sample and O (orthogonal) is the sample heated at transition temperature (80 °C) followed by air cooling to room temperature. Morphology of **DB-C$_{12}$** in c) P- and d) O-form imaged using FE-SEM (scale bar represents 5 μm).

visibility in **DB-C$_6$**, a well-defined feature in **DB-C$_{12}$**, and nearly invisible in **DB-C$_{18}$**. These variations could be associated with subtle differences in their self-assembled structures due to the variation in alkyl side chain length, which in turn affects the vibrational energy levels and corresponding emission spectra.

The spectral shifts associated with heat-induced transition are reflected in their solid-state absorption spectra also (**Figure 2.14a** and **2.14b**). Like **DB-C$_6$**, P-form of both **DB-C$_{12}$** and **DB-C$_{18}$** derivatives displayed broad absorption in the visible region. Upon heating the P-form at their respective transition temperatures and cooled down

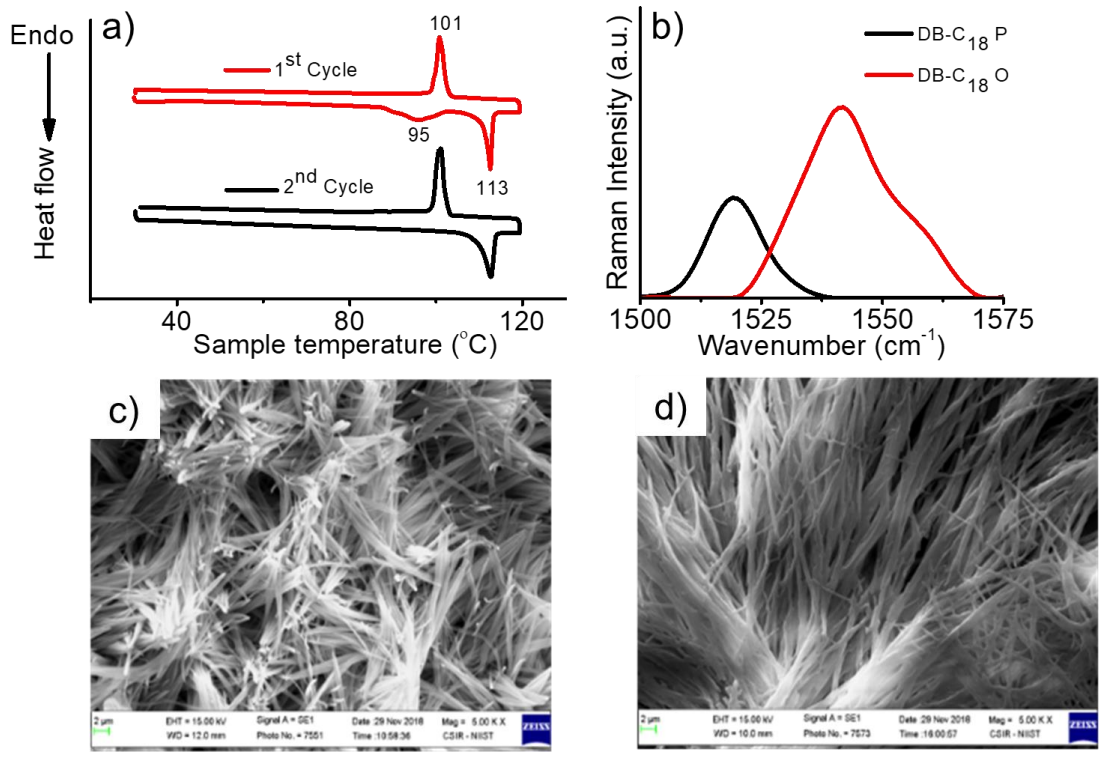

Figure 2.16. a) DSC thermogram and b) Raman spectra of **DB-C$_{18}$** at different conditions; P (parallel) is the pristine sample and O (orthogonal) is the sample heated at transition temperature (95 °C) followed by air cooling to room temperature. Morphology of **DB-C$_{18}$** in c) P- and d) O-form imaged using FE-SEM (scale bar represents 2 μm).

to room temperature generated O-form, which exhibited significantly blue-shifted absorption onset. Similarly, phase transition associated with the luminescence switching in C_{12} and C_{18} were demonstrated using DSC analysis (**Figure 2.15a and 2.16a**). As shown in DSC diagrams, a broad endothermic peak at ~79 °C (for C_{12}) and ~95 °C (for C_{18}) in the first heating cycle corresponds to the phase transition from P-form to O-form. However, such a peak was not there in the second heating cycle, thus confirming the irreversibility of O-form to P-form transition by cooling. The sharp endothermic peaks at 116 °C (for **DB-C$_{12}$**) and 113 °C (for **DB-C$_{18}$**) were recognized

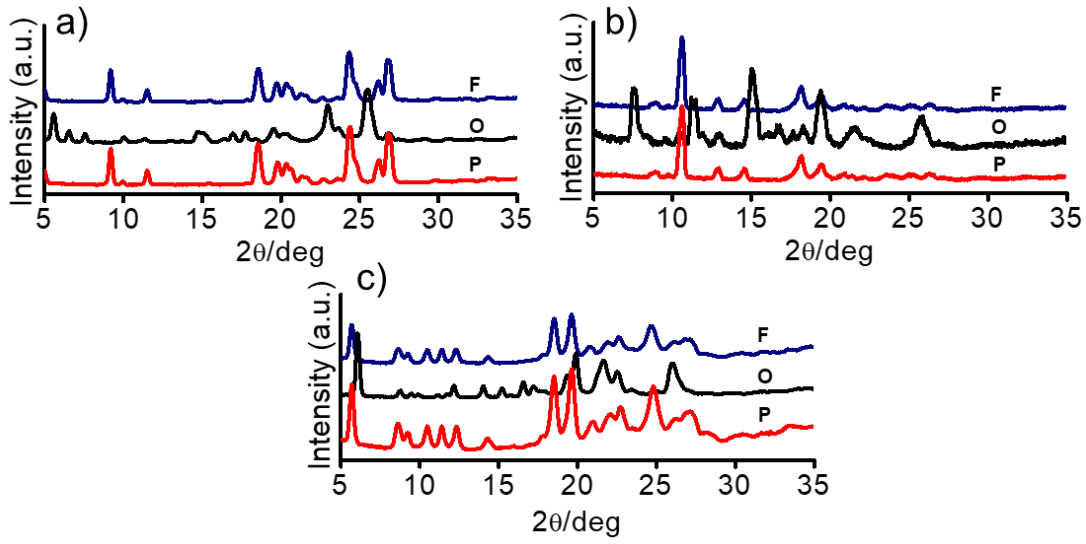

Figure 2.17. XRD patterns of a) **DB-C$_6$** b) **DB-C$_{12}$** and c) **DB-C$_{18}$** as prepared (red line, P), heated at transition temperature and cooled to room temperature (black line, O), and solvent fumed/treated O-form (blue line, F).

as the melting point of the sample, whereas exothermic peaks at ~105 °C (for C_{12}) and ~101 °C (for C_{18}) corresponds to the regeneration of O-form. Further we have recorded the Raman spectra of P-form and O-form of **DB-C$_{12}$** and **DB-C$_{18}$** using the same laser excitation source of 785 nm used for **DB-C$_6$**. As we noticed for **DB-C$_6$** specifically, we observed a vibrational band at ~1520 cm^{-1} in the P-form of C_{12} and C_{18} derivatives showing a remarkable upward frequency shift to ~1545 cm^{-1} ($\Delta\nu$ = 25 cm^{-1}) on changing to O-form (**Figure 2.15b and 2.16b**). Moreover, changes in the intensity pattern are also observed. These spectral changes suggest structural π-conjugation differences and distinct intermolecular interactions operating in both P-form and O-form. The SEM analysis of C_{12} (**Figure 2.15c** and **2.15d**) and C_{18} (**Figure 2.16c** and **2.16d**) derivatives revealed that the transformation from P-form to O-form was accompanied not only with fluorescence switching, but also with changes in the

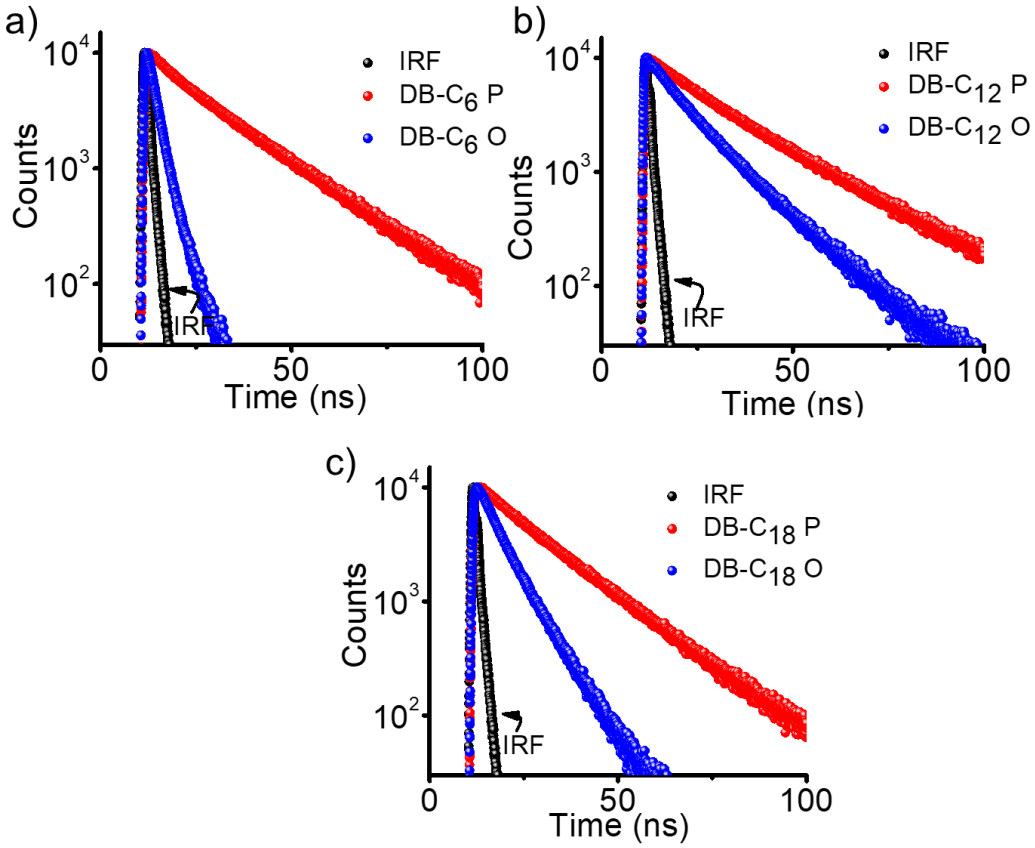

Figure 2.18. Time-resolved fluorescence decay profile of the P- and O-forms of a) **DB-C$_6$**, b) **DB-C$_{12}$**, and c) **DB-C$_{18}$** derivatives.

supramolecular morphology similar to **DB-C$_6$**. **Figure 2.17** displayed the XRD patterns of P-form (as prepared, red line), O-form (heated at transition temperature and cooled to room temperature, black line), and solvent fumed/treated O-form (F, blue line) and fully demonstrated the cycling property of the three derivatives.

Further, time-resolved fluorescence lifetime measurement was conducted to understand the change in excited state lifetime accompanied with the fluorescence changes (**Figure 2.18**). The fluorescence lifetime of the P-form was 12.58 ns and that of O-form was 2.46 ns for **DB-C$_6$**. In the case of **DB-C$_{12}$**, P- and O- forms have an

average fluorescence lifetime of 10.77 ns and 6.03 ns respectively. The P- and O-forms of **DB-C$_{18}$** exhibited a lifetime of 13.94 ns and 5.12 ns correspondingly. All the derivatives show higher lifetime for P-form compared to O-form. In the former, a pronounced π-orbital overlap is possible between the neighboring molecules, leading to significant excited state electronic delocalization and a longer fluorescence lifetime. In contrast, the orbital overlap between the neighboring molecules is weakened in the O-form, causing the disappearance of excited-state electronic delocalization between adjacent molecules, and resulting in a shorter fluorescence lifetime.

Solid-state heat-induced parameters of divinylbenzene-benzoxazole based derivatives are described in **Table 2.4**. Notably, a clear trend of red-shift in the emission maximum of both the P-form and O-form is observed with increasing alkyl chain length. This can be attributed to the van der Waals interaction between the alkyl chains of neighboring molecules, which generally increases with an increase in chain length. This increase in interaction improves planarity and effective conjugation length, resulting in the red-shifted emission in molecules with longer alkyl chains than

Table 2.4. Solid-state parameters of **DB-C$_n$** fluorophores.

Compounds	P-form (nm)	O-form (nm)	Shift (nm)	Transition temperature (°C)	Melting temperature (°C)	Decomposition temperature (°C)	Recovery time (min.)
DB-C_6	616	528	-88	65	156	318	-
DB-C_{12}	636	541	-95	79	116	328	2
DB-C_{18}	655	570	-85	95	113	338	10

those with shorter alkyl chains. Unlike **DB-C_6**, both **DB-C_{12}** and **DB-C_{18}** exhibited easily reversible luminescence switching upon solvent fuming (such as dichloromethane). While the alkyl chains in **DB-C_6** did not facilitate the revival of the P-form from the O-form upon solvent fuming, resulting in a blue-shift in the emission maximum as the material entered a molecularly dissolved state, the C_{12} and C_{18} chains facilitated the recovery of the P-form from the O-form. The O-form of **DB-C_{12}** was able to revert back to the P-form within 1-2 minutes, while it took **DB-C_{18}** approximately 10 minutes to begin recovery and almost 24 hours to complete it. The alkyl chains can be seen as solvent molecules attached to the chromophore backbone, helping to solubilize the chromophores and facilitating self-assembly through van der Waals interactions. While the C_6 chain assists in solubilization, it does not contribute to self-assembly due to poor van der Waals interactions resulting from its low chain length. However, both the C_{12} and C_{18} chains assist in both processes, with the C_{18} chain exhibiting the greatest van der Waals interaction among the three due to its longer chain length and thus slower dissolution process and slower recovery to the O-form.

2.3.5. Smart thermochromic luminescence coating

The two distinct molecular packing states, which are luminescent, stable, and reversible, make these compounds useful for smart coating applications. To demonstrate their potential, we have selected **DB-C_{12}** and incorporated it into the polymethyl methacrylate (PMMA) matrix. A homogeneous and stable thin film was

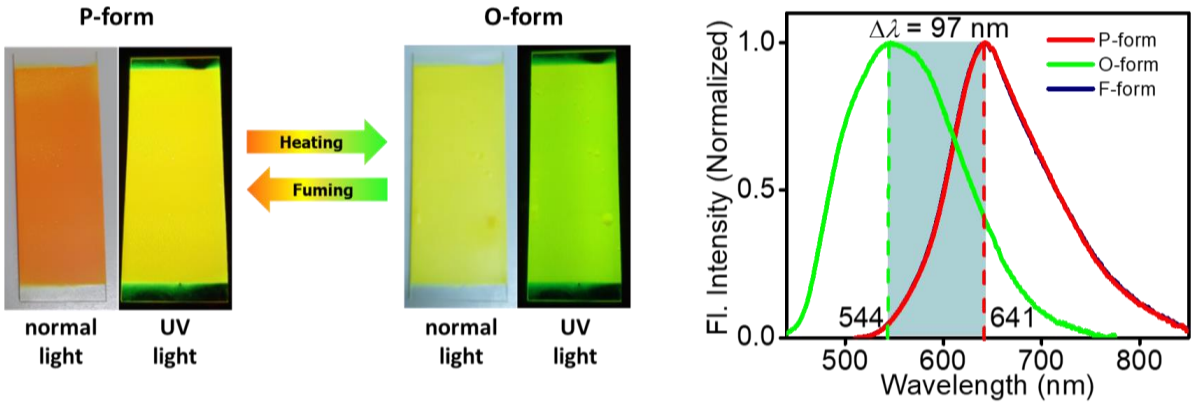

Figure 2.19. Thermoresponsive luminescence switching of **DB-C$_{12}$**/PMMA film on a glass substrate.

fabricated on a glass substrate (7.5 cm x 2.5 cm) by spray-coating a solution of **DB-C$_{12}$** and PMMA (1:9 ratio, 5% w/v) in chloroform. When heated (~80 °C), the film undergoes a color change from orange to yellow, along with a shift in luminescence from yellow to greenish-yellow (**Figure 2.19**). Subsequent exposure to solvent fumes (dichloromethane) allows the material to revert to its original form. The reversible and reproducible thermochromic behavior of the fabricated film demonstrates its potential for real-world applications.

2.4. Conclusions

In summary, the solid-state thermochromic luminescence properties of three divinylbenzene-benzoxazole derivatives with varying alkyl chain lengths were investigated. It was found that the transition between charge transfer On/Off states of the hydrogen-bonded molecular assemblies was responsible for the heat-induced luminescence switching observed in these materials. The alkyl chain lengths

significantly impacted the thermoresponsive properties of the molecules, including the reversibility and range of chromism exhibited. These findings provide insight into the structure-property relationship of luminescent thermochromic materials and have potential for the development of smart sensors for practical applications.

2.5. Experimental section

2.5.1. Materials and methods

Materials: Reagents and solvents for the synthesis were purchased either from local suppliers or from Sigma-Aldrich, Alfa Aesar or TCI and used as received. Air and water-sensitive synthetic procedures were conducted in an inert atmosphere using standard Schlenk techniques.

Measurements: Melting points were measured using a Mel-Temp-II melting point apparatus. FT-IR spectra were recorded on a Shimadzu IRPrestige-21 Fourier transform infrared spectrophotometer. ^{1}H and ^{13}C-NMR spectra of the compounds were recorded on a 500 MHz Bruker Avance II spectrometer. All the chemical shifts were referenced to $(CH_3)_4Si$ (TMS; δ = 0 ppm) for ^{1}H or $CDCl_3$ (δ = 77 ppm) for ^{13}C. High-resolution mass spectral (HRMS) analysis was carried out using a JEOL JM AX 505 HA instrument.

Differential scanning calorimetry (DSC): Differential scanning calorimetry was conducted on a Perkin Elmer Pyris 6 DSC instrument using sealed aluminum pans. **DB-C_6**, **DB-C_{12}**, and **DB-C_{18}** were heated from room temperature to 160 °C, 130 °C, and 120 °C, respectively, at a heating/cooling rate of 5 °C min^{-1} under nitrogen flow.

Absorption and fluorescence spectroscopy: Absorption spectra were measured using a Shimadzu UV-visible 3101 PC NIR spectrophotometer using a quartz cell with a 1 cm path length. Fluorescence spectra were recorded using a SPEX-Fluorolog F112X spectrofluorometer equipped with a 450 W xenon arc lamp. The spectra were corrected using the program installed by the manufacturer.

Fluorescence quantum yield and lifetime: The fluorescence quantum yields in the solution state were determined relative to a standard compound, quinine sulphate (0.1 M H_2SO_4; ϕ_F = 0.546), using optically matching solutions. The fluorescence quantum yield of the powder samples was calculated using a calibrated integrating sphere in the SPEX Fluorolog spectrofluorometer. The samples were excited at 410 nm using the Xe-arc lamp as the excitation source. The absolute quantum yield was determined based on the de Mello method.[53] Fluorescence lifetimes were determined using a picosecond single-photon counting system (Horiba, DeltaFlex) employing the 375 nm LED excitation source and picosecond photon detection modules (PPD-850) as a detector.

Field emission scanning electron microscopy (FE-SEM): For the FE-SEM measurements, the samples were drop cast and air-dried on a flat surface of a SEM brass grid and subjected to a thin gold coating using a JEOL JFC-1200 fine coater. The samples were analyzed with a JEOL JSM-5600 LV scanning electron microscope.

X-ray diffraction measurements: Wide-angle X-ray diffraction patterns of the samples were recorded using an XEUSS WAXS system by Xenocs, operated at 50 kV

and 0.60 mA. The XEUSS WAXS system is equipped with a Linkam THMS 600 hot stage and a Linkam TMS 93 programmable temperature controller to perform the temperature-dependent XRD measurements. The single-crystal diffraction data were collected on a Bruker AXS Smart Apex CCD diffractometer at 297 K. The data was deduced using SAINTPLUS, and an empirical absorption correction was applied using the SADABS program. The crystal structure was solved by direct methods and refined using SHELXS97 present in SHELXTL V6.14. Full-matrix least-squares structure refinement against F^2 was carried out using the WINGX package of programs.

Raman spectrometer: The Raman spectra were recorded in the range of 400-2300 cm^{-1} using a Mira DS Handheld Raman spectrometer (Metrohm India Ltd- Mira Cal DS software) having a 785 nm excitation wavelength laser source with FWHM spectral resolution 8-10 cm^{-1} with a numerical aperture of 0.5. Typical Raman measurement parameters with laser power of 40 mW and integration time of 10 s were used.

Thermal gravimetric analysis (TGA): Thermal gravimetric analysis of the samples was carried out using a Shimadzu DTG-60 TG analyzer. The samples were heated from room temperature to 600 °C at a heating rate of 10 °C/ min in nitrogen atmosphere.

Solvent fuming process: Solvent fuming process of O-form was carried out by exposing the O-form of the compound to dichloromethane vapors for approximately 2

minutes. To achieve this, we placed the O-form sample inside a closed Petri dish containing saturated vapors of the solvent.

2.5.2. Synthesis and characterization

Synthesis of 1,4-Bis(hexyloxy)benzene (2a): A suspension of 1,4-hydroquinone, **1** (5 g, 45.41 mmol, 1equiv.), 1-bromohexane (19.12 mL, 136.23 mmol, 3 equiv.) and NaOH (5.45 g, 136.23 mmol, 3 equiv.) in 40 mL DMF was heated at 100 °C for 24 h. After cooling, the reaction mixture was poured into water, and the precipitate formed was collected by filtration. Recrystallizing the crude product from hot ethanol provided **2a** as a white solid. Yield: 80%; ^{1}H NMR (500 MHz, $CDCl_3$): δ [ppm] = 6.82 (s, 4H), 3.90 (t, J = 6.5 Hz, 4H), 1.78 – 1.72 (m, 4H), 1.46 – 1.43 (m, 4H), 1.34 – 1.31 (m, 8H), 0.90 (t, J = 6.5 Hz, 6H).

Synthesis of 2,5-Bis(bromomethyl)-1,4-bis(hexyloxy)benzene (3a): To a suspension of **2a** (5 g, 17.96 mmol, 1 equiv.) and paraformaldehyde (1.11 g, 36.82 mmol, 2.05 equiv.) in glacial acetic acid (40 mL), 33% HBr in acetic acid (5.0 mL) was added and heated at 70 °C for 8 h. After cooling to room temperature, the reaction mixture was poured into cold water. The precipitated product was filtered and washed several times with water and dried in a vacuum oven to give **3a** as a white solid. Yield: 84%; ^{1}H NMR (500 MHz, $CDCl_3$): δ [ppm] = 6.85 (s, 2H), 4.53 (s, 4H), 3.98 (t, J = 6.5 Hz, 4H), 1.84 – 1.78 (m, 4H), 1.51 – 1.48 (m, 4H), 1.36 – 1.34 (m, 8H), 0.91 (t, J = 7 Hz, 6H).

Synthesis of 2,5-Bis(hexyloxy)benzene-1,4-dialdehyde (4a): 2,5-Bis(bromomethyl)-1,4-bis(hexyloxy)benzene, **3a** (2.5 g, 5.38 mmol, 1 equiv.) and sodium bicarbonate (3.9 g, 46.5 mmol, 15 equiv.) were stirred in 50 mL DMSO at 115 °C for 0.5 h. After cooling to room temperature, the reaction mixture was poured into 150 mL of water. The yellow precipitate was filtered and dried. The mixture was purified by column chromatography (silica gel, 50% CH_2Cl_2 – hexane) yielding a yellow-colored powder as the pure product, **4a**. Yield – 72%; ^{1}H NMR (500 MHz, $CDCl_3$): δ [ppm] = 10.52 (s, 2H), 7.43 (s, 2H), 4.09 (t, J = 6.5 Hz, 4H), 1.85 – 1.82 (m, 4H), 1.49 – 1.46 (m, 4H), 1.35 – 1.34 (m, 8H), 0.92 (t, J = 6.5 Hz, 6H).

Synthesis of 2,2'-((1E,1'E)-(2,5-bis(hexyloxy)-1,4-phenylene)bis(ethene-2,1-diyl)) bis(benzo[d]oxazole) (6a, DB-C_6): Potassium hydroxide (0.202 g, 3.58 mmol, 12 equiv.) was added to DMF (10 mL) and allowed to stir under open air for 15 min at room temperature. 2-methylbenzoxazole, **5** (0.11 mL, 0.89 mmol, 3 equiv.) was then added, followed by the addition of 2,5-dihexylterephthalaldehyde (0.100 g, 0.298 mmol, 1 equiv.). The solution was then allowed to stir for 3h at room temperature, after which the reaction was quenched with 1 M HCl solution. The organic layer was extracted using CH_2Cl_2 and dried over anhydrous Na_2SO_4 and concentrated in vacuo. The crude compound was purified by column chromatography (silica gel, 70% CH_2Cl_2 – hexane) yielding an orange coloured powder as the pure product **6a**. Yield – 54%; ^{1}H NMR (500 MHz, $CDCl_3$): δ [ppm] = 8.06 (d, J = 16.5 Hz, 2H), 7.74 – 7.72 (m, 2H), 7.55 – 7.54 (m, 2H), 7.36 – 7.34 (m, 4H), 7.26 (d, J = 16 Hz, 2H), 7.16 (s,

2H), 4.10 (t, J = 6.5 Hz, 4H), 1.97 – 1.91 (m, 4H), 1.55 – 1.40 (m, 12H), 0.95 (t, J = 7 Hz, 6H). ^{13}C NMR (125 MHz, $CDCl_3$): δ [ppm] = 14.05, 22.63, 25.79, 29.23, 29.47, 31.57, 69.43, 110.35, 111.93, 115.42, 119.86, 124.50, 125.21, 126.46, 134.34, 142.34, 150.51, 151.90, 163.29; FT-IR (KBr): ν_{max} [cm^{-1}] = 2932, 2866, 1637, 1534, 1488, 1453, 1432, 1258, 1216, 1016, 971, 850, 741. ESI-MS m/z = 565.30 (calc. = 564.30).

The synthesis and characterization of 2,5-bis(dodecyloxy)-terephthalaldehyde (**4b**) and **DB-C$_{12}$** derivative were reported earlier.[54-57]

Synthesis of 1,4-Bis(octadecyloxy)benzene (2c): A suspension of 1,4-hydroquinone, **1** (5 g, 45.41 mmol, 1equiv.), 1-bromooctadecane (34 mL, 99.90 mmol, 2.2 equiv.) and NaOH (5.45 g, 136.23 mmol, 3 equiv.) in 40 mL DMF was heated at 100 °C for 24 h. After cooling, the reaction mixture was poured into water, and the precipitate formed was collected by filtration. Recrystallization of the crude product from hot ethanol provided **2c** as a white solid. Yield: 94%; ^{1}H NMR (500 MHz, $CDCl_3$): δ [ppm] = 6.82 (s, 4H), 3.89 (t, J = 6.5 Hz, 4H), 1.83 – 1.78 (m, 4H), 1.52 – 1.47 (m, 40H), 1.44 – 1.28 (m, 20H), 0.88 (t, J = 7 Hz, 6H).

Synthesis of 2,5-Bis(bromomethyl)-1,4-bis(octadecyloxy)benzene (3c): To a suspension of **2c** (5 g, 8.13 mmol, 1 equiv.) and paraformaldehyde (0.73 g, 24.39 mmol, 3 equiv.) in glacial acetic acid (50 mL), 33% HBr in acetic acid (5.0 mL) was added and heated at 70 °C for 8 h. After cooling to room temperature, the reaction mixture was poured into cold water. The precipitated product was filtered and washed

several times with water and dried in a vacuum oven to give **3c** as a white solid. Yield: 90%; ^{1}H NMR (500 MHz, $CDCl_3$): δ [ppm] = 6.85 (s, 2H), 4.52 (s, 4H), 3.98 (t, J = 6.5 Hz, 4H), 1.83 – 1.78 (m, 4H), 1.52 – 1.47 (m, 40H), 1.44 – 1.28 (m, 20H), 0.88 (t, J = 7 Hz, 6H).

Synthesis of 2,5-Bis(octadecyloxy)benzene-1,4-dialdehyde (4c): 2,5-Bis(bromomethyl)-1,4-bis(octadecyloxy)benzene, **3c** (5 g, 6.24 mmol, 1 equiv.) and sodium bicarbonate (7.86 g, 93.6 mmol, 15 equiv.) were stirred in 100 mL DMSO at 115 °C for 0.5h. After cooling to room temperature, the reaction mixture was poured into 300 mL of water. The yellow precipitate was filtered and dried. The mixture was purified by column chromatography (silica gel, 30% CH_2Cl_2 – hexane) yielding a yellow-colored powder as the pure product, **4c**. Yield – 78%; ^{1}H NMR (500 MHz, $CDCl_3$): δ [ppm] = 10.52 (s, 2H), 7.43 (s, 2H), 4.08 (t, J = 6.5 Hz, 4H), 1.86 – 1.80 (m, 4H), 1.50 – 1.47 (m, 40H), 1.45 – 1.28 (m, 20H), 0.88 (t, J = 7 Hz, 6H).

Synthesis of 2,2'-((1E,1'E)-(2,5-bis(octadecyloxy)-1,4-phenylene)bis(ethene-2,1-diyl)) bis(benzo[d]oxazole) (6c, DB-C_{18}): Potassium hydroxide (0.201 g, 3.58 mmol, 12 equiv.) was added to DMF (10 mL) and allowed to stir under open air for 15 min at room temperature. 2-methylbenzoxazole, **5** (0.11 mL, 0.89 mmol, 3 equiv.) was then added, followed by the addition of 2,5-dioctadecylterephthalaldehyde, **4c** (0.200 g, 0.298 mmol, 1 equiv.). The solution was then allowed to stir for 3 h at 55 °C, after which the reaction was quenched with 1 M HCl solution. The organic layer was

extracted using CH_2Cl_2 and dried over anhydrous Na_2SO_4 and concentrated in vacuo. The crude compound was purified by column chromatography (silica gel, 70% CH_2Cl_2 – hexane) yielding red colored powder as the pure product, **6c**. Yield – 57%; ^{1}H NMR (500 MHz, $CDCl_3$): δ [ppm] = 8.05 (d, J = 16.5 Hz, 2H), 7.74 – 7.72 (m, 2H), 7.55 – 7.54 (m, 2H), 7.35 – 7.33 (m, 4H), 7.27 (d, J = 16 Hz, 2H), 7.15 (s, 2H), 4.1 (t, J = 6.5 Hz, 4H), 1.96 – 1.91 (m, 4H), 1.59 – 1.52 (m, 40H), 1.44 – 1.28 (m, 20H), 0.88 (t, J = 7 Hz, 6H). ^{13}C NMR (125 MHz, $CDCl_3$): δ [ppm] = 14.14, 22.71, 26.16, 29.27, 29.38, 29.43, 29.41, 29.65, 29.68, 29.72, 31.94, 69.43, 110.35, 112.00, 115.46, 119.69, 119.86, 124.50, 125.20, 126.45, 134.37, 142.35, 150.51, 151.90, 163.29; FT-IR (KBr): ν_{max} [cm^{-1}] = 2920, 2848, 1634, 1537, 1498, 1460, 1432, 1257, 1215, 1076, 971, 853, 734. ESI-MS m/z = 901.67 (calc. = 900.67).

2.6. References

1. Y. Jiang, Y.-Y. Liu, X. Liu, H. Lin, K. Gao, W.-Y. Lai, W. Huang, *Chem. Soc. Rev.* **2020**, *49*, 5885.
2. J. Gierschner, S. Varghese, S. Y. Park, *Adv. Opt. Mater.* **2016**, *4*, 348.
3. M. K. Bera, P. Pal, S. Malik, *J. Mater. Chem. C* **2020**, *8*, 788.
4. J. Gierschner, J. Shi, B. Milián-Medina, D. Roca-Sanjuán, S. Varghese, S. Y. Park, *Adv. Opt. Mater.* **2021**, *9*, 2002251.
5. S. Ghosh, S. Shankar, D. S. Philips, A. Ajayaghosh, *Mater. Today Chem.* **2020**, *16*, 100242.
6. C. Liu, J.-C. Yang, J. W. Y. Lam, H.-T. Feng, B. Z. Tang, *Chem. Sci.* **2022**, *13*, 611.

7. J. Zhang, A. Li, H. Zou, J. Peng, J. Guo, W. Wu, H. Zhang, J. Zhang, X. Gu, W. Xu, S. Xu, S. H. Liu, A. Qin, J. W. Y. Lam, B. Z. Tang, *Mater. Horiz.* **2020**, *7*, 135.
8. J. Song, H. Lee, E. G. Jeong, K. C. Choi, S. Yoo, *Adv. Mater.* **2020**, 32, 1907539.
9. S. Mattiello, F. Corsini, S. Mecca, M. Sassi, R. Ruffo, G. Mattioli, Y. Hattori, T. Kusamoto, G. Griffini, L. Beverina, *Mater. Adv.* **2021**, *2*, 7369.
10. S. Wu, B. Zhou, D. Yan, *Adv. Opt. Mater.* **2021**, *9*, 2001768.
11. K. Huang, L. Song, K. Liu, A. Lv, M. Singh, K. Shen, J. Shen, J. Wang, H. Wang, H. Shi, H. Ma, M. Gu, G. Sun, W. Yao, Z. An, W. Huang, *npj Flex. Electron.* **2021**, *5*, 22.
12. F. Nie, B. Zhou, K.-Z. Wang, D. Yan, *Chem. Eng. J.* **2022**, *430*, 133084.
13. B. Zhou, Z. Qi, D. Yan, *Angew. Chem. Int. Ed.* **2022**, *61*, e202208735.
14. R. Gao, M. S. Kodaimati, D. Yan, *Chem. Soc. Rev.* **2021**, *50*, 5564.
15. J. Ochi, K. Tanaka, Y. Chujo, *Angew. Chem. Int. Ed.* **2020**, *59*, 9841.
16. A. M. Osterholm, L. Nhon, D. E. Shen, A. M. Dejneka, A. L. Tomlinson, J. R. Reynolds, *Mater. Horiz.* **2022**, *9*, 252.
17. Y. Wang, H. Shang, B. Li, S. Jiang, *J. Mater. Chem. C* **2022**, *10*, 734.
18. C.-H. Wang, M. Horie, *Mater. Today Chem.* **2022**, *24*, 100852.
19. J. Ochi, K. Tanaka, Y. Chujo, *Angew. Chem. Int. Ed.* **2023**, *62*, e202214397.
20. Q. Qi, C. Li, X. Liu, S. Jiang, Z. Xu, R. Lee, M. Zhu, B. Xu, W. Tian, *J. Am. Chem. Soc.* **2017**, *139*, 16036.
21. M. Echeverri, C. Ruiz, S. Gámez-Valenzuela, M. Alonso-Navarro, E. Gutierrez-Puebla, J. L. Serrano, M. C. Ruiz Delgado, B. Gómez-Lor, *ACS Appl. Mater. Inter.* **2020**, *12*, 10929.
22. Y. Chen, X. hang, M. Wang, J. Peng, Y. Zhou, X. Huang, W. Gao, M. Liu, H. Wu, *J. Mater. Chem. C* **2019**, *7*, 12580.

23. Y. Sagara, Y. C. Simon, N. Tamaoki, C. Weder, *Chem. Commun.* **2016**, *52*, 5694.
24. M. Martínez-Abadía, S. Varghese, P. Romero, J. Gierschner, R. Giménez, M. B. Ros, *Adv. Opt. Mater.* **2017**, *5*, 1600860.
25. H. Liu, W. Song, X. Chen, J. Mei, Z. Zhang, J. Su, *Mater. Chem. Front.* **2021**, *5*, 2294.
26. J.-F. Chen, X. Yin, B. Wang, K. Zhang, G. Meng, S. Zhang, Y. Shi, N. Wang, S. Wang, P. Chen, *Angew. Chem. Int. Ed.* **2020**, *59*, 11267.
27. C. H. Shin, K.-I. Hong, J. H. Lee, W.-D. Jang, *Mater. Today Chem.* **2022**, *24*, 100884.
28. P. Yao, W. Qiao, Y. Wang, H. Peng, X. Xie, Z. Li, *Chem. Eur. J.* **2022**, *28*, e202200725.
29. K. Muthamma, D. Sunil, P. Shetty, *Mater. Today Chem.* **2020**, *18*, 100361.
30. T. Yuan, Y. Xu, C. Zhu, Z. Jiang, H.-J. Sue, L. Fang, M. A. Olson, *Chem. Mater.* **2017**, *29*, 9937.
31. W. Zhang, X. Ji, B.-J. Peng, S. Che, F. Ge, W. Liu, M. Al-Hashimi, C. Wang, L. Fang, *Adv. Funct. Mater.* **2020**, *30*, 1906463.
32. Z. Wu, S. Mo, L. Tan, B. Fang, Z. Su, Y. Zhang, M. Yin, *Small* **2018**, *14*, 1802524.
33. S. Ying, M. Chen, Z. Liu, M. Zheng, H. Hang, S. Xue, W. Yang, *J. Mater. Chem. C* **2017**, *5*, 5994.
34. S. Varghese, S. Das, *J. Phys. Chem. Lett.* **2011**, *2*, 863.
35. H. Wu, Z. Chen, W. Chi, A. K. Bindra, L. Gu, C. Qian, B. Wu, B. Yue, G. Liu, G. Yang, L. Zhu, Y. Zhao, *Angew. Chem. Int. Ed.* **2019**, *58*, 11419.
36. C. Wang, Z. Li, *Mater. Chem. Front.* **2017**, *1*, 2174.
37. S.-J. Yoon, J. W. Chung, J. Gierschner, K. S. Kim, M.-G. Choi, D. Kim, S. Y. Park, *J. Am. Chem. Soc.* **2010**, *132*, 13675.

38. M. J. Aliaga-Gosalvez, M. Demitri, M. Dohr, J. C. Roldao, S. K. Park, S. Oh, S. Varghese, S. Oh, S. Y. Park, Y. Olivier, B. Milián-Medina, R. Resel, J. Gierschner, *Adv. Opt. Mater.* **2019**, *7*, 1900749.
39. Y. Liu, Q. Zeng, B. Zou, Y. Liu, B. Xu, W. Tian, *Angew. Chem. Int. Ed.* **2018**, *57*, 15670.
40. S.-J. Yoon, S. Varghese, S. K. Park, R. Wannemacher, J. Gierschner, S. Y. Park, *Adv. Opt. Mater.* **2013**, *1*, 232.
41. Y.-J. Ma, G. Xiao, X. Fang, T. Chen, D. Yan, *Angew. Chem. Int. Ed.* **2023**, *62*, e202217054.
42. D. Yan, D. G. Evans, *Mater. Horiz.* **2014**, *1*, 46.
43. S. Li, B. Lu, X. Fang, D. Yan, *Angew. Chem. Int. Ed.* **2020**, *59*, 22623.
44. T. Mutai, H. Satou, K. Araki, *Nat. Mater.* **2005**, *4*, 685.
45. R. Rao M, C.-W. Liao, W.-L. Su, S.-S. Sun, *J. Mater. Chem. C* **2013**, *1*, 5491.
46. Y. Sagara, A. Lavrenova, A. Crochet, Y. C. Simon, K. M. Fromm, C. Weder, *Chem. Eur. J.* **2016**, *22*, 4374.
47. A. Lavrenova, D. W. R. Balkenende, Y. Sagara, S. Schrettl, Y. C. Simon, C. Weder, *J. Am. Chem. Soc.* **2017**, *139*, 4302.
48. P. Shao, Z. Li, J. Luo, H. Wang, J. Qin, *Synth. Commun.* **2005**, *35*, 49.
49. J. S. Klimavicz, J. F. Mike, A. Bhuwalka, A. L. Tomlinson, M. Jeffries-EL, *Pure Appl. Chem.* **2012**, *84*, 991.
50. A. Milani, L. Brambilla, M. D. Zoppo, G. Zerbi, *J. Phys. Chem. B* **2007**, *111*, 1271.
51. A. Milani, M. D. Zoppo, M. Tommasini, G. Zerbi, *J. Phys. Chem. B* **2008**, *112*, 1619.
52. J. S. Mosca, A. Milani, M. Peña-Álvarez, S. Yamaguchi, V. Hernández, M. C. Ruiz Delgado, C. Castiglioni, *J. Phys. Chem. C* **2018**, *122*, 17537.
53. J. C. de Mello, H. F. Wittmannn, R. H. Friend, *Adv. Mater.* **1997**, *9*, 230.
54. S. J. George, A. Ajayaghosh, *Chem. Eur. J.* **2005**, *11*, 3217.

55. V. K. Praveen, S. J. George, R. Varghese, C. Vijayakumar, A. Ajayaghosh, *J. Am. Chem. Soc.* **2006**, *128*, 7542.
56. B. Wang, M. R. Wasielewski, *J. Am. Chem. Soc.* **1997**, *119*, 12.
57. K. C. Naeem, V. C. Nair, *Mol. Syst. Des. Eng.* **2018**, *3*, 142.

Chapter 3

Light-Induced, Catalyst- and Template-Free Photodimerization of Thienoindole-Benzoxazole-based Fluorophores and Formation of Photoconductive Cyclobutane Crystals

3.1 Abstract

Cyclobutane derivatives serve as crucial structural components in organic chemistry, owing to their high strain energy and versatile applications. In this study, we successfully synthesize a photoconductive cyclobutane derivative via daylight-induced, catalyst- and template-free [2+2] cycloaddition. This dimerization reaction of a benzoxazole-appended N-hexylthienoindole, conducted in solution at ambient temperature, offers exceptional regioselectivity and stereospecificity, along with quantitative yield and thermal irreversibility. X-ray diffraction analysis of the resulting crystals reveals the cyclobutane derivative forms a one-dimensional assembly through intermolecular hydrogen bonding. This unique molecular arrangement fosters π–π interactions between adjacent layers, generating two-dimensional layered structures. Outperforming typical fullerene-based semiconductors in terms of photoconductivity, this material emerges as a potential candidate for use in organic optoelectronic devices.

3.2. Introduction

Cyclobutane scaffolds are integral components of numerous natural products and biologically active compounds, including antibiotics and anti-cancer agents.[1-6] They often require complex and highly stereoselective syntheses, making the cyclobutane derivatives a valuable building block for these molecules. One method of synthesizing cyclobutanes is through the light-assisted [2+2] cycloaddition of carbon-carbon double bonds, which is an atom-economical and environmentally-friendly process.[7-12] However, the inherent challenges of this method, such as the various possible orientations in the transition state and photochemically induced *trans-cis* isomerization of substrates, often result in inseparable or weakly separable stereoisomers during dimerization in solution.[13-14] Furthermore, a majority of these reactions necessitate photo-redox catalysts or templates for achieving products with regio- and stereoselectivity.[15-25] Additionally, the utilization of high-energy and hazardous UV light as the excitation source significantly restricts the flexibility of molecular design.[10,26]

There are limited reports on visible-light-driven, catalyst-free, regioselective, and stereospecific formation of cyclobutane derivatives without any template for the preorganization of olefin moieties. Fedorova *et al.* reported a photocycloaddition reaction between two 2-styrylquinoxaline (**1**, **Figure 3.1**) based molecules exclusively forms *rctt* cyclobutane isomer (**2**, **Figure 3.1**) out of eleven possible isomers in an acetonitrile solution without the use of any catalyst and template.[27] This studied photo

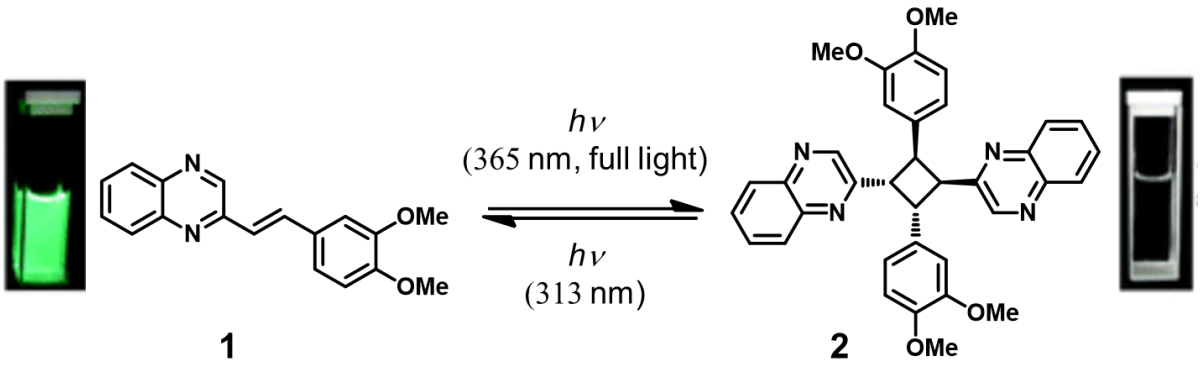

Figure 3.1. Photochemical transformations of compound **1** and **2**. (Adapted from reference 27)

cycloaddition reaction of **1** could be regarded as a photoreversible photochromic process because the observed photocycloaddition reaction is reversible. They achieved the dimer preorganization of olefins in head-to-tail manner *via* dipole interaction between the donor part of one molecule and the acceptor part of the other in solution. The observed [2+2] photocycloaddition process is dependent on the concentration of **1** in the acetonitrile solution. Photodimerization was completed after 7 minute of irradiation of solution having a concentration of **1** equal to or higher than 10^{-3} M. Whereas, a concentration of **1** lower than 10^{-5} M did not yield any cyclobutane derivatives even after 13 minutes of irradiation. The photodimerization of **1** is not observed in the solid-state as well since the essential two criteria for topochemical reaction weren't realized, i.e., the reactive double bonds of crystalline reactants must be arranged in a parallel manner to each other, and the center-to-center distance between C=C bonds must be less than 4.2 Å.

The same group later developed a visible-light-driven intermolecular [2+2] photocycloaddition reaction of azine-containing stilbenes in solution, obtaining regio-

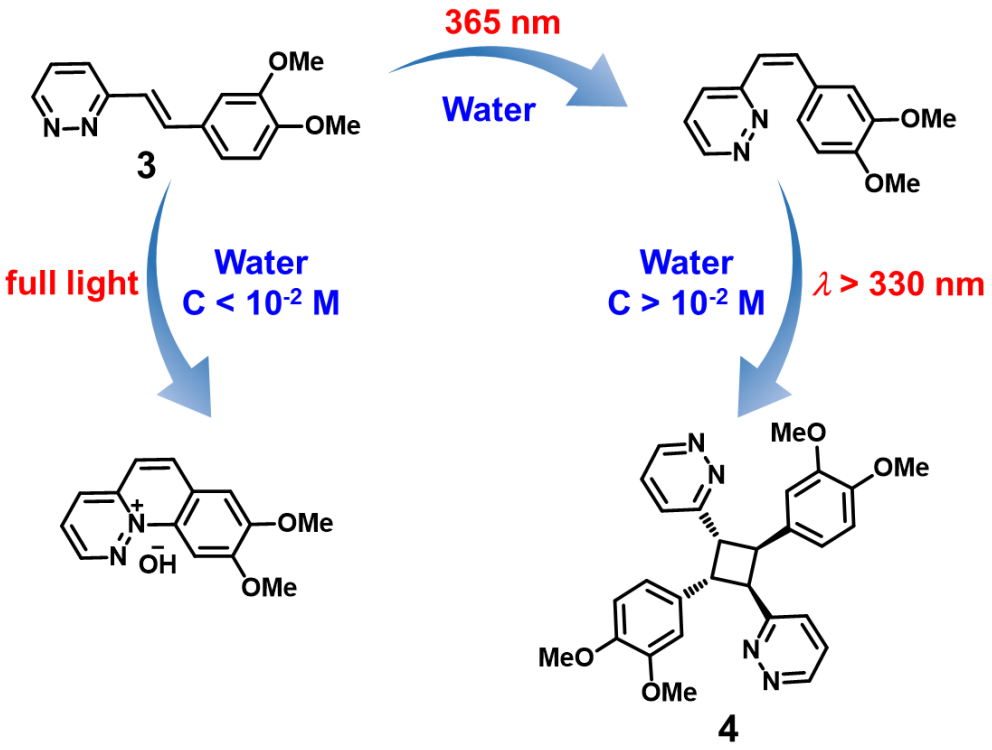

Figure 3.2. Photochemical conversions of a heterostilbene derivative **3**, and the chemical structures of photoproducts formed. (Adapted from reference 28)

and stereoselective dimers under mild reaction conditions without any additives.[28] Photochemical transformations of a pyridazine-based stilbene molecule (**3**) is shown in the **Figure 3.2**. They employed the polar molecules for the dimer preorganization to construct the cyclobutane derivatives in solution. Compound **3** can undergo two parallel reactions such as electrocyclization and intermolecular photodimerization depending on the concentration of the solution. Visible light mediated intermolecular [2 + 2] cycloaddition of compound **3** takes place under mild reaction conditions in water at room temperature. The corresponding *rctt* cyclobutane derivative (**4**) was obtained in a 57 % of yield. Efficiency of this photodimerization reaction depends on the nature of

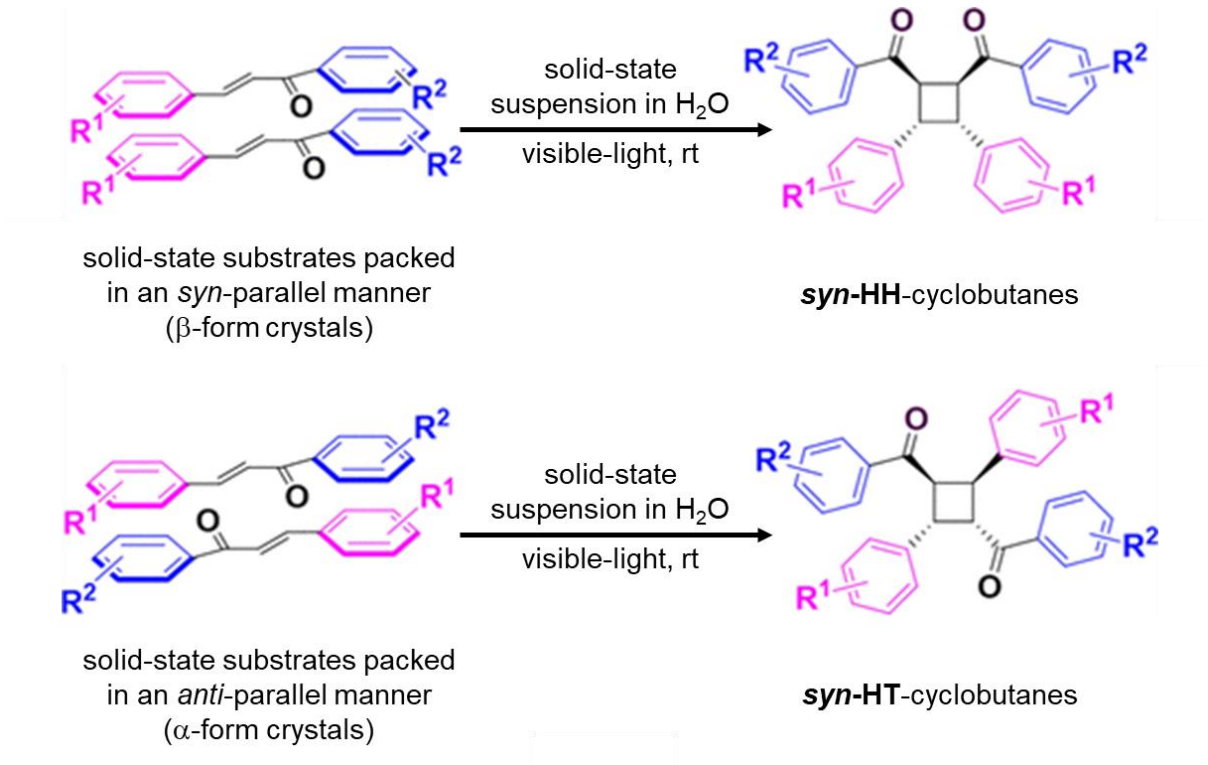

Figure 3.3. Solid-state suspension [2 + 2] photocycloaddition in β-form and α-form crystals of chalcones for *syn*-HH and *syn*-HT cyclobutanes respectively. (Adapted from reference 7)

the solvent used as well as the concentration of the olefins. Cyclobutane formation was observed only in the water solution not even in the highly concentrated solution of **3** in acetonitrile. Strong dipole-dipole interaction at the ground state favors the [2 + 2] cycloaddition and the spatial orientation of molecules in a head-to-tail arrangement affords a regio- and stereoselective photodimer.

Recently, Zou and co-workers developed a mild, green method for visible light-triggered *syn*-selective dimerization. This water-assisted reaction occurred in the metal- and template-free conditions, resulting in *syn*-HH and *syn*-HT cyclobutanes with excellent diastereoselectivity (**Figure 3.3**).[7] Monomer molecules arranged in a

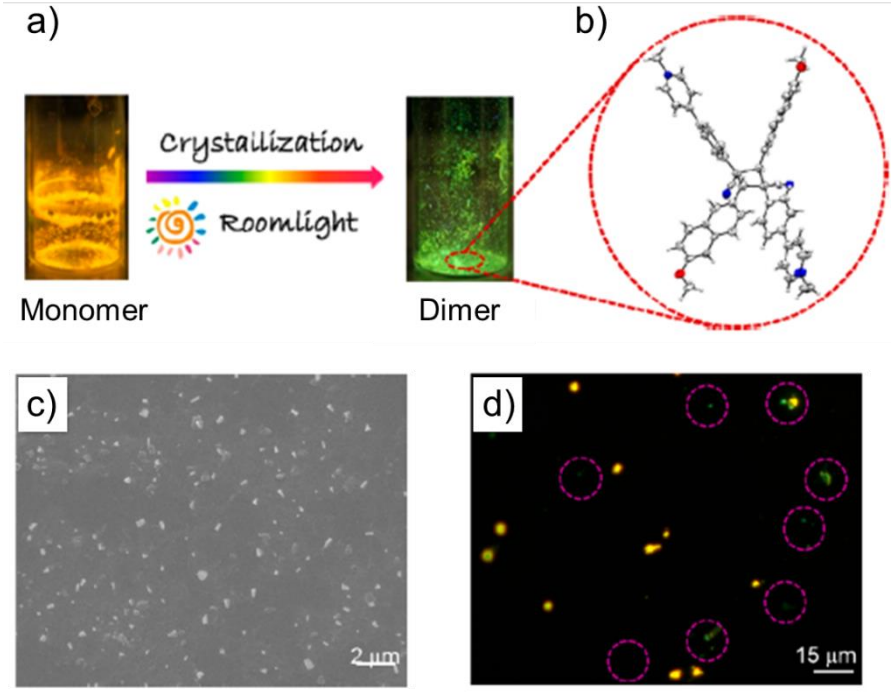

Figure 3.4. a) Crystallization induced photodimerization in aqueous solution and the images of monomer and dimer in the solid state under 365 nm UV light. b) Single crystal structure of dimer. c) SEM and d) fluorescent images of monomer aggregates formed in CH_3CN/H_2O mixture with f_w 99%. (Adapted from reference 29)

syn-parallel manner are known as β-form crystals and form *syn*-HH cyclobutane derivatives under visible light irradiation. Whereas, *anti*-parallel arrangement of monomer molecules (α-form crystals) affords *syn*-HT cyclobutanes. Significant π–π stacking of the neighboring monomers in the crystal lattices act as a supramolecular circumstances, enabling the visible light mediated solid-state photocycloaddition in water.

Tang's group demonstrated a regio- and stereoselective photodimerization in an aqueous medium facilitated by the formation of microcrystals (**Figure 3.4a**).[29] The formation of microcrystals enabled the preorientation of the C=C bond of cyanostilbene

derivative (monomer), leading to a photodimer with solely *anti*-HT conformation. The Single crystal structure of the formed cyclobutane derivative is shown in the **Figure 3.4b**. This cyanostilbene derivative exhibited multiple photoreactions in a controllable manner under different conditions, such as *Z*/*E* isomerization in solution under roomlight and UV-induced photocyclization in solution. While, photodimerization took place in aggregates with regio- and stereoselectivity. Microcrystal formation in the aggregated state during photodimerization was confirmed through SEM analysis and the aggregate morphology of the monomer in CH_3CN/H_2O mixture with 99% water fraction is shown in the **Figure 3.4c**. Photodimerization process is enhanced by the formation of more number of microcrystals. A fluorescence image of monomer in 99% water fraction is given in **Figure 3.4d**. The green emissive dots (encircled with pink dashed lines) near the orange emissive dots demonstrated the excellent efficiency of the photodimerization. UV light from the fluorescence microscopy is enough to induce the photodimerization of monomer microcrystals.

In this chapter, we demonstrated the photochemical dimerization of an *N*-hexylthienoindole-benzoxazole ethylene derivative in daylight conditions without the necessity for photoredox catalysts or templates. The reaction is conducted in solution under ambient conditions and exhibits outstanding regioselectivity and stereospecificity, yielding exclusively *syn*-head-to-tail (*syn*-HT) cyclobutane derivative. Additionally, our results demonstrate the potential of the cyclobutane compound as a versatile building block for the development of organic networks.[30-32]

The versatility of this compound is further enhanced by the possibility of modifying the pendant groups linked to the cyclobutane ring, which is based on the substituents that are already present on the central C=C bond before photoreaction. These attributes open up intriguing possibilities for the design and synthesis of innovative organic functional materials.

3.3. Results and discussion

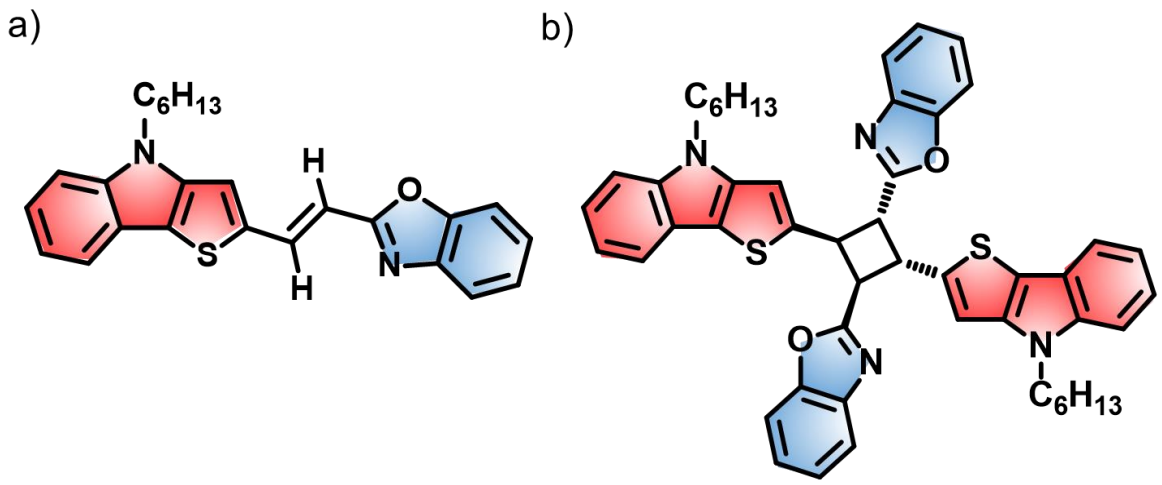

Figure 3.5. Chemical structures of the molecules under study. a) Photoactive monomer, ***E*-TIBO6**. b) Photodimer, ***d*-TIBO6**.

The chemical structures of the *N*-hexylthienoindole-benzoxazole-based photoactive monomer (***E*-TIBO6**) and the resulting *syn*-HT photodimer (***d*-TIBO6**) are shown in **Figure 3.5a** and **3.5b**, respectively. The monomer is a donor-π-acceptor type fluorophore consisting of *N*-hexylthienoindole as the donor and benzoxazole as the acceptor moieties.

3.3.1. Synthetic strategy

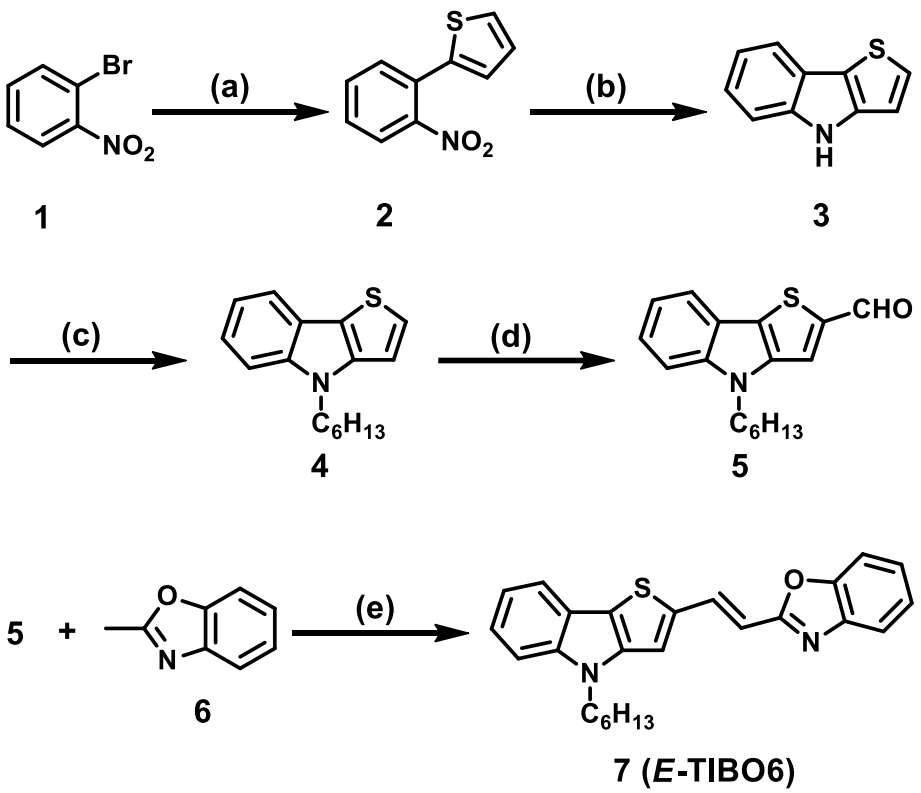

Scheme 3.1. Synthesis of ***E*-TIBO6**; *Reagents and conditions:* (a) tributyl(thiophen-2-yl)stannane, $Pd(PPh_3)_4$, toluene, 110 °C, 48 h (b) PPh_3, 1,2-dichlorobenzene, reflux, 12 h (c) KOH, $C_6H_{13}Br$, Acetone, 5 h (d) dry DCE, $POCl_3$, DMF, 70 °C, overnight (e) KOH, DMF, rt, 3 h.[33-35]

The synthesis of monomer in *trans*-isomer form was accomplished *via* a Knoevenagel condensation reaction between hexyl-substituted thienoindole-2-carbaldehyde and 2-methyl benzoxazole as shown in **Scheme 3.1**. All products were obtained in good yield and characterized by various analytical techniques such as ^{1}H NMR, ^{13}C NMR, and high-resolution mass spectrometry. They were soluble in common organic solvents like hexane, toluene, tetrahydrofuran (THF), *N*,*N*-dimethylformamide (DMF) etc.

3.3.2. Photoresponsive behaviors of *E*-TIBO6 under various conditions

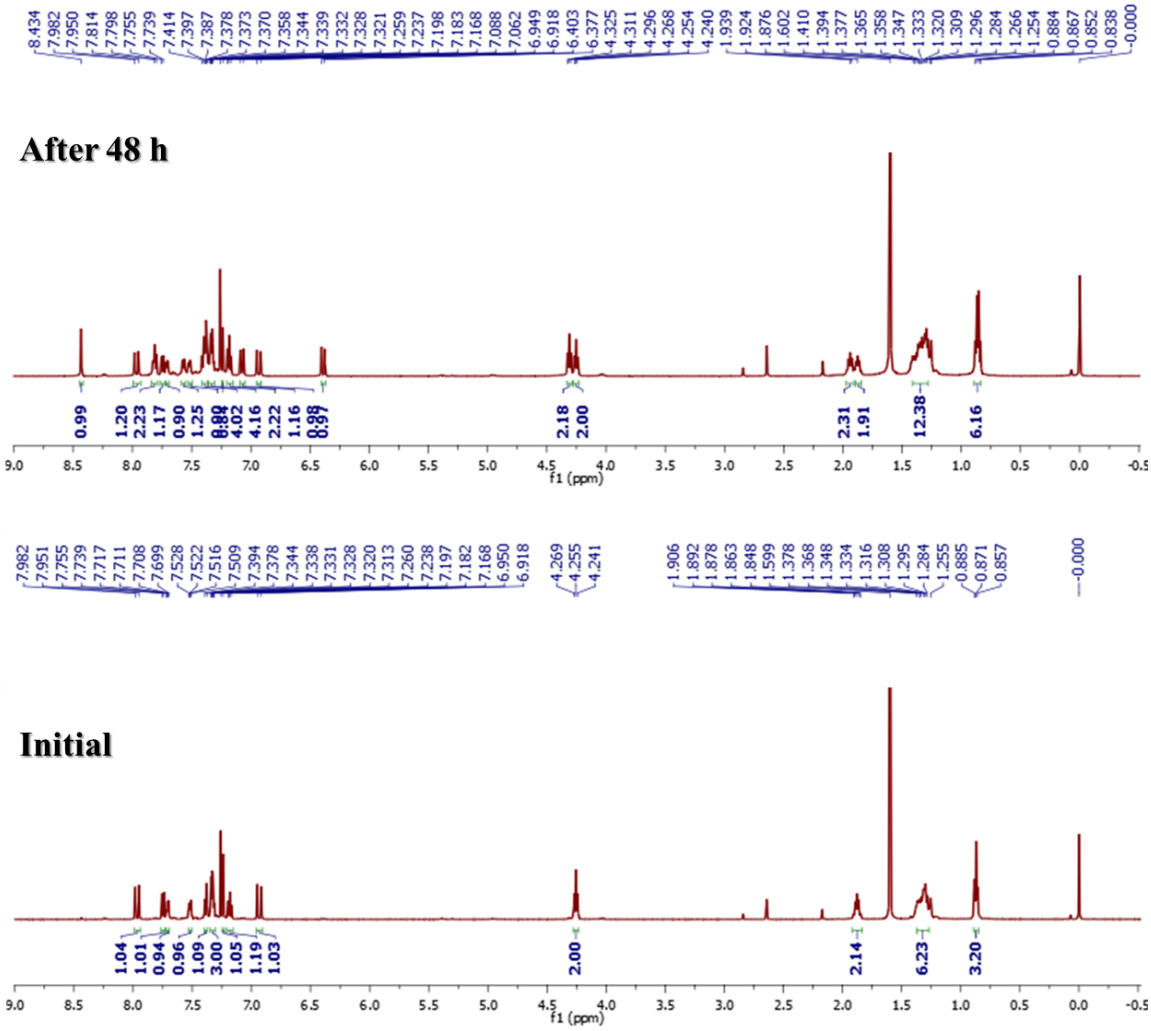

Figure 3.6. ^{1}H NMR spectra of ***E*-TIBO6** in $CDCl_3$ recorded before and after 48h.

The chloroform solution of ***E*-TIBO6** exhibited isomerization at room temperature, with the trans isomer being converted into a mixture containing equal amounts of *cis* and *trans* isomers of ***E*-TIBO6** after 48 hours. ^{1}H NMR spectroscopy was used to follow this process. Results showed that after 48 h, the resonance of its protons was split into two sets, as shown in the **Figure 3.6**. In contrast, the monomer (***E*-TIBO6**) in

a $CHCl_3$/hexane (1:2 vol/vol) solution at room temperature with concentration of approximately 4×10^{-3} M underwent crystallization, forming the dimer molecules upon slow evaporation of the solvent. It is hypothesized that this concentration allows for sufficient proximity between the C=C double bond of the monomer molecules, thus facilitating the cycloaddition reaction. Intermolecular interactions, such as donor-acceptor π–π stacking and dipole-dipole interactions among the ***E*-TIBO6** molecules in the concentrated state, could provide topochemical or supramolecular circumstances, thus yielding a regio- and stereoselective photodimer. In contrast, no dimer formation was observed in the dilute monomer solution.

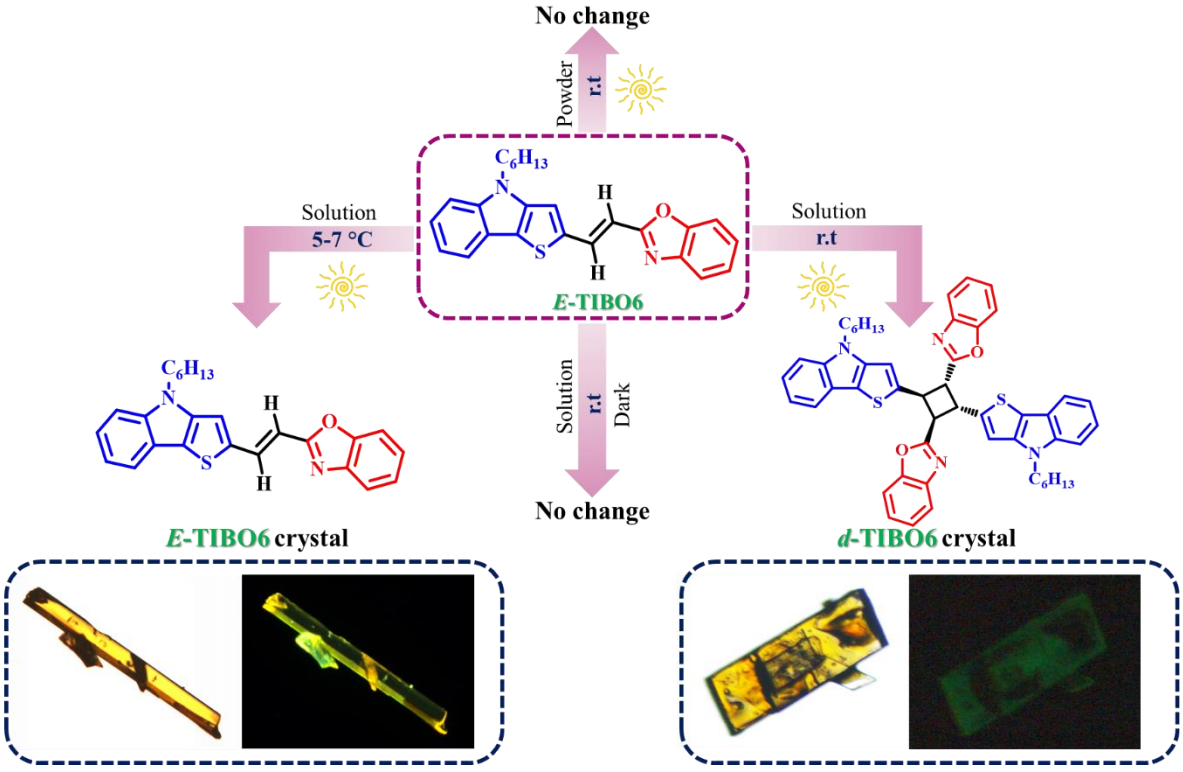

Figure 3.7. ^{1}H NMR Schematic representation of the crystallization of ***E*-TIBO6** under various conditions (r.t. represents room temperature, ~30 °C). Optical microscopic images of ***E*-TIBO6** (bottom left) and ***d*-TIBO6** (bottom right) crystals under normal light (left) and UV light (right).

The impact of various factors on the crystallization of the monomer was investigated. As depicted in **Figure 3.7**, the monomer crystallizes into the dimer in $CHCl_3$/hexane (1:2 vol/vol) solution maintained at room temperature (~30 °C) and under ambient light conditions. Conversely, no dimer formation was observed when the monomer was crystallized in the same solvent system in the dark or at a lower temperature (~5-7 °C). Similarly, the monomer in powder form or as single crystals did not transform into the dimer on exposure to sunlight or 365 nm UV light. As photochemical reactions typically have low activation energies in both solution and solid states, the temperature was expected to have a minimal effect on photoreactions. Nevertheless, the temperature may play a role in topochemical photodimerization by initiating phase transitions or providing energy for molecular motion. It is hypothesized that elevated temperatures increase the mobility of the reactant molecules and expedite the dimerization process, while lower temperatures might impede the dimerization by limiting the mobility of the reactant molecules.[20,36-39] This correlation was supported by our results, which showed that at lower temperatures (~5-7 °C), only ***E*-TIBO6** crystals were obtained, and no dimer formation was observed. The monomer appeared as yellow block-shaped crystals with bright greenish-yellow emission (bottom left of **Figure 3.7**), while the dimer appeared as dark yellow block-shaped crystals with weak green emission (bottom right of **Figure 3.7**). The reduced emission of the dimer must be due to the destruction of the conjugated chromophoric backbone caused by the formation of the cyclobutane ring.

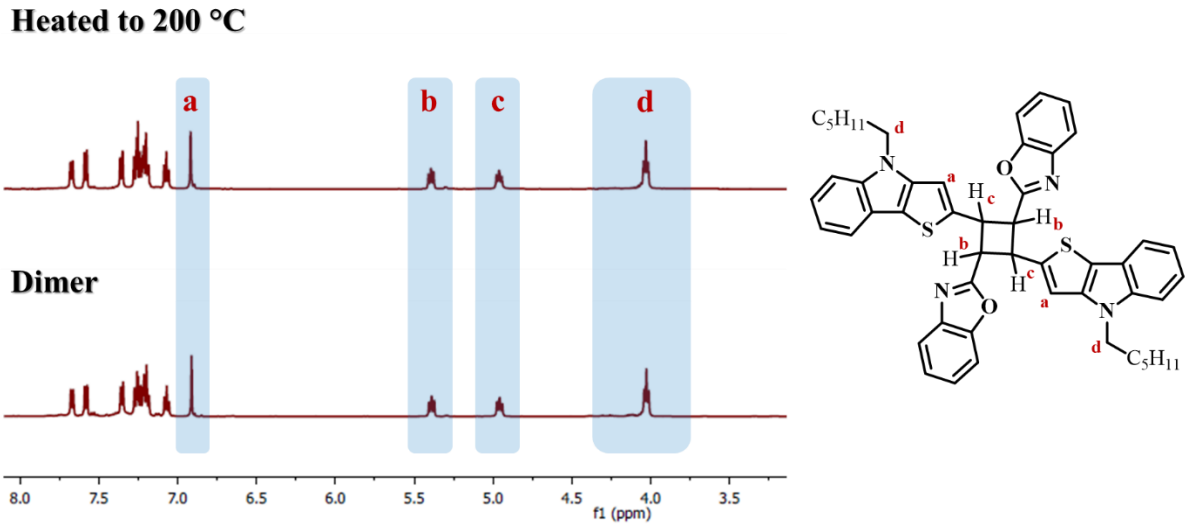

Figure 3.8. ^{1}H NMR spectra of ***d*-TIBO6** recorded before (lower panel) and after (upper panel) heating the solid sample to 200 °C and then dissolving in $CDCl_3$.

The dimer was found to have excellent thermal stability and photostability on exposure to UV and visible light. The ^{1}H NMR spectra of the dimer was recorded in $CDCl_3$ both before and after heating it at 200 °C for 10 minutes (**Figure 3.8**). The observation of identical NMR spectra before and after heating confirms the thermal stability of the photodimer.

3.3.3. Single crystal X-ray analysis of photodimer and monomer

The structure of the dimer was analyzed through the single-crystal X-ray diffraction (SCXRD) technique (**Figure 3.9a**). It also revealed that the photodimer has a triclinic crystal system with the space group *P*-1, consisting of two molecules per unit cell (**Table 3.1** and **Figure 3.9b**). Crystal structure suggests that the interactions between the monomer molecules promotes regioselectivity (*head-to-tail* arrangement; HT) and

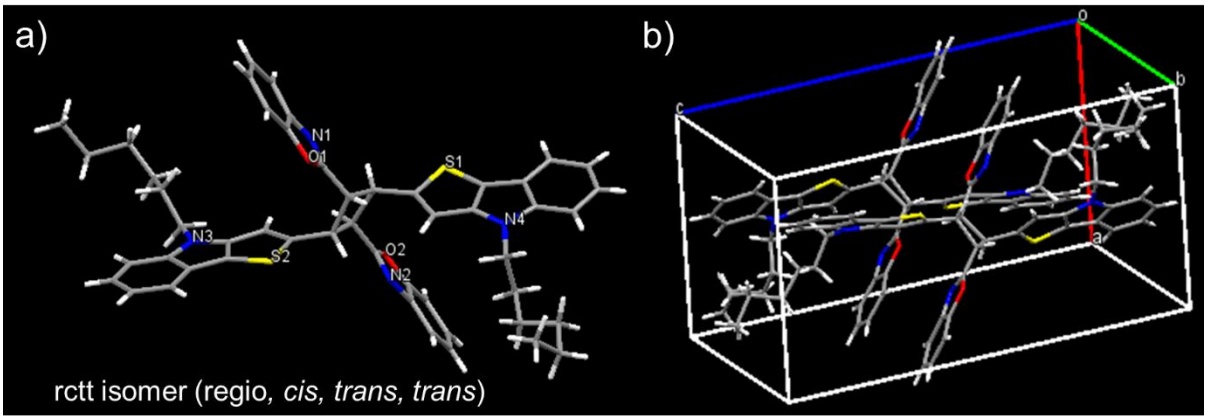

Figure 3.9. Crystal structure of the photodimer. a) Molecular conformation in the crystal. b) Molecular packing of the photodimer in a unit cell.

stereospecificity (*cis*, *trans*, *trans*; ctt), resulting in the formation of a *N*-hexylthienoindole-benzoxazole based tetra substituted cyclobutane dimer with a *syn*-HT conformation in an almost unity conversion yield.

Further, crystal structure of the monomer (***E*-TIBO6**) was analyzed through the SCXRD technique (**Figure 3.10a**). It also revealed that the monomer has a monoclinic crystal system with the space group *C*2/c, consisting of eight molecules per unit cell (**Table 3.2** and **Figure 3.10b**).

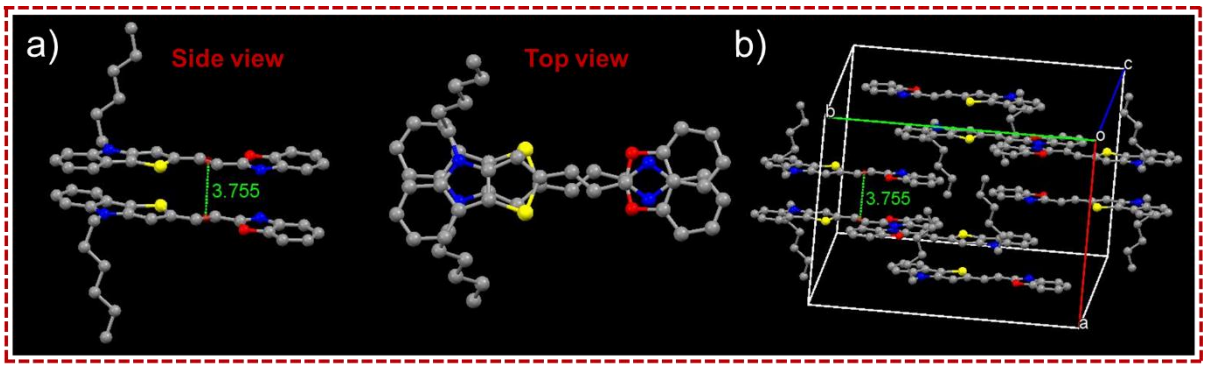

Figure 3.10. Crystal structure of ***E*-TIBO6** molecule. a) Side and top views of the two neighboring molecules. b) Molecular packing in the unit cell.

Table 3.1 Crystallographic data of ***d*-TIBO6** (dimer).

Sample	***d*-TIBO6**	
Empirical formula	C50H48N4O2S2	
Formula weight	801.04	
Temperature	297(2) K	
Wavelength	0.71073 Å	
Crystal system	Triclinic	
Space group	*P*-1	
Unit cell dimensions	a = 10.1419(9) Å	α = 89.270(4)°
	b = 12.2134(12) Å	β = 78.399(3)°
	c = 19.5581(19) Å	γ = 66.729(3)°
Volume	2174.1(4) $Å^3$	
Z	2	
Density (calculated)	1.224 Mg/m^3	
Absorption coefficient	0.167 mm^{-1}	
F(000)	848	
Crystal size	0.200 x 0.150 x 0.100 mm^3	
Theta range for data collection	2.631 to 24.999°	
Index ranges	-12<=h<=12, -14<=k<=14, -23<=l<=23	
Reflections collected	84781	
Independent reflections	7631 [R(int) = 0.0430]	
Completeness to theta = 24.999°	99.7 %	
Absorption correction	Semi-empirical from equivalents	
Max. and min. transmission	0.7454 and 0.6086	
Refinement method	Full-matrix least-squares on F^2	
Data / restraints / parameters	7631 / 674 / 633	
Goodness-of-fit on F^2	1.048	
Final R indices [I>2sigma(I)]	R1 = 0.0771, wR2 = 0.2183	
R indices (all data)	R1 = 0.0992, wR2 = 0.2630	
Largest diff. peak and hole	0.554 and -0.358 $eÅ^{-3}$	

Table 3.2 Crystallographic data of ***E*-TIBO6** (monomer).

Sample	***E*-TIBO6**	
Empirical formula	C25H24N2OS	
Formula weight	400.52	
Temperature	296(2) K	
Wavelength	0.71076 Å	
Crystal system	Monoclinic	
Space group	*C*2/c	
Unit cell dimensions	a = 14.903(3) Å	α = 90°
	b = 21.784(4) Å	β = 115.785(5)°
	c = 14.184(2) Å	γ = 90°
Volume	4146.5(12) $Å^3$	
Z	8	
Density (calculated)	1.283 Mg/m^3	
Absorption coefficient	0.175 mm^{-1}	
F(000)	1696	
Crystal size	0.40 x 0.20 x 0.20 mm^3	
Theta range for data collection	2.80 to 25.00°	
Index ranges	-17<=h<=17, -25<=k<=25, -16<=l<=16	
Reflections collected	15262	
Independent reflections	3518 [R(int) = 0.0879]	
Completeness to theta = 25.00°	96.1 %	
Absorption correction	Semi-empirical from equivalents	
Max. and min. transmission	0.9659 and 0.9334	
Refinement method	Full-matrix least-squares on F^2	
Data / restraints / parameters	3518 / 0 / 264	
Goodness-of-fit on F^2	1.323	
Final R indices [I>2sigma(I)]	R1 = 0.1406, wR2 = 0.2208	
R indices (all data)	R1 = 0.2067, wR2 = 0.2506	
Largest diff. peak and hole	0.420 and -0.295 $eÅ^{-3}$	

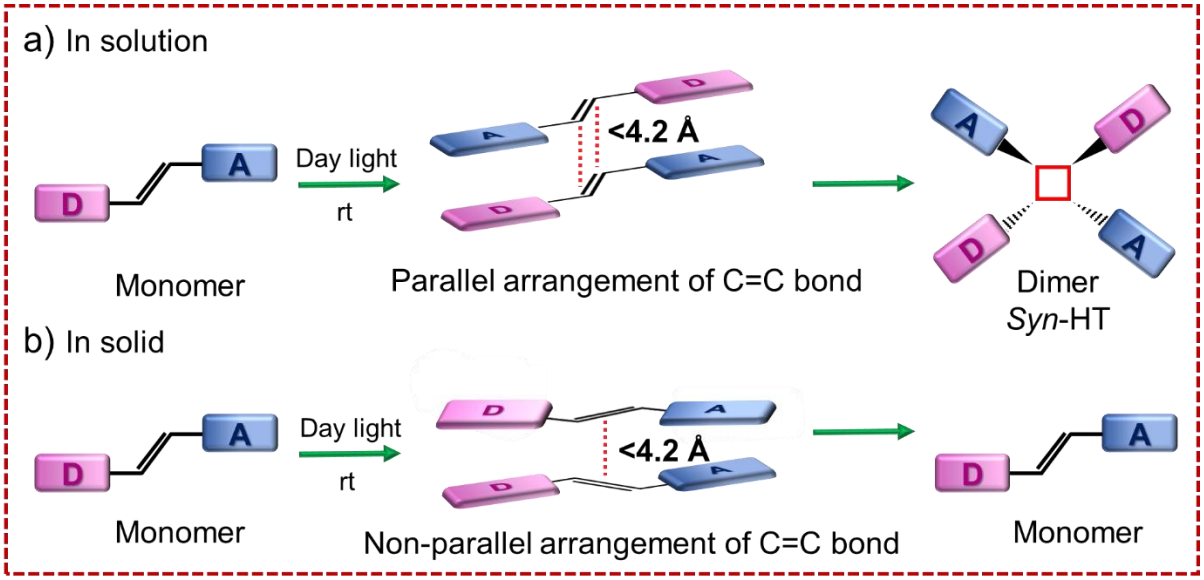

Figure 3.11. Graphical representation of the topochemical arrangement of C=C bond in a) solution and b) solid states.

To elucidate why photodimerization was observed only in solution and not in the solid state, the molecular packing in the crystal lattice of the monomer was analyzed. Schmidt's postulates suggest that the parallel orientation of two olefins, with a distance between reactive C=C double bond that is typically between 3.5 and 4.2 Å; is the key to photochemical reactions.[40] As illustrated in **Figure 3.10**, the C=C bond distance between neighboring ***E*-TIBO6** molecules in the crystal lattice is 3.76 Å, which is ideal for dimerization. However, the alignment of the olefins is not parallel, preventing the topochemical cycloaddition from occurring in the solid state. Probable topochemical arrangements of ***E*-TIBO6** in solution are shown in **Figure 3.11a** and are compared with the arrangement in the solid state, as shown in the **Figure 3.11b**. In solution, monomer molecules must have the head-to-tail organization of the donor and acceptor

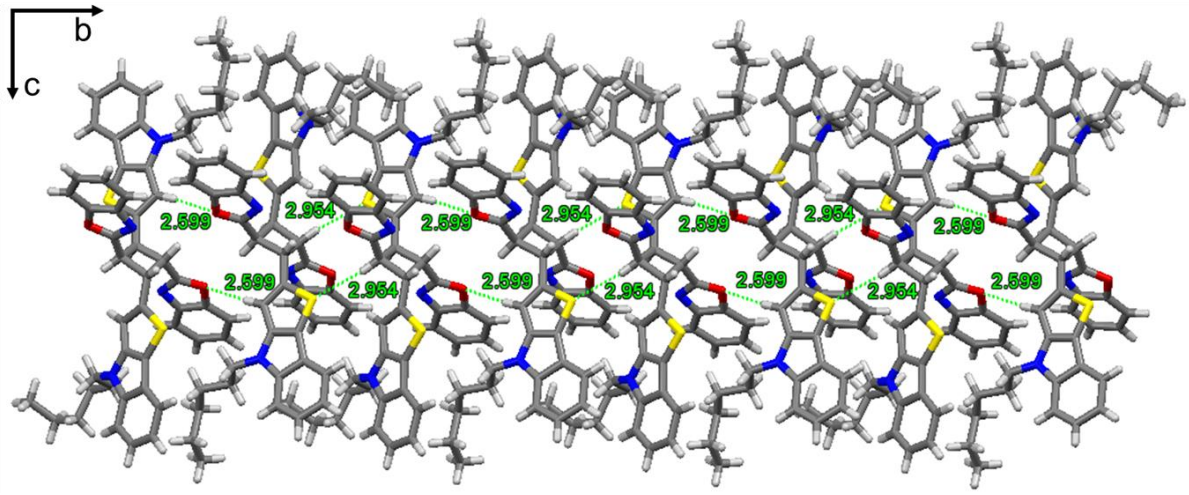

Figure 3.12. H-bonded supramolecular assembly formation of ***d*-TIBO6** molecules along the *b*-axis in the crystal lattice.

units from adjacent molecules, favoring the formation of dimer in a *syn*-head-to-tail fashion. On the other hand, the preorganization of the molecules in the solid state does not promote dimer formation, as their reactive C=C bonds are arranged orthogonally, despite the distance between the centroids of the carbon-carbon double bonds being 3.76 Å.

Interestingly, the ***d*-TIBO6** crystal structure displays an attractive feature in its packing arrangement, where the molecules are organized in a one-dimensional (1D) supramolecular assembly along the *b*-axis *via* intermolecular hydrogen bonds. A single molecule possesses four intermolecular hydrogen bonds, consisting of two C–H···S bonds (2.95 Å) and two C–H···O bonds (2.60 Å), as depicted in **Figure 3.12**. The π–π stacking between two adjacent 1D assemblies along the *a*-axis leads to the formation of a two-dimensional (2D) dimer network (**Figure 3.13**).

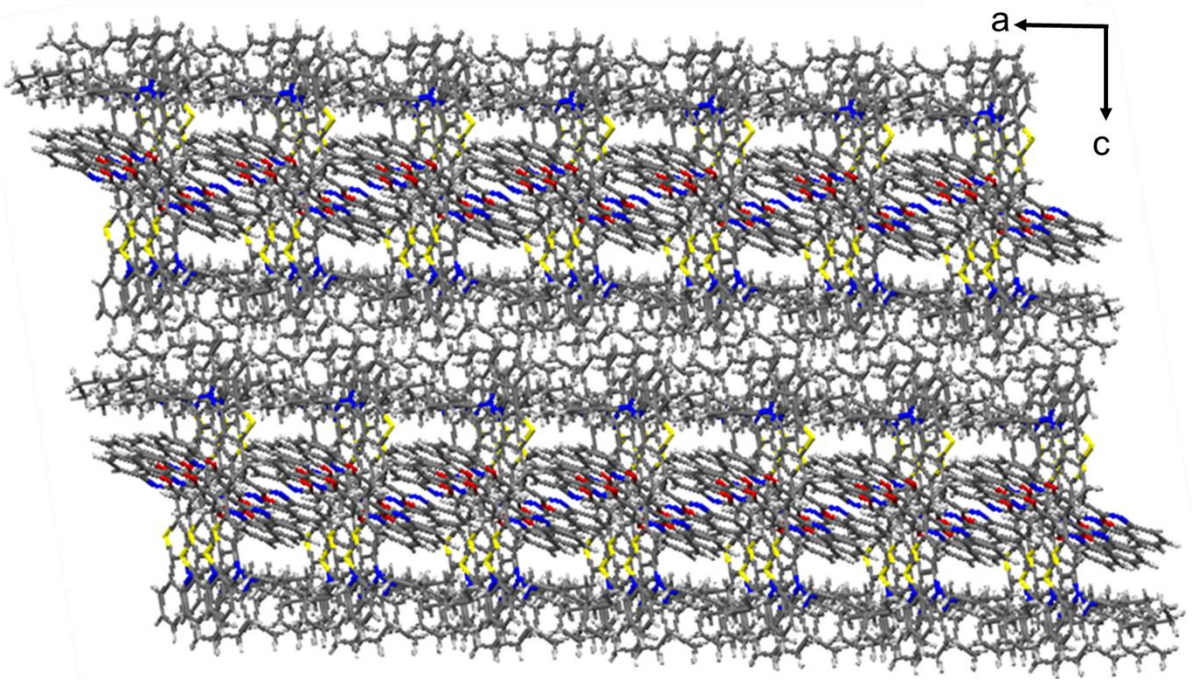

Figure 3.13. The 2D dimer network in the crystal lattice of ***d*-TIBO6**.

Various steps involved in the supramolecular organization of ***d*-TIBO6** molecules are shown in the **Figure 3.14a**. As shown in the figure, two adjacent cyclobutane molecules possess different symmetry operations (indicated by blue and pink colors) and are related by an inversion center. They are held together by intermolecular hydrogen bonds and form a 1D assembly along the *b*-axis in the crystal lattice. Further, each 1D assembly along the *b*-axis interacts with adjacent assemblies through π–π interaction (3.7 Å) between the benzoxazole moieties along the *a*-axis to form a two-dimensional (2D) molecular layer. These layers further assemble into a three-dimensional (3D) architecture with a block-like morphology, as seen through the scanning electron microscopy (SEM) analysis. Cross-sectional image of the single

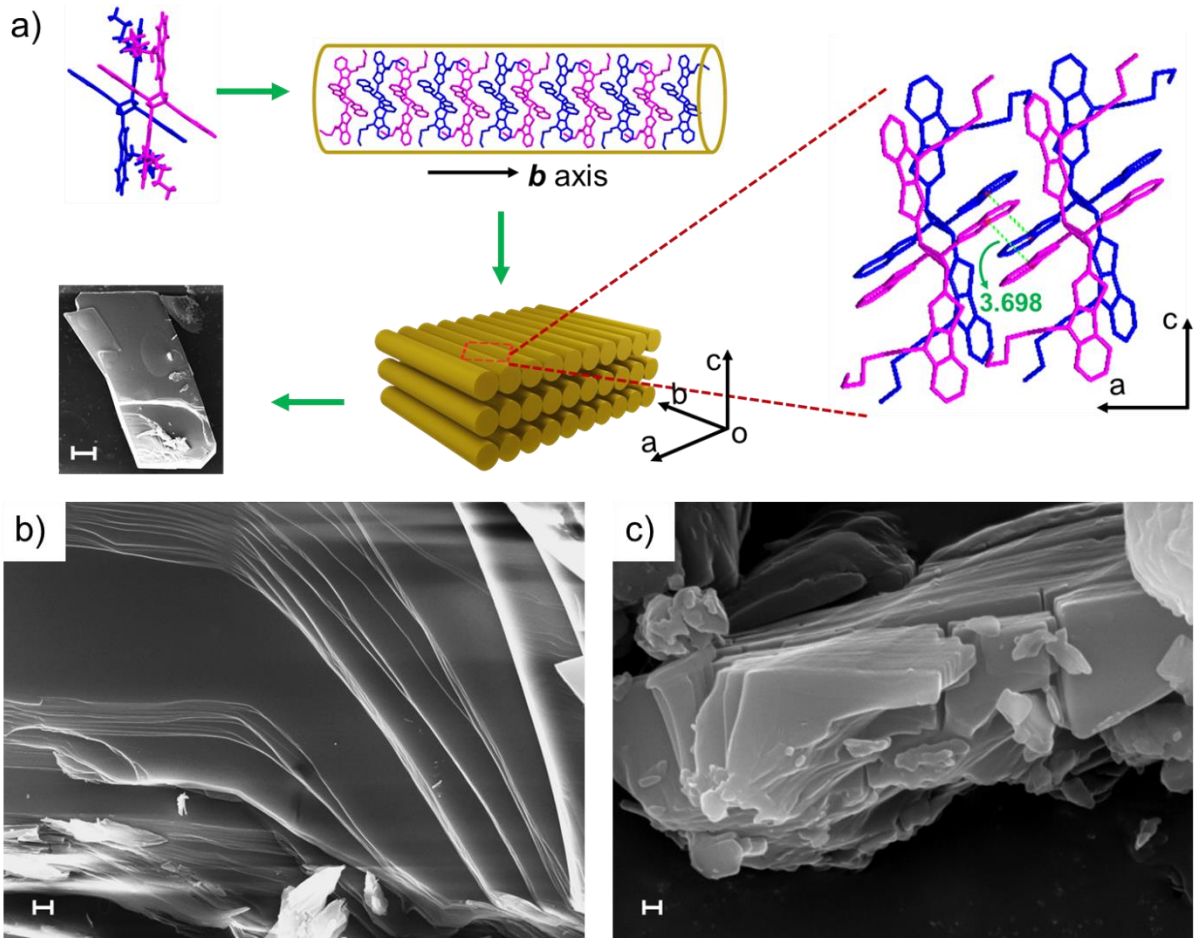

Figure 3.14. a) Illustration of molecular packing in ***d*-TIBO6** resulting in the formation of 3D supramolecular assembly; two adjacent molecules having different symmetry operations are represented by two colors. Scale bar in the SEM image of the single crystal represents 50 μm. SEM images showing b) the cross-sectional area of ***d*-TIBO6** single crystal (scale bar represents 2 μm) and c) microcrystalline powder of ***d*-TIBO6** (scale bar represents 200 nm).

crystal displayed a parallel sheet-like arrangement within the crystal (**Figure 3.14b**). Similarly, the SEM morphology analysis of the microcrystalline powders of ***d*-TIBO6** also exhibited a layer-like arrangement (**Figure 3.14c**). Thus, it is confirmed that crystal is having a block like morphology and the sheet like arrangement of ***d*-TIBO6** molecules within the 3D crystal structure.

3.3.4. FP-TRMC kinetics of *d*-TIBO6 and *E*-TIBO6

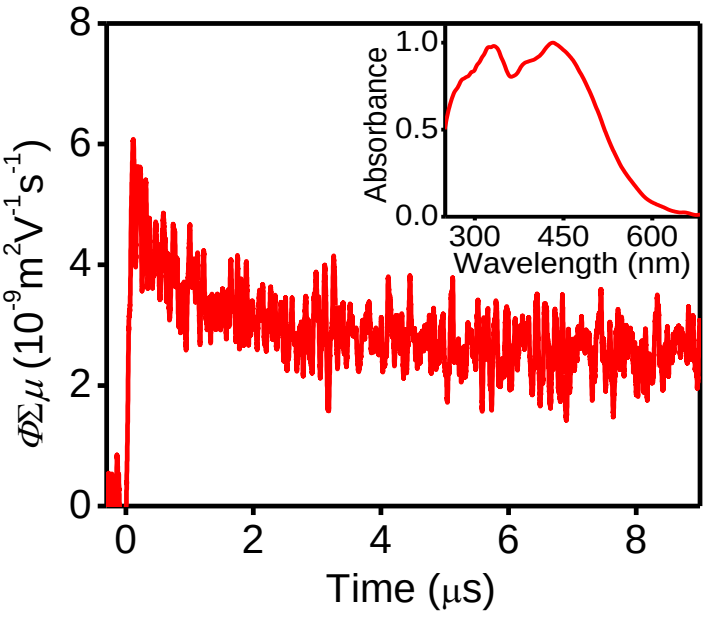

Figure 3.15. Flash photolysis time-resolved microwave conductivity (FP-TRMC) kinetics of ***d*-TIBO6** (λ_{ex} = 355 nm, $I_0 = 8.4 \times 10^{15}$ photons/cm^2); inset shows the normalized absorption spectrum.

The highly ordered and efficient π–π stacking within the crystal structure of ***d*-TIBO6** renders it a prospective candidate as an organic semiconductor material, as it presents a favorable pathway for charge carriers. The material exhibits remarkable absorbance in the 300-500 nm range (inset of **Figure 3.15**), and its photoconductivity has been evaluated using the flash-photolysis time-resolved microwave conductivity (FP-TRMC) technique, which enables the intrinsic photoconductivity of a semiconductor to be assessed with minimal trapping effects.[41-43] The quantification of intrinsic photoconductivity is expressed in terms of $\phi\Sigma\mu$ values (**Figure 3.15**). Where, ϕ refers to the charge-carrier generation quantum yield upon photoexcitation, and $\Sigma\mu$ represents the sum of charge-carrier mobilities. Microcrystalline powder of ***d*-TIBO6**

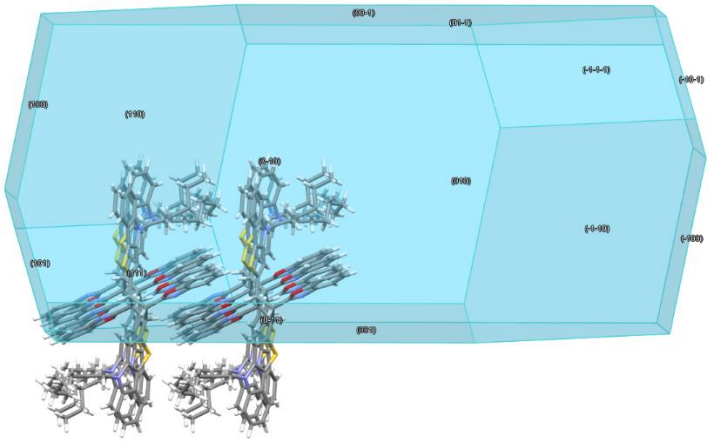

Figure 3.16. Simulated molecular packing and crystal shape of ***d*-TIBO6** using the Bravais-Friedel-Donnay-Harker (BFDH) method.

exhibited exceptional photoconductivity, with a $\phi\Sigma\mu$ value of 5.1×10^{-5} $cm^2V^{-1}s^{-1}$, exceeding that of state-of-the-art organic semiconductor, [6,6]-phenyl-C_{61}-butyric acid methyl ester (PCBM; 1.9×10^{-5} $cm^2V^{-1}s^{-1}$), and other cyclobuteno fullerenes ($1.3 - 3.3 \times 10^{-5}$ $cm^2V^{-1}s^{-1}$).[44] Additionally, it displayed an impressive charge carrier lifetime of 20 μs.

To obtain a more comprehensive understanding of the conductivity, the Bravais-Friedel-Donnay-Harker (BFDH) method was employed to simulate the crystal shape and packing direction. This technique is capable of predicting the morphology of a crystal by utilizing unit cell and symmetry operator data.[45] The BFDH algorithm confirmed the block-like morphology and predicted that the crystal growth occurs along the [100] and [101] planes, *i.e.*, normal to the direction of *c*-axis (**Figure 3.16**). The ***d*-TIBO6** molecules align along the crystal growth direction *via* π–π contacts between the hydrogen-bonded 1D assemblies, creating a 2D conducting layered structure. This

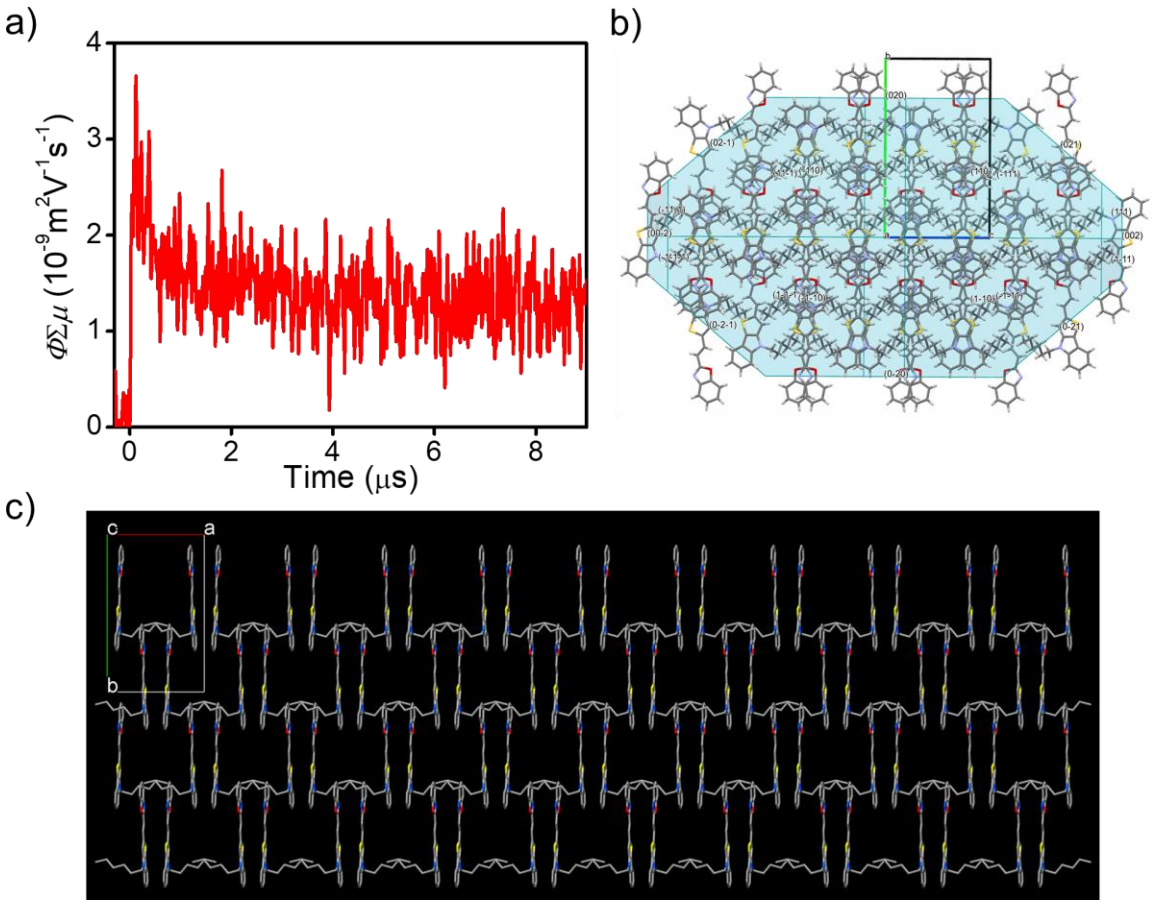

Figure 3.17. a) Flash photolysis time-resolved microwave conductivity (FP-TRMC) kinetics of ***E*-TIBO6** (λ_{ex} = 355 nm, $I_0 = 8.4 \times 10^{15}$ photons/cm^2). b) Simulated molecular packing and crystal shape of ***E*-TIBO6** using the Bravais-Friedel-Donnay-Harker method. c) 2D network along the (*ab*) plane in the crystal lattice of ***E*-TIBO6**.

configuration affords an effortless path for charge carriers to traverse along the (*ab*) plane in the crystal lattice, resulting in a higher $\phi\Sigma\mu$ value.

The photoconductivity of the ***E*-TIBO6** powder was also measured, and it showed a lower $\phi\Sigma\mu$ of 3.5×10^{-5} cm^{2}V^{-1}s^{-1} compared to ***d*-TIBO6** (**Figure 3.17a**). Furthermore, BFDH analysis of ***E*-TIBO6** confirmed the block-like morphology and predicted that the crystal growth occurred along the [002] plane, that is, along the direction of the *c*-

axis (**Figure 3.17b**). Unlike ***d*-TIBO6**, the monomer molecules aligned along the *a*-axis *via* π–π interactions between the aromatic units, which is normal to the crystal growth direction (**Figure 3.17c**). This result highlights the strong impact of noncovalent interactions on molecular packing, thereby governing the charge transport properties. Although the dimer has a broken conjugated backbone, the highly ordered periodic assembly, cooperatively supported by both H-bonding and π–π stacking interactions, is indeed significant for providing effective charge transport pathways, which leads to a 1.5-fold enhancement in photoconductivity when compared to that of the monomer.

3.3.5. Photophysical properties in solution and solid states

The photophysical properties of monomer (***E*-TIBO6**) and dimer (***d*-TIBO6**) forms were studied in solution and solid states (**Figure 3.18**). The absorption spectrum of ***E*-TIBO6** in toluene displayed a peak at 413 nm (**Figure 3.18a**). However, for the photoadduct, the intensity of the absorption band at 413 nm decreased, signifying the destruction of the conjugated chromophoric system. The absorption became broader and extended up to 500 nm. At the same time, a new blue-shifted band appeared at 320 nm, which is a characteristic absorption region for non-conjugated aromatic and heteroaromatic fragments (**Figure 3.18b**).[27] The monomer molecule exhibited an emission peak at 487 nm in toluene (**Figure 3.18c**), while the photoadduct showed a redshifted emission with a maximum at 497 nm, which is 10 nm higher than monomer (**Figure 3.18d**). The fluorescence quantum yields of the monomer and the photoadduct in toluene were calculated as 2.02% and 3.16%, respectively. The emission shift from

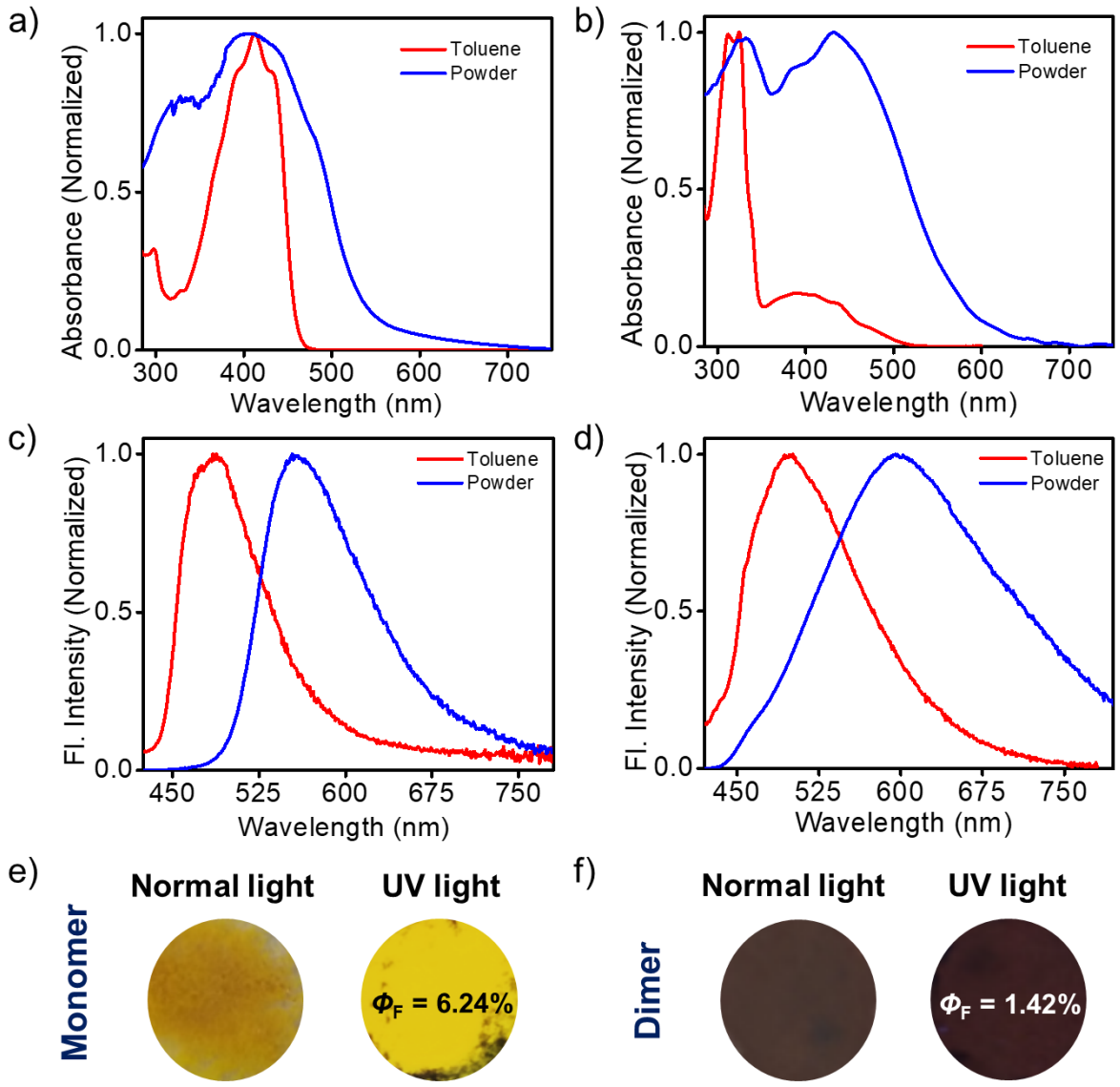

Figure 3.18. Normalized absorption spectra of a) monomer and b) dimer in toluene and in powder form. Emission spectra of c) monomer and d) dimer in toluene and in powder form; (conc. = 10^{-5} M; pathlength, *l* = 1 cm). Photographs of e) monomer and f) dimer powders under normal and 365 nm UV light.

497 nm in toluene solution to 595 nm in the powder form of ***d*-TIBO6** indicate significant intermolecular interactions between the molecules. The absorption of ***E*-TIBO6** and ***d*-TIBO6** powders showed broad absorption features (**Figure 3.18a** and **3.18b**). The absorption onset of the dimer was 600 nm, which was 55 nm redshifted

from the absorption onset of ***E*-TIBO6** at 545 nm. The monomer powder displayed an emission maximum at 555 nm (yellow emission, **Figure 3.18c**) with a fluorescence quantum yield of 6.24%. While, the photoadduct exhibited a quenched broad emission (faint orange, Φ_F = 1.42%), with a maximum centered at 595 nm (40 nm redshifted from ***E*-TIBO6** emission, **Figure 3.18d**). Images of monomer and dimer powders under normal and 365 nm UV light is shown in the **Figure 3.18e** and **3.18f**.

3.3.6. Mechano and acid stimuli-responsive behavior

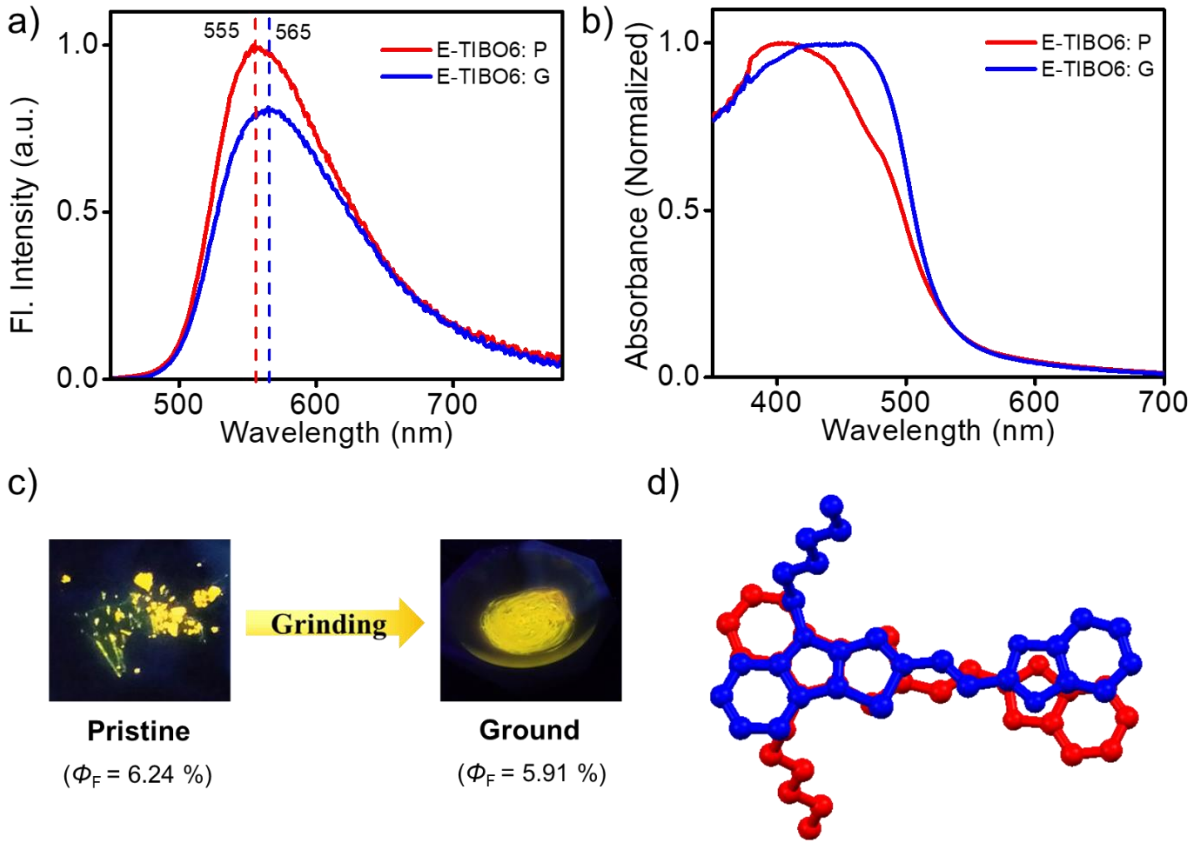

Figure 3.19. a) Photoluminescence spectra, b) normalized absorption, and c) photographs of pristine (P) and ground (G) samples of ***E*-TIBO6**. d) Interaction between acceptor moieties and donor moieties in adjacent ***E*-TIBO6** molecules obtained from single-crystal X-ray analysis.

Mechanofluorochromic property of ***E*-TIBO6** has been investigated and presented in **Figure 3.19**. The pristine (P) sample of ***E*-TIBO6** has bright yellow emission (λ_{max} = 555 nm) with an absolute fluorescence quantum yield of 6.2%. Upon mechanical grinding, ***E*-TIBO6** exhibited only minor changes. About 10 nm redshifted emission and a slight reduction in the emission intensity were observed. The emission maximum of ground (G) sample was positioned at 565 nm (**Figure 3.19a**). This redshift is attributed to the planarization of molecules on grinding. Corresponding absorption spectra of pristine and ground samples in the solid-state were measured using a UV-visible absorption spectrophotometer using the Kubelka-Munk reflectance method by taking the sample in a quartz plate. Both the samples exhibited broad absorption spectra in their solid-state with barely noticeable changes (**Figure 3.19b**). Images of the pristine and ground samples of ***E*-TIBO6** under 365 nm UV light are given in the **Figure 3.19c**. There was no visible differences in the emission color of pristine and ground samples, also the fluorescence quantum yield remained nearly same after grinding (Φ_F = 5.9 % for ground sample).

The single crystal structure of ***E*-TIBO6** was examined in detail to study the luminescence behavior in the solid-state to understand the relationship between mechanoresponsive performance and the supramolecular packing mode of the molecules in the crystal lattice. Significant face-to-face overlap between the *N*-hexylthienoindole (donor) moieties and benzoxazole (acceptor) moieties from the two adjacent molecules (represented in two different colors; blue and red) was observed in

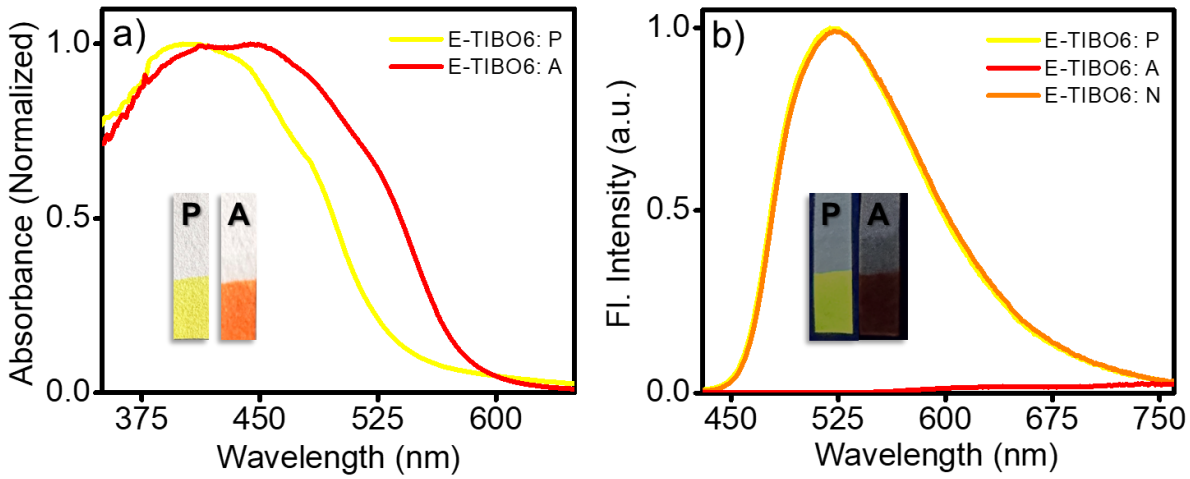

Figure 3.20. a) Absorption changes and b) fluorescence changes in ***E*-TIBO6** upon exposing to HCl vapors and recovery by exposing to NH_3 fumes (***E*-TIBO6** paper samples; P: initial sample, A: HCl vapor fumed sample, N: NH_3 vapor fumed sample). Photographs of the corresponding ***E*-TIBO6** coated filter paper are shown in the inset.

the crystal structure (**Figure 3.19d**). Strong ring overlap in ***E*-TIBO6** makes the π–π stacking of face-to-face type. This strong intermolecular interactions made ***E*-TIBO6** mechanoluminescence (ML) inactive.

The ***E*-TIBO6** molecule is a Lewis base due to the presence of benzoxazole and thienoindole rings in the molecular structure and can be protonated by an acid. Therefore, a filter paper coated with ***E*-TIBO6** was used for acid stimuli-responsive experiments. The filter paper containing ***E*-TIBO6** exhibited an yellow color, which upon exposing to hydrochloric acid (HCl) vapors changes its color from yellow to orange. The initial yellow color was regained by exposing the filter paper to ammonia (NH_3) vapors. Corresponding changes in the absorption spectra is shown in the **Figure 3.20a**. ***E*-TIBO6** coated filter paper shows bright yellow fluorescence under 365 nm

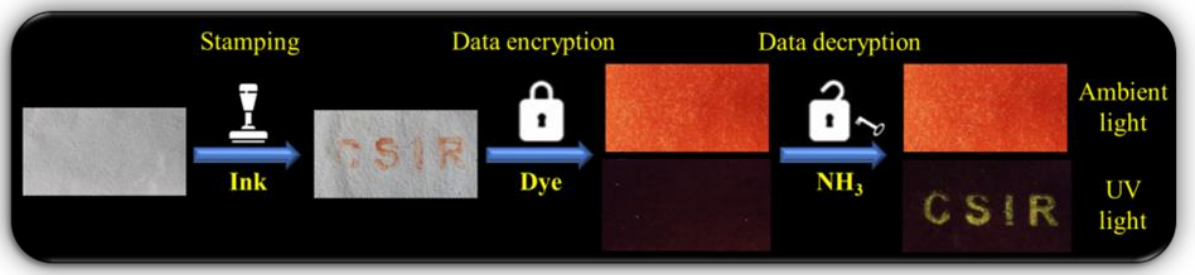

Figure 3.21. Photographic images of data encryption and decryption technique using ***E*-TIBO6**.

UV light. After exposure to HCl vapors, the fluorescence of ***E*-TIBO6** was quenched immediately. Then upon fuming this test filter paper with NH_3 vapors for 10s, the initial bright yellow emission was regained (**Figure 3.20b**). Photographs of the corresponding ***E*-TIBO6** coated filter paper are shown in the inset of **Figure 3.20a** and **3.20b**. This acid/base stimuli-responsive color and luminescence off/on switching cycle can be repeated many times.

A new method for information encryption and decryption was designed and demonstrated in **Figure 3.21** by employing this remarkable fluorescence off-on switching features of ***E*-TIBO6**. For this purpose, ***E*-TIBO6-HCl** was used as the cryptographic ink, while the mixture of dyes, tartrazine (acid yellow 23) and amaranth (acid red 27), were used to form the 'security paper'. Dyes were carefully chosen to provide the background color to cover 'writing' under both normal and UV light. In the encryption stage, the characters 'CSIR' were stamped on a filter paper by using ***E*-TIBO6-HCl** ink, then the paper was immersed in the solution containing dyes (40 mg of acid yellow and 10 mg of acid red in 10 ml glycerol) for a minute and dried at room

temperature. Now the characters ‘CSIR’ were hidden by dye colors and not visible either under ambient light or under UV light. In the decryption process, only the yellow fluorescence of letters ‘CSIR’ revealed clearly after exposing the filter paper to NH_3 vapor for two minutes, whereas the yellow color of letters ‘CSIR’ were still invisible under dye colors. We envisage that these stimuli-responsive protonation-deprotonation effect on luminescent materials have potential applications in data security protection.

3.4. Conclusions

In conclusion, this work has successfully demonstrated a daylight-driven, catalyst- and template-free [2+2] cycloaddition of a thienoindole-benzoxazole ethylene derivative in solution at room temperature, characterized by exceptional regioselectivity and stereospecificity. Donor-acceptor π–π interactions bring the two double bonds closer and arrange them in a specific geometry to yield a single *syn*-HT photodimer during crystallization. The resulting cyclobutane photodimer exhibited an ordered and efficient supramolecular stacking which provides a favorable pathway for charge carriers, producing good photoconductivity and a high charge carrier lifetime. The photoconductivity of the material exceeds that of commonly used organic semiconductors such as PCBM and other cyclobuteno fullerenes. The unique crystal structure and exceptional photoconductivity of the photodimer make it a promising candidate for use in various organic optoelectronic device applications. Future research could focus on the optimization of the charge carrier transport properties of the dimer

and explore its use in different optoelectronic devices. In addition, we have also demonstrated a simple method for data encryption and decryption based on the protonation-deprotonation effect on the monomer molecule.

3.5. Experimental section

3.5.1. Materials and methods

The details of materials, measurements, UV-vis absorption spectrophotometer, spectrofluorimeter, scanning electron microscopy (SEM) and X-ray diffraction measurements are described in the section 2.5.1 of Chapter 2.

Flash-photolysis time-resolved microwave conductivity (FP-TRMC): Transient conductivity was measured by the flash-photolysis time-resolved microwave conductivity (FP-TRMC) technique. A resonant cavity was used to obtain a high degree of sensitivity in the measurement. The resonant frequency and the microwave power were set at 9.1 GHz and 3 mW, respectively. This allowed the electric field of the microwave to be sufficiently small so as not to disturb the motion of charge carriers. The value of conductivity is converted to the product of the quantum yield (ϕ) and the sum of charge carrier mobilities ($\Sigma\mu$) by the following equation.

$$\emptyset \sum \mu = \frac{1}{e \cdot A \cdot I_0 \cdot F_{light}} \cdot \frac{\Delta P_\tau}{P_\tau}$$

Where e, A, I_0, F_{light}t, ΔP_r, and P_r are the unit charge of a single electron, a sensitivity factor [$(S\ m^{-1})^{-1}$], incident photon density of the excitation laser (photons/m^2), a correction (or filling) factor (m^{-1}), a change in reflected microwave power, and a power of the reflected microwave, respectively. The change in conductivity is equivalent to $\Delta P_r/(AP_r)$. 355 nm laser light with a photon density of 8.4×10^{15} photons/cm^2 was used as the excitation source. The sample was set at the highest electric field in a resonant cavity. The experiments were carried out at room temperature.

3.5.2. Synthesis and characterization

Synthesis of 2-(2-nitrophenyl)thiophene (2). A mixture of tributyl (thiophen-2-yl) stannane (3.69 g, 9.90 mmol) and 1-bromo-2-nitrobenzene **1** (2.0 g, 9.90 mmol) was deaerated twice with argon followed by the addition of $Pd(PPh_3)_4$. After stirring at 100 °C for 48 h under argon, the reaction mixture was poured into water and extracted with dichloromethane. The organic layer was washed with water and then dried over anhydrous Na_2SO_4. The crude product was purified by column chromatography on silica gel with hexane as the eluent to afford **2** as an oil (1.88 g, 92 %). ^{1}H NMR (500 MHz, $CDCl_3$) δ: 7.74 (d, J = 8.5 Hz, 1H), 7.59-7.54 (m, 2H), 7.48-7.44 (m, 1H), 7.42-7.41 (dd, $J1$ = 5 Hz, $J2$ = 1 Hz, 1H), 7.10-7.07 (m, 2H).

Synthesis of 4H-thieno[3,2-b]indole (3). A mixture of compound **2** (1.8 g, 8.77 mmol) and triphenylphosphine (6.9 g, 26.31 mmol) in 1,2-dichlorobenzene was refluxed for 12 h under nitrogen, then extracted with CH_2Cl_2. The organic layer was washed with brine and water and dried over anhydrous Na_2SO_4, filtered, and concentrated under a

vacuum. The crude product was purified by column chromatography on silica gel with CH_2Cl_2/n-hexane (10 %) as the eluent, yielding **3** as a white powder (1.14 g, 75%). ^{1}H NMR (500 MHz, $CDCl_3$) δ: 8.21 (s, 1H), 7.75 (d, J = 8 Hz, 1H), 7.44 (d, J = 8Hz, 1H), 7.36 (d, J = 5.5 Hz, 1H), 7.27 (t, J = 7 Hz, 1H), 7.17 (t, J = 7 Hz, 1H), 7.08 (d, J = 5 Hz, 1H).

Synthesis of 4-hexyl-4H-thieno[3,2-b]indole (4). The mixture of compound **3** (1.0 g, 5.77 mmol) and potassium hydroxide (3.24 g, 57.7 mmol) was dissolved in acetone (10 mL). Then bromohexane (1.61 mL, 11.54 mmol) was added to the mixture. The mixture was stirred for 5 h. After the reaction finished, the reactant was extracted with CH_2Cl_2. The organic layer was washed with brine and water and dried over anhydrous Na_2SO_4, then filtered and concentrated under a vacuum. The crude product was purified by column chromatography on silica gel with hexane as an eluent to afford **4** as a pale-yellow oil (1.10 g, 74%). ^{1}H NMR (500 MHz, $CDCl_3$) δ: 7.73 (d, J = 8 Hz, 1H), 7.35 (d, J = 8 Hz, 1H), 7.31 (d, J = 5 Hz, 1H), 7.26 (t, J = 7.5 Hz, 1H), 7.14 (t, J = 7.5 Hz, 1H), 7.01 (d, J = 5Hz, 1H), 4.18 (t, J = 7.5 Hz, 2H), 1.81 (t, J = 7 Hz, 2H), 1.28 (t, J = 7.5 Hz, 6H), 0.85 (t, J = 7 Hz, 3H).

Synthesis of 4-hexyl-4H-thieno[3,2-b]indole-2-carbaldehyde (5). To a solution of **4** (1.0 g, 03.89 mmol) and *N*,*N*-dimethylformamide (1.20 mL, 15.56 mmol) in 1,2-dichloroethane was slowly added $POCl_3$ (1.45 mL, 15.56 mmol) at 0 °C, and stirred for 1 h under argon. Then, the reaction mixture was allowed to heat to 60 °C and stirred overnight. The mixture was cooled to 0 °C and neutralized using aqueous $NaHCO_3$.

The organic layer was extracted using CH_2Cl_2 and dried over anhydrous Na_2SO_4 and concentrated under vacuum. The crude compound was purified by column chromatography on silica gel with CH_2Cl_2/n-hexane (40 %) as the eluent to afford **5** as a yellow oil (0.83 g, 75%). 1H NMR (500 MHz, $CDCl_3$) δ: 9.96 (s, 1H), 7.85 (d, J = 8 Hz, 1H), 7.73 (s, 1H), 7.42 (d, J = 3.5 Hz, 2H), 7.23-7.20 (m, 1H), 4.29 (t, J = 7 Hz, 2H), 1.90-1.86 (m, 2H), 1.36-1.28 (m, 6H), 0.86 (t, J = 7 Hz, 3H).

Synthesis of 2-(2-(4-hexyl-4H-thieno[3,2-b]indol-2-yl)vinyl)benzo[d]oxazole (*E*-TIBO6). Potassium hydroxide (0.729 g, 13 mmol) was added to DMF (5 mL) and allowed to stir under open air for 15 min at room temperature. 2-methylbenzoxazole (0.23 mL, 1.95 mmol) was then added, turning the solution yellow, followed by the addition of compound **5** (0.370 g, 1.30 mmol). The solution was then stirred for 3 h at room temperature, after which the reaction was quenched with 1 M HCl solution. The organic layer was extracted using ethyl acetate and dried over anhydrous Na_2SO_4, and concentrated under a vacuum. The crude compound was purified by column chromatography on silica gel with CH_2Cl_2/hexane (40 %) as the eluent to afford ***E*-TIBO6** as a yellow solid (0.402 g, 77%). m.p.: 118 °C. ^{1}H NMR (500 MHz, $CDCl_3$): δ [ppm] = 7.97 (d, J = 15.5 Hz, 1H), 7.75 (d, J = 8 Hz, 1H), 7.72-7.70 (m, 1H), 7.53-7.51 (m, 1H), 7.39 (d, J = 8 Hz, 1H), 7.34-7.31 (m, 3H), 7.24 (s, 1H), 7.18 (t, J = 7.5 Hz, 1H), 6.93 (d, J = 16 Hz, 1H), 4.26 (t, J = 7 Hz, 2H), 1.91-1.85 (m, 2H), 1.37-1.26 (m, 6H), 0.87 (t, J = 7 Hz, 3 H). ^{13}C NMR (125 MHz, $CDCl_3$): δ [ppm] = 162.8, 150.5, 144.9, 142.4, 141.9, 141.4, 133.6, 125.0, 124.5, 123.7, 121.4, 119.7, 119.5, 119.5,

118.1, 112.6, 111.5, 110.2, 110.0, 45.3, 31.5, 29.7, 26.8, 22.5, 14.0. ESI-MS m/z = 401.1692 (calc. = 400.1609).

TIBO6 (***E* & *Z*** mixture, 1:1). ^{1}H NMR (500 MHz, $CDCl_3$): δ [ppm] = 8.43 (s, 1H), 7.97 (d, *J* = 16 Hz, 1H), 7.83-7.80 (m, 2H), 7.75 (d, *J* = 8 Hz, 1H), 7.72-7.70 (m, 1H), 7.58-7.56 (m, 1H), 7.53-7.51 (m, 1H), 7.40-7.36 (m, 4H), 7.34-7.31 (m, 4H), 7.24 (s, 1H), 7.18 (t, *J* = 7.5 Hz, 2H), 7.08 (d, *J* = 13 Hz, 1H), 6.93 (d, *J* = 15.5 Hz, 1H), 6.39 (d, *J* = 13 Hz, 1H), 4.31 (t, *J* = 7 Hz, 2H), 4.25 (t, *J* = 7 Hz, 2H), 1.97-1.91 (m, 2H), 1.89-1.85 (m, 2H), 1.44-1.25 (m, 12H), 0.88-0.84 (m, 6H). ESI-MS m/z = 401.1692 (calc. = 400.1609).

Synthesis of 2,2'-((1*R*,2*R*,3*S*,4*S*)-2,4-bis(4-hexyl-4*H*-thieno[3,2-*b*]indol-2-yl)cyclobutane-1,3-diyl)bis(benzo[*d*]oxazole) (*d*-TIBO6). The anti-solvent method was used for the synthesis and crystallization of the photodimer. Briefly, powders of ***E*-TIBO6** were dissolved in 400 μL of $CHCl_3$, and about 800 μL of hexane were added to this solution through the sides of the vial. Then the crystallization vial was sealed with parafilm and kept at room temperature. Single crystals of ***d*-TIBO6** were grown from 1:2 chloroform-hexane solution of ***E*-TIBO6** (4×10^{-3} M) by slow evaporation of the solvent at room temperature. Crystal formation was observed within 2 days. m.p.: 185 °C. ^{1}H NMR (500 MHz, $CDCl_3$): δ [ppm] = 7.67 (d, *J* = 7.5 Hz, 2H), 7.58 (d, *J* = 7.5 Hz, 2H), 7.35 (d, *J* = 8 Hz, 2H), 7.27-7.18 (m, 8H), 7.07 (t, *J* = 7.5 Hz, 2H), 6.91 (s, 2H), 5.39 (t, *J* = 8.5 Hz, 2H), 4.96 (t, *J* = 8.5 Hz, 2H), 4.03 (t, *J* = 7.5 Hz, 4H), 1.58-1.55 (m, 4H), 1.28-1.20 (m, 12H), 0.87 (t, *J* = 7 Hz, 6H). ^{13}C NMR (125 MHz, $CDCl_3$):

δ [ppm] = 164.3, 144.3, 140.5, 127.4, 125.8, 125.0, 124.4, 124.4, 122.2, 121.6, 119.8, 118.8, 118.7, 114.4, 110.6, 109.7, 109.2, 45.8, 45.0, 41.9, 31.4, 29.4, 26.7, 22.5, 14.0. ESI-MS m/z = 823.3091 (calc. = 800.3219).

3.6. References

1. A. Sergeiko, V. V. Poroikov, L. O. Hanuš, V. M. Dembitsky, *Open Med. Chem. J.* **2008**, *2*, 26.
2. T. Bach, J. P. Hehn, *Angew. Chem. Int. Ed.* **2011**, *50*, 1000.
3. J. C. Namyslo, D. E. Kaufmann, *Chem. Rev.* **2003**, *103*, 1485.
4. A. A. Q. Al-Khdhairawi, P. Krishnan, C.-W. Mai, F.-L. Chung, C.-O. Leong, K.-T. Yong, K.-W. Chong, Y.-Y. Low, T.-S. Kam, K.-H. Lim, *J. Nat. Prod.* **2017**, *80*, 2734.
5. V. M. Dembitsky, Phytomedicine **2014**, *21*, 1559.
6. A. Çukurovali, I. Yilmaz, H. ¨Ozmen, *Transit. Met. Chem.* **2001**, *26*, 619.
7. X. Song, J. Gu, E. Zhang, Y. Jiang, M. Xin, Y. Meng, A. S. C. Chan, Y. Zou, *ACS Sustainable Chem. Eng.* **2022**, *10*, 16399.
8. K. K. Neena, P. Sudhakar, P. Thilagar, *Angew. Chem. Int. Ed.* **2018**, *57*, 16806.
9. Q.-Q. Zhou, Y.-Q. Zou, L.-Q. Lu, W.-J. Xiao, *Angew. Chem. Int. Ed.* **2019**, *58*, 1586.
10. S. Poplata, A. Troester, Y.-Q. Zou, T. Bach, *Chem. Rev.* **2016**, *116*, 9748.
11. T. P. Yoon, M. A. Ischay, J. Du, *Nat. Chem.* **2010**, *2*, 527.
12. M. A. Ischay, M. S. Ament, T. P. Yoon, *Chem. Sci.* **2012**, *3*, 2807.
13. H.-A. Brune, T. Debaerdemaeker, U. Günther, G. Schmidtberg, U. Ziegler, *J. Photochem. Photobiol. A: Chem.* **1994**, *83*, 113.
14. A. Natarajan, J. T. Mague, K. Venkatesan, V. Ramamurthy, *Org. Lett.* **2005**, *7*, 1895.

15. T. Lei, C. Zhou, M.-Y. Huang, L.-M. Zhao, B. Yang, C. Ye, H. Xiao, Q.-Y. Meng, V. Ramamurthy, C.-H. Tung, L.-Z. Wu, *Angew. Chem. Int. Ed.* **2017**, *56*, 15407.
16. J. Du, K. L. Skubi, D. M. Schultz, T. P. Yoon, *Science* **2014**, *344*, 392.
17. J. M. R. Narayanam, C. R. J. Stephenson, *Chem. Soc. Rev.* **2011**, *40*, 102.
18. R. Li, B. C. Ma, W. Huang, L. Wang, D. Wang, H. Lu, K. Landfester, K. A. I. Zhang, *ACS Catal.* **2017**, *7*, 3097.
19. T. R. Blum, Z. D. Miller, D. M. Bates, I. A. Guzei, T. P. Yoon, *Science* **2016**, *354*, 1391.
20. V. Ramamurthy, J. Sivaguru, *Chem. Rev.* **2016**, *116*, 9914.
21. B. Bibal, C. Mongin, D. M. Bassani, *Chem. Soc. Rev.* **2014**, *43*, 4179.
22. D. M. Bassani, V. Darcos, S. Mahony, J.-P. Desvergne, *J. Am. Chem. Soc.* **2000**, *122*, 8795.
23. Y. Jiang, C. Wang, C. R. Rogers, M. S. Kodaimati, E. A. Weiss, *Nat. Chem.* **2019**, *11*, 1034.
24. Y.-F. Han, G.-X. Jin, F. E. Hahn, *J. Am. Chem. Soc.* **2013**, *135*, 9263.
25. Y.-F. Han, G.-X. Jin, C. G. Daniliuc, F. E. Hahn, *Angew. Chem. Int. Ed.* **2015**, *54*, 4958.
26. T. Wu, L.-H. Weng, G.-X. Jin, *Chem. Commun.* **2012**, *48*, 4435.
27. O. A. Fedorova, A. E. Saifutiarova, E. N. Gulakova, E. O. Guskova, T. M. Aliyeu, N. E. Shepel, Y. V. Fedorov, *Photochem. Photobiol. Sci.* **2019**, *18*, 2208.
28. A. E. Saifutiarova, Y. V. Fedorov, F. Maurel, E. N. Gulakova, V. A. Karnoukhova, O. A. Fedorova, *J. Photochem. Photobiol. A: Chem.* **2022**, *427*, 113804.
29. P. Wei, J.-X. Zhang, Z. Zhao, Y. Chen, X. He, M. Chen, J. Gong, H. H.-Y. Sung, I. D. Williams, J. W. Y. Lam, B. Z. Tang, *J. Am. Chem. Soc.* **2018**, *140*, 1966.
30. G. R. Desiraju, *Acc. Chem. Res.* **2002**, *35*, 565.
31. S. M. Oburn, C. L. Santana, E. Elacqua, R. H. Groeneman, *CrystEngComm* **2020**, *22*, 4349.

32. M. A. Sinnwell, C. L. Santana, E. Bosch, L. R. MacGillivray, R. H. Groeneman, *CrystEngComm* **2020**, *22*, 6780.
33. Y. K. Eom, S. H. Kang, I. T. Choi, Y. Yoo, J. Kim, H. K. Kim, *J. Mater. Chem. A* **2017**, *5*, 2297.
34. T. Ghosh, A. Gopal, S. Nagasawa, N. Mohan, A. Saeki, C. Vijayakumar, *ACS Appl. Mater. Interfaces* **2016**, *8*, 25396.
35. J. S. Klimavicz, J. F. Mike, A. Bhuwalka, A. L. Tomlinson, M. Jeffries-EL, *Pure Appl. Chem.* **2012**, *84*, 991.
36. M. S. K. Dhurjati, J. A. R. P. Sarma, G. R. Desiraju, *J. Chem. Soc., Chem. Commun.* **1991**, 1702.
37. G. S. Murthy, P. Arjunan, K. Venkatesan, V. Ramamurthy, *Tetrahedron* **1987**, *43*, 1225.
38. S. K. Kearsley, in *Organic solid state chemistry*, ed. G. R. Desiraju, Elsevier, **1987**, pp. 69-115.
39. M. D. Cohen, B. S. Green, Z. Ludmer, G. M. J. Schmidt, *Chem. Phys. Lett.* **1970**, *7*, 486.
40. G. M. J. Schmidt, *Pure Appl. Chem.* **1971**, *27*, 647.
41. A. Saeki, Y. Koizumi, T. Aida, S. Seki, *Acc. Chem. Res.* **2012**, *45*, 1193.
42. S. Seki, A. Saeki, T. Sakurai, D. Sakamaki, *Phys. Chem. Chem. Phys.* **2014**, *16*, 11093.
43. A. Saeki, Y. Yamamoto, Y. Koizumi, T. Fukushima, T. Aida, S. Seki, *J. Phys. Chem. Lett.* **2011**, *2*, 2549.
44. S. Reboredo, R. M. Girón, S. Filippone, T. Mikie, T. Sakurai, S. Seki, N. Martín, *Chem. Eur. J.* **2016**, *22*, 13627.
45. P. R. Edgington, P. McCabe, C. F. Macrae, E. Pidcock, G. P. Shields, R. Taylor, M. Towler, J. Van De Streek, *J. Appl. Cryst.* **2006**, *39*, 453.

Chapter 4

Near-Infrared, Mechanoresponsive Luminescence Turn-on in Thienoindole-Thiazolothiazole-based Fluorophores

4.1. Abstract

*Organic π-Conjugated compounds that exhibit luminescence turn-on in the solid state under external mechanical stimulus have potential applications in sensors, security printing, and deformation detectors. Two nearly planar Donor–Acceptor–Donor systems (**TiTz-1** and **TiTz-6**) were designed to illustrate the feasibility of achieving near-infrared mechanoresponsive luminescence turn-on behaviors. These behaviors were realized by mechanically disturbing their initial weakly or non-emissive metastable self-assembled states, thus transitioning them into emissive states with quantum yields exceeding 30%. Detailed investigations suggested that this mechanoresponsive luminescence turn-on could be primarily attributed to the disturbance of the π–π stacking interactions in the initial weakly or non-emissive J-aggregates by the applied mechanical force. The π–π stacking interactions are significant in this context as they help maintain the initial metastable state of these compounds. When disturbed by mechanical force, the disruption of these interactions alters the molecular configuration, leading to the observed luminescence turn-on behavior.*

4.2. Introduction

Organic fluorescent materials with tunable luminescence under mechanical stimulus in the solid-state have gained considerable attention due to their potential use in optoelectronic devices, sensors, data storage, and anti-counterfeiting.[1-13] Controlling the mode of molecular packing in organic luminescent materials is an attractive way for achieving the solid-state luminescence switching and thus the development of mechanoresponsive luminescent (MRL) materials.[14-19] Numerous MRL materials displaying dichromic luminescence or 'turn-off' characteristics have been reported.[20-21] However, the practical demand leans towards MRL compounds exhibiting 'turn-on' characteristics.[22-23] This trait is often difficult to achieve with conventional MRL materials, primarily those using aggregation-induced emission (AIE) luminophores.[24-29] Various strategies for attaining mechanoresponsive 'turn-on' luminescence have been proposed, including the switching of intramolecular charge transfer (ICT),[30] disruption of donor-acceptor (D-A) interactions,[31-32] structural rearrangement in cocrystallized D-A systems,[33] introduction of shear- and UV-induced reversible chemical changes,[34] and the control of photo-induced electron transfer in molecular assemblies.[35-36]

Near-infrared (NIR) fluorophores, which emit fluorescence in the NIR window (650-900 nm), are of particular interest among stimuli-responsive organic luminescent materials.[37-38] Their suitability for applications such as security printing, *in vivo* bio-imaging, and flaw detection stems from their high signal-to-noise ratios and ability to

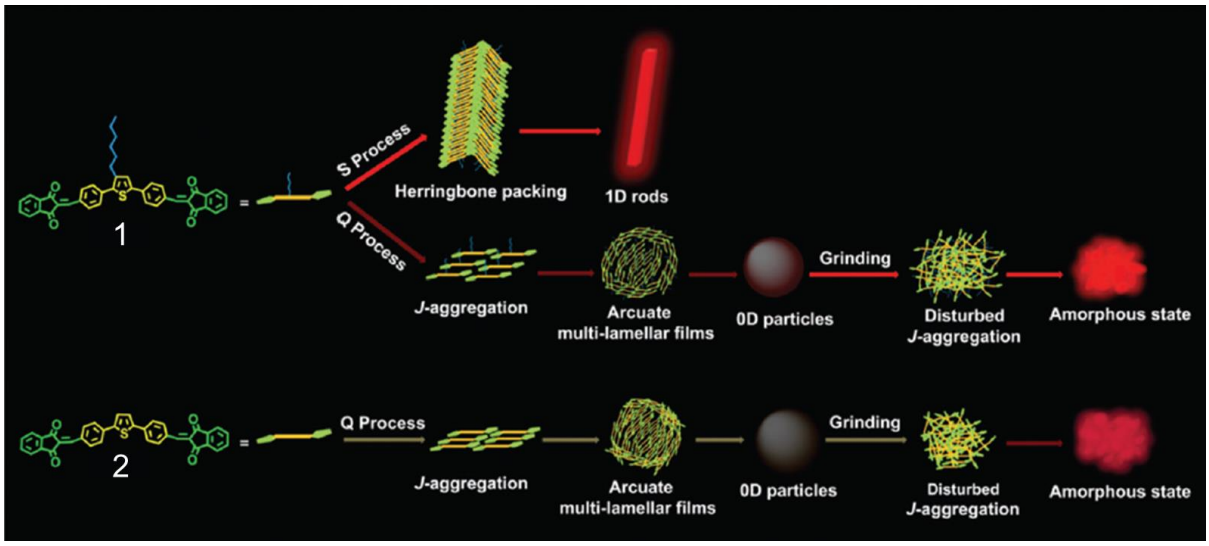

Figure 4.1. Proposed self-assembly processes and mechanoresponsive luminescence turn-on mechanism in compound **1** and **2**. (Adapted from reference 45)

penetrate greater depths due to the low scattering of NIR emissions.[39-44] Recently, advancements have been made in the realm of NIR-emitting, mechanoresponsive luminescent (MRL) 'turn-on' materials.

Guo's research group introduced new methodologies for creating such materials. Their work acknowledged the challenges posed by the often weakly emissive nature of NIR organic compounds in solid states, a result of strong dipole-dipole and π-π interactions. As a solution, they developed fluorophores with slightly or moderately twisted molecular geometry. The remarkable MRL 'turn-on' behaviors of these fluorophores can be attributed to the disruption of π-π interactions in *J*-aggregates of emission-quenched metastable structures.[45,46] **Figure 4.1** revealed the red/NIR mechanoresponsive luminescence turn-on in two diphenyl substituted thiophene derivatives (**1** and **2**). Chemical structure of the compound **1** and **2** varied only by the

presence of hexyl chain in **1**. Both the compounds were sensitive to the self-assembly process and two distinct film formation procedures were adopted to study the luminescence properties, such as fast evaporation (Q process) and slow recrystallization (S process) methods. Compound **1** formed a metastable assembly under Q process and upon mechanical grinding of 0D particles of this compound exhibited bright red luminescence turn-on. While under the S process, red emissive flocculent fibers were obtained, which were not mechanoresponsive. Similarly, under

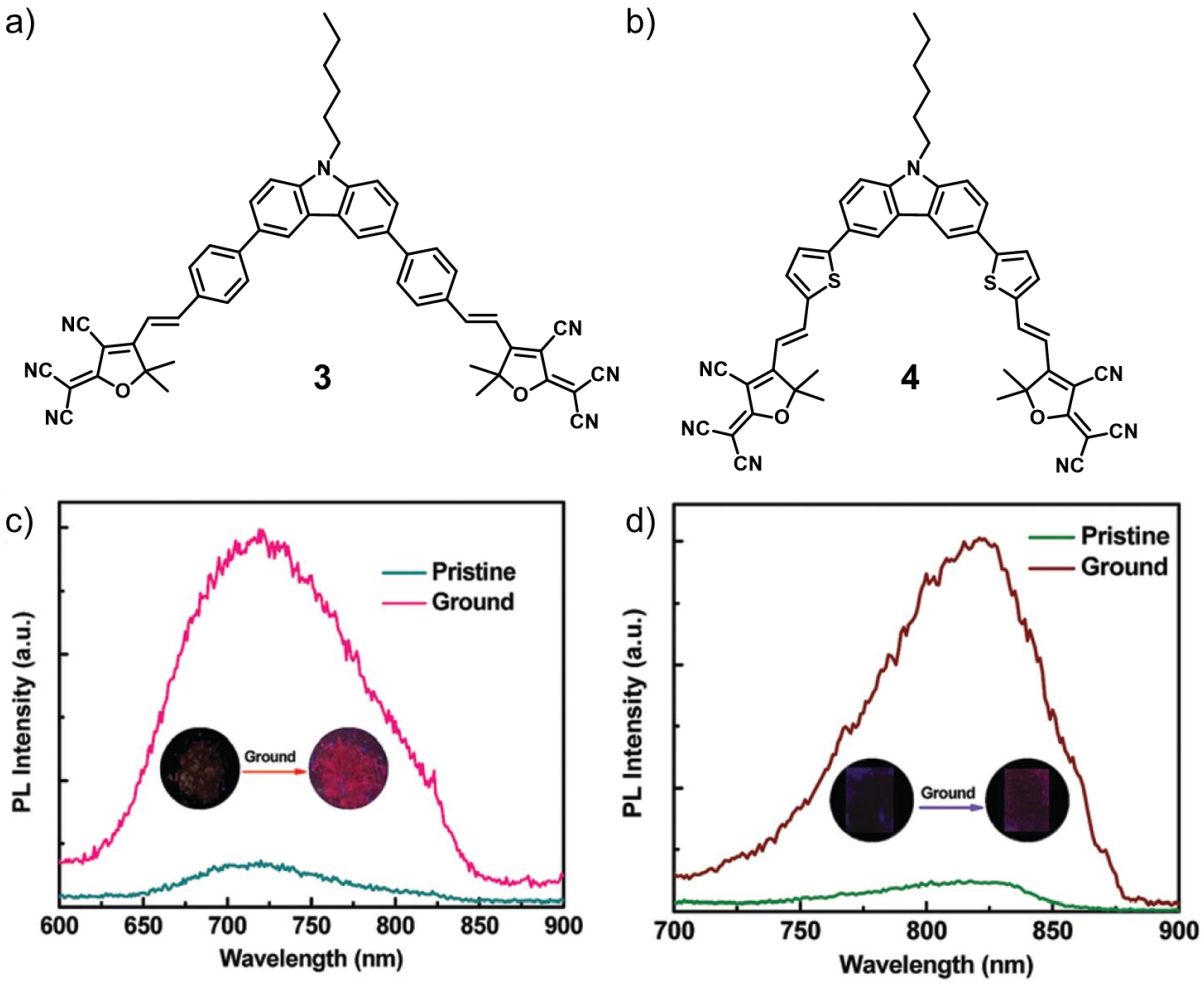

Figure 4.2. Chemical structure of compound a) **3** and b) **4**. Fluorescence spectra of the pristine and ground samples of c) **3** and d) **4**; inset: corresponding fluorescence images. (Adapted from reference 47)

the Q process, compound **2** formed metastable assembly and exhibited NIR mechanoresponsive luminescence turn-on. In the case of compound **2**, the molecule adopted a more planar conformation due to the absence of the hexyl chain and resulted in a redshifted emission that extended to the NIR region and more compact *J*-aggregates formed during the Q process. The plausible mechanism for this MRL turn-on behavior is shown in the **Figure 4.1** and by mechanically disrupting the non-emissive/weakly emissive metastable nanostructures produced emissive amorphous aggregates with disturbed *J*-aggregation.[45]

The same group proposed an alternative strategy aimed at achieving force-induced NIR emission 'turn-on'. This involved the development of two metal-free carbazole based organic fluorophores with ultrastrong dipole moments (**3** and **4**, **Figure 4.2a** and **4.2b**). Both the derivatives exhibited remarkable NIR mechanoresponsive luminescence turn-on behavior upon grinding. For compound **3** emission peak observed at 720 nm (**Figure 4.2c**), whereas maximum emission intensity positioned at 822 nm (**Figure 4.2d**) for compound **4** after mechanically grinding the pristine samples. Here, MRL 'turn-on' was realized by destabilizing dominant dipole-dipole interactions and activating radiative pathways upon mechanical grinding.[47]

While significant strides have been made in the field of MRL 'turn-on' materials, the development of such materials that emit in the NIR region and have fluorescence quantum yields of over 10% still faces hurdles. These challenges are primarily rooted in the complexities of molecular structural modification and the control of packing

motifs. In this study, we introduce two novel π-conjugated NIR fluorophores, exhibiting high contrast MRL 'turn-on' behavior with luminescence quantum yields exceeding 30%. Our strategy relies on generating metastable, kinetically trapped states of chromophores that are sensitive to their surrounding environment.[3,45-49] When a mechanical stimulus is applied, these metastable states transition into thermodynamically stable states, unveiling new emission characteristics. A comprehensive understanding of luminescence change has been achieved through precise correlation of optical, morphological, and structural properties. This study presents exciting pathway for the design and synthesis of new organic functional materials intended for high-contrast optical recording, mechanical force sensor, and security application.

4.3. Results and discussion

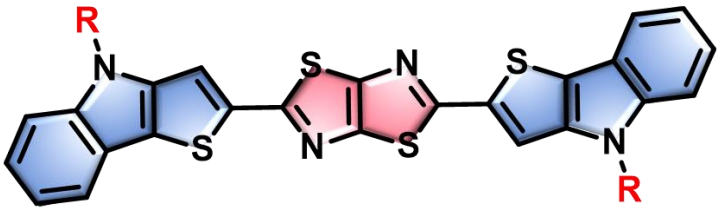

TiTz-1: R = CH_3

TiTz-6: R = C_6H_{13}

Figure 4.3. Chemical structures of the thienoindole-thiazolothiazole derivatives under study.

In this chapter, two donor-acceptor-donor (D-A-D) type chromophores were designed and synthesized. Both chromophores were structured utilizing thienoindole

as the donor unit and thiazolothiazole as the acceptor unit, forming the D-A-D configuration. The synthesized molecules, while bearing similar core structures, were distinguished by their differing side chains. Specifically, the first molecule (**TiTz-1**) was characterized by its methyl side chain. In contrast, the second molecule (**TiTz-6**), incorporates a hexyl side chain. These side chains play a crucial role in modifying the overall properties of the chromophores, especially, their solubility and processability. The molecular structures of **TiTz-1** and **TiTz-6** are depicted in **Figure 4.3**.

4.3.1. Synthetic strategy

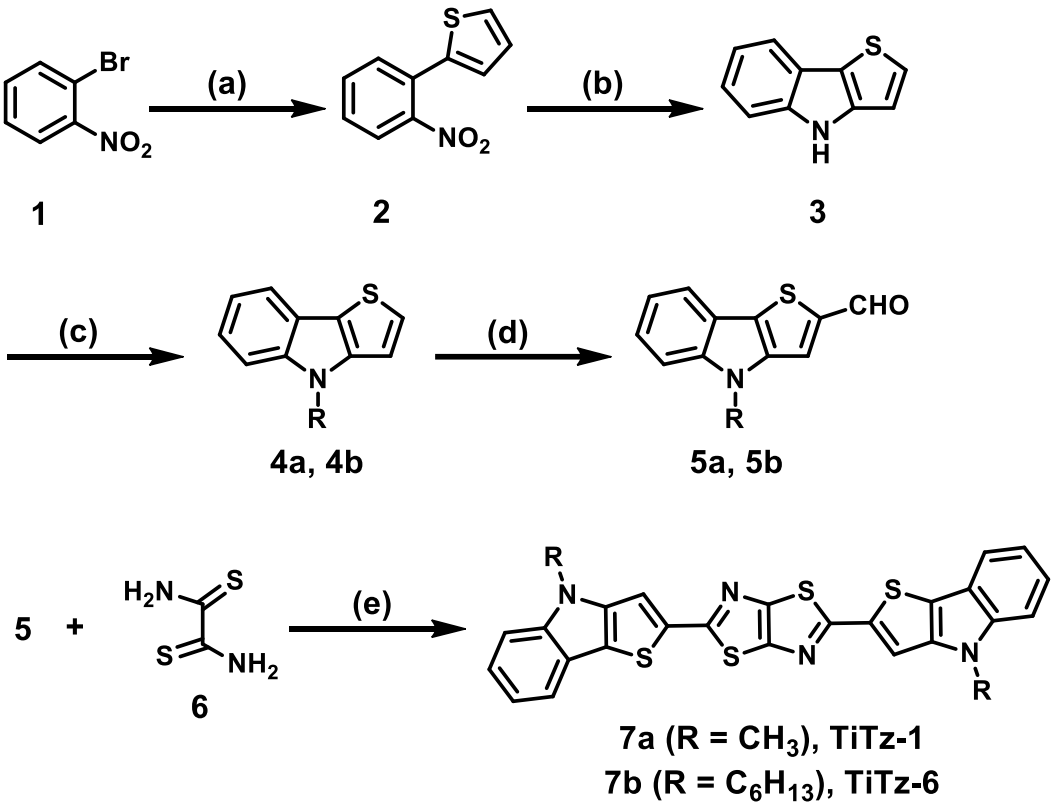

Scheme 4.1. *Reagents and conditions:* (a) Tributyl(thiophen-2-yl)stannane, $Pd(PPh_3)_4$, Toluene, 110 °C, 48h (b) PPh_3, 1,2-dichlorobenzene, Reflux, 12h (c) KOH, CH_3I/$C_6H_{13}Br$, Acetone, 5h (d) dry DCE, $POCl_3$, DMF, 70 °C, overnight (e) Nitrobenzene, 130 °C, 24h.[50-52]

The target compounds were synthesized *via* condensation reaction between *N*-alkylthienoindole-2-carbaldehyde and dithiooxamide. Details of the reagents and reaction conditions are shown in **Scheme 4.1**. All compounds were obtained in good yield and characterized by various analytical techniques such as, ^{1}H NMR, ^{13}C NMR and high-resolution mass spectrometry (HRMS). They were soluble in organic solvents like chloroform ($CHCl_3$), dichloromethane (CH_2Cl_2), tetrahydrofuran (THF), *N*,*N*-dimethylformamide (DMF) etc.

4.3.2. Density functional theory (DFT) calculations

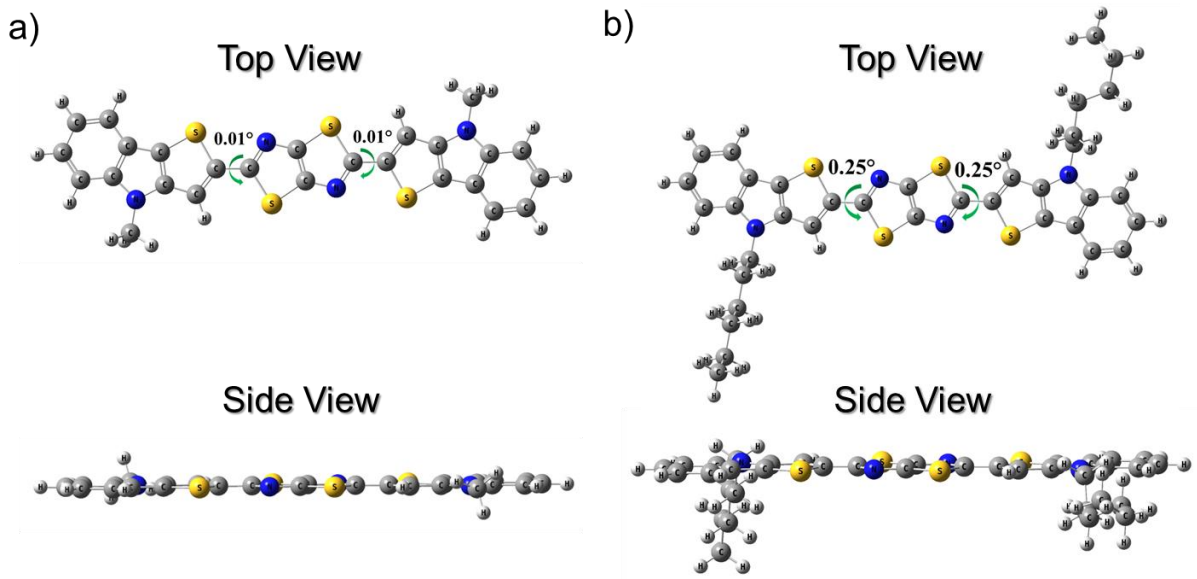

Figure 4.4. Geometrically optimized molecular structures of a) **TiTz-1** and b) **TiTz-6** obtained *via* DFT B3LYP/6-31G(d) calculations.

Energy optimized geometry of the molecules using density functional theory (DFT) calculations revealed that the both the molecules (**TiTz-1** and **TiTz-6)** adopted a nearly planar molecular conformation (**Figure 4.4a** and **4.4b**), which can facilitate

their aggregation and self-assembly under suitable conditions. Torsional angle about the carbon-carbon single bond between thiazolothiazole moiety and thienoindole moiety was calculated as 0.01° for **TiTz-1**, whereas 0.25° for **TiTz-6**. Two hexyl chains in the **TiTz-6** molecule are not in the same plane as that of the molecular backbone containing thiazolothiazole ring and thienoindole ring.

4.3.3. Photophysical properties in the solution state

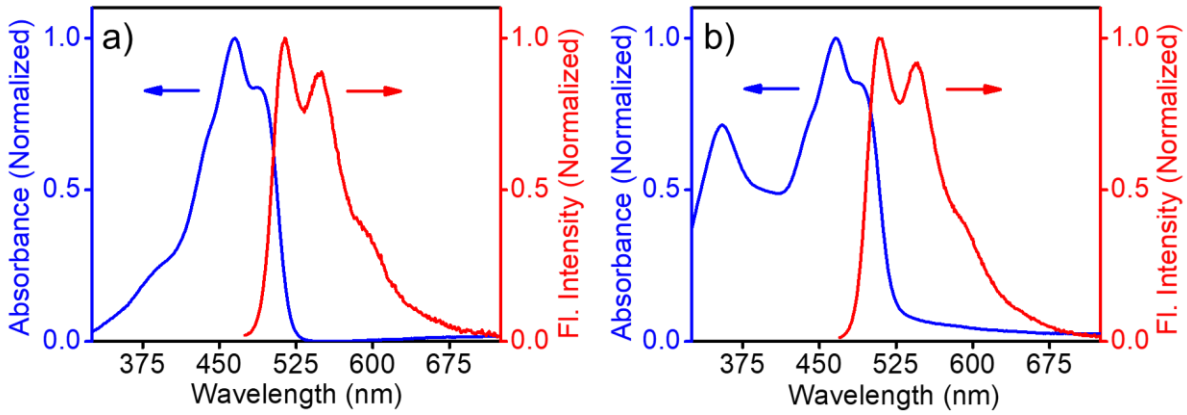

Figure 4.5. Normalized absorption and emission spectra of a) **TiTz-1** and b) **TiTz-6** in chloroform (conc. = 10^{-5} M, pathlength, *l* = 1 cm).

Figure 4.5a present the absorption and emission profiles of **TiTz-1** in chloroform. It exhibits vibrational features with an absorption maximum around 465 nm and a shoulder peak at 489 nm. Similar vibrational features were observed in the emission spectra, with an emission maximum at 514 nm and a shoulder peak at 548 nm. **TiTz-1** showed a fluorescence quantum yield of 42% in chloroform. Similarly, absorption, and emission features in chloroform for hexyl derivative (**TiTz-6**) is shown in the **Figure 4.5b**. Solution state properties of the both compounds exhibited negligible

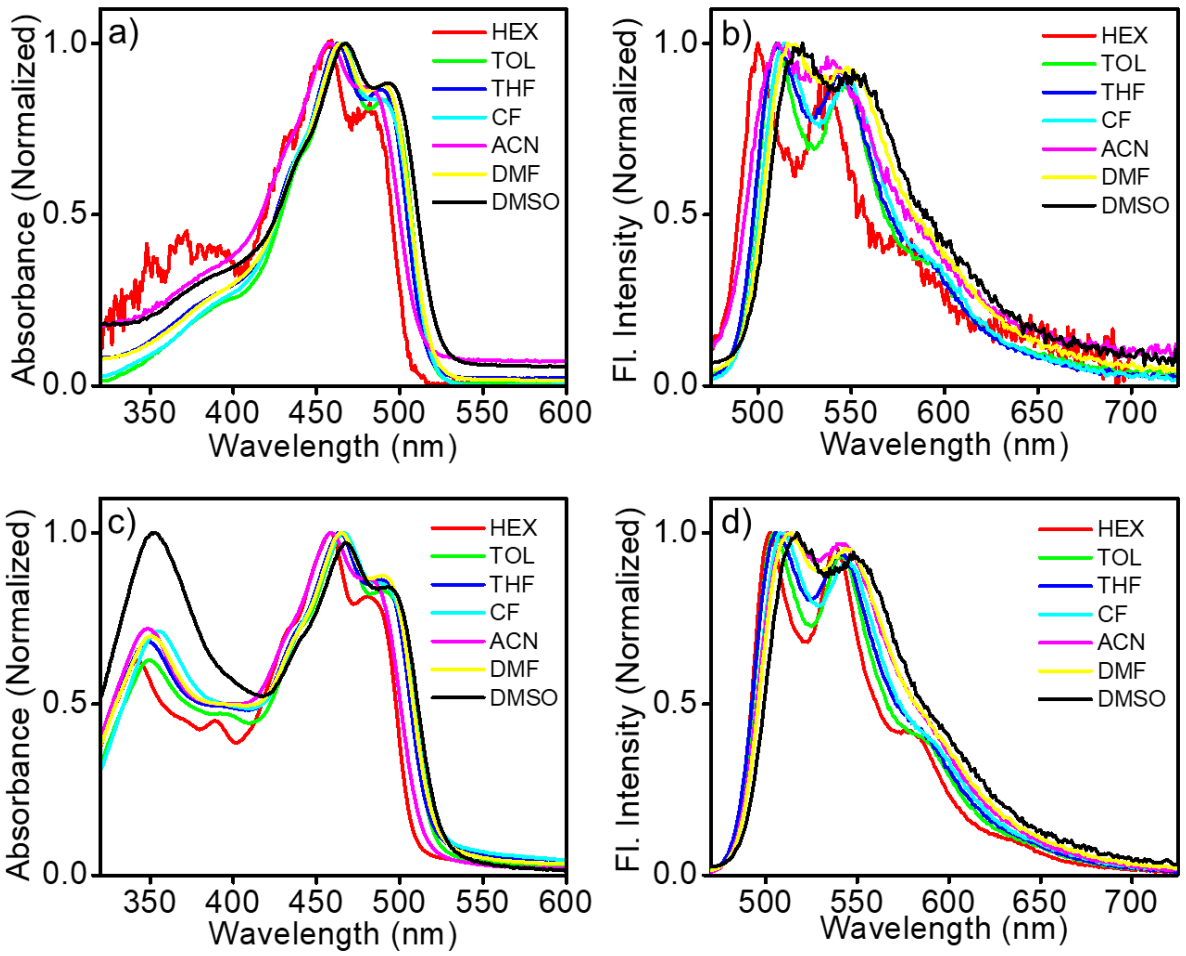

Figure 4.6. Normalized a, c) absorption spectra and b, d) emission spectra recorded in different solvents (conc. = 10^{-5} M; pathlength, *l* = 1 cm) for **TiTz-1** and **TiTz-6**.

changes. The hexyl derivative also exhibited vibrational features with an absorption maximum around 466 nm and shoulder peak at 490 nm. In the same way, vibrational features were observed in the emission spectra, with an emission maximum at 509 nm and a shoulder peak at 545 nm. **TiTz-6** showed a fluorescence quantum yield of 34% in chloroform. Further, we have recorded the absorption and emission of these compounds in various organic solvents. As the solvent polarity increased, a

significant red-shift was noted in the absorption and emission spectra, indicative of the molecules' charge transfer nature (**Figure 4.6**). A summary of the photophysical characteristics of **TiTz-1** and **TiTz-6** molecules in various solvents such as hexane, toluene, tetrahydrofuran (THF), chlororform ($CHCl_3$), acetonitrile (ACN), *N*,*N*-dimethylformamide (DMF), dimethylsulfoxide (DMSO) are summarized in the **Table 4.1**. It is noted that the variation in alkyl chain length did not have any significant impact on the photophysical properties of molecules in solution.

Table 4.1. Photophysical parameters of **TiTz-1** and **TiTz-6** in various solvents.

Compound	Solvent	λ_{abs} (nm)	λ_{em} (nm)
TiTz-1	Hexane	458, 482	500, 536
	Toluene	465, 492	510, 546
	THF	463, 489	511, 543
	$CHCl_3$	465, 489	514, 548
	ACN	458, 482	511, 546
	DMF	464, 490	518, 549
	DMSO	467, 495	521, 551
TiTz-6	Hexane	458, 480	502, 538
	Toluene	466, 490	505, 541
	THF	464, 490	506, 540
	$CHCl_3$	466, 490	509, 545
	ACN	458, 483	512, 542
	DMF	465, 491	514, 545
	DMSO	468, 494	517, 548

4.3.4. Aggregation-caused quenching effect in THF-H_2O mixture

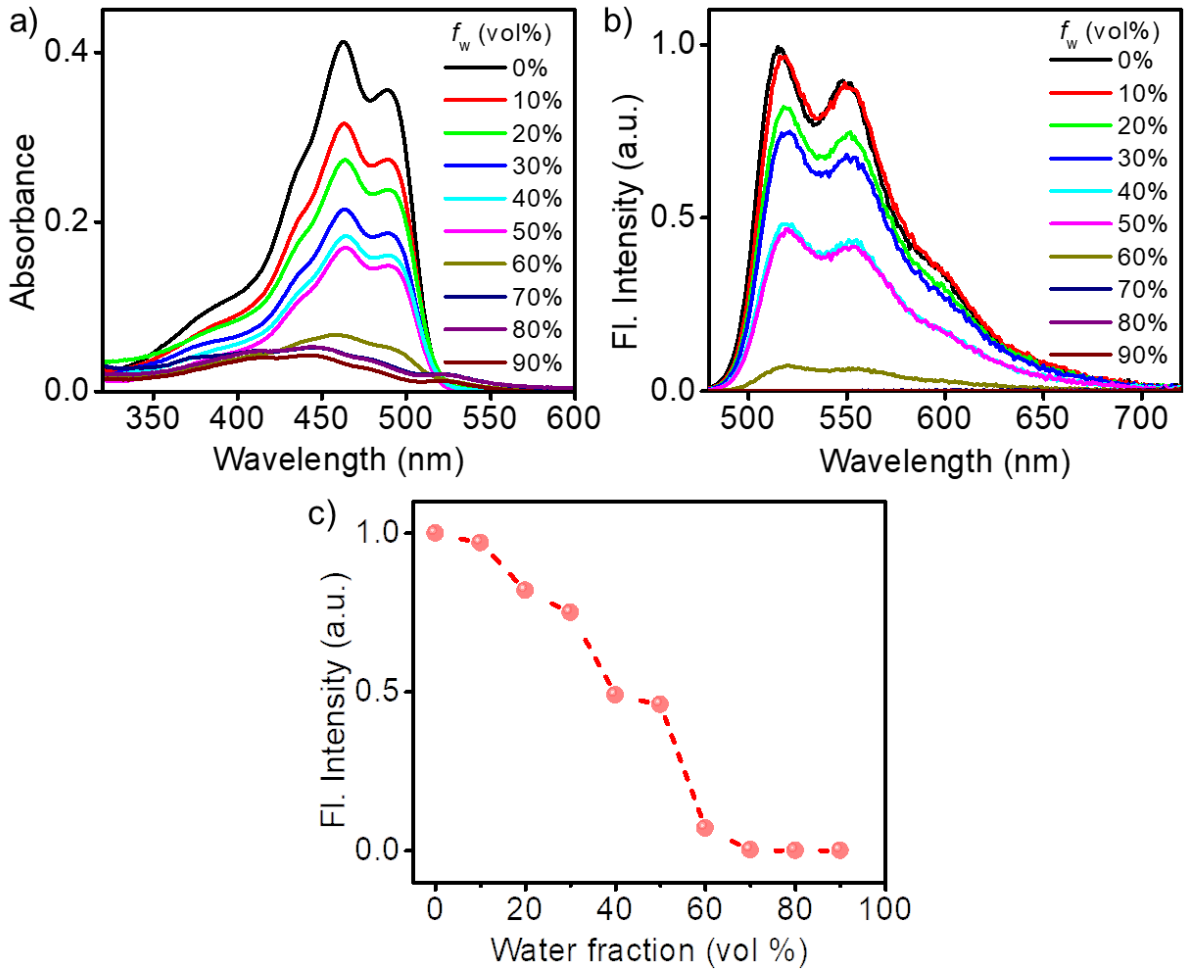

Figure 4.7. Aggregation behavior of **TiTz-1** (10^{-5} M) in THF/H_2O mixture with different water fractions: a) UV-Vis absorption spectra b) fluorescence spectra and c) effect of water fractions on the fluorescence intensity.

The fluorescence behaviors of **TiTz-1** and **TiTz-6** in their aggregated state were studied in THF/H_2O mixture with different water fractions (0-90% of water; **Figure 4.7** and **4.8**). The emission intensity of **TiTz-1** and **TiTz-6** were evidently decreased at higher water fractions, suggesting the aggregation-caused quenching (ACQ) effect. In the case of **TiTz-1**, when the water fraction (f_w) was increased to 80% and 90%, the

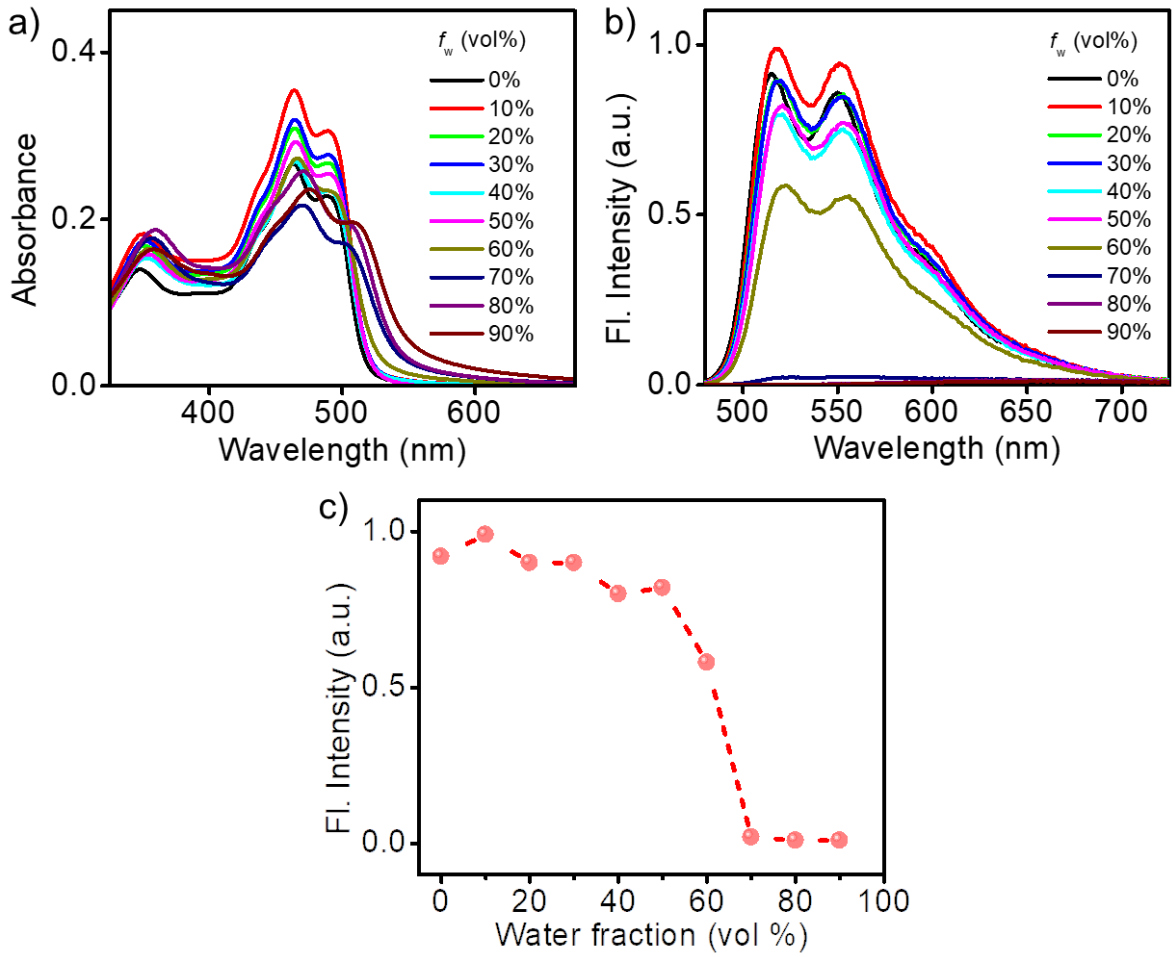

Figure 4.8. Aggregation behavior of **TiTz-6** (10^{-5} M) in THF/H_2O mixture with different water fractions: a) UV-Vis absorption spectra b) fluorescence spectra and c) effect of water fractions on the fluorescence intensity.

absorption spectra showed notable changes and leveled off tails visibly appeared in the longer wavelength region (**Figure 4.7a**). This can be ascribed to the well-known Mie scattering caused by nanosized particles, which indicates that **TiTz-1** molecules aggregate in higher water fractions. The red-shifts in the absorption when f_w reaches 90% indicate that *J*-aggregations may occur. Besides, the emission intensity of the **TiTz-1** was evidently decreased at higher water fractions (**Figure 4.7b** and **4.7c**),

suggesting aggregation-caused quenching (ACQ) effect. For **TiTz-1** with a planar skeleton, the π–π interactions primarily contributed to aggregates due to the reduced steric hindrance, resulting in fluorescence quenching. This ACQ behavior may be attributed to the unfavorable π–π interactions between the molecules in the *J*-aggregates. During addition of H_2O to THF solution, the aggregates precipitated rapidly from their molecularly dissolved state, forming kinetically stable arrangements. Like **TiTz-1**, the hexyl derivative exhibited ACQ behavior as well and the corresponding absorption, fluorescence, and effect of water fractions on the fluorescence intensity of **TiTz-6** (10^{-5} M) in THF/H_2O mixture with different water fractions are shown in the **Figure 4.8**. When the water fraction (f_w) of **TiTz-6** solution increased to 70%, 80%, and 90%, obsevations similar to **TiTz-1** were noticed in the absorption and emission features.

4.3.5. Mechanoresponsive luminescence turn-on

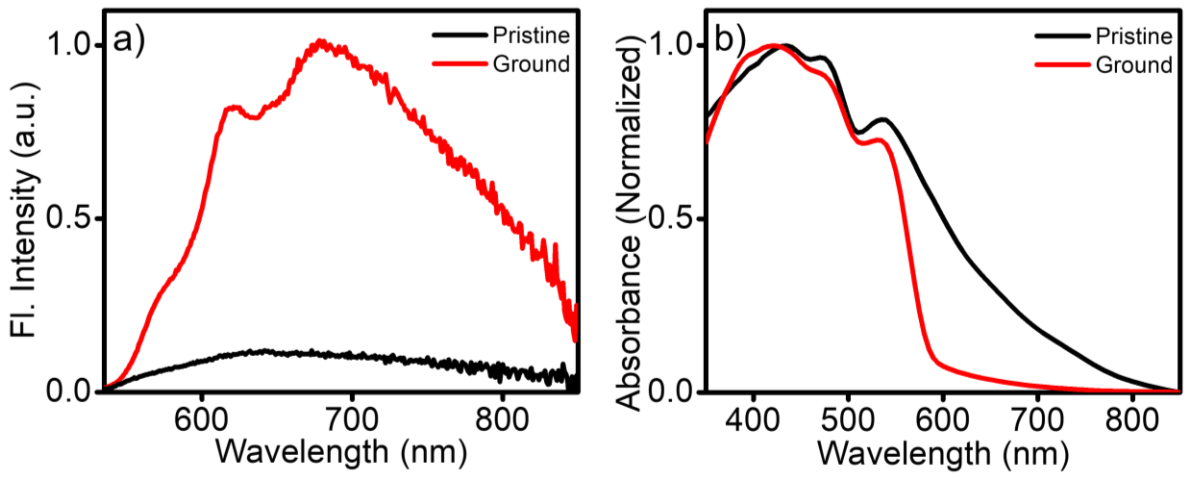

Figure 4.9. a) Photoluminescence, and b) normalized absorption spectra of the pristine and ground samples of **TiTz-1**.

The pristine powder sample of **TiTz-1** was obtained by the evaporation of CH_2Cl_2 solvent. In the solid state, pristine sample of **TiTz-1** was weakly luminescent with a broad emission covering the wavelength range from 500-900 nm (λ_{em} = 620 nm) and has a fluorescence quantum yield of 1.4%. Upon grinding with a pestle, it showed a remarkable enhancement in the fluorescence intensity (λ_{em} = 680 nm) with 22-fold increase in quantum yield (Φ_F = 31.3%), indicating a high-contrast red/NIR luminescence turn-on behavior response to mechanical stimulus. The fluorescence spectra of both pristine and ground samples are shown in **Figure 4.9a**. Corresponding changes were observed in the absorption spectra also, as depicted in **Figure 4.9b**. The absorption spectra of the pristine sample showed a broad absorption from 350-800 nm, indicating the strong intermolecular charge transfer and π–π interactions. After being ground, absorption band of the ground sample converted to the narrow band

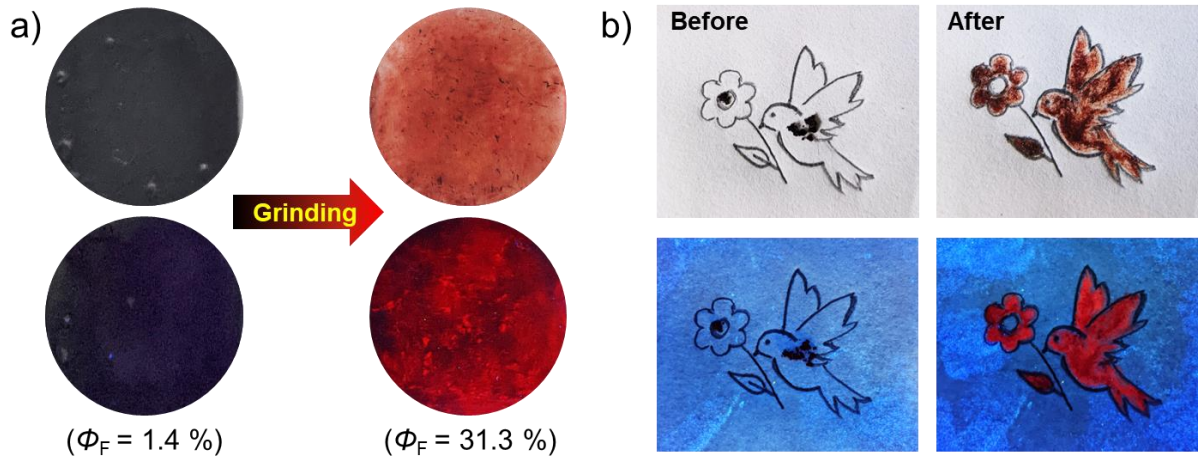

Figure 4.10. a) Photographs of **TiTz-1** before and after grinding, and b) images of force drawing on pristine powder of **TiTz-1** on filter paper taken under ambient light (top) and 365 nm UV light (bottom).

extending up to 600 nm, which clearly indicated the weakened π–π and charge transfer interactions.

The photographs of the samples under room light and 365 nm UV light provided the visual evidence for the color and luminescence changes, respectively, on applying mechanical stimuli (**Figure 4.10a**). The pristine sample was greyish-black in color under room light, which become brownish-red after applying mechanical force. The pristine sample was non-emissive under 365 nm UV light, exhibited an intense red fluorescence on applying mechanical force. This MRL 'turn-on' behavior positions the material as a promising candidate for sensitive, high-contrast optical recording systems and mechanical sensing systems. A simple demonstration of this was performed by spreading the solid sample of **TiTz-1** on a filter paper; after grinding the

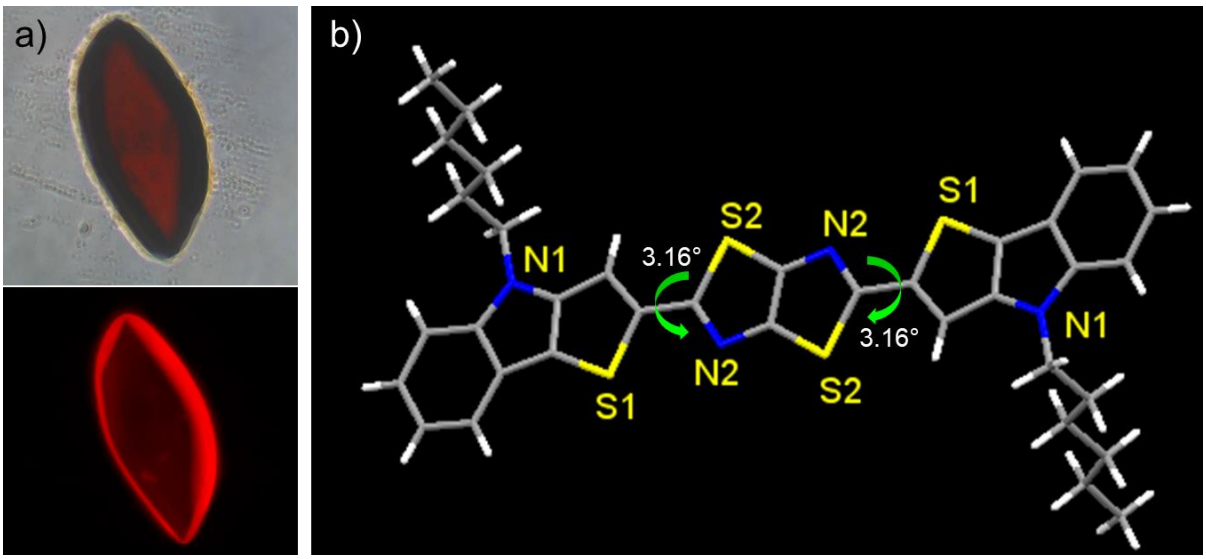

Figure 4.11. a) Microscopic images of the single crystal of **TiTz-6** under ambient (top) and 568 nm (bottom) light. b) The crystal structure of **TiTz-6** obtained from the single-crystal X-ray diffraction analysis.

spreaded powder with the tip of a spatula, the color change and the luminescence turn-on became apparent, distinguishing itself from the background under room light and 365 nm UV light (**Figure 4.10b**).

To establish a correlation between the color/luminescence switching and the chromophore packing, we tried to make single crystals of **TiTz-1**. Though a variety of attempts were made, we failed to obtain single crystals due to the poor solubility of the molecule in most of the common organic solvents and solvent mixtures. Subsequently, we synthesized **TiTz-6**, the same chromophore unit attached with hexyl chain. The presence of longer hexyl chains instead of the shorter methyl chains imparted solubility to the molecule in common organic solvents. Single crystals of **TiTz-6** were obtained through the slow evaporation of its saturated solution in a 1:1 volume ratio of $CHCl_3$/THF. **TiTz-6** crystallizes into a triclinic crystal system with the space group *P*-1, consisting of two molecules per unit cell. Crystal data and structure refinement details of **TiTz-6** crystal is provided in the **Table 4.2**. The obtained crystals of **TiTz-6** were brownish-red in color with bright red luminescence (**Figure 4.11a**). The structure of the molecule obtained from the single-crystal X-ray diffraction (SCXRD) analysis is shown in **Figure 4.11b**. The SCXRD analysis revealed the nearly planar conformation of the molecular backbone with ~3° of torsion between the central thiazolothiazole unit and the end group (**Figure 4.11b**), which is in tune with the theoretical calculations.

Table 4.2. Crystallographic data of **TiTz-6**.

Sample	**TiTz-6**	
Empirical formula	C36H36N4S4	
Formula weight	652.93	
Temperature	297(2) K	
Wavelength	1.54178 Å	
Crystal system	Triclinic	
Space group	*P*-1	
Unit cell dimensions	a = 9.7796(2) Å	α = 71.2420(10)°
	b = 12.5584(3) Å	β = 74.9910(10)°
	c = 15.4380(3) Å	γ = 69.995(2)°
Volume	1663.19(7) $Å^3$	
Z	2	
Density (calculated)	1.304 Mg/m^3	
Absorption coefficient	2.866 mm^{-1}	
F(000)	688	
Crystal size	0.082 x 0.042 x 0.029 mm	
Theta range for data collection	3.066 to 68.942°	
Index ranges	-11<=h<=11, -15<=k<=15, -18<=l<=18	
Reflections collected	51834	
Independent reflections	6093 [R(int) = 0.0998]	
Completeness to theta = 67.679°	99.5 %	
Absorption correction	Semi-empirical from equivalents	
Max. and min. transmission	0.7531 and 0.6430	
Refinement method	Full-matrix least-squares on F^2	
Data / restraints / parameters	6093 / 83 / 453	
Goodness-of-fit on F^2	1.091	
Final R indices [I>2sigma(I)]	R1 = 0.0873, wR2 = 0.2427	
R indices (all data)	R1 = 0.1681, wR2 = 0.3475	
Extinction coefficient	0.0024(9)	
Largest diff. peak and hole	0.779 and -0.338 $eÅ^{-3}$	

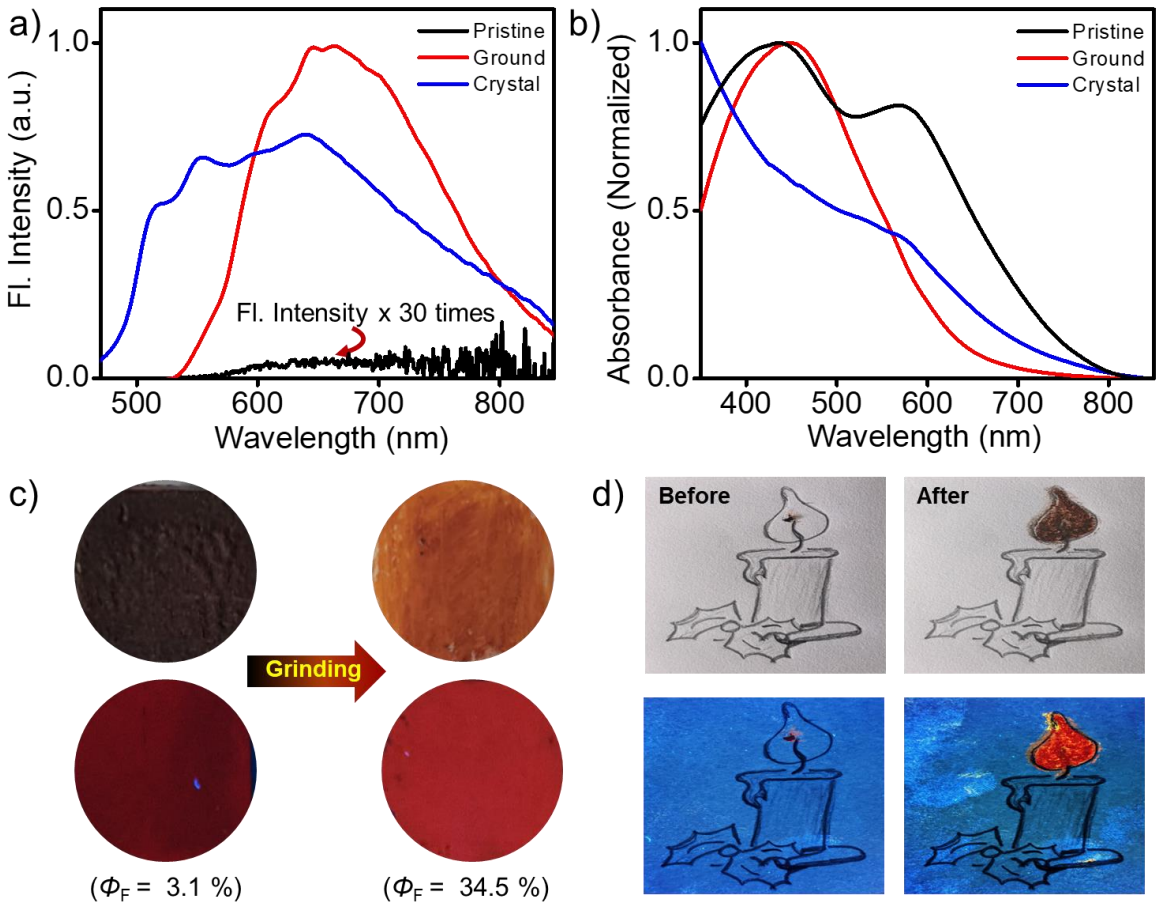

Figure 4.12. a) Photoluminescence, and b) normalized absorption spectra of pristine, ground, and crystal samples of **TiTz-6**. c) Photographs of **TiTz-6** before and after grinding, and d) images of force drawing on pristine powder of **TiTz-6** on filter paper taken under ambient light (top) and 365 nm UV light (bottom).

As in the case of **TiTz-1**, **TiTz-6** also exhibited prominent NIR MRL turn-on behavior, which revealed the intense NIR MRL turn-on at ~665 nm with a 11-fold higher quantum yield value (Φ_F = 34.5%) than that of the pristine sample, which is weakly emitting at ~660 nm with 3.1% quantum yield (**Figure 4.12a**). Corresponding absorption spectra of the pristine and ground samples showed broad and narrow bands respectively (**Figure 4.12b**). Photographic images of the pristine and ground samples

are provided in the **Figure 4.12c** and the images of force drawing on pristine powder of **TiTz-6** on filter paper are given in **Figure 4.12d** under room light (top) and 365 nm UV light (bottom). Interestingly, the emission and absorption features obtained for **TiTz-6** crystal is comparable with that of the ground form (see **Figure 4.12a** and **4.12b**). However, emission spectrum of ground sample is slightly redshifted from the crystal emission. Under mechanical grinding molecule underwent planarization, which in turn yield enhanced effective conjugation length and hence a bathochromic shift in the emission spectrum. Both the compounds, **TiTz-1** and **TiTz-6** act in a similar way except for a 20 nm red-shifted NIR MRL turn-on in the case of **TiTz-1**. This can be attributed to the presence of methyl chains (short alkyl chain) in **TiTz-1**; thus **TiTz-1** adopted a more planar conformation compared to the **TiTz-6** with hexyl chains (long alkyl chain). Single crystal X-ray investigations and DFT calculations of **TiTz-6** confirmed the slight deviation from the planar structure (See **Figure 4.11b** and **Figure 4.4b**) compared to methyl derivative.

Further, we looked into the molecular packing of **TiTz-6** in the crystal lattice for better understanding of the MRL behavior. The asymmetric unit of **TiTz-6** contains two crystallographically distinct molecules with conformational changes in the alkyl chain in nearly perpendicular manner to each other and **Figure 4.13a** shows the unit cell of **TiTz-6** with crystallographically distinct molecules in different color (blue and green). Distance between the two adjacent molecules having similar crystallographic symmetry were measured and confirmed that there are no π–π and intermolecular

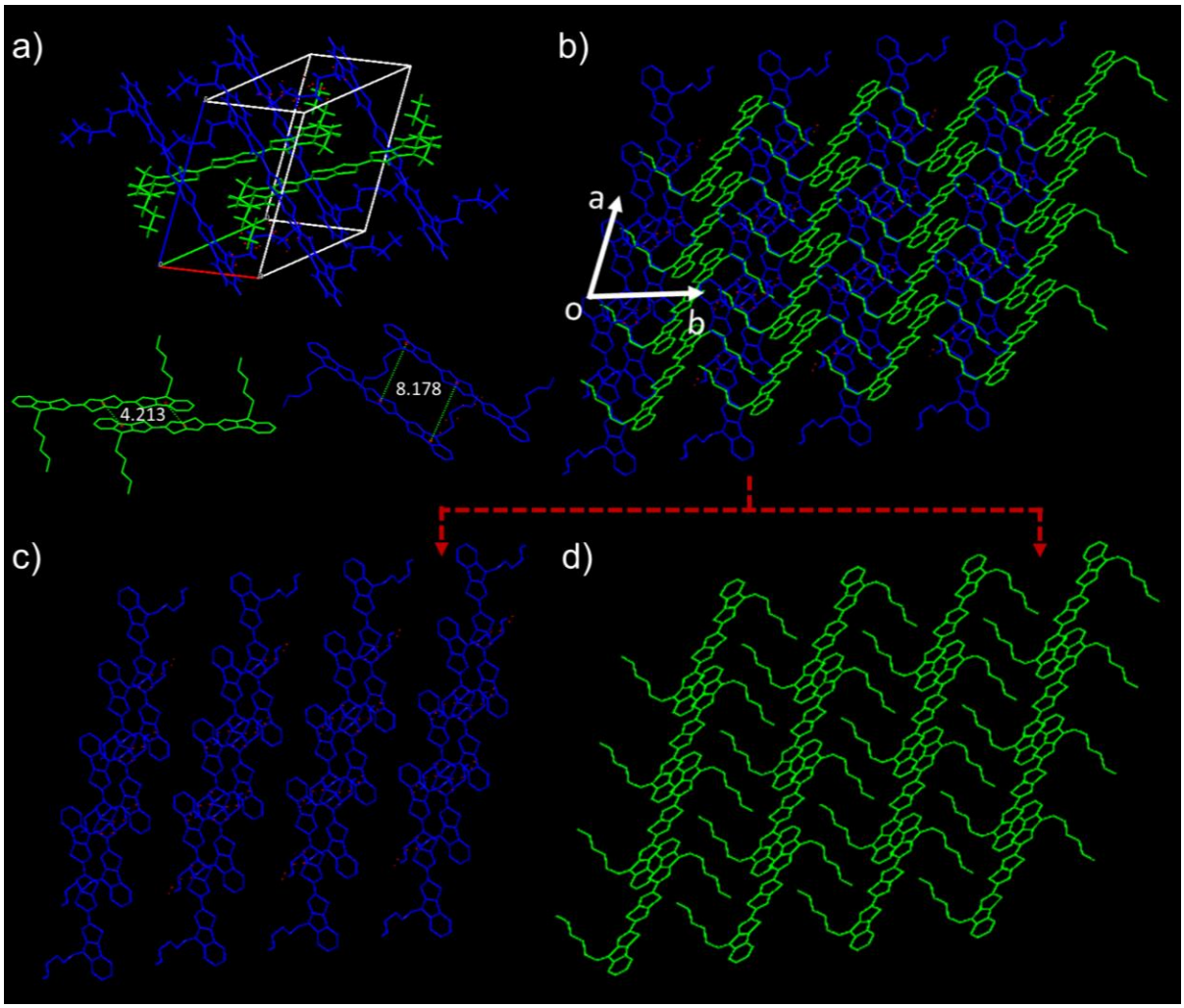

Figure 4.13. Molecular packing of **TiTz-6** in crystal lattice: a) Unit cell with crystallographically distinct molecules in different colors (blue and green); distance between two adjacent crystallographically similar molecules stacked along the crystallographic *c*-axis (green) and *a*-axis (blue). b) Packing of the asymmetric unit in the crystal structure, for clarity stacking of these two crystallographically distinct molecules shown separately (c, d).

charge transfer interaction. The distance between two adjacent symmetry equivalent molecules in green color is 4.2 Å and 8.2 Å for the blue colored adjacent molecules (**Figure 4.13a**). Molecular arrangement in the crystal lattice show that two crystallographically distinct molecules stack in two different directions, one along the

a-axis (blue) and other along the *c*-axis (green) resulting in a staggered arrangement (**Figure 4.13b**). The non/weak emission in the pristine state is attributed to the strong donor-acceptor interactions resulting in intermolecular charge transfer state. While, the intense emission of the ground sample is from the locally-excited (LE) state due to the weakened intermolecular interactions in the ground state. This aspect is confirmed through the SCXRD analysis of the **TiTz-6** crystal, whose emission is comparable to the ground state. Crystal structure investigations revealed that there are no donor-acceptor π–π interactions is observed in the crystal lattice. The molecules along the *c*-axis have a very weak donor-acceptor interaction with a slipped stacked structure (green color, see **Figure 4.13b** and **4.13d**) and there are no interaction between the adjacent molecules in the molecular stack along the *a*-axis (blue color, see **Figure 4.13b** and **4.13c**). The solid-state absorption spectrum of the **TiTz-6** in pristine and ground state further validate this aspect. The broad absorption features of pristine form extending to the longer wavelengths (λ_{onset} = 765 nm, see **Figure 4.12b**) indicates strong intermolecular charge transfer and π–π interactions. Whereas, ground sample displayed a narrow absorption band (λ_{onset} = 630 nm, see **Figure 4.12b**) with a blueshift from the pristine form signifying the diminished intermolecular interactions and the absence of CT state.

To establish a correlation between the color/luminescence switching and the self-assembly process, films of **TiTz-1** were prepared using both fast and slow evaporation methods. Two types of films were fabricated: a fast-evaporated film from

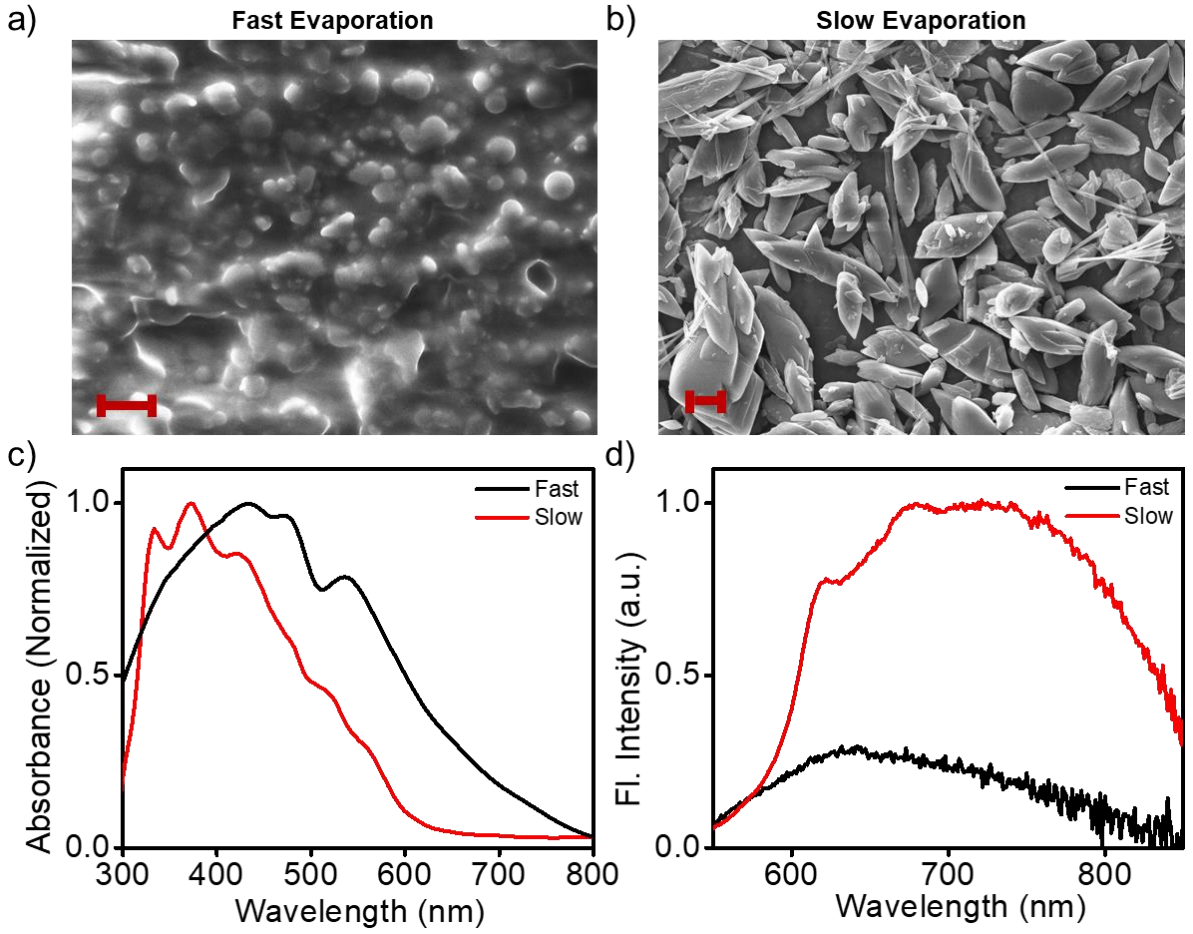

Figure 4.14. SEM images of the a) fast and b) slow evaporated films (scale bar represents 6 μm) of **TiTz-1**. c) Normalized absorption and d) emission of fast and slow evaporated films of **TiTz-1**.

a dichloromethane solution (quick aggregation of the chromophores), and a slow-evaporated film from a tetrahydrofuran solution (slow aggregation of the chromophores). Distinct morphologies of the samples under these different fabrication methods were revealed through scanning electron microscopy (SEM) images. Fast evaporation resulted in a featureless aggregate (**Figure 4.14a**), while slow evaporation led to the formation of well-defined, leaf-like aggregates (**Figure 4.14b**). The fast-evaporated film exhibit very broad absorption extending up to the longer wavelengths

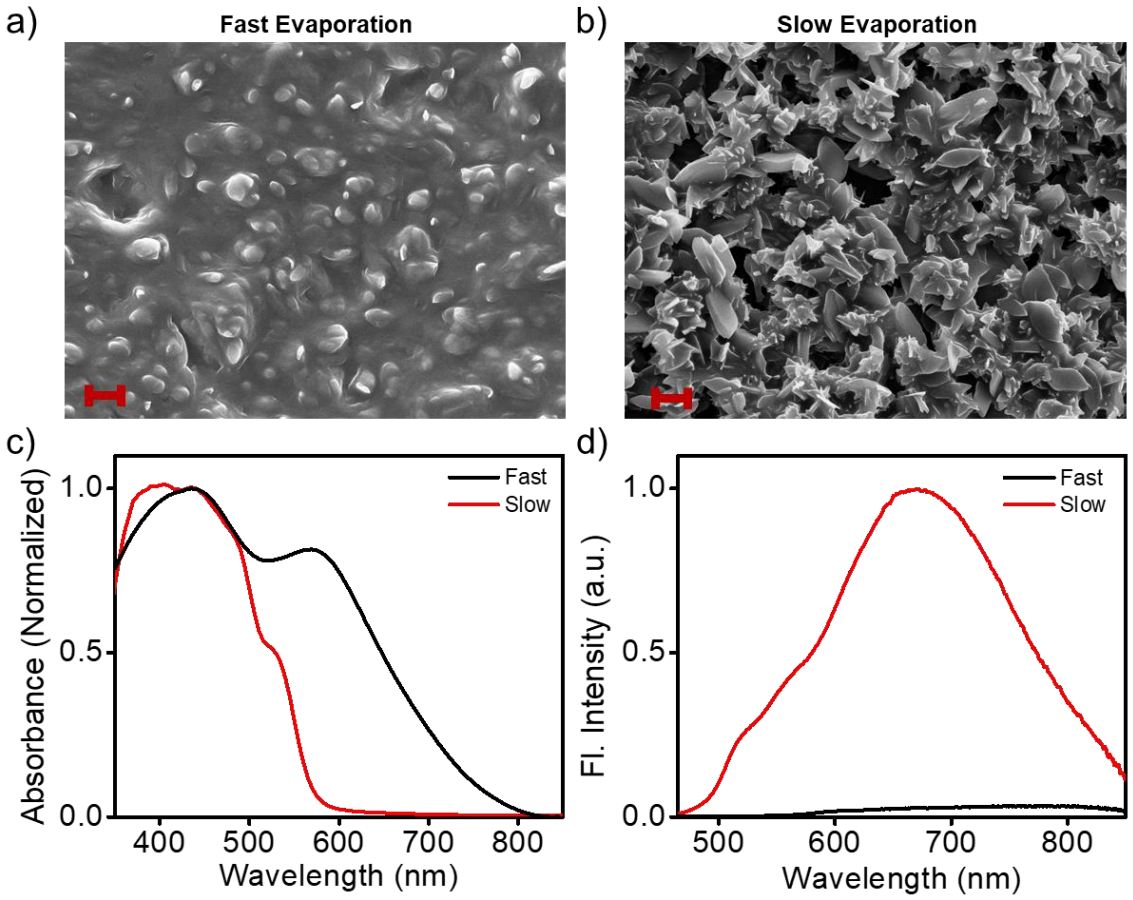

Figure 4.15. SEM images of the a) fast and b) slow evaporated films (scale bar represents 4 μm) of **TiTz-6**. c) Normalized absorption and d) emission of fast and slow evaporated films of **TiTz-6**.

(~800 nm), similar to the pristine sample discussed earlier. Conversely, the slow-evaporated film displayed a narrow absorption centered at 375 nm, akin to the ground sample previously discussed. **Figure 4.14c** presents the corresponding absorption spectra. The fluorescence profile of these two films exhibited notable changes in the NIR range. The fast evaporated film is weakly emissive with a broad emission centered at ~640 nm, while slow evaporated one exhibits higher emission intensity with maximum centered at ~720 nm (**Figure 4.14d**). The fast-evaporated sample's

emission spectrum was similar to the pristine sample, while the slow-evaporated sample's emission was more akin to the ground sample. These observations suggest that the fast evaporation process encourages morphology and structures associated with a metastable yet kinetically favored high-energy state, while molecules tend towards a thermodynamically stable morphology and packing conformation with slow solvent evaporation.

Compound **TiTz-6** also exhibit sensitivity towards the aggregation/self-assembly process like **TiTz-1**. Thus, similar kind of results were obtained for **TiTz-6** derivative as well. For **TiTz-6**, two types of films were obtained with fast and slow evaporation approaches and scanning electron microscopy (SEM) images revealed the different morphologies of the samples under distinct fabrication methods (**Figure 4.15a** and **4.15b**). The fast and slow evaporated films have broad and narrow absorption features respectively (**Figure 4.15c**) as observed in the case of **TiTz-1**. In the same way, fluorescence profile of these two films exhibited notable changes in the NIR range. The fast evaporated film is weakly/non emissive, while slow evaporated one exhibits higher emission intensity with maximum centered at ~ 670 nm (**Figure 4.15d**). These results state that the self-assembly process plays a key role in controlling the molecular arrangement of the **TiTz** chromophores, hence leading to distinct fluorescence ‘‘on’’ or ‘‘off’’ characteristics.

Based on all these results, the plausible molecular assembly mechanism of the metastable pristine sample and the mechanoresponsive NIR luminescence turn-on for

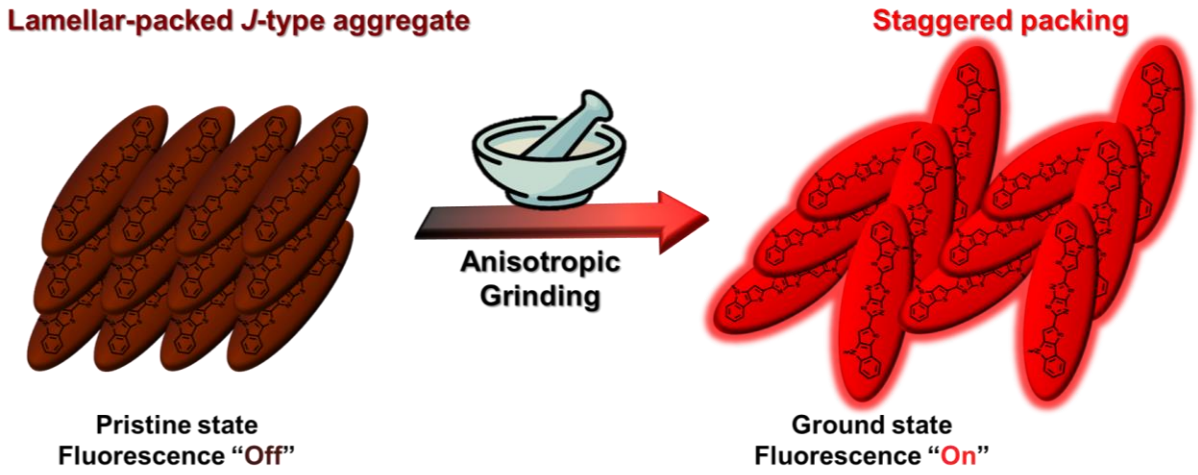

Figure 4.16. Schematic representation of the proposed stimuli-responsive molecular rearrangement upon anisotropic grinding.

TiTz-1 and **TiTz-6** derivatives are proposed and illustrated in **Figure 4.16**. During the fast evaporation process (pristine sample), the π–π and intermolecular charge transfer interactions of the chromophores played a major role to form CT mediated lamellar-packed *J*-type aggregates, resulting in an emission quenched state. Under mechanical grinding, this metastable packing was disturbed and led to a more stable staggered arrangement of the D-A-D molecules, which resulted in a strongly emissive state. In this staggered assembly, there is no π–π and intermolecular charge transfer interactions observed which results in suppression of non-radiative path and activation of radiative decay, thereby leading to the remarkable MRL turn-on.

4.3.6. AFM nanoindentation

Further, we investigated their mechanical properties by nanoindentation measurement.[53,54] Using atomic force microscope (AFM), the mechanical properties

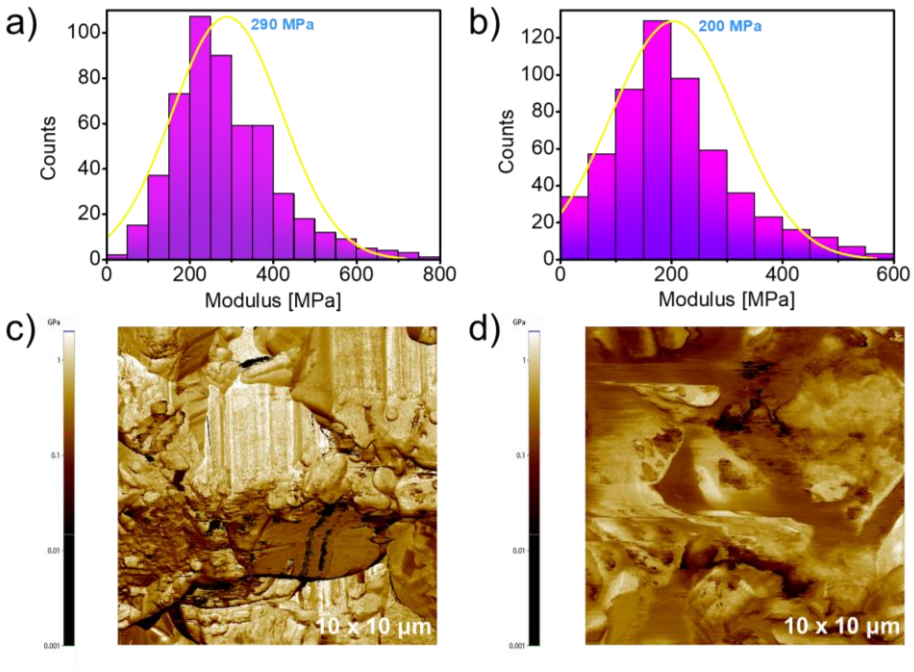

Figure 4.17. Mechanical properties of a) **TiTz-1** and b) **TiTz-6** films on glass substrate studied by nanoindentation measurement (histogram of calculated Young's modulus). Modulus maps of c) **TiTz-1** and d) **TiTz-6** films on glass substrate.

of the particles can be quantified, indentations (pinpoint nanomechanical) in the pristine samples of **TiTz-1** and **TiTz-6** were carried out. The results given in **Figure 4.17a** and **4.17b** showed the histograms of values of Young's modulus (corresponding modulus maps are shown in **Figure 4.17c** and **4.17d**), and the mean values obtained for both the samples are 290 MPa (**TiTz-1**) and 200 MPa (**TiTz-6**). The lower value for hexyl derivative compared to methyl derivative indicating that **TiTz-6** can be deformed in much easier way than that of **TiTz-1** in the presence of mechanical force. This can be attributed to the strong chromophore-chromophore interactions present in the **TiTz-1**, which is having more planar conformation and less steric effect than the

chromophore with hexyl side chains. Thus, the chemical environment affects the molecular packing/conformational state of the compounds and concomitantly the nanomechanical properties.[55]

4.4. Conclusions

In conclusion, we demonstrate that organic D-A-D π-conjugated systems with planar conformation can form distinct self-assembled states with different molecular packing and emission properties by controlling the mode of molecular packing. The developed two novel thiazolothiazole based fluorophores exhibited remarkable NIR MRL turn-on behavior with high contrast and fluorescence quantum yield. The rationale for this behavior involves the transformation from a metastable aggregation state to a more stable packing state by the application of mechanical stimulus. The present study provides a basic molecular strategy for the development of new π-conjugated luminophores with NIR mechano-responsive luminescence turn on characteristics, which have great potential for highly sensitive and high-contrast optical recording, bioimaging and security applications.

4.5. Experimental section

4.5.1. Materials and methods

The details of materials, measurements, UV-vis absorption spectrophotometer, spectrofluorimeter, scanning electron microscopy (SEM) and X-ray diffraction measurements are described in the section 2.5.1 of Chapter 2. The UV−vis spectra of

solid state samples were obtained using an Ocean Optics 124 UV−vis modular spectrometer (DH-2000-BAL). The fluorescence quantum yields in the solution state were determined relative to a standard compound, Rhodamine B in ethanol (ϕ_F = 0.5), using optically matching solutions. AFM (Nano indentation) measurements were done using Veeco Nanoscope III and Asylum MFP-3D AFM instruments. They were employed for extracting force–indentation curves in the contact mode as well as for imaging in the tapping mode. Forcemodulation silicon cantilevers were used with average spring constants of ≈1Nm^{-1} (Olympus AC240) and ≈3Nm^{-1} (Budget Sensor Multi75DLC). The typical tip speed for the indentation was 500 nm s^{-1} with a repeating frequency of 0.5 Hz.

4.5.2. Synthesis and characterization

Synthesis of 2-(2-nitrophenyl)thiophene (2). A mixture of tributyl (thiophen-2-yl)stannane (3.69 g, 9.90 mmol) and 1-bromo-2-nitrobenzene **1** (2.0 g, 9.90 mmol) was deaerated twice with argon followed by the addition of $Pd(PPh_3)_4$. After being stirred at 100 °C for 48 h under argon, the reaction mixture was poured into water and extracted with dichloromethane. The organic layer was washed with water and then dried over anhydrous Na_2SO_4. The crude product was purified by column chromatography on silica gel with hexane as the eluent to afford **2** as an oil (1.88 g, 92 %). ^{1}H NMR (500 MHz, $CDCl_3$) δ [ppm]: 7.74 (d, J = 8.5 Hz, 1H), 7.59-7.54 (m, 2H), 7.48-7.44 (m, 1H), 7.42-7.41 (dd, $J1$= 5 Hz, $J2$ = 1 Hz, 1H), 7.10-7.07 (m, 2H).

Synthesis of 4*H*-thieno[3,2-*b*]indole (3). A mixture of compound **2** (1.8 g, 8.77 mmol) and triphenylphosphine (6.9 g, 26.31 mmol) in 1,2-dichlorobenzene was refluxed for 12 h under nitrogen, then extracted with CH_2Cl_2. The organic layer was washed with brine and water and dried over anhydrous Na_2SO_4, filtered, and concentrated in vacuum. The crude product was purified by column chromatography on silica gel with CH_2Cl_2/n-hexane (10 %) as eluent to yield **3** as a white powder (1.14 g, 75%). ^{1}H NMR (500 MHz, $CDCl_3$) δ [ppm]: 8.21 (s, 1H), 7.75 (d, J = 8 Hz, 1H), 7.44 (d, J = 8Hz, 1H), 7.36 (d, J = 5.5 Hz, 1H), 7.27 (t, J = 7 Hz, 1H), 7.17 (t, J = 7 Hz, 1H), 7.08 (d, J = 5 Hz, 1H).

Synthesis of 4-methyl-4*H*-thieno[3,2-*b*]indole (4a). The mixture of compound **3** (1.0 g, 5.77 mmol) and potassium hydroxide (3.24 g, 57.7 mmol) was dissolved in acetone (10 mL). Then iodomethane (0.72 mL, 11.54 mmol) was added to the mixture. The mixture was stirred for 5 h. After the reaction finished, the reactant was extracted with CH_2Cl_2. The organic layer was washed with brine and water and dried over anhydrous Na_2SO_4, then filtered and concentrated in a vacuum. The crude product was purified by column chromatography on silica gel with hexane as the eluent to afford **4a** as a white crystalline powder (1.01 g, 75%). ^{1}H NMR (500 MHz, $CDCl_3$) δ [ppm]: 7.75 (d, J = 8 Hz, 1H), 7.39-7.38 (m, 2H), 7.31 (t, J = 7.5 Hz, 1H), 7.18 (t, J = 7.5 Hz, 1H), 7.08 (d, J = 5Hz, 1H), 3.88 (s, 3H).

Synthesis of 4-hexyl-4*H*-thieno[3,2-*b*]indole (4b). The mixture of compound **3** (1.0 g, 5.77 mmol) and potassium hydroxide (3.24 g, 57.7 mmol) was dissolved in acetone

(10 mL). Then bromohexane (1.61 mL, 11.54 mmol) was added to the mixture. The mixture was stirred for 5 h. After the reaction finished, the reactant was extracted with CH_2Cl_2. The organic layer was washed with brine and water and dried over anhydrous Na_2SO_4, then filtered and concentrated in a vacuum. The crude product was purified by column chromatography on silica gel with hexane as the eluent to afford **4b** as a pale-yellow oil (1.10 g, 74%). ^{1}H NMR (500 MHz, $CDCl_3$) δ [ppm]: 7.73 (d, J = 8 Hz, 1H), 7.35 (d, J = 8 Hz, 1H), 7.31 (d, J = 5 Hz, 1H), 7.26 (t, J = 7.5 Hz, 1H), 7.14 (t, J = 7.5 Hz, 1H), 7.01 (d, J = 5Hz, 1H), 4.18 (t, J = 7.5 Hz, 2H), 1.81 (t, J = 7 Hz, 2H), 1.28 (t, J = 7.5 Hz, 6H), 0.85 (t, J = 7 Hz, 3H).

Synthesis of 4-methyl-4*H*-thieno[3,2-*b*]indole-2-carbaldehyde (5a). To a solution of **4a** (1.0 g, 5.35 mmol) and *N*,*N*-dimethylformamide (1.65 mL, 21.40 mmol) in 1,2-dichloroethane was slowly added $POCl_3$ (2 mL, 21.40 mmol) at 0 °C, and stirred for 1 h under argon. Then, the reaction mixture was allowed to heat to 60 °C and stirred overnight. The mixture was cooled to 0 °C and neutralized using $NaHCO_3$ (aq.). The organic layer was extracted using CH_2Cl_2 and dried over anhydrous Na_2SO_4 and concentrated in vacuum. The crude compound was purified by column chromatography on silica gel with CH_2Cl_2/n-hexane (40 %) as the eluent to afford **5a** as a pale-yellow powder (0.92 g, 80%). ^{1}H NMR (500 MHz, $CDCl_3$) δ [ppm]: 9.97 (s, 1H), 7.85 (d, J = 8 Hz, 1H), 7.75 (s, 1H), 7.47-7.41 (m, 2H), 7.23 (t, J = 7 Hz, 1H), 3.92 (s, 3H).

Synthesis of 4-hexyl-4*H*-thieno[3,2-*b*]indole-2-carbaldehyde (5b). To a solution of **4b** (1.0 g, 3.89 mmol) and *N*,*N*-dimethylformamide (1.20 mL, 15.56 mmol) in 1,2-dichloroethane was slowly added $POCl_3$ (1.45 mL, 15.56 mmol) at 0 °C, and stirred for 1 h under argon. Then, the reaction mixture was allowed to heat to 60 °C and stirred overnight. The mixture was cooled to 0 °C and neutralized using $NaHCO_3$ (aq.). The organic layer was extracted using CH_2Cl_2 and dried over anhydrous Na_2SO_4 and concentrated in vacuo. The crude compound was purified by column chromatography on silica gel with CH_2Cl_2/n-hexane (40 %) as the eluent to afford **5b** as a yellow oil (0.83 g, 75%). ^{1}H NMR (500 MHz, $CDCl_3$) δ [ppm]: 9.96 (s, 1H), 7.85 (d, J = 8 Hz, 1H), 7.73 (s, 1H), 7.42 (d, J = 3.5 Hz, 2H), 7.24-7.20 (m, 1H), 4.29 (t, J = 7 Hz, 2H), 1.90-1.86 (m, 2H), 1.36-1.28 (m, 6H), 0.86 (t, J = 7 Hz, 3H).

Synthesis of 2,5-bis(4-methyl-4*H*-thieno[3,2-*b*]indol-2-yl)thiazolo[5,4-*d*]thiazole (TiTz-1, 7a). The compound was prepared by adding **5a** (500 mg, 2.32 mmol) and dithiooxamide **6** (140 mg, 1.16 mmol) to nitrobenzene (10 mL). The reaction mixture was heated at 130 °C for 24 h under argon atmosphere. Following cooling to room temperature, Et_2O (50 mL) was added and the resultant precipitate was filtered, dried, and purified by column chromatography on neutral alumina with CH_2Cl_2/n-hexane (50 %) as the eluent to afford **TiTz-1**, **7a** as a reddish brown solid (452 mg, 76%). m.p.: 350 °C. ^{1}H NMR (500 MHz, $CDCl_3$) δ [ppm]: 7.79 (d, J = 8 Hz, 2H), 7.58 (s, 2H), 7.40-7.36 (m, 4H), 7.22 (t, J = 7 Hz, 2H), 3.90 (s, 6H). ESI-MS m/z = 513.0332 (calc. = 512.0258).

Synthesis of 2,5-bis(4-hexyl-4*H*-thieno[3,2-*b*]indol-2-yl)thiazolo[5,4-*d*]thiazole (TiTz-6, 7b). The compound was prepared by adding **5b** (500 mg, 1.75 mmol) and dithiooxamide **6** (105 mg, 0.88 mmol) to nitrobenzene (10 mL). The reaction mixture was heated at 130 °C for 24 h under argon atmosphere. Following cooling to room temperature, Et_2O (50 mL) was added and the resultant precipitate was filtered, dried, and purified by column chromatography on neutral alumina with CH_2Cl_2/n-hexane (40 %) as the eluent to afford **TiTz-6**, **7b** as a reddish brown solid (415 mg, 72%). m.p.: 150 °C. ^{1}H NMR (500 MHz, $CDCl_3$) δ [ppm]: 7.78 (d, J = 8 Hz, 2H), 7.54 (s, 2H), 7.39-7.33 (m, 4H), 7.20 (t, J = 7 Hz, 2H), 4.24 (t, J = 7 Hz, 4H), 1.92-1.86 (m, 4H), 1.39-1.25 (m, 12H), 0.88 (t, J = 7 Hz, 6H). ^{13}C NMR (125 MHz, $CDCl_3$) δ [ppm]: 163.2, 144.6, 142.0, 123.9, 121.3, 119.7, 119.6, 110.1, 109.5, 45.3, 31.5, 29.7, 26.8, 22.6, 14.02. ESI-MS m/z = 653.1921 (calc. = 652.1823).

4.6. References

1. P. Xue, J. Ding, P. Wang, R. Lu, *J. Mater. Chem. C* **2016**, *4*, 6688.
2. H. Sun, S. Liu, W. Lin, K. Y. Zhang, W. Lv, X. Huang, F. Huo, H. Yang, G. Jenkins, Q. Zhao, W. Huang, *Nat. Commun.* **2014**, *5*, 3601.
3. Y. Sagara, T. Kato, *Nat. Chem.* **2009**, *1*, 605.
4. S. Yoshimitsu, Y. Shogo, M. Masato, W. Christoph, K. Takashi, *Adv. Mater.* **2016**, *28*, 1073.
5. Z. G. Chi, X. Q. Zhang, B. J. Xu, X. Zhou, C. P. Ma, Y. Zhang, S. W. Liu, J. R. Xu, *Chem. Soc. Rev.* **2012**, *41*, 3878.
6. L. L. Huang, Y. X. Qiu, C. Y. Wu, Z. Y. Ma, Z. H. Shen, X. R. Jia, *J. Mater. Chem. C* **2018**, *6*, 10250.

7. Y. Hou, J. R. Du, J. D. Hou, P. J. Shi, K. Wang, S. Zhang, T. Y. Han, Z. F. Li, *Dyes Pigments* **2019**, *160*, 830.
8. P. S. Hariharan, E. M. Mothi, D. Moon, S. P. Anthony, *ACS Appl. Mater. Interfaces* **2016**, *8*, 33034.
9. G. I. Peterson, M. B. Larsen, M. A. Ganter, D. W. Storti, A. J. Boydston, *ACS Appl. Mater. Interfaces* **2015**, *7*, 577.
10. C. F. Feng, K. Wang, Y. X. Xu, L. Q. Liu, B. Zou, P. Lu, *Chem. Commun.* **2016**, *52*, 3836.
11. R. X. Zhao, L. Zhao, M. Y. Zhang, Z. F. Li, Y. Liu, T. Y. Han, Y. A. Duan, K. Gao, *Dyes Pigments* **2019**, *167*, 181.
12. W. J. Zhao, Z. K. He, Q. Peng, J. W. Y. Lam, H. L. Ma, Z. J. Qiu, Y. C. Chen, Z. Zhao, Z. G. Shuai, Y. Q. Dong, B. Z. Tang, *Nat. Commun.* **2018**, *9*, 3044.
13. D. R. T. Roberts, S. J. Holder, *J. Mater. Chem.* **2011**, *21*, 8256.
14. Y. Gong, S. He, Y. Li, Z. Li, Q. Liao, Y. Gu, J. Wang, B. Zou, Q. Li, Z. Li, *Adv. Optical Mater.* **2020**, *8*, 1902036.
15. Y. B. Gong, P. Zhang, Y. R. Gu, J. Q. Wang, M. M. Han, C. Chen, X. J. Zhan, Z. L. Xie, B. Zou, Q. Peng, Z. G. Chi, Z. Li, *Adv. Optical Mater.* **2018**, *6*, 1800198.
16. M. M. Fang, J. Yang, Q. Y. Liao, Y. B. Gong, Z. L. Xie, Z. G. Chi, Q. Peng, Q. Q. Li, Z. Li, *J. Mater. Chem. C* **2017**, *5*, 9879.
17. C. Wang, Z. Li, *Mater. Chem. Front.* **2017**, *1*, 2174.
18. Y. Takeda, T. Kaihara, M. Okazaki, H. Higginbotham, P. Data, N. Tohnai, S. Minakata, *Chem. Commun.* **2018**, *54*, 6847.
19. Y. B. Guo, L. Xu, H. B. Liu, Y. J. Li, C. M. Che, Y. L. Li, *Adv. Mater.* **2015**, *27*, 985.
20. S.-J. Yoon, J. W. Chung, J. Gierschner, S. Kim, M.-G. Choi, D. Kim, S. Y. Park, *J. Am. Chem. Soc.* **2010**, *132*, 13675.
21. Z. G. Guo, Z. X. Jin, Y. Y. Wang, J. Pei, *Chem. Commun.* **2014**, *50*, 6088.

22. T. Butler, W. A. Morris, J. Samonina-Kosicka, C. L. Fraser, *Chem. Commun.* **2015**, *51*, 3359.
23. M. Sameiro, T. Goncalves, *Chem. Rev.* **2009**, *109*, 190.
24. B. J. Xu, J. J. He, Y. X. Mu, Q. Z. Zhu, S. K. Wu, Y. F. Wang, Y. Zhang, C. J. Jin, C. C. Lo, Z. G. Chi, A. Lien, S. W. Liu, J. R. Xu, *Chem. Sci.* **2016**, *7*, 5307.
25. J. Mei, J. Wang, A. Qin, H. Zhao, W. Yuan, Z. Zhao, H. H. Y. Sung, C. Deng, S. Zhang, I. D. Williams, J. Z. Sun, B. Z. Tang, *J. Mater. Chem.* **2012**, *22*, 4290.
26. Y. Gong, Y. Tan, J. Liu, P. Lu, C. Feng, W. Z. Yuan, Y. Lu, J. Z. Sun, G. He, Y. Zhang, *Chem. Commun.* **2013**, *49*, 4009.
27. X. K. Zheng, Y. Zheng, L. Peng, Y. Xiang, A. J. Tong, *J. Phys. Chem. C* **2017**, *121*, 21610.
28. P. J. Shi, R. X. Zhao, M. Y. Zhang, M. Q. Lin, Y. A. Duan, T. Y. Han, *Mater. Lett.* **2019**, *243*, 38.
29. T. Butler, W. A. Morris, J. Samonina-Kosicka, C. L. Fraser, *ACS Appl. Mater. Interfaces* **2016**, *8*, 1242.
30. Q. K. Qi, J. Y. Qian, X. Tan, J. B. Zhang, L. J. Wang, B. Xu, B. Zou, W. J. Tian, *Adv. Funct. Mater.* **2015**, *25*, 4005.
31. M. Zhang, Y. Li, K. Gao, Z. Li, Y. Liu, Y. Liao, Y. Duan, T. Han, *Dyes Pigments* **2020**, *173*, 107928.
32. J. Luo, L. Y. Li, Y. Song, J. Pei, *Chem. Eur. J.* **2011**, *17*, 10515.
33. Y. Liu, Q. Zeng, B. Zou, Y. Liu, B. Xu, W. Tian, *Angew. Chem. Int. Ed.* **2018**, *57*, 15670.
34. J. W. Chung, Y. You, H. S. Huh, B. K. An, S. J. Yoon, S. H. Kim, S. W. Lee, S. Y. Park, *J. Am. Chem. Soc.* **2009**, *131*, 8163.
35. M. S. Kwon, J. Gierschner, S. J. Yoon, S. Y. Park, *Adv. Mater.* **2012**, *24*, 5487.
36. M. S. Kwon, J. Gierschner, J. Seo, S. Y. Park, *J. Mater. Chem. C* **2014**, *2*, 2552.
37. Z. Guo, S. Park, J. Yoon, I. Shin, *Chem. Soc. Rev.* **2014**, *43*, 16.

38. H. Lu, Y. Zheng, X. Zhao, L. Wang, S. Ma, X. Han, B. Xu, W. Tian, H. Gao, *Angew. Chem. Int. Ed.* **2016**, *55*, 155.
39. G. Qian, Z. Y. Wang, *Chem. Asian J.* **2010**, *5*, 1006.
40. F. Zhang, L. Zhai, S. Feng, W. Mi, J. Sun, M. Sun, J. Zhao, R. Lu, *Dyes Pigments* **2018**, *156*, 140.
41. Z. Liu, K. Zhang, Q. Sun, Z. Zhang, L. Tang, S. Xue, D. Chen, H. Zhang, W. Yang, *J. Mater. Chem. C* **2018**, *6*, 1377.
42. J. Chen, D. Li, W. Chi, G. Liu, S. H. Liu, X. Liu, C. Zhang, J. Yin, *Chem. Eur. J.* **2018**, *24*, 3671.
43. X. Cheng, D. Li, Z. Zhang, H. Zhang, Y. Wang, *Org. Lett.* **2014**, *16*, 880.
44. J. Qi, C. Sun, D. Li, H. Zhang, W. Yu, A. Zebibula, J. W. Y. Lam, W. Xi, L. Zhu, F. Cai, P. Wei, C. Zhu, R. T. K. Kwok, L. L. Streich, R. Prevedel, J. Qian, B. Z. Tang, *ACS Nano* **2018**, *12*, 7936.
45. K. Guo, F. Zhang, S. Guo, K. Li, X. Lu, J. Li, H. Wang, J. Cheng, Q. Zhao, *Chem. Commun.* **2017**, *53*, 1309.
46. P. Wen, Z. Gao, R. Zhang, A. Li, F. Zhang, J. Li, J. Xie, Y. Wu, M. Wu, K. Guo, *J. Mater. Chem. C* **2017**, *5*, 6136.
47. J. Li, J. Xie, R. Zhang, S. Guo, F. Zhang, K. Guo, S. Dong, *Chem. Commun.* **2018**, *54*, 11455.
48. F. Zhang, R. Zhang, X. Liang, K. Guo, Z. Han, X. Lu, J. Xie, J. Li, D. Li, X. Tian, *Dyes Pigments* **2018**, *155*, 225.
49. S. Yagai, S. Okamura, Y. Nakano, M. Yamauchi, K. Kishikawa, T. Karatsu, A. Kitamura, A. Ueno, D. Kuzuhara, H. Yamada, T. Seki, H. Ito, *Nat. Commun.* **2014**, *5*, 4013.
50. Y. K. Eom, S. H. Kang, I. T. Choi, Y. Yoo, J. Kim, H. K. Kim, *J. Mater. Chem. A* **2017**, *5*, 2297.
51. T. Ghosh, A. Gopal, S. Nagasawa, N. Mohan, A. Saeki, C. Vijayakumar, *ACS Appl. Mater. Interfaces* **2016**, *8*, 25396.

52. R. C. Knighton, A. J. Hallett, B. M. Kariuki, S. J. A. Pope, *Tetrahedron Lett.* **2010**, *51*, 5419.
53. H. J. Butt, B. Cappella, M. Kappl, *Surf. Sci. Rep.* **2005**, *59*, 1.
54. D. Passeri, A. Bettucci, A. Biagioni, M. Rossi, A. Alippi, E. Tamburri, M. Lucci, I. Davoli, S. Berezina, *Ultramicroscopy* **2009**, *109*, 1417.
55. M. Słowikowska, K. Wolski, A. J. Wójcik, D. Wesner, H. Schönherr, S. Zapotocznya, *Polym. Chem.* **2020**, *11*, 7050.

ABSTRACT

Name of the Student: **Ms. Susanna Poulose** Registration No.: 10CC17A39017
Faculty of Study: Chemical Sciences Year of Submission: 2023
AcSIR academic centre/CSIR Lab: CSIR-National Institute for Interdisciplinary Science and Technology (CSIR-NIIST) Name of the Supervisor: Dr. Vijayakumar C.

Title of the thesis: **Design, Synthesis, and Characterization of Stimuli-Responsive Organic Fluorescent Materials: An Exploration into Functional Molecular Assemblies**

Creating organic molecules capable of dynamic, high-contrast, and reproducible switching of solid-state luminescence presents a formidable but essential challenge for numerous optoelectronic applications. A thorough comprehension of molecular structure-packing-performance relationships, as well as a careful molecular design featuring different substituents as functional units to alter various intermolecular interactions, could yield superior stimuli-responsive materials. Supramolecular self-assembly has emerged as an efficient tool to organize functional molecules into nano- or microscopic structures *via* diverse non-covalent interactions. This method allows the optoelectronic properties of the assembled organic chromophores to be readily controlled by altering the molecular packing mode and/or modulating the supramolecular interactions. Employing external stimuli to control the mode of solid-state molecular stacking of functional chromophores stands as an effective strategy in this direction. **The first chapter** provides an overview of fluorescent organic stimuli-responsive materials, in-depth analysis of the current state of the field, and major objectives of the present thesis.

In chapter 2, we successfully synthesized three acceptor-donor-acceptor type divinylbenzene-benzoxazole-based derivatives with different alkyl chains. Our findings confirmed that heat-induced control over charge-transfer interactions in chromophore assemblies provides a promising approach for developing materials with switchable, high-contrast solid-state luminescence. Notably, characteristics of the luminescence switching, such as its reversibility, color range, and transition temperature, are found to be dependent on the length of the alkyl chains. This observation underscores the importance of alkyl chain length as a significant parameter in controlling the stimuli-responsive properties of these molecules.

The chapter 3 describes the synthesis of a novel thienoindole-benzoxazole based donor-π-acceptor type fluorophore and demonstrated its daylight-induced, regioselective and stereospecific, catalyst- and template-free [2+2] cycloaddition and the stimuli-responsive properties. Donor-acceptor π–π interactions between the fluorophores bring the two reacting double bonds closer and arrange them in a specific geometry to yield a single *syn*-HT photodimer during crystallization. The photodimer exhibited remarkable photoconductivity, a property that outperforms typical fullerene-based semiconductors. This material offers promising potential in the domain of organic optoelectronic devices and exhibited remarkable fluorescence off-on switching upon protonation-deprotonation effect.

In chapter 4, we synthesized two thiazolothiazole-thienoindole based novel π-conjugated donor-acceptor-donor type NIR fluorophores with different alkyl chains, showcasing high-contrast mechanoresponsive luminescence turn-on in the NIR region. A detailed study of these materials allowed us to understand the structural and environmental factors influencing their luminescence properties, opening exciting possibilities for high-contrast optical recording, mechanical force sensors, and security applications. In conclusion, our work underscores the significance of understanding the molecular structure and non-covalent interactions of organic chromophores, which are key to manipulating their stimuli-responsive properties. The remarkable results obtained from our research hold promise for the continued development of stimuli-responsive organic materials and their applications, demonstrating the untapped potential in this rapidly evolving field.

List of Publications Emanating from the Thesis

1. **Susanna Poulose**, Karattu Chali Naeem, and Chakkooth Vijayakumar,* Heat-Induced 'Parallel' to 'Orthogonal' Switching of Fluorophores and Reversible Luminescence Changes in Divinylbenzene-Benzoxazole Crystals, *Mater. Today Chem.* **2023**, *31*, 101614.

2. **Susanna Poulose**, Akinori Saeki, and Chakkooth Vijayakumar,* Catalyst- and Template-Free [2+2] Cycloaddition: Regioselective and Stereospecific Synthesis of Photoconductive Cyclobutane Crystals (Manuscript submitted).

3. **Susanna Poulose**, and Chakkooth Vijayakumar,* Thiazolothiazole-Thienoindole based D-A-D Fluorophores with Remarkable Near-Infrared Mechanoresponsive Luminescence Turn-on (Manuscript to be submitted).

List of Publications not Related to Thesis Work

1. Chakkooth Vijayakumar,* Kalathil K. Kartha, Bijitha Balan, **Susanna Poulose**, and Masayuki Takeuchi,* Protein-Assisted Supramolecular Control over Fluorescence Resonance Energy Transfer in Aqueous Medium, *J. Phys. Chem. C* **2019**, *123*, 13141-13146.

2. Sheba Ann Babu, Varsha P. V., **Susanna Poulose**, Sunil Varughese, and Jubi John,* Copper-Catalyzed Annulation of Electrophilic Benzannulated Heterocycles with 2-Aminopyridine and 2-Aminoquinoline: Direct Access towards Polyring-fused Imidazo[1,2-a]pyridines, *J. Org. Chem.* **2023**, DOI: https://doi.org/10.1021/acs.joc.3c00849

3. **Susanna Poulose**, Neethi Raveendran, Navin Jacob, and Chakkooth Vijayakumar,* Sustainable Thermoelectric Composite from Rice Husk (Manuscript under preparation).

List of Papers/Posters Presented in Conference

1. **Susanna Poulose**, and C. Vijayakumar,* Heat-Induced Tunable Solid-State Photoluminescence in Divinylbenzene-Benzoxazole based Charge Transfer Molecular Assemblies, 16th JNCASR research conference on chemistry of materials, Jawaharlal Nehru Centre for Advanced Scientific Research (JNCASR), Bengaluru, October 2022 (**Poster Presentation**).

2. **Susanna Poulose**, and C. Vijayakumar,* H-bonded Supramolecular "Hanging Bridge-Type" Thienoindole-Benzoxazole based Cyclobutane Derivative with a High Photoconductivity, International Conference on Chemistry and Applications of Soft Materials (CASM 2022), CSIR-National Institute for Interdisciplinary Science and Technology (NIIST), Trivandrum, July 2022 (**Poster Presentation**).

3. **Susanna Poulose**, Karattu Chali Naeem, Vijayakumar Chakkooth,* Heat-Induced Tunable Solid-State Photoluminescence in Divinylbenzene-Benzoxazole Derivatives, The 22nd RIES-HOKUDAI International Symposium, Japan, December 2021 (**Poster Presentation**).

4. **Susanna Poulose**, K. C. Naeem, C. Vijayakumar,* Alkyl Chains Assisted Control over Heat-Induced Photoluminescence Switching in Divinylbenzene-Benzoxazole Derivatives, International Conference on Emerging Frontiers in Chemical Sciences (EFCS-2021), Department of Chemistry, Farook College, October 2021 (**Oral Presentation**).

5. **Susanna Poulose**, and C. Vijayakumar,* Reversible Switching of Visible-to-NIR Absorption and Fluorescence in Novel Thiazolothiazole-Thienoindole based Electrochromic Devices, RSC-IISER Desktop Seminar with PCCP, May 2021 (**Poster Presentation**).

6. **Susanna Poulose**, C. Vijayakumar,* Thiazolothiazole-Thienoindole Derivative based Electrochromic Devices: Reversible Switching of Visible-to-NIR Absorption and Fluorescence, International Conference on Materials for the Millennium (MatCon 2021), Department of Applied Chemistry, Cochin University of Science and Technology, March 2021 (**Poster Presentation**).

7. **Susanna Poulose**, Naeem K. C., Vijayakumar C. Nair,* Heat-induced Switching of Solid-state Luminescence in Benzoxazole based Oligomers, 14th International Conference on Ecomaterials (ICEM), CSIR-National Institute for Interdisciplinary

Science and Technology (NIIST), Trivandrum, February 2020 (**Poster Presentation**).

8. **Susanna Poulose**, CEMSupra 2019, RIKEN Center for Emergent Matter Science, Ito Hall, The University of Tokyo, Japan, December 2019 (**Participation**).
9. **Susanna Poulose**, Karattu Chali Naeem, Sreedevi T. E, Vijayakumar C. Nair,* Thermally induced dynamic switching of solid-state luminescence for smart optoelectronic device applications, 31st Kerala Science Congress, Kollam, February 2019 (**Poster Presentation**).
10. **Susanna Poulose**, Karattu Chali Naeem, Sreedevi T. E, Vijayakumar C. Nair,* Thermally induced solid-state fluorescence switching in benzoxazole based oligomers, International Symposium on New Trends in Applied Chemistry (NTAC2019), SH College, Kochi, January 2019 (**Poster Presentation**).
11. **Susanna Poulose**, 8th East Asia Symposium on Functional Dyes and Advanced Materials (EAS8), CSIR-National Institute for Interdisciplinary Science and Technology (NIIST), Trivandrum, September 2017 (**Participation**).

Materials Today Chemistry 31 (2023) 101614

Contents lists available at ScienceDirect

Materials Today Chemistry

journal homepage: www.journals.elsevier.com/materials-today-chemistry/

Heat-induced 'parallel' to 'orthogonal' switching of fluorophores and reversible luminescence changes in divinylbenzene-benzoxazole crystals

S. Poulose [a, b], K.C. Naeem [a, b], C. Vijayakumar [a, b, *]

[a] Chemical Science and Technology Division, CSIR-National Institute for Interdisciplinary Science and Technology (NIIST), Thiruvananthapuram, 695019, India
[b] Academy of Scientific and Innovative Research (AcSIR), Ghaziabad, 201002, India

ARTICLE INFO

Article history:
Received 31 January 2023
Received in revised form
22 April 2023
Accepted 2 June 2023
Available online 24 June 2023

Keywords:
Luminescent materials
Thermoresponsive
Chromophore packing
Charge transfer
Supramolecular forces

ABSTRACT

Organic crystals that exhibit reversible solid-state luminescence triggered by heat stimulus have garnered great research interest in recent years. In this work, we demonstrate thermoresponsive, reversible color and photoluminescence switching in divinylbenzene-benzoxazole derivatives. The fluorescence switching is caused by differential chromophore packing and the resulting charge transfer On/Off states induced by heat. It is noteworthy that the reversibility, range of colors, and transition temperature associated with the luminescence switching are dependent on the length of the alkyl chains. Our results suggest that controlling charge-transfer interactions in chromophore assemblies may offer a versatile approach for creating functional organic materials with switchable, high-contrast solid-state luminescence. These findings have implications for the development of sensors, data storage devices, dynamic optical materials, and security inks.

1. Introduction

Organic luminescent crystals have a wide range of applications, including lasers, light-emitting diodes, data storage devices, and solar concentrators [1–14]. In recent years, many solid-state photoluminescent materials that respond to temperature, light, pressure, mechanical force, chemical, and electrical stimuli have been reported [15–24]. These smart materials undergo reversible changes to their superstructures or crystalline phases in response to external stimuli, resulting in different emission colors. Among organic smart materials, those that exhibit thermoresponsive luminescence, or reversible emission color induced by heat, have gained particular attention due to their potential for use in next-generation thermal sensors, information storage devices, dynamic optical materials and anti-counterfeiting paintings [25–33]. As a result, research groups have focused on developing advanced luminescent organic materials with improved temperature sensing performance. In this context, controlling molecular packing modes to fine-tune emission characteristics of luminescent crystals has become increasingly crucial, paving the way for innovations in the field [34–43].

Araki et al. were among the first to report on the efficient on-off switching of solid-state luminescence through heat-induced conversion in a terpyridine derivative [44]. Afterwards, Park et al. created a material based on cyanostilbene that displayed a change in luminescence due to the ability of the molecular layers to slide in two dimensions. This was achieved through intermolecular hydrogen bonds formed by C–H···N and C–H···O, which were triggered by external stimuli [40]. Rao et al. reported on quinoxaline-based molecules exhibiting thermoresponsive emission due to the alteration of two-dimensional herringbone to one-dimensional J-type stacks [45]. Weder and co-workers synthesized a derivative of cyanostilbene that can form five distinct solid-state molecular assemblies and changes its luminescence in response to thermal and mechanical stimuli [46]. They also developed a derivative of cyclophane that displays changes in solid-state fluorescence in response to mechanical and thermal stimuli, which are enabled by changes in molecular assembly [23]. Recently, the same group developed a supramolecular polymer that exhibits thermoresponsive luminescence [47]. These findings collectively suggest that modifying molecular stacking modes serves as an effective

* Corresponding author.
E-mail address: cvijayakumar@niist.res.in (C. Vijayakumar).

https://doi.org/10.1016/j.mtchem.2023.101614
2468-5194/

method for fine-tuning the optical and electronic properties of π-conjugated organic materials.

While significant progress has been made in the development of thermoresponsive luminescent materials, as evidenced by the aforementioned research, there remains a gap in understanding how to precisely control the charge transfer interactions in molecular assemblies to achieve high-contrast luminescence switching. Addressing this research gap, our work aims to provide insights into the manipulation of acceptor-donor-acceptor (A-D-A) type molecules for optimal performance in thermoresponsive applications. In this study, we demonstrate reversible On/Off control of charge transfer interaction between A-D-A type molecules through a 'crystal' to 'crystal' transition, which involves a change in fluorophore stacking mode from "parallel" (P-form) to "orthogonal" (O-form), resulting in efficient switching of solid-state luminescence with high contrast (Fig. 1a). To achieve this, we designed and synthesized three derivatives of divinylbenzene-benzoxazole-based molecules containing different lengths of alkyl sidechains: hexyl (**DB-C$_6$**), dodecyl (**DB-C$_{12}$**), and octadecyl (**DB-C$_{18}$**), as shown in Fig. 1b. Our findings reveal that the reversibility, transition temperatures, and range of wavelengths associated with luminescence switching can be controlled by varying the alkyl chain length.

2. Results and discussion

The molecules under study were synthesized *via* Knoevenagel condensation reaction between alkoxy-substituted terephthalaldehyde and 2-methylbenzoxazole (Scheme S1). All three derivatives displayed good thermal stability up to 300 °C (Fig. S1). The Supporting Information includes the photophysical characteristics of the molecules in solution. The absorption spectra were relatively unchanged by variations in solvent polarity, but the emission spectra exhibited a notable shift towards red as the solvent polarity increased. Variations in alkyl chain length did not have an impact on the photophysical properties of the molecules in solution.

High quality single crystals of **DB-C$_6$** were synthesized through the slow evaporation of its saturated solution in a 1:1 vol ratio of CH_2Cl_2/CH_3OH. Upon heating, the orange color of the crystals changed to yellow and the emission switched from red to green. Fig. 2a and b shows photographs of the parallel (P-form) and orthogonal (O-form) crystals under room light and 365 nm UV light, respectively. The P-form displayed broad absorption in the visible region with an onset at 565 nm and an absorption maximum at 420 nm (Fig. 2c). Upon heating at 65 °C (O-form), the absorption

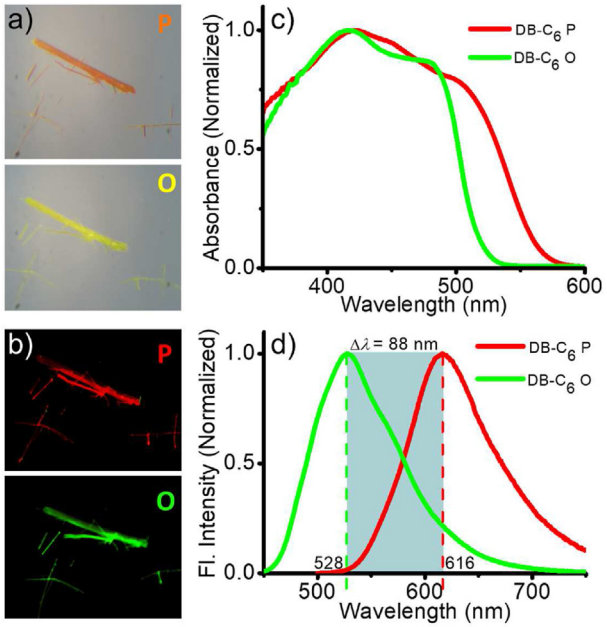

Fig. 2. Photographs of **DB-C$_6$** crystals in the parallel (P-form) and orthogonal (O-form) states under a) room light and b) 365 nm UV light. The corresponding normalized c) absorption and d) photoluminescence spectra of the crystals.

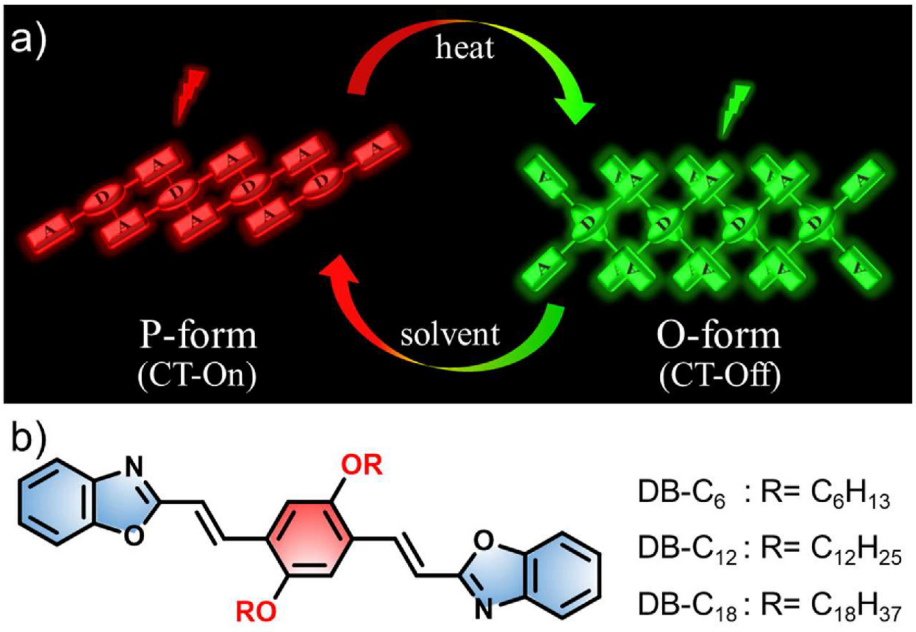

Fig. 1. a) Schematic illustration of the heat-induced switching of molecular packing in divinylbenzene-benzoxazole derivatives, leading to the charge transfer On/Off (CT-On/Off) states and corresponding luminescence color changes. b) Chemical structures of the divinylbenzene-benzoxazole derivatives under study.

onset was significantly blue-shifted to 520 nm with a slight blue-shift of 5 nm to the absorption maximum. **DB-C_6** exhibited two emissive states corresponding to the P- and O-forms. The P-form had an emission maximum at 616 nm with red luminescence. Upon heating, the emission maximum shifted to 528 nm with a green luminescence (Fig. 2d). The absolute quantum yield of the P- and O-forms were 37% and 54%, respectively. The O-form was stable at ambient temperature, maintaining the same emission maximum and intensity. The P-form was recovered by dissolving the O-form in a suitable solvent (such as chloroform, dichloromethane, or tetrahydrofuran) and then precipitating it by adding cold hexane.

The phase transition related to the change in luminescence was studied using differential scanning calorimetry (DSC; as shown in Fig. 3a). A wide endothermic peak was observed at 65 °C during the initial heating cycle, corresponding to the transformation of P-form to the O-form. However, this peak was not observed during the second heating cycle, indicating that the change from O- to P-form is irreversible upon cooling. A sharp endothermic transition was also seen at 156 °C, which is the melting point of the sample, and the exothermic change at 129 °C is believed to be the result of the regeneration of the O-form. Raman spectroscopy was used to analyze the molecules, as it would provides precise structural information such as the degree of π-electron delocalization, molecular order, and supramolecular arrangement [48–50]. The Raman spectra of the P- and O-forms were recorded using a laser excitation source of 785 nm (Fig. 3b). The most intense Raman bands in the 1200-1700 cm^{-1} region are associated with the skeletal C=C/C–C stretching vibrations of the conjugated backbone. Notably, a vibrational band at 1520 cm^{-1} in the P-form showed a significant upward frequency shift to 1545 cm^{-1} ($\Delta\nu = 25$ cm^{-1}) in the O-form. This frequency shift indicates changes in the structural π-conjugation between the benzoxazole unit and the central phenyl group due to changes in the torsional dihedral angle. The associated changes in intensity patterns suggest differences in the intermolecular interactions operating in both the P- and O-forms. Milani et al. demonstrated that higher intermolecular interactions due to efficient molecular packing can induce "pinning effects," resulting in reduced Raman intensity [48]. Therefore, it can be concluded that the P-form has more effective packing compared to the O-form. The morphologies of the P-form and O-form were studied using scanning electron microscopy (SEM), which showed that the transformation from P-form to O-form was accompanied not only with fluorescence switching, but also with changes in the supramolecular morphology (Fig. 3c and d).

In order to understand the heat-induced switching of color and luminescence of **DB-C_6**, we conducted single-crystal X-ray diffraction (SCXRD) analysis on both P- and O-form crystals. Both have a triclinic crystal system with a space group of *P-1*. The P-form crystals form planar molecular sheets through the combination of four intermolecular C–H···N (2.69 Å) and two intramolecular C–H···O (2.22 Å) hydrogen bonds, as well as π-π stacking between donor-acceptor moieties and van der Waals interactions between alkyl chains (Fig. 4a). As the central phenyl ring with two alkoxy-substituents is electron-rich (electron donor, D) while the outer benzoxazole moieties are electron-poor (electron acceptors, A), **DB-C_6** belongs to the class of A-D-A-type molecules, which have two local dipoles that add up to a net zero dipole moment. Upon self-assembly, the antiparallel dipole coupling places the central 'D' ring of the upper sheet just above the 'A' ring of the lower sheet (Fig. 4b), resulting in a parallel arrangement of the molecules. The distance between adjacent molecular sheets is 3.7 Å, consistent with the typical π-π stacking distance.

O-form crystals also form molecular sheets through multiple intermolecular C–H···N (2.65 Å) and intramolecular C–H···O (2.24 Å) hydrogen bonds (Fig. 4c). However, unlike P-form, π-π stacking is observed between the donor moieties of neighboring molecules in O-form, with a relatively larger interlayer distance of 4.15 Å (Fig. 4d). Additionally, the molecular arrangement in O-form is different, with two neighboring molecules from adjacent layers stacked in an orthogonal manner. Only alternate molecules within the layer have four intermolecular and two intramolecular hydrogen bonds due to the 74° turning of alternate molecules in the

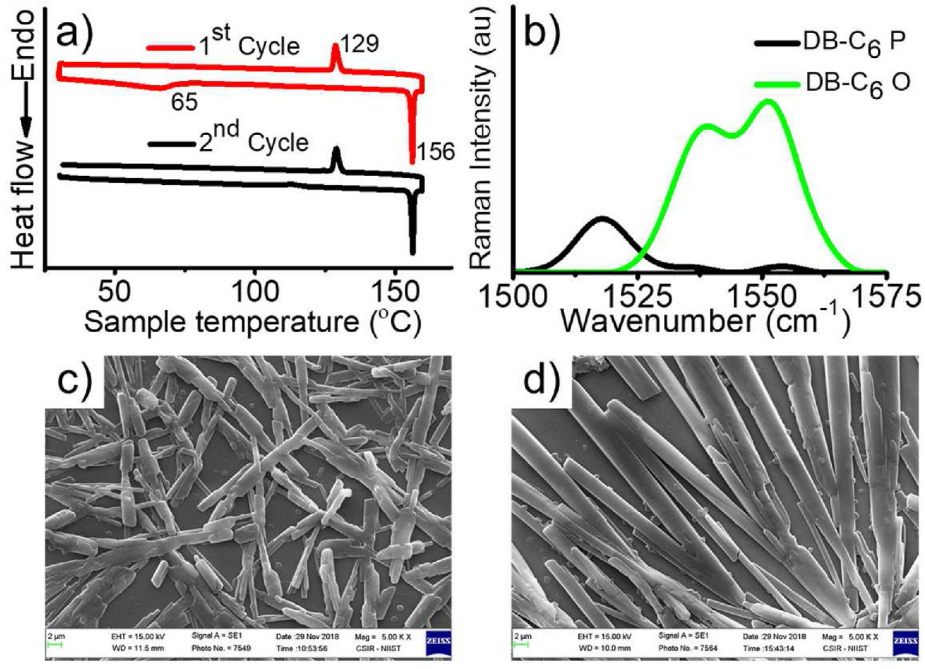

Fig. 3. a) DSC thermogram and b) Raman spectra of **DB-C_6** at different conditions; P (parallel) is the pristine sample and O (orthogonal) is the sample heated at transition temperature (65 °C) followed by air cooling to room temperature. Morphology of **DB-C_6** in c) P- and d) O-form imaged using FE-SEM (scale bar represents 2 μm).

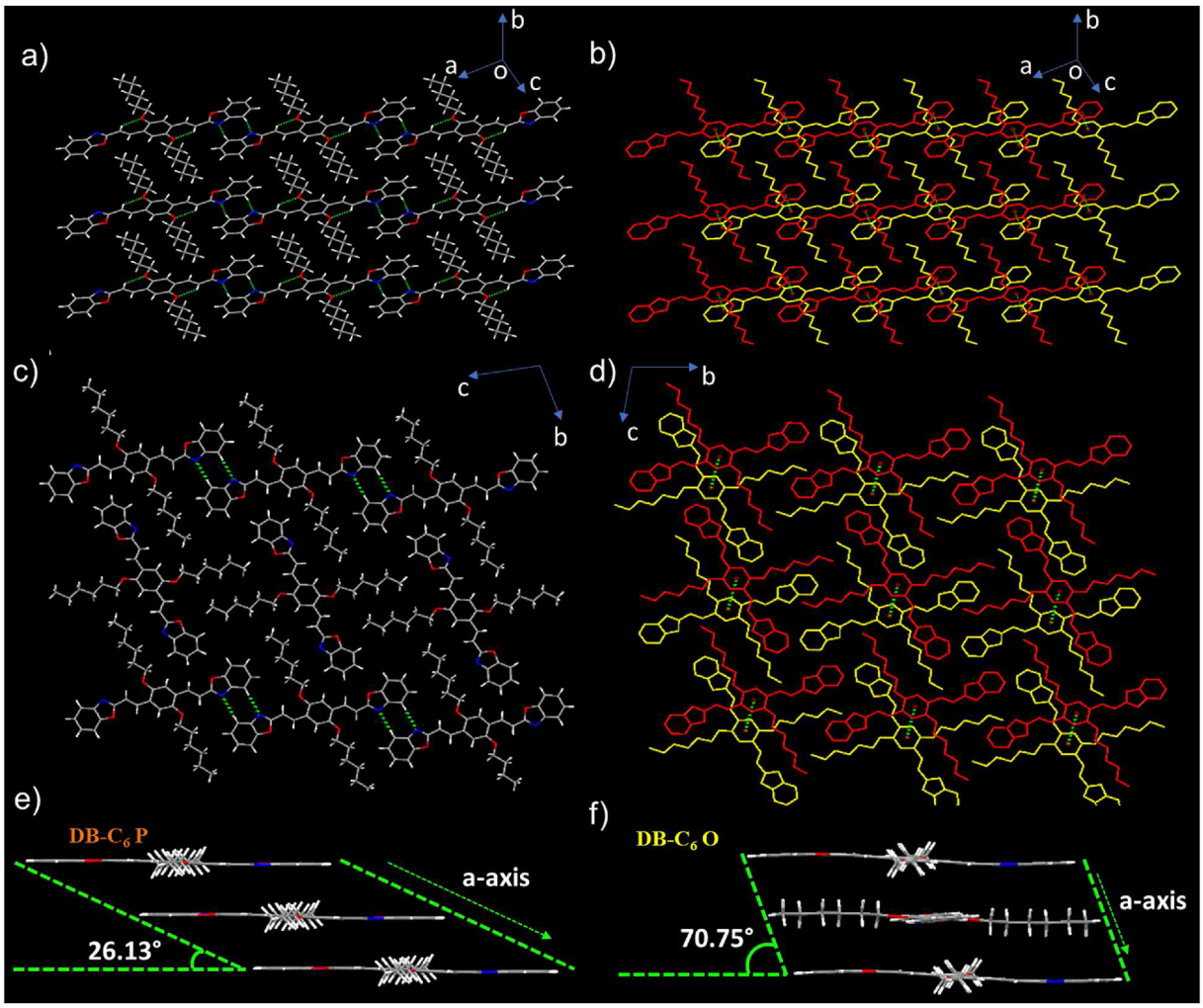

Fig. 4. Molecular packing of **DB-C$_6$** in P- and O-forms; a) Molecular sheets in P-form with a 'parallel' arrangement of chromophores; green lines indicate the intermolecular C—H···N hydrogen-bonding (distance of 2.69 Å) and intramolecular C—H···O hydrogen-bonding (distance of 2.22 Å) b) Stacking of donor - acceptor units in two adjacent molecular sheets in P-form; green lines indicate the π-stacking (distance of 3.68 Å) c) Molecular sheets in O-form with an 'orthogonal' arrangement of chromophores; green lines indicate the intermolecular C—H···N hydrogen-bonding (distance of 2.65 Å) and intramolecular C—H···O (distance of 2.24 Å) d) Stacking of donor - donor units in two adjacent molecular sheets in O-form; green lines indicate the π-stacking (distance of 4.15 Å). Side view and illustration of slip angle of **DB-C$_6$** molecules in e) P-form and f) O-form.

same layer along the *b*-axis. The molecular sheets in the P-form crystal are arranged in slip stacks along the *a*-axis with a slipping angle of 26° (Fig. 4e), while the O-form consists of cross-stacked layers along the *a*-axis with a larger slipping angle of 71° (Fig. 4f).

The alteration in angle demonstrates a smooth sliding of molecules in adjacent layers accompanied along with the transition from a parallel to an orthogonal arrangement. The heat-induced transformation from a slipped "parallel" stacking of molecules in the P-form to "orthogonal" cofacial arrangement in the O-form is unprecedented. The dihedral angle between the central benzene ring and the terminal benzoxazole rings is 3.08° in the P-form, while it is 8.27° in the O-form (Fig. S7). The P-form consists of one molecule per unit cell, while the O-form has two molecules per unit cell. Additionally, the volume of the O-form unit cell is 102% larger (1598.42 Å^3) than the P-form unit cell (791.19 Å^3). These observations are in accordance with the Raman analysis. The driving force behind the P- to O-form transition could be the entropy gain that occurs during heating, which promotes loose packing in the latter and reduces H-bonding interactions and overlap of π-systems. In contrast, the driving force for the O- to P-form transition might be the enthalpy gain through compact packing in the P-form, aided by H-bonding, charge transfer, π-π, and van der Waals interactions.

The observed switching in color and luminescence can be explained by analyzing the molecular packing in the P- and O-form crystals. The donor-acceptor interaction between two neighboring molecular sheets in the P-form facilitates intermolecular charge transfer interaction (CT-On state), leading to red-shifted absorption and emission characteristics. Since the supramolecular binding interactions are weak, heating results in molecular rearrangements (O-form), turning off the charge transfer interaction (CT-Off state) and causing absorption and emission to shift to shorter wavelengths. The increase in absolute quantum yield from the P-form (37%) to the O-form (54%) can be attributed to changes in chromophore packing. In the P-form, parallel arrangement of molecules promotes strong donor-acceptor interactions between adjacent molecules, increasing non-radiative pathways resulting in lower fluorescence quantum efficiency. In contrast, the O-form's orthogonal cross-stacking configuration weakens hydrogen bonding, π-π, and donor-acceptor interactions, reducing non-radiative pathways

yielding improved quantum efficiency. Time-resolved fluorescence lifetime measurement was conducted to understand the change in excited state lifetime accompanied with the fluorescence changes. The fluorescence lifetime of the P-form was 12.58 ns and that of O-form was 2.46 ns. In the former, a pronounced π-orbital overlap is possible between the neighboring molecules, leading to significant excited state electronic delocalization and a longer fluorescence lifetime. In contrast, the orbital overlap between the neighboring molecules is weakened in the O-form, causing the disappearance of excited-state electronic delocalization between adjacent molecules and resulting in a shorter fluorescence lifetime.

Two additional derivatives of the chromophore consisting of dodecyl (**DB-C$_{12}$**) and octadecyl (**DB-C$_{18}$**) chains were synthesized to investigate the influence of the alkyl chain on thermochromic properties. An attempt was made to prepare single crystals of these molecules using the method employed for **DB-C$_6$**, but it was unsuccessful due to the presence of longer alkyl chains, which give the molecules an amorphous nature. However, both derivatives showed a similar trend in heat-induced luminescence switching as that of **DB-C$_6$** (Fig. 5a and b). The P-form of **DB-C$_{12}$** has an emission maximum at 636 nm, which was blue-shifted about 95 nm with an emission maximum centered at 541 nm upon heating at 80 °C, and subsequently cooling to room temperature (O-form). As a result, the emission color changed from red to greenish-yellow. The P-form has an absolute quantum yield of 45%, while the O-form has a quantum yield of 56%. For **DB-C$_{18}$**, the P-form has an emission maximum at 655 nm with red emission, which upon heating at approximately 95 °C, followed by cooling to room temperature, exhibited about 85 nm blue-shifted emission with a maximum centered at 570 nm and bright yellow emission (O-form). The P-form has an absolute quantum yield of 39%, while the O-form has a higher quantum yield of 59%.

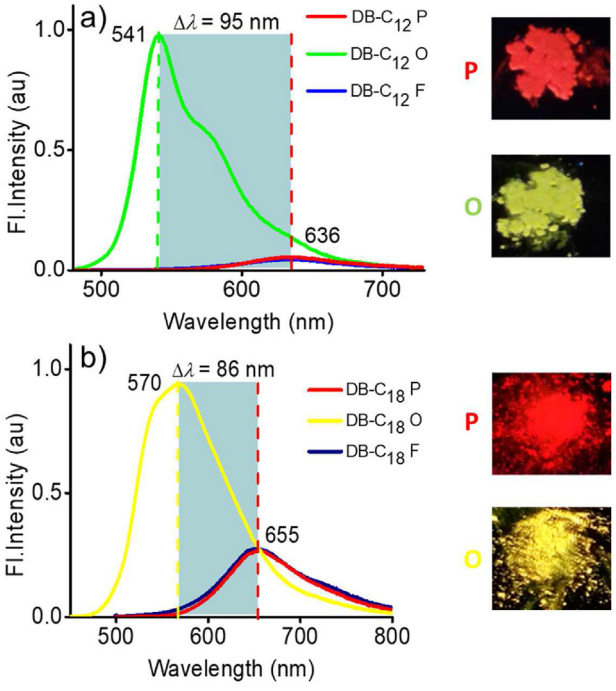

Fig. 5. Photoluminescence spectra of a) **DB-C$_{12}$** and b) **DB-C$_{18}$** in pristine powder form (P), heated at transition temperature and cooled to room temperature (O), and after solvent fuming (see supporting information) of the O-form (F). Photographs of the P- and O-forms under UV light (365 nm) are shown on the right side of the corresponding graphs.

The lower energy shoulder observed at ~580 nm for **DB-C$_{12}$** suggests the presence of distinct vibrational levels in the excited state of the molecule. Emission spectra are associated with radiative transitions between electronic energy levels, typically from an excited state to a lower energy state, such as the ground state. Vibrational features in the emission spectrum arise from transitions between vibrational energy levels associated with the molecular structure of the material. As molecules absorb or emit energy, they can undergo vibrational transitions in addition to electronic transitions, which can result in peaks or bands in the emission spectrum that correspond to the energy difference between different vibrational levels. In fact, the O-forms of all three derivatives exhibit lower energy shoulders in their emission spectra, with slight visibility in **DB-C$_6$**, a well-defined feature in **DB-C$_{12}$**, and nearly invisible in **DB-C$_{18}$**. These variations could be associated with subtle differences in their self-assembled structures due to the variation in alkyl side chain length, which in turn affect the vibrational energy levels and corresponding emission spectra. Notably, a clear trend of red-shift in the emission maximum of both the P-form and O-form is observed with increasing alkyl chain length. This can be attributed to the van der Waals interaction between the alkyl chains of neighboring molecules, which generally increases with an increase in chain length. This increase in interaction improves planarity and effective conjugation length, resulting in red-shifted emission in molecules with longer alkyl chains than those with shorter alkyl chains.

Unlike **DB-C$_6$**, both **DB-C$_{12}$** and **DB-C$_{18}$** exhibited easily reversible luminescence switching upon solvent fuming (such as dichloromethane). While the alkyl chains in **DB-C$_6$** did not facilitate the revival of the P-form from the O-form upon solvent fuming, resulting in a blue-shift in the emission maximum as the material entered a molecularly dissolved state, the C_{12} and C_{18} chains facilitated the recovery of the P-form from the O-form. The O-form of **DB-C$_{12}$** was able to revert back to the P-form within 1–2 min, while it took **DB-C$_{18}$** approximately 10 min to begin recovery and almost 24 h to complete it. The alkyl chains can be seen as solvent molecules attached to the chromophore backbone, helping to solubilize the chromophores and facilitating self-assembly through van der Waals interactions. While the C_6 chain assists in solubilization, it does not contribute to self-assembly due to poor van der Waals interactions resulting from its low chain length. However, both the C_{12} and C_{18} chains assist in both processes, with the C_{18} chain exhibiting the greatest van der Waals interaction among the three due to its longer chain length and thus slower dissolution process and slower recovery to the O-form. The DSC profiles, solid-state absorption, fluorescence lifetime, Raman spectra, temperature-dependent XRD patterns, XRD data to fully demonstrate the cycling property, SEM morphologies of the P- and O-forms of **DB-C$_{12}$** and **DB-C$_{18}$** and NMR spectra of the products are provided in the Supporting Information.

The two distinct molecular packing states, which are luminescent, stable, and reversible, make these compounds useful for smart coating applications. To demonstrate their potential, we have selected **DB-C$_{12}$** and incorporated it into the polymethyl methacrylate (PMMA) matrix. A homogeneous and stable thin film was fabricated on a glass substrate (7.5 cm × 2.5 cm) by spray-coating a solution of **DB-C$_{12}$** and PMMA (1:9 ratio, 5% w/v) in chloroform. When heated (~80 °C), the film undergoes a color change from orange to yellow, along with a shift in luminescence from yellow to greenish-yellow (Fig. 6). Subsequent exposure to solvent vapors (dichloromethane) allows the material to revert to its original form. The reversible and reproducible thermochromic behavior of the fabricated film demonstrates its potential for real-world applications.

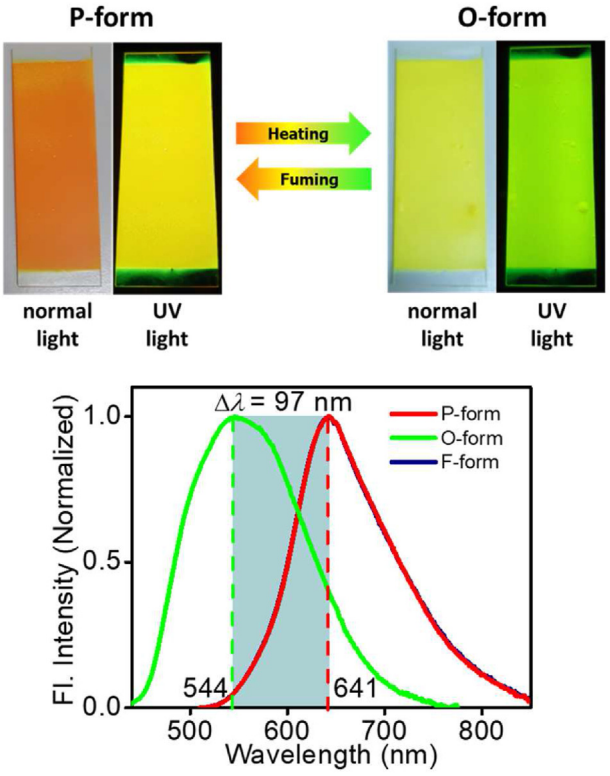

Fig. 6. Thermoresponsive luminescence switching of **DB-C_{12}**/PMMA film on a glass substrate.

3. Conclusions

In summary, the solid-state thermochromic luminescence properties of three divinylbenzene-benzoxazole derivatives with varying alkyl chain lengths were investigated. It was found that the transition between charge transfer On/Off states of the hydrogen-bonded molecular assemblies was responsible for the heat-induced luminescence switching observed in these materials. The alkyl chain lengths significantly impacted the thermoresponsive properties of the molecules, including the reversibility and range of chromism exhibited. These findings provide insight into the structure-property relationship of luminescent thermochromic materials and have potential for the development of smart sensors for practical applications.

CRediT author statement

Susanna Poulose: Methodology, Data curation, Validation, Formal analysis, Investigation, Writing - Original draft preparation, Visualization; **Karattu Chali Naeem:** Investigation; **Chakkooth Vijayakumar:** Conceptualization, Methodology, Validation, Formal analysis, Data curation, Writing - Reviewing and Editing, Visualization, Supervision, Project administration, Funding acquisition.

Declaration of competing interest

The authors declare that they have no known competing financial interests or personal relationships that could have appeared to influence the work reported in this paper.

Data availability

Data will be made available on request.

Acknowledgment

C.V. thanks the Department of Science and Technology (No. CRG/2020/002756) and Kerala State Council for Science, Technology, and Environment (No. KSCSTE/1538/2018-KSYSA-RG) funding. S.P. and K.C.N. thank UGC for the Senior Research Fellowship. We thank Dr. E. Bhoje Gowd for XRD and DSC measurements. We thank Prof. Masayuki Takeuchi for TGA measurements. We thank Dr. Sudha Devi for SCXRD analysis.

Appendix A. Supplementary data

Supplementary data to this article can be found online at https://doi.org/10.1016/j.mtchem.2023.101614.

References

[1] Y. Jiang, Y.-Y. Liu, X. Liu, H. Lin, K. Gao, W.-Y. Lai, W. Huang, Organic solid-state lasers: a materials view and future development, Chem. Soc. Rev. 49 (2020) 5885–5944, https://doi.org/10.1039/D0CS00037J.
[2] J. Gierschner, S. Varghese, S.Y. Park, Organic single crystal lasers: a materials view, Adv. Opt. Mater. 4 (2016) 348–364, https://doi.org/10.1002/adom.201500531.
[3] M.K. Bera, P. Pal, S. Malik, Solid-state emissive organic chromophores: design, strategy and building blocks, J. Mater. Chem. C 8 (2020) 788–802, https://doi.org/10.1039/C9TC04239C.
[4] J. Gierschner, J. Shi, B. Milián-Medina, D. Roca-Sanjuán, S. Varghese, S.Y. Park, Luminescence in crystalline organic materials: from molecules to molecular solids, Adv. Opt. Mater. 9 (2021), 2002251, https://doi.org/10.1002/adom.202002251.
[5] S. Ghosh, S. Shankar, D.S. Philips, A. Ajayaghosh, Diketopyrrolopyrrole-based functional supramolecular polymers: next-generation materials for opto-electronic applications, Mater. Today Chem. 16 (2020), 100242, https://doi.org/10.1016/j.mtchem.2020.100242.
[6] C. Liu, J.-C. Yang, J.W.Y. Lam, H.-T. Feng, B.Z. Tang, Chiral assembly of organic luminogens with aggregation-induced emission, Chem. Sci. 13 (2022) 611–632, https://doi.org/10.1039/D1SC02305E.
[7] J. Zhang, A. Li, H. Zou, J. Peng, J. Guo, W. Wu, H. Zhang, J. Zhang, X. Gu, W. Xu, S. Xu, S.H. Liu, A. Qin, J.W.Y. Lam, B.Z. Tang, A "simple" donor–acceptor AIEgen with multi-stimuli responsive behavior, Mater. Horiz. 7 (2020) 135–142, https://doi.org/10.1039/C9MH01041F.
[8] J. Song, H. Lee, E.G. Jeong, K.C. Choi, S. Yoo, Organic light-emitting diodes: pushing toward the limits and beyond, Adv. Mater. 32 (2020), 1907539, https://doi.org/10.1002/adma.201907539.
[9] S. Mattiello, F. Corsini, S. Mecca, M. Sassi, R. Ruffo, G. Mattioli, Y. Hattori, T. Kusamoto, G. Griffini, L. Beverina, First demonstration of the use of open-shell derivatives as organic luminophores for transparent luminescent solar concentrators, Mater. Adv. 2 (2021) 7369–7378, https://doi.org/10.1039/D1MA00659B.
[10] S. Wu, B. Zhou, D. Yan, Recent advances on molecular crystalline luminescent materials for optical waveguides, Adv. Opt. Mater. 9 (2021), 2001768, https://doi.org/10.1002/adom.202001768.
[11] K. Huang, L. Song, K. Liu, A. Lv, M. Singh, K. Shen, J. Shen, J. Wang, H. Wang, H. Shi, H. Ma, M. Gu, G. Sun, W. Yao, Z. An, W. Huang, Elastic organic crystals with ultralong phosphorescence for flexible anti-counterfeiting, npj Flex. Electron. 5 (2021) 22–27, https://doi.org/10.1038/s41528-021-00117-9.
[12] F. Nie, B. Zhou, K.-Z. Wang, D. Yan, Highly tunable ultralong room-temperature phosphorescence from ionic supramolecular adhesives for multifunctional applications, Chem. Eng. J. 430 (2022), 133084, https://doi.org/10.1016/j.cej.2021.133084.
[13] B. Zhou, Z. Qi, D. Yan, Highly efficient and direct ultralong all-phosphorescence from metal–organic framework photonic glasses, Angew. Chem. Int. Ed. 61 (2022), e202208735, https://doi.org/10.1002/anie.202208735.
[14] R. Gao, M.S. Kodaimati, D. Yan, Recent advances in persistent luminescence based on molecular hybrid materials, Chem. Soc. Rev. 50 (2021) 5564–5589, https://doi.org/10.1039/D0CS01463J.
[15] J. Ochi, K. Tanaka, Y. Chujo, Recent progress in the development of solid-state luminescent *o*-carboranes with stimuli responsivity, Angew. Chem. Int. Ed. 59 (2020) 9841–9855, https://doi.org/10.1002/anie.201916666.
[16] A.M. Osterholm, L. Nhon, D.E. Shen, A.M. Dejneka, A.L. Tomlinson, J.R. Reynolds, Conquering residual light absorption in the transmissive states of organic electrochromic materials, Mater. Horiz. 9 (2022) 252–260, https://doi.org/10.1039/D1MH01136G.
[17] Y. Wang, H. Shang, B. Li, S. Jiang, Reversible luminescence "off-on" regulation based on tunable photodimerization via crystal-to-cocrystal transformation, J. Mater. Chem. C 10 (2022) 734–741, https://doi.org/10.1039/D1TC04401J.
[18] C.-H. Wang, M. Horie, Photo and thermal responsive pseudorotaxane crystals comprising ferrocene-containing ammonium salts and crown ethers, Mater.

Today Chem. 24 (2022), 100852, https://doi.org/10.1016/j.mtchem.2022.100852.
[19] J. Ochi, K. Tanaka, Y. Chujo, Alternately π-stacked systems assisted by *o*-carborane: dual excimer emission and color modulation by b_{cage}-methylation, Angew. Chem. Int. Ed. 62 (2023), e202214397, https://doi.org/10.1002/anie.202214397.
[20] Q. Qi, C. Li, X. Liu, S. Jiang, Z. Xu, R. Lee, M. Zhu, B. Xu, W. Tian, Solid-state photoinduced luminescence switch for advanced anticounterfeiting and super-resolution imaging applications, J. Am. Chem. Soc. 139 (2017) 16036–16039, https://doi.org/10.1021/jacs.7b07738.
[21] M. Echeverri, C. Ruiz, S. Gámez-Valenzuela, M. Alonso-Navarro, E. Gutierrez-Puebla, J.L. Serrano, M.C. Ruiz Delgado, B. Gómez-Lor, Stimuli-Responsive benzothiadiazole derivative as a dopant for rewritable polymer blends, ACS Appl. Mater. Interfaces 12 (2020) 10929–10937, https://doi.org/10.1021/acsami.9b21209.
[22] Y. Chen, X. hang, M. Wang, J. Peng, Y. Zhou, X. Huang, W. Gao, M. Liu, H. Wu, Mechanofluorochromism, polymorphism and thermochromism of novel D–π–A piperidin-1-yl-substituted isoquinoline derivatives, J. Mater. Chem. C 7 (2019) 12580–12587, https://doi.org/10.1039/C9TC03942B.
[23] Y. Sagara, Y.C. Simon, N. Tamaoki, C. Weder, A mechano- and thermoresponsive luminescent cyclophane, Chem. Commun. 52 (2016) 5694–5697, https://doi.org/10.1039/C6CC01614F.
[24] M. Martínez-Abadía, S. Varghese, P. Romero, J. Gierschner, R. Giménez, M.B. Ros, Highly light-sensitive luminescent cyanostilbene flexible dimers, Adv. Opt. Mater. 5 (2017), 1600860, https://doi.org/10.1002/adom.201600860.
[25] H. Liu, W. Song, X. Chen, J. Mei, Z. Zhang, J. Su, Temperature-responsive molecular liquids based on dihydrophenazines for dynamic multicolor-fluorescent anti-counterfeiting and encryption, Mater. Chem. Front. 5 (2021) 2294–2302, https://doi.org/10.1039/D0QM00903B.
[26] J.-F. Chen, X. Yin, B. Wang, K. Zhang, G. Meng, S. Zhang, Y. Shi, N. Wang, S. Wang, P. Chen, Planar chiral organoboranes with thermoresponsive emission and circularly polarized luminescence: integration of pillar[5]arenes with boron chemistry, Angew. Chem. Int. Ed. 59 (2020) 11267–11272, https://doi.org/10.1002/anie.202001145.
[27] C.H. Shin, K.-I. Hong, J.H. Lee, W.-D. Jang, Multimodal stimuli-responsive behaviors of photochromic spiropyran-bearing telechelic poly(2-isopropyl-2-oxazoline), Mater. Today Chem. 24 (2022), 100884, https://doi.org/10.1016/j.mtchem.2022.100884.
[28] P. Yao, W. Qiao, Y. Wang, H. Peng, X. Xie, Z. Li, Deep-red emissive squaraine-AIEgen in elastomer enabling high contrast and fast thermoresponse for anti-counterfeiting and temperature sensing, Chem. Eur J. 28 (2022), e202200725, https://doi.org/10.1002/chem.202200725.
[29] K. Muthamma, D. Sunil, P. Shetty, Luminophoric organic molecules for anti-counterfeit printing ink applications: an up-to-date review, Mater. Today Chem. 18 (2020), 100361, https://doi.org/10.1016/j.mtchem.2020.100361.
[30] T. Yuan, Y. Xu, C. Zhu, Z. Jiang, H.-J. Sue, L. Fang, M.A. Olson, Tunable thermochromism of multifunctional charge-transfer-based supramolecular materials assembled in water, Chem. Mater. 29 (2017) 9937–9945, https://doi.org/10.1021/acs.chemmater.7b03273.
[31] W. Zhang, X. Ji, B.-J. Peng, S. Che, F. Ge, W. Liu, M. Al-Hashimi, C. Wang, L. Fang, High-performance thermoresponsive dual-output dye system for smart textile application, Adv. Funct. Mater. 30 (2020), 1906463, https://doi.org/10.1002/adfm.201906463.
[32] Z. Wu, S. Mo, L. Tan, B. Fang, Z. Su, Y. Zhang, M. Yin, Crystallization-induced emission enhancement of a deep-blue luminescence material with tunable mechano- and thermochromism, Small 14 (2018), 1802524, https://doi.org/10.1002/smll.201802524.
[33] S. Ying, M. Chen, Z. Liu, M. Zheng, H. Hang, S. Xue, W. Yang, Unusual mechanohypsochromic luminescence and unique bidirectional thermofluorochromism of long-alkylated simple DPP dyes, J. Mater. Chem. C 5 (2017) 5994–5998, https://doi.org/10.1039/C7TC01453H.
[34] S. Varghese, S. Das, Role of molecular packing in determining solid-state optical properties of π-conjugated materials, J. Phys. Chem. Lett. 2 (2011) 863–873, https://doi.org/10.1021/jz200099p.
[35] H. Wu, Z. Chen, W. Chi, A.K. Bindra, L. Gu, C. Qian, B. Wu, B. Yue, G. Liu, G. Yang, L. Zhu, Y. Zhao, Structural engineering of luminogens with high emission efficiency both in solution and in the solid state, Angew. Chem. Int. Ed. 58 (2019) 11419–11423, https://doi.org/10.1002/anie.201906507.
[36] C. Wang, Z. Li, Molecular conformation and packing: their critical roles in the emission performance of mechanochromic fluorescence materials, Mater. Chem. Front. 1 (2017) 2174–2194, https://doi.org/10.1039/C7QM00201G.
[37] S.-J. Yoon, J.W. Chung, J. Gierschner, K.S. Kim, M.-G. Choi, D. Kim, S.Y. Park, Multistimuli two-color luminescence switching via different slip-stacking of highly fluorescent molecular sheets, J. Am. Chem. Soc. 132 (2010) 13675–13683, https://doi.org/10.1021/ja1044665.
[38] M.J. Aliaga-Gosalvez, M. Demitri, M. Dohr, J.C. Roldao, S.K. Park, S. Oh, S. Varghese, S. Oh, S.Y. Park, Y. Olivier, B. Milián-Medina, R. Resel, J. Gierschner, Crossed 2D versus slipped 1D π-stacking in polymorphs of crystalline organic thin films: impact on the electronic and optical response, Adv. Opt. Mater. 7 (2019), 1900749, https://doi.org/10.1002/adom.201900749.
[39] Y. Liu, Q. Zeng, B. Zou, Y. Liu, B. Xu, W. Tian, Piezochromic luminescence of donor–acceptor cocrystals: distinct responses to anisotropic grinding and isotropic compression, Angew. Chem. Int. Ed. 57 (2018) 15670–15674, https://doi.org/10.1002/anie.201810149.
[40] S.-J. Yoon, S. Varghese, S.K. Park, R. Wannemacher, J. Gierschner, S.Y. Park, Color-tuned, highly emissive dicyanodistyrylbenzene single crystals: manipulating intermolecular stacking interactions for spontaneous and stimulated emission characteristics, Adv. Opt. Mater. 1 (2013) 232–237, https://doi.org/10.1002/adom.201200064.
[41] Y.-J. Ma, G. Xiao, X. Fang, T. Chen, D. Yan, Leveraging crystalline and amorphous states of a metal-organic complex for transformation of the photosalient effect and positive-negative photochromism, Angew. Chem. Int. Ed. 62 (2023), e202217054, https://doi.org/10.1002/anie.202217054.
[42] D. Yan, D.G. Evans, Molecular crystalline materials with tunable luminescent properties: from polymorphs to multi-component solids, Mater. Horiz. 1 (2014) 46–57, https://doi.org/10.1039/C3MH00023K.
[43] S. Li, B. Lu, X. Fang, D. Yan, Manipulating light-induced dynamic macromovement and static photonic properties within 1D isostructural hydrogen-bonded molecular cocrystals, Angew. Chem. Int. Ed. 59 (2020) 22623–22630, https://doi.org/10.1002/anie.202009714.
[44] T. Mutai, H. Satou, K. Araki, Reproducible on–off switching of solid-state luminescence by controlling molecular packing through heat-mode interconversion, Nat. Mater. 4 (2005) 685–687, https://doi.org/10.1038/nmat1454.
[45] R. Rao M, C.-W. Liao, W.-L. Su, S.-S. Sun, Quinoxaline based D–A–D molecules: high contrast reversible solid-state mechano- and thermo-responsive fluorescent materials, J. Mater. Chem. C 1 (2013) 5491–5501, https://doi.org/10.1039/C3TC31179A.
[46] Y. Sagara, A. Lavrenova, A. Crochet, Y.C. Simon, K.M. Fromm, C. Weder, A thermo- and mechanoresponsive cyano-substituted oligo(p-phenylene vinylene) derivative with five emissive states, Chem. Eur J. 22 (2016) 4374–4378, https://doi.org/10.1002/chem.201600272.
[47] A. Lavrenova, D.W.R. Balkenende, Y. Sagara, S. Schrettl, Y.C. Simon, C. Weder, Mechano- and thermoresponsive photoluminescent supramolecular polymer, J. Am. Chem. Soc. 139 (2017) 4302–4305, https://doi.org/10.1021/jacs.7b00342.
[48] A. Milani, L. Brambilla, M.D. Zoppo, G. Zerbi, Raman dispersion and intermolecular interactions in unsubstituted thiophene oligomers, J. Phys. Chem. B 111 (2007) 1271–1276, https://doi.org/10.1021/jp066933k.
[49] A. Milani, M.D. Zoppo, M. Tommasini, G. Zerbi, The effect of intermolecular Dipole–Dipole interaction on Raman spectra of polyconjugated molecules: density functional theory simulations and mathematical models, J. Phys. Chem. B 112 (2008) 1619–1625, https://doi.org/10.1021/jp075763o.
[50] J.S. Mosca, A. Milani, M. Peña-Álvarez, S. Yamaguchi, V. Hernández, M.C. Ruiz Delgado, C. Castiglioni, Mechanochromic luminescent tetrathiazolylthiophenes: evaluating the role of intermolecular interactions through pressure and temperature-dependent Raman spectroscopy, J. Phys. Chem. C 122 (2018) 17537–17543, https://doi.org/10.1021/acs.jpcc.8b05423.